

Jordan Journal of P H Y S I C S

An International Peer-Reviewed Research Journal

Volume 18, No. 1, March. 2025, Shawwal 1446 H

Jordan Journal of Physics (JJP): An International Peer-Reviewed Research Journal funded by the Scientific Research and Innovation Support Fund, Jordan, and published quarterly by the Deanship of Research and Graduate Studies, Yarmouk University, Irbid, Jordan.

EDITOR-IN-CHIEF: Muhammad S. Bawa'aneh

Department of Physics, Yarmouk University, Irbid, Jordan.
msbawaaneh@yu.edu.jo

EDITORIAL BOARD:	ASSOCIATE EDITORIAL BOARD
<p>Prof. M-Ali H. Al-Akhras (AL-Omari) <i>Department of Physics, Jordan University of Science & Technology, Irbid, Jordan.</i> alakmoh@just.edu.jo</p> <p>Prof. Riyad S. Manasrah <i>Department of Physics, The University of Jordan, Amman, Jordan.</i> r.manasrah@ju.edu.jo</p> <p>Prof. Ibrahim A. Bsoul <i>Department of Physics, Al al-Bayt University, Mafrqa, Jordan.</i> Ibrahimbsoul@yahoo.com</p> <p>Prof. Ahmed M. Al-Khateeb <i>Department of Physics, Yarmouk University, Irbid, Jordan.</i> a.alkhateeb67@gmail.com</p> <p>Prof. Khalid I. Nawafleh <i>Department of Physics, Mutah University, Al-Karak, Jordan.</i> knawaflehh@yahoo.com</p>	<p>Prof. Mark Hagmann <i>Desert Electronics Research Corporation, 762 Lacey Way, North Salt Lake 84064, Utah, U. S. A.</i> MHagmann@NewPathResearch.Com</p> <p>Dr. Richard G. Forbes <i>Dept. of Electrical and Electronic Engineering, University of Surrey, Advanced Technology Institute and Guildford, Surrey GU2 7XH, UK.</i> r.forbes@surrey.ac.uk</p> <p>Prof. Roy Chantrell <i>Physics Department, The University of York, York, YO10 5DD, UK.</i> roy.chantrell@york.ac.uk</p> <p>Prof. Susamu Taketomi <i>2-35-8 Higashisakamoto, Kagoshima City, 892-0861, Japan.</i> staketomi@hotmail.com</p>

Editorial Secretary: Majdi Al-Shannaq.

Languages Editor: Olga Golubeva

Manuscripts should be submitted to:

Prof. Muhammad S. Bawa'aneh
Editor-in-Chief, Jordan Journal of Physics
Deanship of Research and Graduate Studies
Yarmouk University-Irbid-Jordan
Tel. 00 962 2 7211111 Ext. 2075
E-mail: jjp@yu.edu.jo
Website: <https://jjp.yu.edu.jo>

Jordan Journal of
P H Y S I C S

An International Peer-Reviewed Research Journal

Volume 18, No. 1, March. 2025, Shawwal 1446 H

INTERNATIONAL ADVISORY BOARD:

Prof. Dr. Humam B. Ghassib

Department of Physics, The University of Jordan, Amman 11942, Jordan.

humamg@ju.edu.jo

Prof. Dr. Sami H. Mahmood

Department of Physics, The University of Jordan, Amman 11942, Jordan.

s.mahmood@ju.edu.jo

Prof. Dr. Nihad A. Yusuf

Department of Physics, Yarmouk University, Irbid, Jordan.

nihadyusuf@yu.edu.jo

Prof. Dr. Hardev Singh Virk

#360, Sector 71, SAS Nagar (Mohali)-160071, India.

hardevsingh.virk@gmail.com

Dr. Mgr. Dinara Sobola

Department of Physics, Brno University of Technology, Brno, Czech Republic.

Dinara.Dallaeva@ceitec.vutbr.cz

Prof. Dr. Shawqi Al-Dallal

Department of Physics, Faculty of Science, University of Bahrain, Manamah, Kingdom of Bahrain.

Prof. Dr. Jozef Lipka

Department of Nuclear Physics and Technology, Slovak University of Technology, Bratislava, Ilkovicova 3, 812 19 Bratislava, Slovakia.

Lipka@elf.stuba.sk

Prof. Dr. Mohammad E. Achour

Laboratory of Telecommunications Systems and Decision Engineering (LASTID), Department of Physics, Faculty of Sciences, Ibn Tofail University, BP.133, Kenitra, Morocco (Morocco)

achour.me@univ-ibntofail.ac.ma

Prof. Dr. Ing. Alexandr Knápek

Group of e-beam lithography, Institute of Scientific Instruments of CAS, Královopolská 147, 612 64 Brno, Czech Republic.

knapek@isibrno.cz

Prof. Dr. Ahmad Salem

Department of Physics, Yarmouk University, Irbid, Jordan.

salema@yu.edu.jo



The Hashemite Kingdom of Jordan



Yarmouk University

Jordan Journal of PHYSICS

An International Peer-Reviewed Research Journal
Funded by the Scientific Research and Innovation Support Fund

Volume 18, No. 1, March. 2025, Shawwal 1446 H

Instructions to Authors

Instructions to authors concerning manuscript organization and format apply to hardcopy submission by mail, and also to electronic online submission via the Journal homepage website (<http://jjp.yu.edu.jo>).

Manuscript Submission

Manuscripts are submitted electronically through the journal's website:

<https://jjp.yu.edu.jo/>

Original *Research Articles*, *Communications* and *Technical Notes* are subject to critical review by minimum of two competent referees. Authors are encouraged to suggest names of competent reviewers. *Feature Articles* in active Physics research fields, in which the author's own contribution and its relationship to other work in the field constitute the main body of the article, appear as a result of an invitation from the Editorial Board, and will be so designated. The author of a *Feature Article* will be asked to provide a clear, concise and critical status report of the field as an introduction to the article. *Review Articles* on active and rapidly changing Physics research fields will also be published. Authors of *Review Articles* are encouraged to submit two-page proposals to the Editor-in-Chief for approval. Manuscripts submitted in *Arabic* should be accompanied by an Abstract and Keywords in English.

Organization of the Manuscript

Manuscripts should be typed double spaced on one side of A4 sheets (21.6 x 27.9 cm) with 3.71 cm margins, using Microsoft Word 2000 or a later version thereof. The author should adhere to the following order of presentation: Article Title, Author(s), Full Address and E-mail, Abstract, PACS and Keywords, Main Text, Acknowledgment. Only the first letters of words in the Title, Headings and Subheadings are capitalized. Headings should be in **bold** while subheadings in *italic* fonts.

Title Page: Includes the title of the article, authors' first names, middle initials and surnames and affiliations. The affiliation should comprise the department, institution (university or company), city, zip code and state and should be typed as a footnote to the author's name. The name and complete mailing address, telephone and fax numbers, and e-mail address of the author responsible for correspondence (designated with an asterisk) should also be included for official use. The title should be carefully, concisely and clearly constructed to highlight the emphasis and content of the manuscript, which is very important for information retrieval.

Abstract: A one paragraph abstract not exceeding 200 words is required, which should be arranged to highlight the purpose, methods used, results and major findings.

Keywords: A list of 4-6 keywords, which expresses the precise content of the manuscript for indexing purposes, should follow the abstract.

PACS: Authors should supply one or more relevant PACS-2006 classification codes, (available at <http://www.aip.org/pacs/pacs06/pacs06-toc.html>)

Introduction: Should present the purpose of the submitted work and its relationship to earlier work in the field, but it should not be an extensive review of the literature (e.g., should not exceed 1 ½ typed pages).

Experimental Methods: Should be sufficiently informative to allow competent reproduction of the experimental procedures presented; yet concise enough not to be repetitive of earlier published procedures.

Results: should present the results clearly and concisely.

Discussion: Should be concise and focus on the interpretation of the results.

Conclusion: Should be a brief account of the major findings of the study not exceeding one typed page.

Acknowledgments: Including those for grant and financial support if any, should be typed in one paragraph directly preceding the References.

References: References should be typed double spaced and numbered sequentially in the order in which they are cited in the text. References should be cited in the text by the appropriate Arabic numerals, enclosed in square brackets. Titles of journals are abbreviated according to list of scientific periodicals. The style and punctuation should conform to the following examples:

1. Journal Article:

- a) Heisenberg, W., Z. Phys. 49 (1928) 619.
- b) Bednorz, J. G. and Müller, K. A., Z. Phys. B64 (1986) 189
- c) Bardeen, J., Cooper, L.N. and Schrieffer, J. R., Phys. Rev. 106 (1957) 162.
- d) Asad, J. H., Hijjawi, R. S., Sakaji, A. and Khalifeh, J. M., Int. J. Theor. Phys. 44(4) (2005), 3977.

2. Books with Authors, but no Editors:

- a) Kittel, C., "Introduction to Solid State Physics", 8th Ed. (John Wiley and Sons, New York, 2005), chapter 16.
- b) Chikazumi, S., C. D. Graham, JR, "Physics of Ferromagnetism", 2nd Ed. (Oxford University Press, Oxford, 1997).

3. Books with Authors and Editors:

- a) Allen, P. B. "Dynamical Properties of Solids", Ed. (1), G. K. Horton and A. A. Maradudin (North-Holland, Amsterdam, 1980), p137.
- b) Chantrell, R. W. and O'Grady, K., "Magnetic Properties of Fine Particles" Eds. J. L. Dormann and D. Fiorani (North-Holland, Amsterdam, 1992), p103.

4. Technical Report:

Purcell, J. "The Superconducting Magnet System for the 12-Foot Bubble Chamber", report ANL/HEP6813, Argonne Natl. Lab., Argonne, III, (1968).

5. Patent:

Bigham, C. B., Schneider, H. R., US patent 3 925 676 (1975).

6. Thesis:

Mahmood, S. H., Ph.D. Thesis, Michigan State University, (1986), USA (Unpublished).

7. Conference or Symposium Proceedings:

Blandin, A. and Lederer, P. Proc. Intern. Conf. on Magnetism, Nottingham (1964), P.71.

8. Internet Source:

Should include authors' names (if any), title, internet website, URL, and date of access.

9. Prepublication online articles (already accepted for publication):

Should include authors' names (if any), title of digital database, database website, URL, and date of access.

For other types of referenced works, provide sufficient information to enable readers to access them.

Tables: Tables should be numbered with Arabic numerals and referred to by number in the Text (e.g., Table 1). Each table should be typed on a separate page with the legend above the table, while explanatory footnotes, which are indicated by superscript lowercase letters, should be typed below the table.

Illustrations: Figures, drawings, diagrams, charts and photographs are to be numbered in a consecutive series of Arabic numerals in the order in which they are cited in the text. Computer-generated illustrations and good-quality digital photographic prints are accepted. They should be black and white originals (not photocopies) provided on separate pages and identified with their corresponding numbers. Actual size graphics should be provided, which need no further manipulation, with lettering (Arial or Helvetica) not smaller than 8 points, lines no thinner than 0.5 point, and each of uniform density. All colors should be removed from graphics except for those graphics to be considered for publication in color. If graphics are to be submitted digitally, they should conform to the following minimum resolution requirements: 1200 dpi for black and white line art, 600 dpi for grayscale art, and 300 dpi for color art. All graphic files must be saved as TIFF images, and all illustrations must be submitted in the actual size at which they should appear in the journal. Note that good quality hardcopy original illustrations are required for both online and mail submissions of manuscripts.

Text Footnotes: The use of text footnotes is to be avoided. When their use is absolutely necessary, they should be typed at the bottom of the page to which they refer, and should be cited in the text by a superscript asterisk or multiples thereof. Place a line above the footnote, so that it is set off from the text.

Supplementary Material: Authors are encouraged to provide all supplementary materials that may facilitate the review process, including any detailed mathematical derivations that may not appear in whole in the manuscript.

Revised Manuscript and Computer Disks

Following the acceptance of a manuscript for publication and the incorporation of all required revisions, authors should submit an original and one more copy of the final disk containing the complete manuscript typed double spaced in Microsoft Word for Windows 2000 or a later version thereof. All graphic files must be saved as PDF, JPG, or TIFF images.

Allen, P.B., “.....”, in: Horton, G.K., and Muradudin, A. A., (eds.), “Dynamical.....”, (North.....), pp....

Reprints

Twenty (20) reprints free of charge are provided to the corresponding author. For orders of more reprints, a reprint order form and prices will be sent with the article proofs, which should be returned directly to the Editor for processing.

Copyright

Submission is an admission by the authors that the manuscript has neither been previously published nor is being considered for publication elsewhere. A statement transferring copyright from the authors to Yarmouk University is required before the manuscript can be accepted for publication. The necessary form for such transfer is supplied by the Editor-in-Chief. Reproduction of any part of the contents of a published work is forbidden without a written permission by the Editor-in-Chief.

Disclaimer

Opinions expressed in this Journal are those of the authors and neither necessarily reflects the opinions of the Editorial Board or the University, nor the policy of the Higher Scientific Research Committee or the Ministry of Higher Education and Scientific Research. The publisher shoulders no responsibility or liability whatsoever for the use or misuse of the information published by JJP.

Indexing

JJP is currently indexing in:

	Emerging Sources Citation Index (ESCI) Journal Impact Factor 2022 0.7
 ULRICHSWEB™ GLOBAL SERIALS DIRECTORY	

Jordan Journal of P H Y S I C S

An International Peer-Reviewed Research Journal

Volume 18, No. 1, March. 2025, Shawwal 1446 H

Table of Contents:

Articles	Pages
Optimizing Optoelectronic, Antimicrobial Activity and Electrical Properties of Composite ZnO/ZnS with Fe Doped Nanocomposite towards Applications in Water Treatment J. Barman, M. Bhattacharjee and D. J. Haloi	1-9
Synthesis and Characterization of ZrTiO₄ for Bioceramic Applications Fadhil K. Farhan, Abothur Almohana, Zinab F. Nazal and B. A. Almayahi	11-17
Study of Elements, Functional Groups and UV Characteristics of Trapped Dust in the Filters of Air Conditioners for the Purpose of Air Quality Awareness Francis O. Aweda, Jacob A. Akinpelu, Christopher O. Olufunmilayo and Bukunmi S. Olatinwo	19-31
Field Emission Characteristics of Carbon Black Particles and Various Types of Carbon Nanotubes Using Glass Tubes Hatem A. Al-Braikat, Samer I. Daradkeh, M-Ali H. Al-Akhras and Marwan S. Mousa	33-40
Negative Ion Formation in H + H Collisions at Low- to High- Energies Saed J. Al Atawneh	41-48
Soliton Type Solutions for Electromagnetic Wiggler Free Electron Laser Mustafa Abu Safa	49-59
The Influence of Multiwall Carbon Nanotubes Additives on the Structural and Mechanical Properties of Alumina Composites Abdulsattar K. Hasan, Thamir A. Jumah and Kassim M. Wadi	61-71
Application of the Matrix Mechanics Method to Solve the Schrodinger Equation of the Bottomonium System Aissa Belhouari	73-80
Performance of a Thin Layer of Plastic Scintillator Material to be Used as a Charged Particle Detector Using Geant4 K. Al-Khasawneh, B. Brückner, P. Erbacher, S. Fiebiger, K. Göbel, T. Heftrich, Kisselbach, D. Kurtulgil, C. Langer, M. Reich, R. Reifarth, M. Volknandt and M. Weigand	81-88
Dust Ion Acoustic Solitary Waves in A Relativistic Ion Plasma with Kappa Described Electrons and Positrons Jeslin Sara Jose, P.S. Abishek, Anjumol Babu, S. Shilpa, Sijo Sebastian, Lini Devassy and Manesh Michael	89-96
Identifying Leachate Plume Accumulation Zones at Lapite Dumpsite in Nigeria Employing Very Low Frequency Electromagnetic (VLF-EM) Method Saheed A. Ganiyu	97-106
Exploring the Relationship Linking the Radius and Potential Difference in Hemispherical Analyzer Energy Ataullah. A. Alsheikh Essa, Khalid. Q. Kheder and Abdullah I. M. Alabdullah	107-112

Optimizing Optoelectronic, Antimicrobial Activity and Electrical Properties of Composite ZnO/ZnS with Fe Doped Nanocomposite towards Applications in Water Treatment

J. Barman^a, M. Bhattacharjee^b and D. J. Haloi^c

^a Department of Physics, ADP College, Nagaon, Assam-782002, India.

^b Department of Chemistry, Bodoland University, Kokrajhar, Assam-783370, India.

^c Department of Applied Science, Tezpur University, Assam-784028, India.

Doi: <https://doi.org/10.47011/18.1.1>

Received on: 20/03/2023;

Accepted on: 21/12/2023

Abstract: Composite ZnO and ZnS nanostructured with Fe doping thin films, exhibiting high antimicrobial activity, have been synthesized by chemical route. The optimized parameters, including composition ratio, doping concentration, temperature, UV exposure, and thickness of the composite ZnO and ZnS films, have been optimized in thin-film form. The synthesized samples were identified and analyzed by XRD, HR-SEM, EDX, and HRTEM. The band gap was estimated from absorption spectra, and the Stokes shift energy was calculated from emission and absorption spectra. The conductivity of the samples increased with higher Fe content and it depended on the composite ratio of ZnO and ZnS. Antimicrobial properties were studied using four bacterial strains, revealing that a concentration of 3.5 wt% was the optimal value for the most efficient activity.

Keywords: Nanocrystalline thin films, ZnO/ZnS, Antimicrobial, XRD, Optical, Electrical properties.

Introduction

Composite materials like ZnO and ZnS have tremendous importance in frontier research due to their extraordinary physical, chemical, biological, and electrical properties. These semiconductor materials can be used as eco material of choice for key applications in water treatment. The properties of composite materials depend on the synthesis method, including starting parameters.

The promising applications of nanocomposites have been widely explored across various fields. The nanocomposite materials exhibit significant potential in optoelectronics as well as electrical conductivity. When these compound materials are doped with suitable elements, they acquire enhanced properties, that can be applied in various fields, including biomedical applications [1-3].

Among the various nanocomposite materials, ZnO/ZnS is an attractive candidate due to its distinguished performance in conductivity and high performance in antimicrobial activity. When ZnO/ZnS composite is doped with Fe, its application range becomes wider, making it highly suitable for water treatment due to the dependence property of conductivity and antimicrobial properties [4-7].

The existence of bacteria in drinking water is a major issue in most of the country. In this context, composite ZnO/ZnS doped with Fe exhibits attractive antibacterial properties. These composite nanomaterials have a large surface-to-volume ratio. From the literature, it was observed that the toxicity of ZnO/ZnS has minimal effect on living cells [8-11]. Various mechanisms in ZnO/ZnS nanocomposites

contribute to their antibacterial activity due to the ion exchange with cell membranes [12-18]. ZnO/ZnS has ferromagnetic properties at room temperature. When doped with Fe, it becomes an attractive candidate for application in antimicrobial activity [19]. Doping with Fe alters the conductivity and enhances antimicrobial effects. The present work focuses on the fabrication process to determine the optimal parameters of composite ratio, doping concentration, photon-induced time, and reaction rate for high efficiency in antimicrobial activity for the reduction of environmental burden. The prepared samples were analyzed with XRD, UV-visible spectrometer, EDX, SEM, PL, and electrical measurements.

Experimental

Sample Preparation and Characterization Techniques

The composite nanoparticles were synthesized by the chemical method at different wt% of the doping material. The doping concentration ranged from 0.5 to 4.0 wt%. The key chemicals were mainly sourced from Merck, India. All the materials used were of analytic grade and were used without further purification. ZnS and NaOH with Na₂S. The materials used were of analytical grade. The required chemicals were dissolved in double-distilled water and stirred for 12 hours, both under vacuum and non-vacuum conditions, until the solution became clear and transparent. After preparation, the doping material Fe was added in different wt% concentrations, poured into a silica crucible, and subjected to microwave exposure. After 24 hours, the prepared samples were cast onto a glass substrate to form thin films and dried in a vacuum environment for 6 hours. The final samples were washed multiple times with alcohol to remove any remaining ions and then dried in a hot air oven at 70°C for 2 h.

The synthesized Fe-doped ZnO/ZnS nanocomposite was characterized using UV- VIS spectrophotometry (Systronics), XRD (Phillips

X'Pert Pro Powder X-ray Diffractometer), SEM (JSM-6360, JEOL), TEM (Model: JEM-100 CX II), and photoluminescence studies.

Test for Antibacterial Activity

Escherichia coli (MTCC 739), *Klebsiella pneumonia* (MTCC 432), *Pseudomonas aeruginosa* (MTCC-424), and *Staphylococcus aureus* (MTCC-740) were used for antibacterial screening. The microbial cultures were purchased from the "Microbial Type Culture Collection and Gene Bank" (MTCC), Chandigarh, India. The bacterial cultures were maintained on nutrient agar slants and were stored at -4°C. The solutions were made at concentrations of 10, 30, and 50 µg/ml by adding 100 mg of each sample in 1 ml of DMSO with proper dilution.

The antimicrobial activity of Fe-doped and undoped ZnO/ZnS composites was analyzed using the well-diffusion method [20-22]. Nutrient agar plates were used, and 2.5 mL of bacterial inoculum was spread evenly over each plate. Standard antibiotics (Tetracycline) were used as reference antibacterial agents for both gram-negative and gram-positive bacteria. The ZnO/ZnS composites were loaded onto the agar plates and incubated at 37°C for 24 hours. The inhibition zone diameters were measured using a traveling microscope. Antimicrobial activity was assessed for different wt% doping concentrations and ZnO/ZnS composite ratios.

Results and Discussions

Structural Analysis by XRD

Figure 1 shows the composite ZnO/ZnS at different composite ratios and different doping concentrations. The diffraction pattern in the XRD peaks was identified at $2\theta = 31.730^\circ$, 47.380° , and 51.220° , corresponding to (100), (002), and (101) planes, respectively, for a ZnO/ZnS ratio of 3:5 and a doping concentration of 3.5 wt%.

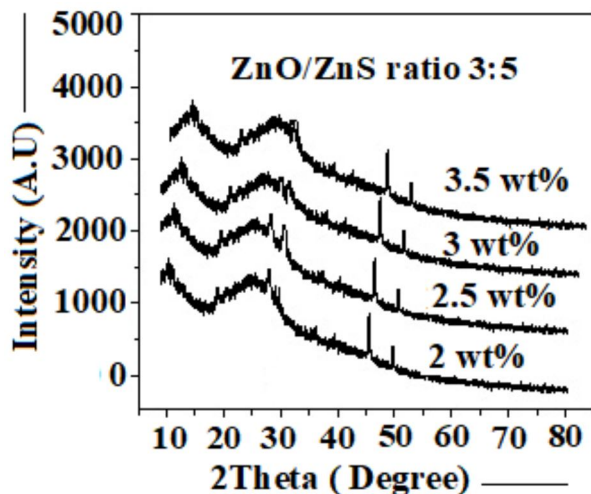


FIG. 1. XRD patterns of the ZnO/ZnS composite at 3:5 ratio for various doping concentrations.

The diffraction peaks are in good agreement with the hexagonal wurtzite-type structure (space group P63mc). With an increase in doping concentration from 2 wt% to 3.5 wt% at the ZnO/ZnS ratio 3:5, the peaks are slightly diffracted to a higher diffraction angle and broadened, indicating a decrease in crystallinity. The optimum doping concentration is found at 3.5 wt%, as evidenced by the most significant structural refinement. Additionally, Fe peaks are observed at $2\theta = 46^\circ$.

The XRD spectrum shows a mixed-phase structure, which explains the multiple peaks observed in the absorption spectra. The replacement of ZnO/ZnS lattice ions by Fe^{2+} ions is further confirmed by TEM. The average crystallite size was calculated using the Debye-

Scherrer equation by considering full-width at the half-maximum (FWHM) of the first intense peak (100) [23, 24].

$$D_{hkl} = F\lambda/M \cos \theta \quad (1)$$

In Eq. (1), D represents the average crystallite size, θ the Bragg angle, and M the FWHM. The value of F is 0.89 for spherical shape and shape (confirmed by HRTEM). The crystallite size was found to be in the range of 8-14 nm for all samples. Again, it is observed that when the doping concentration increases from 2.0 wt% to 3.5 wt%, the crystallite size decreases. However, for doping levels beyond 3.5 wt%, the crystallite size increases due to rapid nucleation growth, suggesting that 3.5 wt% is the optimal doping concentration [25].

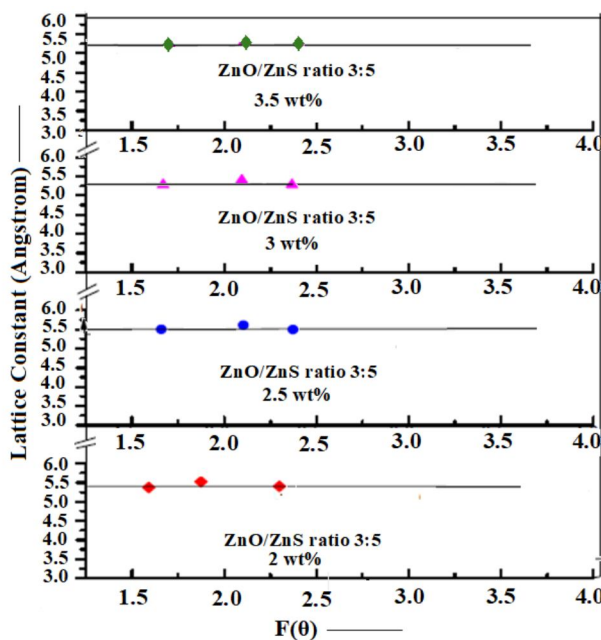


FIG. 2. Nelson-Riley plot of ZnO/ZnS nanocomposite at a 3:5 under different doping concentrations.

Rietveld refinement (RR) analysis was used to characterize in detail the crystalline structure. The lattice parameter increased with an increase of doping concentration beyond 3.5 wt%, clearly indicating that Fe^{2+} ions substitute Zn^{2+} ions in the composite material [26]. The lattice constant was calculated using the Nelson–Riley plot to eliminate strain effects, yielding an average value of 5.4012 Å. Figure 2 shows the Nelson–Riley plot.

From the RR analysis, the values of a and c were calculated, which allowed us to estimate the nearest Zn–O bond length along the c -direction [27].

$$L = \sqrt{\frac{a^2}{3} + \left(\frac{1}{2} - u\right)^2 c^2},$$

where a and c represent the lattice parameters, u is the internal parameter, and L is the bond length. The value of c/a was 1.603, which is in good agreement with the hexagonal close-packed structure [27].

TEM Result Analysis

The particle distribution was analyzed by TEM. It was observed that particles were uniformly distributed. Figure 3 represents the optimum condition ZnO/ZnS ratio of 3:5 with 3.5 wt% Fe doping. The average particle diameter was 40 nm, which differs from the values obtained via XRD and optical modeling because XRD gives the average grain size.

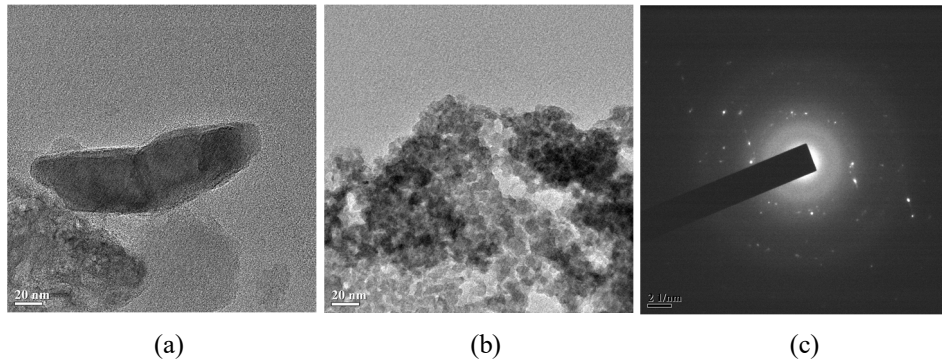


FIG. 3. TEM micrographs of (a) ZnO/ZnS at a 3:5 ratio, (b) ZnO/ZnS at a 3:5 ratio with Fe doping, and (c) SAED pattern of Fe-doped ZnO/ZnS composite.

TEM EDX Analysis

Elemental analysis was performed through energy dispersive X-ray attached to the TEM. EDX were captured from regions where particles were uniformly distributed, confirming the presence of Zn, S, and Fe. Some silicon peaks were also observed, likely originating from the

glass substrate. Multiple regions were analyzed, revealing that Fe-doped areas exhibited larger particle sizes due to the doping concentration. Data analysis indicated that the 3.5 wt% Fe-doped sample contained the highest percentages of Zn, S, and Fe.

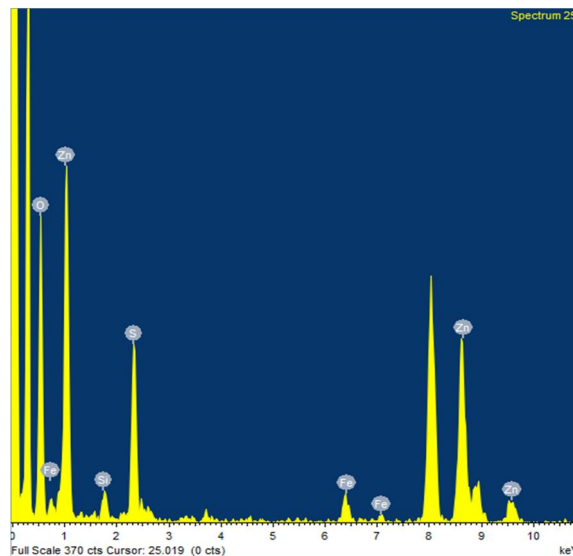


FIG. 4. EDX results of Fe-doped ZnO/ZnS at 3:5.

SEM Analysis

The morphology of the samples was analyzed using an SEM available at NEHU (JSM-6360, JEOL). The SEM analysis confirms that doped samples have larger grain sizes, ranging from 22 to 40 nm. Some samples exhibited a hexagonal shape at a doping concentration of 3.5 wt%.

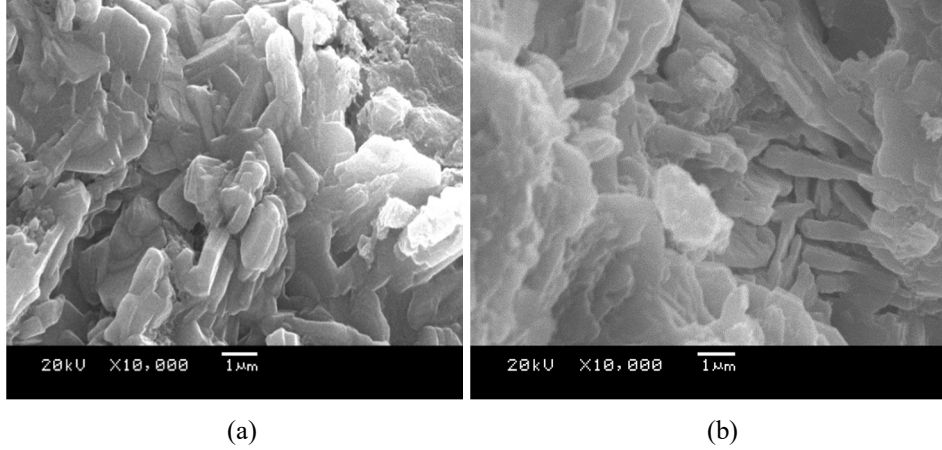


FIG. 5. SEM images of the nanocomposite: (a) ZnO/ZnS at 3:5 and (b) ZnO/ZnS at 3:5 with 3.5 wt% Fe.

Photoluminescence Studies

Figure 6 shows the PL spectrum of Fe²⁺-doped ZnO/ZnS composite at 3:5 for different doping concentrations at room temperature. The excitation wavelength is 200 nm. The effect of doping with Fe²⁺ ions on the photoluminescence activity of ZnO/ZnS crystals is evident. The PL spectrum shows five characteristic peaks in all samples at different doping concentrations. Two broad peaks are observed in the ranges of 400 nm and 536 nm. It is noted that as the doping concentration increases, the position of the peaks shifts, indicating a size effect. The doping concentration alters the lattice structure,

Figure 5(a) shows the undoped ZnO/ZnS nanocomposite at a 3:5 ratio, while Figure 5(b) shows the ZnO/ZnS nanocomposite doped with 3.5 wt% Fe, exhibiting a hexagonal shape that is in good agreement with the XRD pattern. Doping leads to an increase in grain size compared to the undoped samples.

affecting the Zn²⁺, S²⁻, and neighboring OH⁻ ions. The broad peaks may arise due to trap states [28-30].

A blue emission peak is observed in all samples around 425 nm, attributed to Zn vacancies [31]. Low-intensity peaks are observed in the range of 480–570 nm due to sulfur vacancies. A sharp peak is observed at 627 nm, corresponding to the mismatch of Fe²⁺ ions. From the absorbance and emission peaks, the positive Stokes shift energy is calculated, revealing that the Stokes shift energy is larger at lower doping concentrations, which suggests stronger coupling to lattice phonons [32].

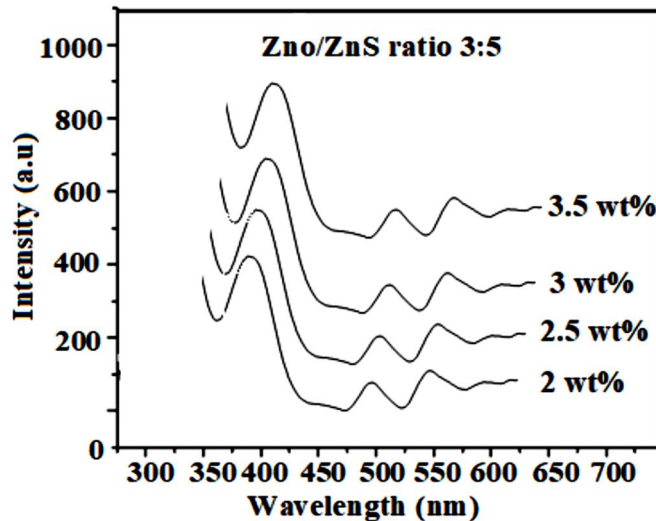


FIG. 6. Photoluminescence spectra.

UV Spectrometric Analysis

The UV-Vis spectrum was analyzed in the range of 300 to 800 nm for all samples. It was found that the absorption shows a blue shift, as shown in Fig. 7. The blue shift energy was calculated using the Tauc plot and was observed to change with varying doping concentrations. Table 1 shows the blue shift energy for different doping concentrations. The blue shift energy depends on both the composite ratio and the doping concentration. It increases up to 4.1 eV with increasing doping concentration, then decreases. The ZnO/ZnS ratio of 3:5 with 3.5

wt% doping concentration is found to be the maximum tunable condition. The decrease in particle size leads to a shift in the blue shift energy, which results in quantum confinement and an increase in the band gap.

The composite ZnO/ZnS shows the best fit for a direct band gap. From Fig. 8, the band gap range is 3.8–4.1 eV, which is an important parameter related to electrical conductivity. Table 1 shows the variation of the band gap with different doping concentrations [32–37].

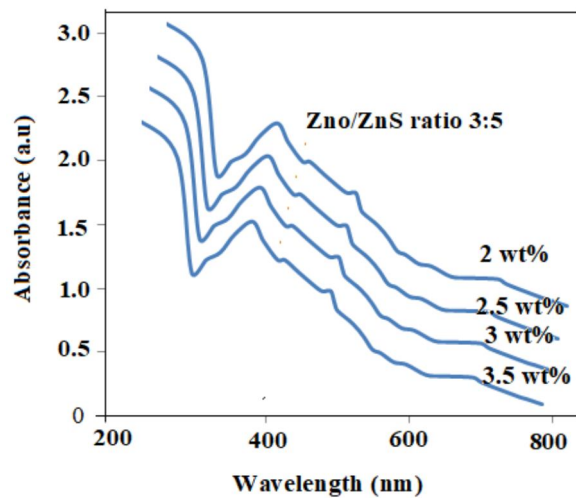


FIG. 7. UV-visible absorption of Fe-doped ZnO/ZnS nanocomposite with a 3:5 ratio.

TABLE 1. Blue shift energy and band gap energy with particle size at different Fe doping concentrations.

Sample No.	Composite Ratio of ZnO and ZnS	Fe Doping Concentration	Energy Band Gap [eV]	Blue Shift Energy [eV]	Particle radius [nm]
A	3:5	2 wt%	3.83	0.16	6.3
B	3:5	2.5 wt%	3.85	0.21	5.9
C	3:5	3 wt%	3.95	0.36	5.2
D	3:5	3.5 wt%	4.03	0.39	4.8

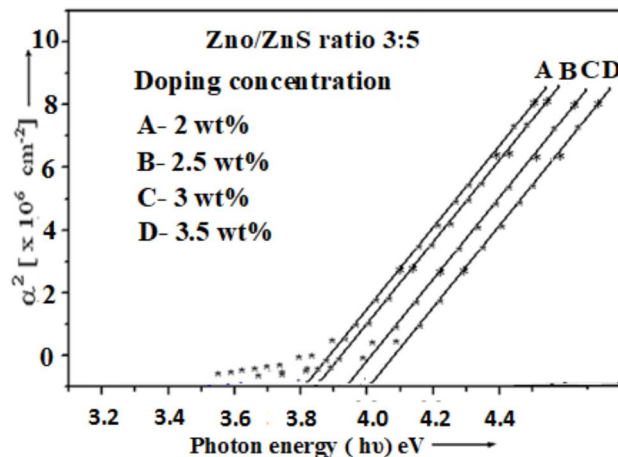


FIG. 8. Tauc plot of composite ZnO /CdS (3:5) at different doping concentrations (2.0 wt% to 3.5 wt%).

The particle radius (r) was calculated using the effective mass approximation method (EMA) with the calculated band gap energy:

$$E_{gn} = [E_{gb}^2 + 2\hbar^2 E_{gb} (\pi/R)^2 / m^*], \quad (2)$$

where E_{gb} is the average bulk band gap of ZnO and ZnS, E_{gn} is the calculated band gap energy, and m^* is the effective mass of the specimen. The average particle radius is in the range of 4-7 nm.

Antimicrobial Assay

Antibacterial activity was studied for doped and undoped Fe at different wt% with varying composite ratios of ZnO/ZnS against four pathogenic bacteria species: *E. coli*, *B. subtilis*, *K. pneumoniae*, and *S. aureus*. Tetracycline (1 mg/mL) was used as a control antibacterial agent. The maximum zone of inhibition was

found with 3.5 wt% Fe-doped ZnO/ZnS composite at a 3:5 ratio, as shown in Table 2. It was observed that when the doping concentration was too high, the antimicrobial efficiency decreased. The optimum doping concentration was found to be 3.5 wt%.

The antibacterial activity was determined in vitro by measuring the zone of inhibition (in mm) for samples at different concentrations. As indicated in Table 2, the maximum zone of inhibition was observed for the 3.5 wt% Fe-doped ZnO/ZnS composite at a 3:5 ratio. When the doping concentration was increased beyond this optimal level, the antimicrobial efficiency decreased due to an increase in crystallite size and changes in ionic radius related to the composite ratio.

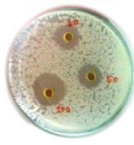
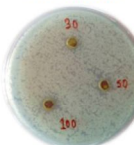
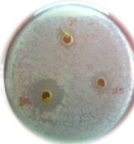
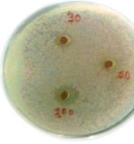
ZnO-ZnS ratio and Doping concentration	Antimicrobial assay with	Zone inhibition (diameter in nm)	Antimicrobial assay with	Zone inhibition (diameter in nm)
3:5 and 3.5 wt%	<i>S. aureus</i> 	19 nm	<i>B. subtilis</i> 	16 nm
3:5 and 3.5 wt%	<i>K. pneumoniae</i> 	17 nm	<i>E. coli</i> 	9 nm

FIG. 9. Zone inhibition of ZnO-ZnS at a 3:5 ratio and 3.5 wt% doping concentration against four bacterial cultures.

TABLE 2. Zone inhibition of ZnO-ZnS at a 3:5 ratio of Fe-doped ZnO/ZnS nanocomposite with standard bacterial strains.

Bacteria	Diameter of zone inhibition [nm]			Tetracyclin [1 mg/mL]
	ZnO/ZnS nanocomposite at 3:5 at 3.5 wt% Fe Doping			
	10 μ L	30 μ L	50 μ L	
<i>E. coli</i>	7 \pm 0.14	18 \pm 0.11	24 \pm 0.13	35 \pm 0.08
<i>B. subtilis</i>	6 \pm 0.11	16 \pm 0.16	21 \pm 0.15	32 \pm 0.09
<i>P. aeruginosa</i>	5 \pm 0.15	12 \pm 0.14	21 \pm 0.11	31 \pm 0.09
<i>S. aureus</i>	7 \pm 0.11	17 \pm 0.08	23 \pm 0.11	34 \pm 0.11

Electrical Study

The electrical resistivity of Fe-doped nanocomposite ZnO/ZnS thin films was studied using the D.C. two-point probe method. The resistivity of the samples was calculated using the following relation:

$$\rho = \rho_0 \exp(E_a/kT), \quad (3)$$

where ρ represents resistivity at temperature T , ρ_0 is a constant, and k is the Boltzmann constant. Figure 10 shows that the resistivity decreases as the temperature increases. As the doping concentration increases from 2.0 wt% to 3.5

wt%, conductivity increases, but at higher doping concentrations, conductivity decreases again [38]. Doping creates traps within the

crystal, which may decrease the conductivity of the samples.

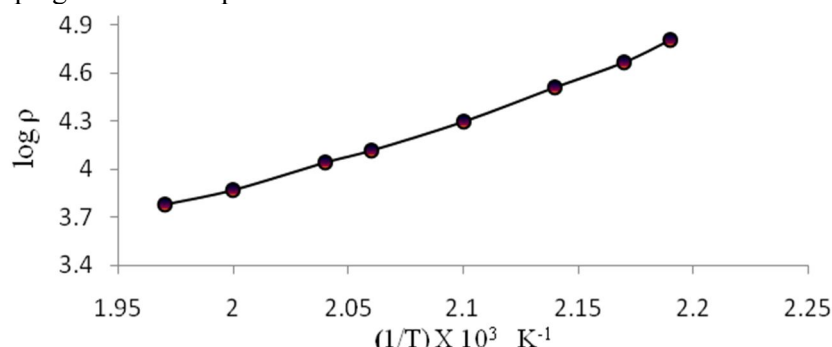


FIG. 10. Variation of $\log \rho$ with $1/T$ for as-deposited Fe-doped ZnO/ZnS at 3.5 wt%.

Conclusion

Composite ZnO and ZnS nanostructured thin films with Fe doping, exhibiting high antimicrobial activity, were synthesized by the chemical route. The optimized parameters, including composition ratio, doping concentration, temperature, and thickness of the film, were optimized in thin film form. Absorption spectra provided the optimum band gap energy, which was found to be in the range of 3.8–4.1 eV. The nanocomposite ZnO/ZnS at 3:5 with 3.5 wt% demonstrated the highest efficiency in all analyses, with a Stokes shift energy of 3.64 eV.

Conductivity increased with higher Fe doping and depended on the composite ratio. The

highest antimicrobial activity was observed in the ZnO/ZnS composite with a 3:5 ratio and 3.5 wt% Fe doping concentration. Additionally, at 3.5 wt% Fe doping, electrical conductivity reached its maximum, providing a better understanding of the relationship between particle size, antimicrobial activity, and band gap energy, which increased under these conditions. Energy-dispersive X-ray (EDX) analysis confirmed the presence of Fe, S, Zn, and O in the sample.

Acknowledgments

This work is part of the activities of Biotech Hub and Star College. The authors acknowledge the Department of Biotechnology, Government of India, for financial support.

References

- [1] Irimpan L., Nampoori V.P.N., and Radhakrishnan P., *J. Appl. Phys.*, 103 (2008) 1.
- [2] Nayak J., Sahu S.N., Kasuya J., and Nozaki S., *Appl. Surf. Sci.*, 254 (2008) 7215.
- [3] Sadoun, B., Mouetsi, S., Hocini, A., and Derdour, R., *Jordan J. Phys.*, 16 (2023) 105.
- [4] Manoj Kumar, M., Nandi, M., and Pakshirajan, K., *J. Environ. Manag.*, 278 (2021) 111555.
- [5] Rao, G.T., Babu, B., Stella, R.J., Manjari, V.P., Reddy, C.V., Jaesool, S., and Ravikumar, R.V.S.S.N., *J. Mol. Struct.*, 1081 (2015) 254.
- [6] Liu, J., Zhu, K., Sheng, B., Li, Z., Tai, G., Qiu, J., Wang, J., Chen, J., You, Y., Gu, Q., and Liu, P., *J. Alloy. Compd.*, 618 (2015) 67.
- [7] Jana, T.K., Pal, A., and Chatterjee, K., *J. Alloy Compd.*, 583 (2014) 510.
- [8] Brayner, R., Ferrari-Iliou, R., Brivois, N., Djediat, S., Benedetti, M.F., and Fievet, F., *Nano Lett.*, 6 (2006) 866.
- [9] Thill, A., Zeyons, O., Spalla, O., Chauvat, F., Rose, J., Auffan, M., and Flank, A.M., *Environ. Sci. Technol.*, 40 (2006) 6151.
- [10] Reddy, K.M., Feris, K., Bell, J., Wingett, D.G., Hanley, C., and Punnoose, A., *Appl. Phys. Lett.*, 90 (2007) 2139021.
- [11] Zhang, L.L., Jiang, Y.H., Ding, Y.L., Povey, M., and York, D., *J. Nanopart. Res.*, 9 (2007) 479.
- [12] Kajbafvala, A., Ghorbani, H., Paravar, A., Samberg, J.P., Kajbafvala, E., and

- Sadrnezhaad, S.K., Superlattices Microstruct., 52 (2012) 512.
- [13] Tarwal, N.L., Devan, R.S., Ma, Y.R., Patil, R.S., Karanjkar, M.M., and Patil, P.S., Electrochim. Acta, 72 (2012) 32.
- [14] Yang, W.F., Wu, Z.Y., Liu, Z.G., and Kong, L.M., Appl. Surf. Sci., 256 (2010) 7591.
- [15] Luo, L.J., Tao, W., Hu, X.Y., Xiao, T., Heng, B.J., Huang, W., Wang, H., Han, H.W., Jiang, Q.K., Wang, J.B., and Tang, Y.W., J. Power Sources, 196 (2011) 10518.
- [16] Pawar, B.N., Cai, G., Hama, D., Mane, R.S., Ganesh, T., Ghule, A., Sharma, R., Jadhava, K.D., and Han, S.H., Sol. Energy Mater. Sol. Cells, 93 (2009) 524.
- [17] Park, Y.C., Kong, E.H., Chang, Y.J., Kum, B.G., and Jang, H.M., Electrochim. Acta, 56 (2011) 7371.
- [18] Chen, Y., Tao, Q., Fu, W., Yang, H., Zhou, X., Zhang, Y., Su, S., Wang, P., and Li, M., Electrochim. Acta, 118 (2014) 176.
- [19] Hsu, S.H., Hung, S.F., and Chien, S.H., J. Power Sources, 233 (2013) 236.
- [20] Zhang, C., Huang, Z., Liao, X., Yin, G., and Gu, J., J. Coat. Technol. Res., 9 (2012) 621.
- [21] Gummuluri, S., Kavalipurapu, V.T., and Kaligotla, A.V., Braz. Dent. Sci., 22 (2019) 365.
- [22] Adeyemi, A.I., Vincent, O.I., and Olujenyo, O.M., Asian J. Med. Biol. Res., 4 (2018) 7.
- [23] Ahmed, F., Kumar, S., Arshi, N., Anwar, M.S., Koo, B.H., and Lee, C.G., Microelectron. Eng., 89 (2012) 1290.
- [24] Ansari, S.A., Nisar, A., Fatma, B., Khan, W., and Naqvi, A.H., Mater. Sci. Eng. B, 177 (2012) 428.
- [25] Mohapatra, J., Misra, D.K., Perumal, A., Medicherla, V.R.R., Phase, D.M., and Singh, S.K., Mater. Res. Bull., 47 (2012) 1417.
- [26] Lemine, O.M., Bououdina, M., Sajieddine, M., Saie, A.M.A., Shafi, M., Khatab, A., Alhilali, M.A., and Henini, M., Physica B, 406 (2011) 1989.
- [27] Barman, J., Sultana, F., and Banik, B., Romanian J. Biophysics, 31 (2021) 165.
- [28] Liu, S.M., Liu, F.Q., Guo, H.Q., Zhang, Z.H., and Wang, Z.G., Solid State Commun., 115 (2000) 615.
- [29] Reddy, A.J., Kokila, M.K., Nagabhushana, H., Rao, J.L., Nagabhushana, M., Shivakumara, C., and Chakradhar, R.P.S., Spectrochim. Acta A, 79 (2011) 476.
- [30] Wu, D., Huang, Z., Yin, G., Yao, Y., Liao, X., Han, D., Huang, X., and Gu, J., Cryst. Eng. Comm., 12 (2010) 192.
- [31] Zeng, H., Cai, W., Hu, J., Duan, G., Liu, P., and Li, Y., Appl. Phys. Lett., 88 (2006) 1.
- [32] Misra, M., Kapur, P., Ghanshyam, C., and Singla, M.L., J. Mater. Sci. Mater. Electron., 24 (2013) 3800.
- [33] Mollaa, A.R., Chakradhar, R.P.S., Kesavulu, C.R., Rao, J.L., and Biswas, S.K., J. Alloy. Compd., 512 (2012) 105.
- [34] Burstin, E., Phys. Rev., 93 (1954) 632.
- [35] Moss, T.S., Proc. Phys. Soc. Sect. B, 67 (1954) 775.
- [36] Barman, J., Banik, B., and Sultana, F., Romanian J. Biophysics., 31 (2021) 175.
- [37] Barman, J., J. Nanostructure., 11 (2021) 661.
- [38] Chen, W., Wang, J., and Wang, M.R., Vacuum, 81 (2007) 894.

Synthesis and Characterization of ZrTiO₄ for Bioceramic Applications

Fadhil K. Farhan^a, Abothur Almohana^b, Zinab F. Nazal^a
and B. A. Almayahi^c

^a Department of Medical Physics, College of Science, AL-Karkh University of Science, Baghdad, Iraq.

^b College of Medicine, Jabir Ibn Hayyan Medical University, Najaf, Iraq.

^c Department of Physics, University of Kufa, Faculty of Science, Najaf, Iraq.

Doi: <https://doi.org/10.47011/18.1.2>

Received on: 01/06/2023;

Accepted on: 22/10/2023

Abstract: This study presents the synthesis and characterization of bio-ceramic powder composed of zirconium titanate (ZrTiO₄) using a combination of the powder method and the hydrothermal technique. The objective was to investigate the feasibility of this approach in producing high-purity ZrTiO₄ nanocomposites with potential applications in various fields. The raw materials, titanium dioxide (TiO₂) and zirconium dioxide (ZrO₂), were mixed in equal proportions and subjected to a series of processing steps. The resulting powder was analyzed using X-ray diffraction (XRD), scanning electron microscopy (SEM), and energy-dispersive spectroscopy (EDS). XRD analysis confirmed the crystalline structure of the nanocomposites, while SEM revealed diverse granule shapes, resembling cotton fibers or clusters of zirconium and titanium compounds. EDS analysis confirmed the elemental composition and the absence of impurities, demonstrating the high purity of the prepared ZrTiO₄ nanocomposites. The findings highlight the successful synthesis of bio-ceramic ZrTiO₄ nanocomposites through the combined powder method and hydrothermal technique. These materials hold promise for various applications, including biomedical and electronic devices, due to their unique properties and high purity.

Keywords: Bioceramic, ZrTiO₄, Hydrothermal technique, X-ray diffraction, SEM, EDX, Elemental composition.

Introduction

This work focuses on synthesis and characterization only not the application. Ceramic materials are used in electronic and microwave devices, as well as in the manufacturing of heat-resistant materials, paints, and dyes. Their widespread utility has driven an industrial revolution that has caught the interest of many researchers [1, 2]. There are several methods for preparing ceramic composites, including chemical preparation, gel preparation, chemical precipitation, hydrothermal preparation, and powder method. Although powder technology is an effective method that can produce a large amount of compound

powder, it requires time, equipment, and devices [3, 4]. In this study, we employed an efficient mechanical mixing technique to fabricate nanomaterials based on ceramics through a hydrothermal process. The synthesis of these nanoparticles necessitated the use of cutting-edge technologies, including high-speed electric mills with durable grinding balls and precise high-temperature sintering furnaces [5, 6]. This research holds great importance in the pursuit of creating non-toxic ceramic-based nanocomposites that seamlessly integrate with human body tissues. Recently, the scientific community has directed its efforts toward

devising diverse ceramic systems for various biological purposes, including the fabrication of bone and dental prosthetics, cosmetic fillings, and medical lenses. In this context, the primary objective of our study is to advance ceramic-based nanocomposites through the powder method, specifically tailored for medical applications in orthopedic and dental surgery, by meticulously modifying their structural properties. Our ultimate aim is to draw the attention of researchers who are inclined towards exploring alternative materials to autologous bone and preserved cadaveric bones, given the potential adverse consequences associated with their usage in the future. Zirconium titanate is a bio-ceramic material that has attracted significant attention in recent years due to its exceptional properties and potential applications in various fields. It has a high wear factor, corrosion resistance, and biocompatibility with body tissues, which is particularly noteworthy [7-10].

Zirconium titanate exhibits excellent biocompatibility, chemical stability, and unique electrical and optical properties, making it suitable for use in diverse areas such as biomedicine, electronics, and catalysis.

In the field of biomedicine, bio-ceramic materials have gained prominence in applications such as bone tissue engineering, drug delivery systems, and dental implants [11]. ZrTiO₄, with its bioactivity and biocompatibility, holds great promise in these areas. Its ability to promote osteointegration, the process of bonding between bone and implant, makes it an ideal candidate for bone restoration and implantable medical devices [12]. Furthermore, ZrTiO₄ has shown potential in combating harmful bacteria in the digestive system. These medical applications highlight the importance of synthesizing high-quality ZrTiO₄ nanomaterials with precise control over their properties [13].

To date, several methods have been employed for the synthesis of ZrTiO₄, including solid-state reactions, sol-gel methods, and hydrothermal techniques [14]. Among these, the combination of the powder method and the hydrothermal technique has shown promise in achieving high-purity ZrTiO₄ nanocomposites with enhanced properties. Powder offers advantages in terms of homogeneous mixing, while the hydrothermal technique enables the formation of well-defined crystalline structures with controlled

morphology. In this study, we aimed to synthesize ZrTiO₄ using a combination of the powder method and the hydrothermal technique. The utilization of these techniques allows for the preparation of highly pure ZrTiO₄ powders with tailored characteristics. The resulting nanocomposites can possess unique features, such as specific surface area, particle size distribution, and crystalline structure, which are crucial for their application in various fields. In terms of recent references, studies have reported on the synthesis and characterization of bio-ceramic nanocomposites using similar approaches. For instance, a recent publication by Li *et al.* demonstrated the fabrication of ZrTiO₄ nanocomposites through a combination of the powder method and hydrothermal synthesis, highlighting their enhanced properties for biomedical applications [15]. Additionally, in the vast realm of metal-organic frameworks (MOFs), Zr-based MOFs stand out due to their diverse structures, remarkable stability, and intriguing properties. They are hailed as promising materials for real-world applications, despite being in the early stages of development. Recent years have witnessed substantial progress in this field. This review focuses on advances in Zr-MOFs since 2008, exploring design, synthesis, structure, and applications. It starts with four synthesis strategies, emphasizing eco-friendly and scalable approaches. Zr-MOFs are then categorized by structural variations based on Zr-based building units and organic ligands. Furthermore, the review highlights the utility of Zr-MOFs in catalysis, molecule adsorption, drug delivery, fluorescence sensing, and their role as porous carriers. This specialized overview is poised to guide deeper investigations into MOFs for practical uses [16].

These references demonstrate the ongoing research efforts in the field and the significance of our study in contributing to the existing body of knowledge. In this study, we present a detailed synthesis and characterization of bio-ceramic ZrTiO₄ prepared through the combined powder method and hydrothermal technique. A comprehensive understanding of the synthesis process and the properties of the resulting nanocomposites is crucial for their successful application in various fields. By elucidating the methodology and analyzing the obtained nanocomposites, we aim to provide valuable insights for the further development and

utilization of ZrTiO₄ in biomedical, electronic, and catalytic applications.

Materials and Methods

The materials and methods employed in this study aimed to produce and characterize the ZrTiO₄ nanocomposites using specific techniques. The powder synthesis involved the heat and pressure method at 800°C under standard conditions. The calcination process was carefully executed with two key conditions in mind: precise control over the presence of oxygen gas within the reaction system and a controlled temperature gradient rate of 5°C per minute. These conditions were essential to maintain the compound's atomic structure and to influence the material's properties during calcination. A highly ordered and crystalline atomic structure was achieved through calcination at 800°C for 2 hours with a gradient rate of 5°C per minute. Scanning electron microscopy (SEM) analysis was conducted using a typical SEM instrument (Sigma 300, USA). The SEM setup included an electron column, sample chamber, electronics console, and visual display monitor, with magnifications of 50.00 KX (1 µm), 300.00 KX (200 nm), 100.00 KX (1 µm), and 300.00 KX (300 nm). SEM was used to observe the surface topography and granule shapes of the resulting powder. Energy dispersive spectroscopy (EDS) using X-rays was performed to identify the reactants and their proportions used in preparing the nanoparticles. Analysis of the weight and atomic ratios confirmed a close match with the ratios employed in the preparation process, thereby validating the accuracy of the synthesis.

To prepare ZrTiO₄, the following steps were followed: First, titanium dioxide (TiO₂) with a particle size of 1 micrometer and zirconium dioxide (ZrO₂) with a granular size of 5 micrometers were mixed in equal proportions by weight (Fig. 1). The mixture was then subjected to continuous stirring for 6 hours at a temperature of 40°C. After stirring, the mixture underwent grinding using an electric mixing device with grinding balls for 4 hours at a rotational speed of 350 revolutions per minute to obtain a homogeneous powder.

Subsequently, the powder was treated using a hydrothermal technique in a pressure and temperature system within a hydrothermal device. The system was placed in an oven at 100°C for 72 hours. The resulting mixture was filtered, washed, and dried until a homogeneous powder was obtained. Afterward, the powder was thermally treated at 800°C (calcination). Structural tests were conducted to evaluate the purity and composition of the ZrTiO₄.

The materials used in this study included titanium dioxide (TiO₂) and zirconium dioxide (ZrO₂), both with a purity of over 99%. Titanium dioxide had a particle size of 1 micrometer, while zirconium dioxide had a particle size of 5 micrometers. Both materials were sourced from the IPEN (Institute of Energy and Nuclear Research) in Brazil, a renowned research institution specializing in energy and nuclear technologies. The materials obtained from IPEN ensured the quality and reliability of the raw materials used in this study.

The combination of these powders proved to be a promising method for producing high-purity bio-ceramic zirconium titanate (ZrTiO₄) with a desirable composition (Fig. 1).



FIG. 1. Preparation of ZrTiO₄ nanocomposites.

Results and Discussion

Figure 2 displays the X-ray diffraction (XRD) pattern of the nanocomposites obtained through powder combination. The regularity in the crystalline nature and structure of the

nanocomposites is reflected by the highest intensity peaks at $2\theta = 30.495^\circ$ ($hkl = 111$) and $2\theta = 27.565^\circ$ ($hkl = 110$), which is consistent with the findings in Ref. [11]. The crystal size was also determined using XRD.

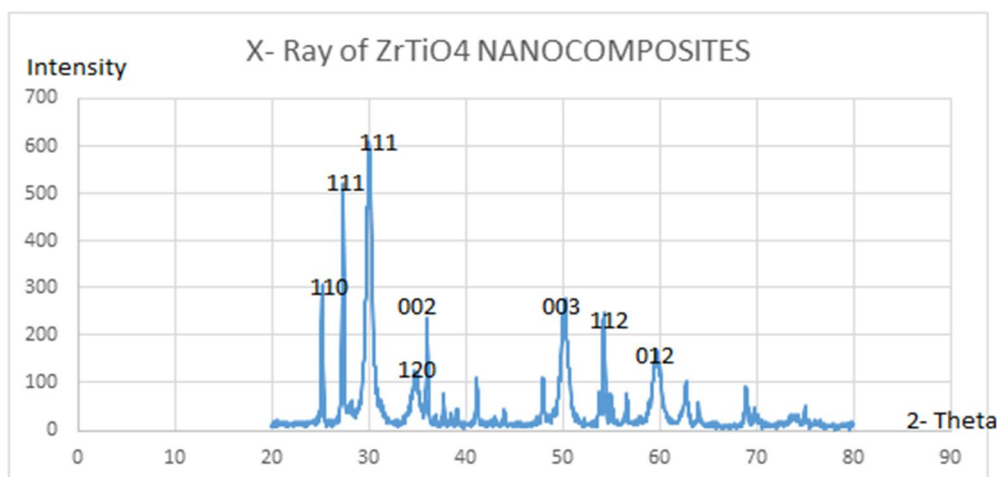
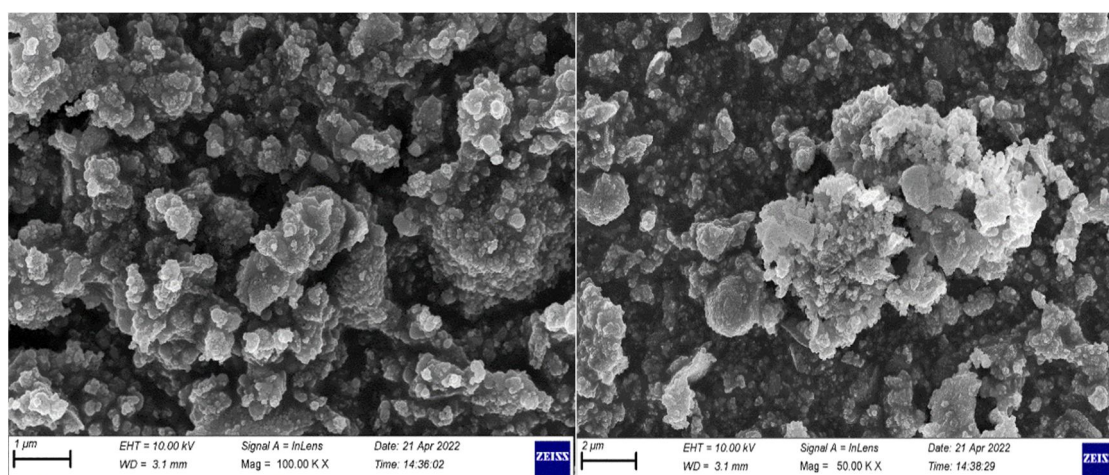


FIG. 2. X-ray diffraction patterns of the ZrTiO_4 bio ceramic, prepared by the hydrothermal technique and calcined at 800°C for 2 hours.

Figure 3 displays the surface topography of the powder produced through the heat and pressure method under standard conditions. The scanning electron microscope images reveal various granule shapes attached to a pattern resembling cotton fibers or a cluster pattern of zirconium and titanium compounds, which aligns with previous research [17, 18]. The magnification used in the examination aids in interpreting the granular sizes of the nanoparticles created using the hydrothermal method. These different shapes have potential medical applications, such as in bone restoration and combating harmful bacteria in the digestive system. Understanding the granular shape of the nanocomposites is crucial for such applications and distinguishes them from other methods [19, 21]. The SEM images show granule shapes resembling cotton fibers or clusters of zirconium and titanium compounds, with grain sizes

ranging from 44 to 55 nm and up to 76 nm, all under 100 nm, which is consistent with previous findings. The magnification measurements facilitated the interpretation of the granular sizes obtained through the hydrothermal method. These unique granular shapes highlight the material's potential for medical applications, including bone restoration and combating harmful bacteria in the digestive system. The absence of impurities further validates the purity and precision of the preparation method. Notably, the observed zirconium-to-titanium ratios were identical to the molar ratios used during manufacturing, providing additional support for the suitability of ZrTiO_4 in various high-purity medical and industrial applications. SEM images of ZrTiO_4 show varying magnifications and grain sizes, with the smallest grains measuring less than 100 nm (Fig. 4).



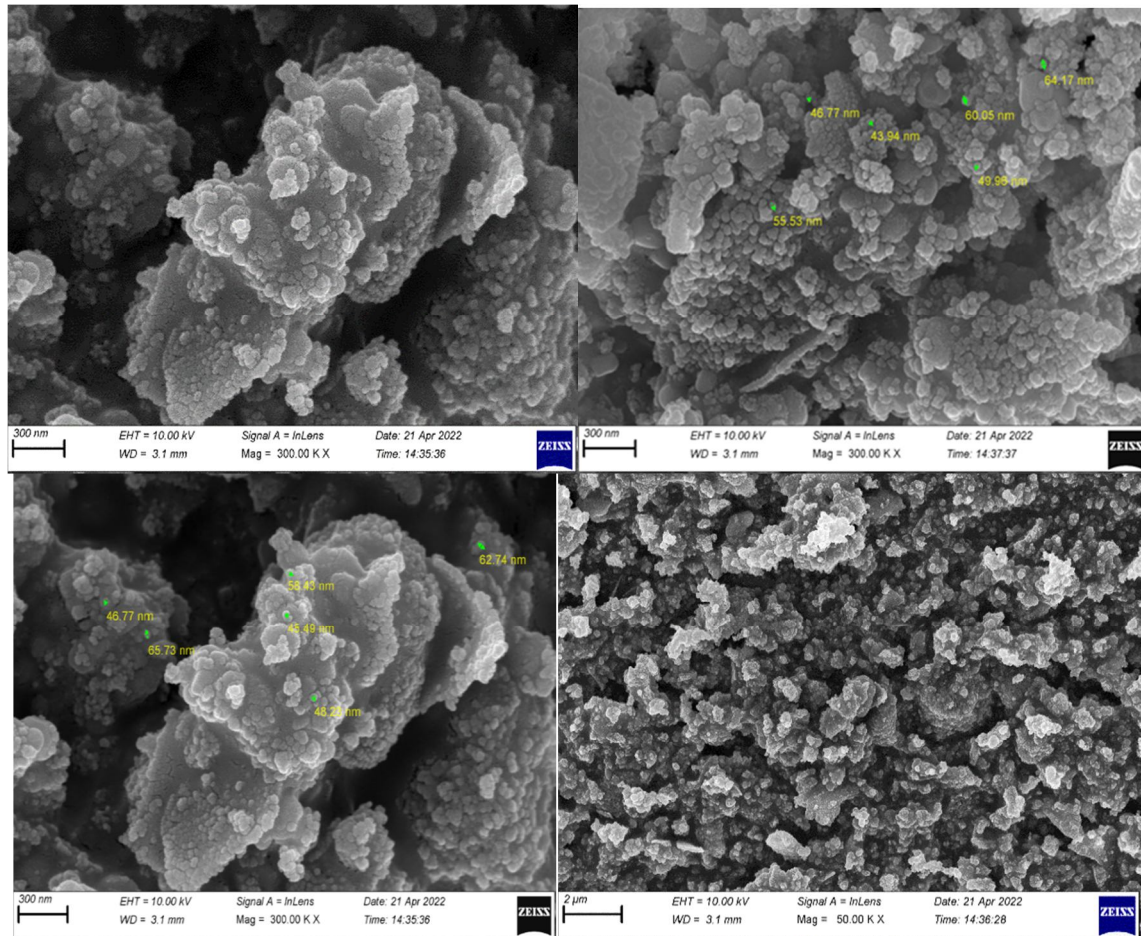


FIG. 3. Scanning electron microscope images of ZrTiO_4 at varying magnifications with grain sizes ranging from 44 to 55 nm and up to 76 nm, all under 100 nm.

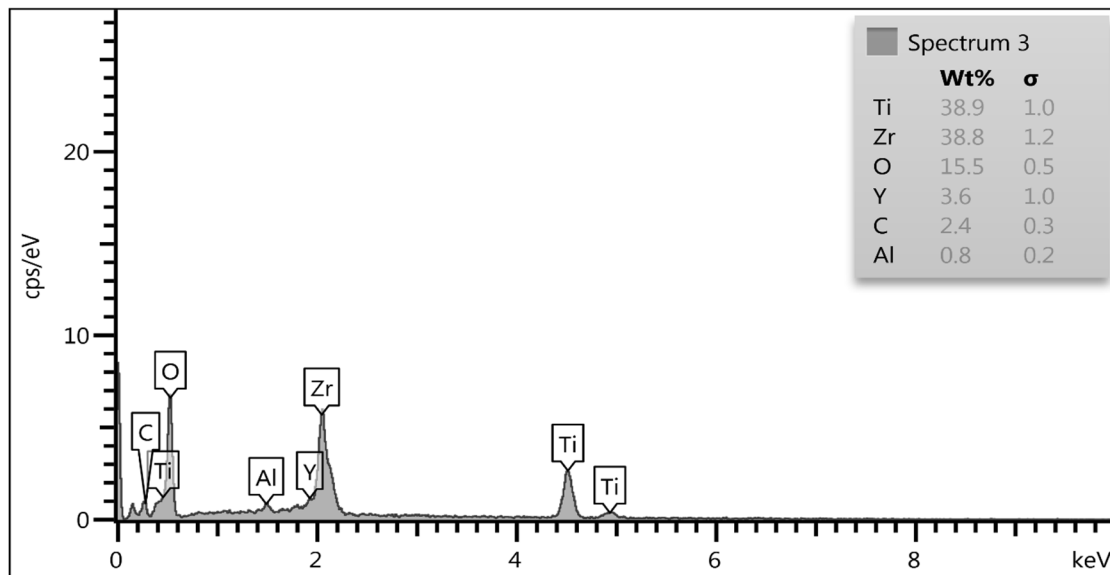


FIG. 4. EDX (energy dispersive X-ray) analysis of the ZrTiO_4 nanocomposites, depicted through images and a table.

Elements	Zr	Ti	O	another
Wt%	38.8	38.9	15.5	6.8

The diagram in Fig. 5 demonstrates the ability of ZrTiO_4 with a bio-ceramic structure to absorb and transmit infrared waves within the

range of 400 to 4000 cm^{-1} , based on the energy used and the wave number. The examination results indicate that the highest permeability

value for the prepared nanoparticles was observed at 1701 cm^{-1} , as depicted in Fig. 5. Additionally, the value of transmittance at 1220.2 cm^{-1} was observed. This composite has the potential for use in electronic devices that require materials with high permeability.

Table 1 provides valuable insights into the transmittance characteristics of the composite material. Notably, the highest transmittance, at 75%, occurs at a wave number of 1701.22 cm^{-1} . In contrast, the lowest transmittance is recorded at 99%, corresponding to a wave number of 2866.22 cm^{-1} . These findings indicate specific

wavelength regions where the composite demonstrates its highest and lowest transparency, which is of significance for understanding its optical properties and potential applications.

TABLE 1. FTIR ZrTiO_4 .

T%	K cm^{-1}
95%	3475.73
98%	2981.95
99%	2866.22
75%	1701.22
82%	1431.18
85%	1323.17

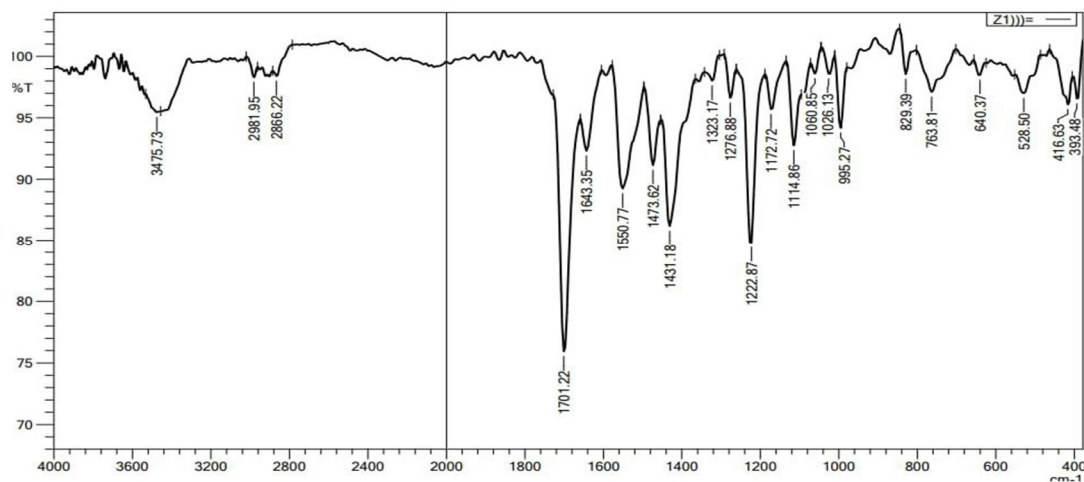


FIG. 5. The analysis of transmittance and absorbance of the ZrTiO_4 nanocomposites.

Conclusions

In summary, the results of this work have led us to the following conclusions:

The pressure and heat technique successfully produced ceramic nanoparticles with high purity and without any loss in the amount of material prepared. The method used in this work resulted in the formation of various forms of granules composed of zirconium and titanium that formed ZrTiO_4 at a temperature of 800°C . All the techniques used to interpret the atomic

composition of the nanoparticles confirmed the accuracy of the preparation method. The values of the materials involved in the preparation were consistent with the values of the prepared products in the ZrTiO_4 . These nanoparticles can be potentially used in various medical applications since they are free from any impurities that could pose risks to biological tissues.

References

- [1] Romania, C., D'asta, F., and Brandi, M.L., *Clin. Cases Miner. Bone Metab.*, 10 (3) (2013) 155.
- [2] Athanasiou, K.A., Zhu, C.F., Lanctot, D.R., Agrawal, C.M., and Wang, X., *Tissue Eng.*, 6 (4) (2000) 361.
- [3] Carter, C. and Norton, M., "Ceramic Materials: Science and Engineering", (Springer, New York, 2007).
- [4] Marsh, A.C., Chamorro, N.P., and Chatzistavrou, X., "Long-Term Performance and Failure of Orthopedic Devices, in Bone Repair Biomaterials" (Woodhead Publishing, 2019), p 379.
- [5] Benazzo, F., Falez, F., Dietrich, M., *Bioceramics and Alternative Bearings in Joint Arthroplasty: 11th BIOLOX Symposium Proc.*, (Springer Science & Business Media, 2006).
- [6] Daculsi, G., "History of Development and Use of the Bioceramics and Biocomposites, in Handbook of Bioceramics and Biocomposites (2016) p 1.
- [7] Damm, P., Kutzner, I., Bergmann, G., Rohlmann, A., and Schmidt, H., *J. Biomech.*, 51 (2017) 128.
- [8] Boch, P. and Niepce, J.C., "Ceramic Materials: Processes, Properties and Applications" (ISTE Ltd., 2007).
- [9] Thamaraiselvi, T. and Rajeswari, S., *Carbon*, 24 (31) (2004) 172.
- [10] Mohamad Yunos, D., Bretcanu, O., and Boccaccini, A.R., *J. Mater. Sci.*, 43 (2008) 4433.
- [11] Banjuraizah, J., Mohamad, H., and Ahmad, Z.A., *J. Alloys Compd.*, 482 (1-2) (2009) 429.
- [12] Torres, F.J. and Alarcón, J., *Ceram. Int.*, 31 (5) (2005) 683.
- [13] Gilewicz, A., Chmielewska, P., Murzynski, D., Dobruchowska, E., and Warcholinski, B., *Surf. Coat. Technol.*, 299 (2016) 7.
- [14] Shi, T., Livi, S., Duchet, J., and Gérard, J.F., *Nanomaterials*, 10 (5) (2020) 881.
- [15] Umemura, K., Ohtsuki, S., Nagaoka, M., Kusamori, K., Inoue, T., Takahashi, Y., Takakura, Y., and Nishikawa, M., *Nanomed.-Nanotechnol.*, 34 (2021) 102386.
- [16] Bai, Y., Dou, Y., Xie, L.H., Rutledge, W., Li, J.R., and Zhou, H.C., *Chem. Soc. Rev.*, 45 (8) (2016) 2327.
- [17] Megías-Sayago, C., Blanes, J.M., Szyja, B.M., Odriozola, J.A., and Ivanova, S., *Microporous Mesoporous Mater.*, 322 (2021) 111160.
- [18] Kumar, A., Ibraheem, S., Nguyen, T.A., Gupta, R.K., Maiyalagan, T., and Yasin, G., *Coord. Chem. Rev.*, 446 (2021) 214122.
- [19] Molla, A.R., Kumar, B.V.M., and Basu, B., *J. Eur. Ceram. Soc.*, 29 (12) (2009) 2481.
- [20] Xiao, H., Cheng, Y., Yang, Q., and Senda, T., *Mater. Sci. Eng. A*, 423 (1-2) (2006) 170.
- [21] Zum Gahr, K.H. and Neumann, P., *Wear*, 203-204 (1997) 107.

Jordan Journal of Physics

ARTICLE

Study of Elements, Functional Groups and UV Characteristics of Trapped Dust in the Filters of Air Conditioners for the Purpose of Air Quality Awareness

Francis O. Aweda^a, Jacob A. Akinpelu^a, Christopher O. Olufunmilayo^b and Bukunmi S. Olatinwo^a

^a Physics Programme, College of Agriculture, Engineering and Science, Bowen University, Iwo.

^b Chemistry Programme, College of Agriculture, Engineering and Science, Bowen University, Iwo.

Doi: <https://doi.org/10.47011/18.1.3>

Received on: 31/05/2023;

Accepted on: 06/11/2023

Abstract: The current study on air quality awareness at Bowen University was undertaken to determine elements, functional groups, and UV characteristics of air conditioning (AC) filter dust collected from various buildings on campus. Atomic absorption spectroscopy (AAS), Fourier transform infrared spectroscopy (FTIR), and ultraviolet (UV) analysis were performed on the samples to raise community awareness. AAS revealed the presence of eleven elements in the samples: Na, K, Ca, Mg, Fe, Cd, Zn, Mn, Cu, and Cr. FTIR analysis identified thirteen functional groups with origin = N – H, C – N, N – H, SiO₃, C – S, C – H, -NCS, = N – H, -O-C≡N, C = C – C, -C=N-, P – O – C, and C≡C, with maximum wavenumber peaks ranging from 3350 to 3320 cm⁻¹. The transmittance ray's visibility showed the presence of the orange-to-red spectrum at wavelengths between 650 and 750 nm. The study concludes that the presence of these elements, functional groups, and UV rays in the dust accumulated on AC filters underscores the importance of regular cleaning and maintenance. Proper upkeep of AC filters can help prevent dust inhalation, reducing the risk of nasal and respiratory diseases within the community.

Keywords: Dust sample, Elements, Functional groups, Air quality, Location.

Introduction

Indoor dust composition varies depending on location and is influenced by outdoor activities that occur in any area. Textile fibers, decomposing organisms, animal and human skin, rusted food, polyester bags, roadway and sand dust, and other factors all add to the number of tiny particles in interior dust. Pollutants such as zinc, nickel, lead, copper, and cadmium are commonly associated with automobile emissions in all parts of the world [1-4]. Fossil fuel use, as a result of waste material generated from various stations such as refineries, industries, brick-laying activity, and mining, may also contribute to harmful components found in the atmosphere

that penetrate various residential and commercial locations [5, 6].

Most people spend the majority of their lives indoors, either at home or at work, where air quality reflects their health efficiency [5, 7, 8]. This is in contrast to outdoor air quality, where different particles are inhaled in varying quantities, most of which may be toxic [3]. indoor air quality is determined by the condition of air filters in the interior unit of an air conditioner (AC) in residential and commercial buildings [5]. Dealing with the issue of critical indoor dust knowledge has a significant impact on the composition of air quality [9-11].

According to many authors, heavy metal composition and other harmful pollutants are researched in various locations around the world [12, 13], particularly roadway dust, soil dust, and air quality within and outside residential areas [10, 14-22].

It is a well-known truth that interior dust in the vicinity of any busy roadway has a substantial impact on settlers due to the huge or tiny amount of dust inhaled by them [5, 23, 24]. Large metropolitan characteristics and air quality of roadside dust are known to be one of the ecological contaminations in the environment, according to authors such as Sezgin *et al.* [16], Pagotto *et al.* [25], and Elik [26]. According to research, harmattan dust at the height of about 300 m above ground level, which is above the stratospheric region of the atmosphere, contributes to dust accumulation in air conditioning (AC) units at Bowen University. However, the transportation and deposit of this Saharan dust have a significant impact on the Earth's radiation budget [27-29]), with both beneficial and detrimental effects on human health [15, 30-33]. Dust particles contribute to the nasal congestion experienced by humans [34, 35]. Reports indicate that dust accumulation is widespread in both residential and commercial areas [8, 27, 29, 35-47]. Sunnu *et al.* [35] discovered that the impacts of dust are related to climate-related effects rather than the physical properties of the dust. This demonstrates that dust has been identified as a significant contributor to the global radiation balance [41-46]. It has been noted that some commercial districts in Nigeria have a significantly higher number of air conditioners (ACs) than residential areas. However, in business areas, most of these air conditioners are in operation from January to April which is Nigeria's hot season, and dust is

particularly noticeable at this time of year. It has been stated that during this time of year, AC filters capture more dust, providing greater information on the indoor air quality. Because of the activities that take place in these locations, a study conducted in Lahore, Pakistan's second-largest city, revealed that the dust content of AC filters in commercial areas is substantially higher than in residential areas [48, 49]. Nigeria is a country with a unique perspective on cleaning its surroundings, in which environmental dust settles into homes [50], potentially causing health problems owing to poor cleaning and poor air quality all over the country. Bowen University is no exception. Therefore, the goal of this study is to determine the elemental composition and functional groups present in AC filter dust within Bowen University's indoor environments. The findings will help raise awareness about the importance of cleaning AC filters for the benefit of the community's residents' health.

Sampling City Site

Bowen University, located in the ancient city of Iwo, was used for the collection of the samples (7.6401°N, 4.1770°E). The city is located in the western portion of Nigeria, and the vegetation is rainforest. The land area of the city is 7,543km². The city's highest temperature is 24°C, with a relative humidity of 92%. Bowen University features a variety of structures, including administrative buildings, classrooms, dormitories, offices, cafeterias, a worship center, and other facilities. To ensure comfort for staff and students, most of these buildings are equipped with different brands of air conditioners (ACs). The sampling locations are shown in Fig. 1.

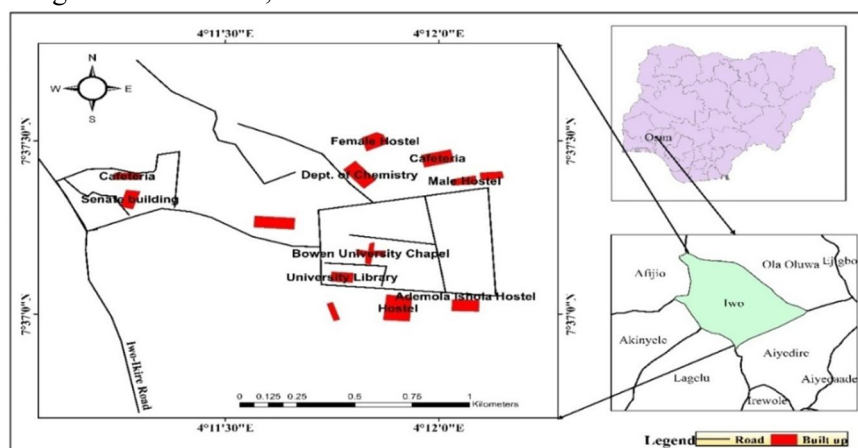


FIG. 1. Map of Bowen University showing the sampling location.

Materials and Methodology

Sample Collection

Dust particles were collected from the air filters of indoor air conditioning units installed in various buildings at Bowen University. The collection sites included the Senate building (administrative), university library, worship center (chapel), offices, classrooms, student hostels, and the cafeteria. Samples were obtained using a direct collection method in which dust particles were suspended in distilled water and subsequently extracted for analysis. This approach aligns with previous studies by Aweda et al. [2] and Falaiye et al. [31], who used a direct deposition method involving distilled water.

To avoid contamination from external sources, the collected samples were sealed in polythene polyamide bags and stored in a refrigerator until analysis. For accuracy, both dust samples from AC filters and a controlled AC filter dust sample were collected to ensure meaningful results.

Sample Preparation and Analysis

- Method for Preparing AAS Samples

The collected dust samples were analyzed in the laboratory using Atomic Absorption Spectroscopy (AAS). The AAS instrument used was an Agilent Technologies PG990 model (Buck Scientific). Before analysis, the dust samples were digested to extract trace elements.

The digestion process involved transferring the sample quantitatively into a beaker, followed by the addition of hydrochloric acid (HCl) and heating on a hot plate. For safety, digestion was performed inside a fume cupboard.

Each liquid sample (six samples in total) was prepared by adding 50 ml of solution, which was then heated until reduced to 20 ml by adding 5 ml of hydrochloric acid. The filtered samples and filtrates were chemically analyzed to determine the trace element composition. This procedure follows the methodology reported by Aweda *et al.* [15] and Chineke and Chiemeka [51].

- Standard Solution for AAS

The standard solution used in this study was prepared from a stock solution of 1000 mg/L. Dilutions were performed in stages, with nitric acid (>1%) added to prevent precipitation. The sensitivity or characteristic concentration was defined as the analyte concentration yielding an absorbance signal of 0.0044 units. The detection limit was determined as three times the standard deviation of a blank solution.

Table 1 presents the standard values used in analyzing the AAS data. It also includes the working range of the samples, along with the instrument parameters, alternative wavelengths, standard solutions, and potential interferences identified using the PG990 series instrument.

TABLE 1. Elements and their calibration and detection limits.

Elements	Analytical Line (nm)	Bandwidth (nm)	Filter Factor	Lamp Current (ma)	Integration Time (sec)	Sensitivity (mg/l)	Detection Limit (mg/l)	Working Range (mg/l)
Na	589.0	0.2	1.0	5.0	3.0	0.003	0.002	0.02-1.0
K	766.5	0.4	1.0	5.0	3.0	0.008	0.001	0.008-1.2
Ca	422.7	0.4	1.0	5.0	3.0	0.01	0.0042	0.02-2.00
Fe	248.3	0.2	1.0	5.0	3.0	0.05	0.0046	0.03-8.0
Cd	228.8	0.4	1.0	5.0	3.0	0.012	0.0028	0.02-2.20
Zn	213.9	0.4	1.0	5.0	3.0	0.01	0.003	0.01-3.0
Mn	279.5	0.4	1.0	5.0	3.0	0.002	0.002	0.01-3.5
Cu	324.7	0.4	1.0	5.0	3.0	0.03	0.004	0.018-4.0
Cr	357.9	0.4	1.0	5.0	3.0	0.05	0.005	0.04-8.0

Sample Preparation for Fourier-Transform Infrared Spectroscopy (FT-IR)

The samples were taken to the laboratory for analysis utilizing an FTIR instrument installed in the Bowen University's central laboratory for this study. The equipment, manufactured by Agilent Technologies, is the CARY 630 FT-IR

model. To prevent the liquid sample from settling in the container, it was vigorously agitated with a magnetic stirrer. A 0.2 ml portion of the sample was dropped on the machine's sensor. The sample was then exposed to radiation to determine the spectrum it contained. The FT-IR machine was calibrated using

polystyrene film, which was coupled with an ATR (attenuated total reflectance) with a diamond crystal surface. Table 2 shows the resolution and wavenumber values used for the

analysis of the samples. The interferometer is permanently designed using Michelson 45⁰ mechanical flexures to enhance the machine's sensitivity.

TABLE 2. The resolution of the FTIR machine used for the analysis.

Resolution (cm ⁻¹)	Wave number Accuracy (cm ⁻¹)	Wave number reproducibility (cm ⁻¹)	Interferometer (mm)	Spectral Range (cm ⁻¹)
4.00	0.05	0.005	25	4000-650

UV Sample Preparation

Dust samples were collected from several locations across Bowen University and evaluated using a UV-1800 spectrophotometer with serial number A114550 made by USA Inc. 50196 in absorbance measurement mode. The spectra were obtained by exposing the samples to a standard wavelength range of 200 to 800 nm at a speed of 0.5 m/s. The peaks in the spectra were determined accordingly. The settled samples were stirred using a magnetic stirrer, and then 5 ml of each sample was dropped into the machine sample analyzer for examination. A spectrum-generating machine was used to create the spectrum for each sample.

Additionally, the resulting spectrum was standardized by identifying the peaks in the spectrum using the standard waveband. The UV-1800 spectrophotometer used is a double-beam UV-visible spectrometer, incorporating a tungsten lamp to supply radiation in the visible region and a deuterium lamp to supply radiation in the ultraviolet region. The detector used for measurements is a photocell.

Results and Discussions

AAS Analysis of Air Conditioner Dust at Different Locations

The AAS results, as shown in Table 3, reveal the presence of ten elements: Na, K, Ca, Mg, Fe, Cd, Zn, Mn, Cu, and Cr. The concentrations of these elements vary by location at Bowen University. The elemental compositions and their concentrations (in mg/m³) are summarized in the table. The AAS analysis revealed that these elements are present in different concentrations across the locations.

As demonstrated by the AAS data, dust directly influences the climate by scattering or absorbing incoming solar radiation. Additionally, dust indirectly affects the climate by acting as nuclei on which clouds can form, as discussed by researchers including Chineke and Chiemeka [51], Temmerman et al. [52], Gupta and Mandariya [53], and the World Health Organization [54]. The direct influence of dust on climate is largely due to human activities, such as fossil fuel combustion (including from vehicles), metal processing industries, and waste incineration near the university, which contribute to the presence of dust particles in the environment.

TABLE 3. AAS results of the selected locations in Bowen University

Stations	Na	K	Ca	Mg	Fe	Cd	Zn	Mn	Cu	Cr
Senate	25.97	4.12	2.93	7.51	7.53	0.158	0.079	0.076	0.046	1.822
Library	22.65	4.78	1.99	7.44	7.00	0.168	0.089	0.095	0.056	1.833
Chapel	19.42	3.98	2.55	7.01	7.67	0.254	0.098	0.085	0.067	1.755
Offices	24.67	2.99	2.79	6.99	7.56	0.169	0.075	0.075	0.047	1.835
Cafeteria	23.50	4.56	3.00	7.43	7.45	0.211	0.057	0.055	0.672	1.834
Hostel	25.33	4.15	2.58	7.23	7.78	0.155	0.097	0.072	0.045	1.847
WHO [54]	0.005	8.7	0.4	0.4	0.4	5.0	0.4	0.01	0.03	0.5

Atomic Absorption Spectroscopy (AAS). Unit: mg/m³.

The acceptable levels for Fe, Ca, Mg, and Zn in air for human respiration are set at 0.4 mg/m³ for twenty-four hours, according to Gupta and Mandariya [53] and the World Health Organization [54]. Meanwhile, according to the AAS machine, the average concentrations of these elements in this study were found to be: Fe

7.50 mg/m³, Ca 2.64 mg/m³, Mg 7.27 mg/m³, and Zn 0.08 mg/m³. This demonstrates that the dust levels at various locations on the Bowen University campus are both above and below the WHO's recommended standard values for human health. The variation in these values could be attributed to activities occurring in the

surrounding environment, such as vehicular movement, abattoir operations, and industrial activities at the university.

Although there is a slight increase in iron content across the area, the air at Bowen University may not be entirely clean. Iron, however, is essential for the survival of plants and animals, as it plays a crucial role in the production of chlorophyll during photosynthesis. Additionally, iron is a vital component of hemoglobin, the substance responsible for oxygen transport in red blood cells. The WHO [54] warns that excessive iron in the body can lead to liver and heart diseases.

The results also show that the concentration of magnesium in the air across all studied locations averaged 7.27 mg/m^3 , which exceeds the WHO's recommended standard for air quality. Furthermore, the average Ca concentration of 2.64 mg/m^3 was found to be higher than the WHO's acceptable level for air quality.

Manganese, a metal used in the production of battery cells and as an oxidizing agent in chemical industries, has a tolerable average value of 0.01 mg/m^3 , according to the WHO. However, in this study, the average concentration of manganese in the air at Bowen University was observed to be 0.076 mg/m^3 ,

which is significantly higher than the recommended value [54].

Zinc (Zn) is an essential component of dust because it is essential for human health and all living organisms. According to research, Zn can be toxic to human health if the concentration is much higher than the World Health Organization's recommendations [54]. The average value observed for this research was 0.08 mg/m^3 , indicating that the Zn level in the air is below the World Health Organization's recommended acceptable level [54]. This is potentially due to lower population density in Iwo metropolis and the university itself.

The average potassium (K) concentration in Iwo was found to be 4.10 mg/m^3 , which is below the WHO's recommended acceptable level of 8.7 mg/m^3 [54]. Potassium is a pent borate white, odorless, powerful substance that is flammable, combustible, or explosive and has a high dermal toxicity, as indicated by research from various sources, including Chineke and Chiemeka [51], WHO [54], Zdrowia [55], and Harrison et al. [56].

Figure 2 illustrates the average elemental variations, where Na was found to have the highest concentration, while Mg and Fe showed nearly equal values. Mn had the lowest concentration in the air samples collected.

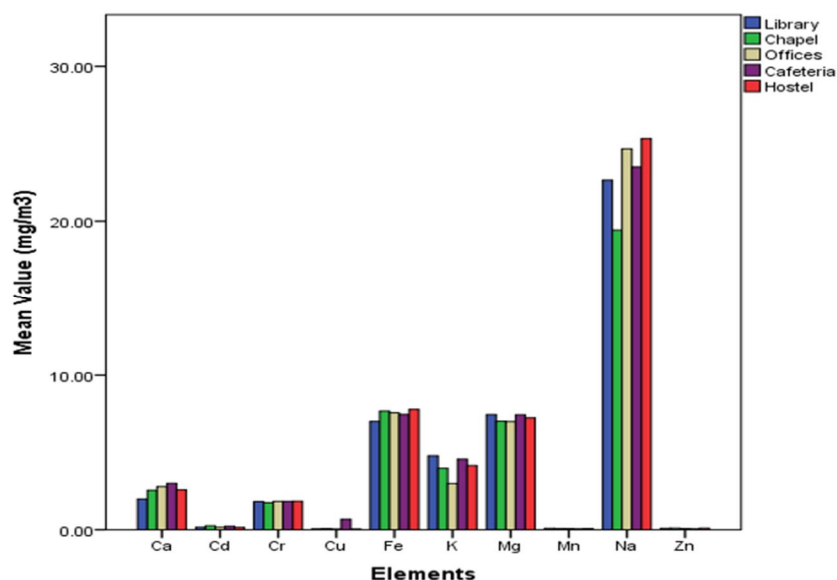


FIG. 2. Average value of each element at different locations.

FTIR Spectral Analysis of Air Conditioner Dust at Different Wavebands

The results of the FTIR spectrum analysis of dust collected from air conditioner filters at

Bowen University, as shown in Figs. 3-8, reveal that the spectral waveband peaks and transmittance vary from location to location. The observed corresponding wavebands are

3322.9 cm^{-1} , 3317.3 cm^{-1} , 3322.9 cm^{-1} , 3289.4 cm^{-1} , 3267.0 cm^{-1} , and 3268.9 cm^{-1} , which appear across all study locations. These wavebands are associated with the hydroxyl group, the H single bond of OH stretch observed in the out-of-plane, and are likely present due to the distilled water used to extract the dust sample from the air conditioner.

The bands observed in the spectrum could be attributed to both in-plane and out-of-plane stretches of N-H and O-H single bonds. Additionally, the stretches at 1638.2 cm^{-1} and 1636.3 cm^{-1} indicate the presence of an olefinic/alkene group with a stretch band of C=C

present in all of the samples collected. The stretch at 1981.1 cm^{-1} , as shown in Figures 5 and 7, suggests the presence of a C-C single bond in the samples.

Similarly, the stretch values at 1006.4 cm^{-1} and 1028.7 cm^{-1} indicate the presence of phosphate groups in the dust samples from specific locations. Furthermore, based on studies by Cameron [57], Coates [58], and Workman and Springsteen [59], the peak at 1015.7 cm^{-1} , observed at the University Worship Centre and Offices, may be attributed to a P-O-C stretch (aliphatic phosphate) that could result from road construction activities in these areas.

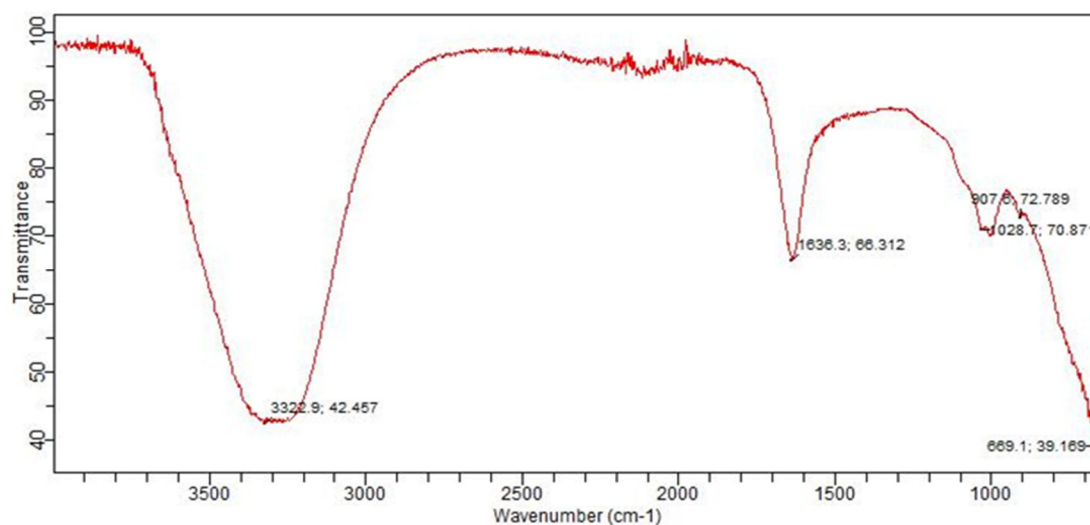


FIG. 3. FT-IR spectrum of samples from the Senate building at Bowen University.

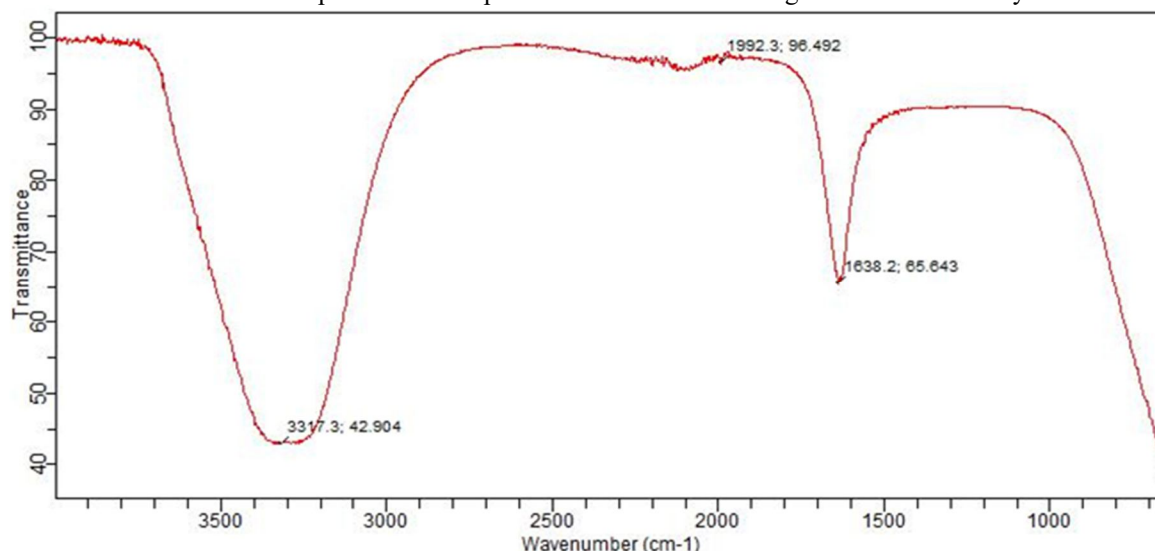


FIG. 4. FT-IR spectrum of samples from the library at Bowen University.

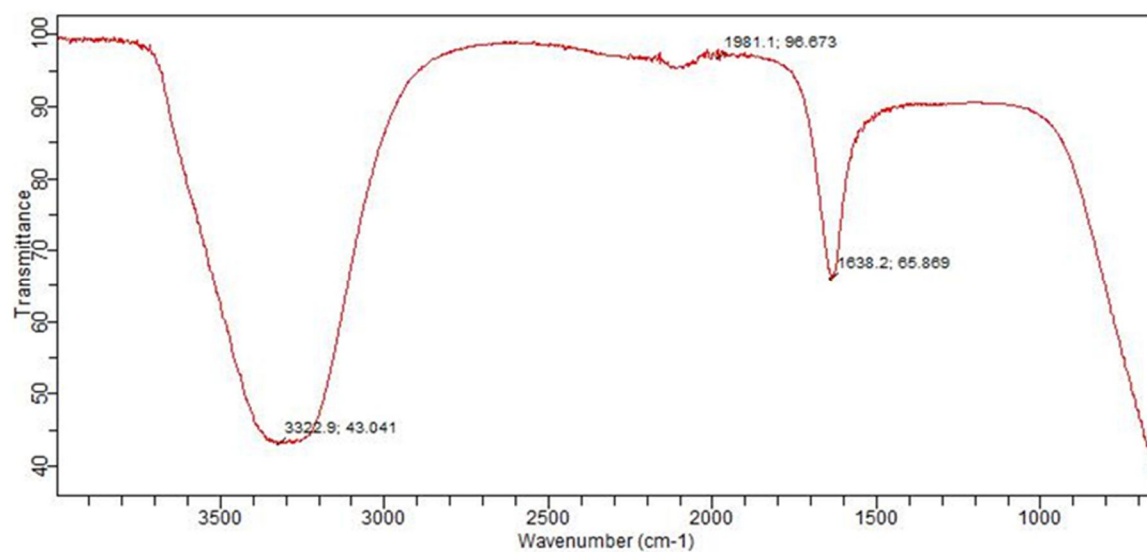


FIG. 5. FT-IR spectrum of samples from worship center at Bowen University.

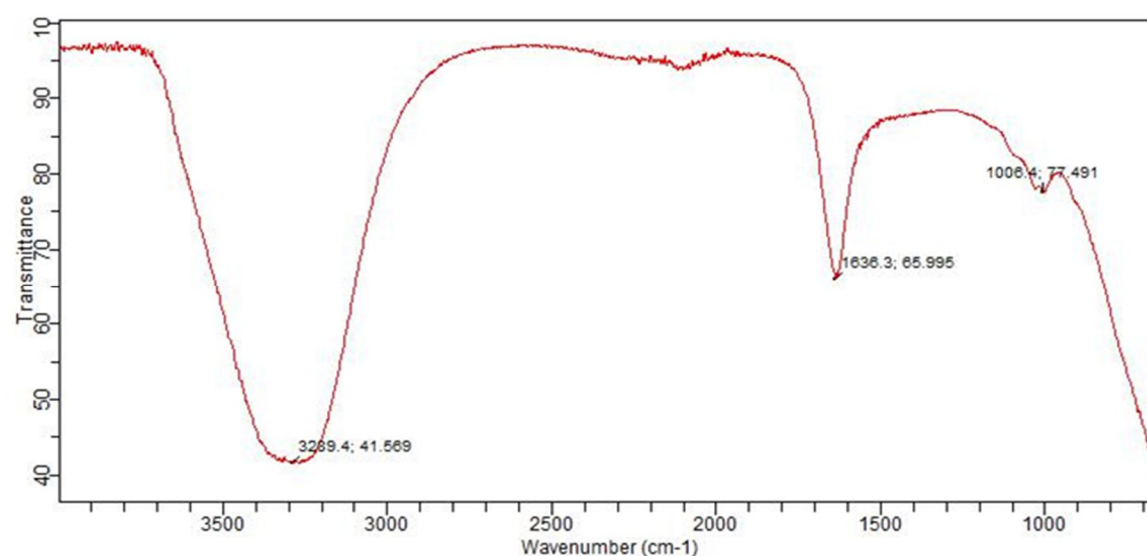


FIG. 6. FT-IR spectrum of samples from selected offices at Bowen University.

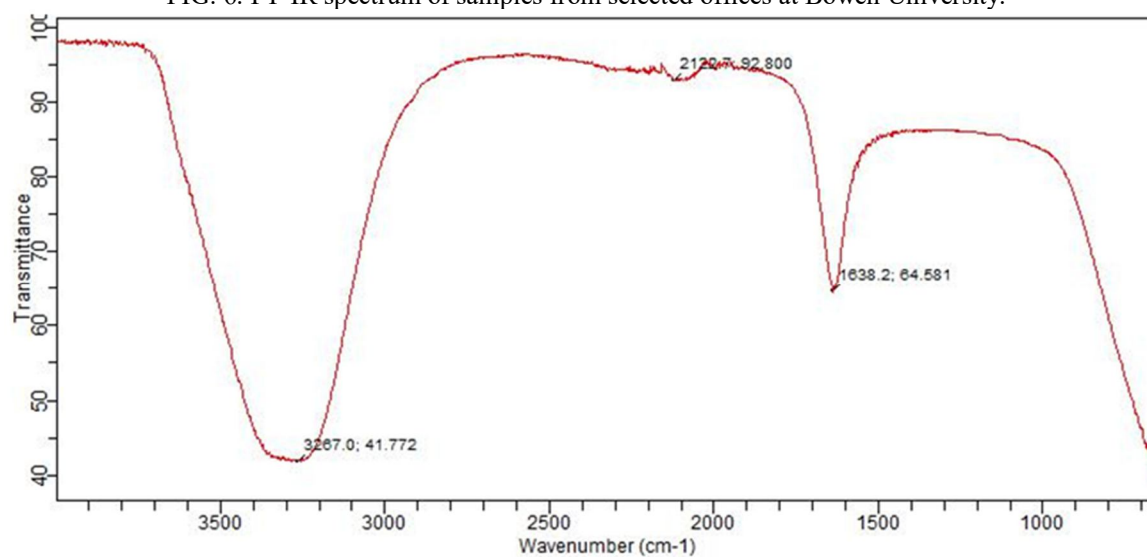


FIG. 7. FT-IR spectrum of samples from the cafeteria at Bowen University.

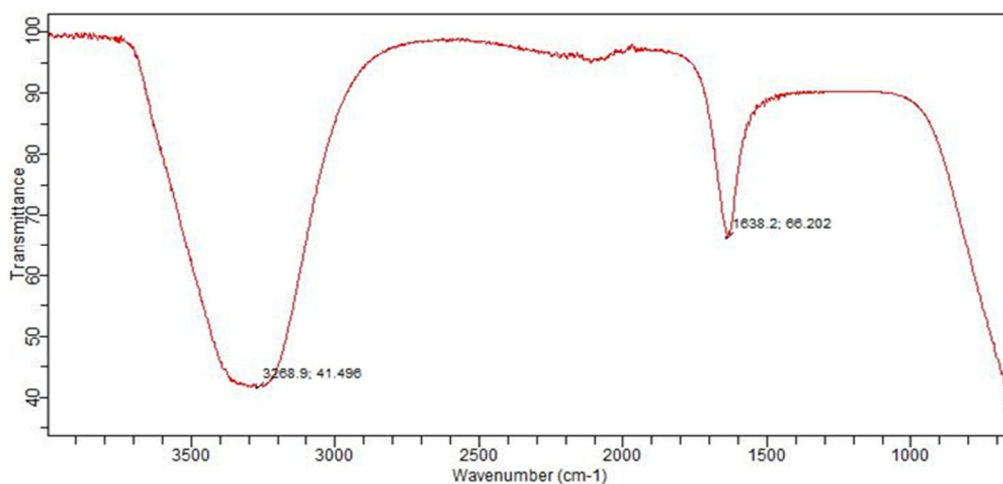


FIG. 8. FT-IR spectrum of samples from the Bowen University hotel.

The broadband in the $3700\text{--}3000\text{cm}^{-1}$ range may be attributed to the O-H stretch, which corresponds to hydroxyl groups that are completely removed when the sample is sintered at temperatures above 973 K, as reported by Dey and Ghose [60] and Alpert *et al.* [61]. Thus, the FTIR analysis confirms the presence of harmattan dust in the country's atmosphere.

The results in Table 4 show = N-H with a wavenumber of 3322.9cm^{-1} and a transmittance of 42.457. This value corresponds to imino compounds, characterized by an NH stretch with both double and single bonds. The nitrogen double-bonded groups, including imino and azo groups, exhibit absorption bands similar to the N-H single bond. The Bowen University Senate building appears to contain examples of these frequency bands, observed in a few multiple

single bonds and accumulated in the double-bonded region of the spectrum. However, these groups are not as prevalent in other locations due to dust transportation.

The sample exhibits a frequency range of $1680\text{--}1630\text{ cm}^{-1}$, corresponding to the amide functional group, with C-N and N-H single bonds detected at a wavenumber of 1636.3 cm^{-1} and a transmittance of 66.312. This suggests that compounds such as anhydrides and acid halides may react with water, potentially forming amides and esters in the presence of amines and alcohols. Furthermore, infrared spectroscopy provides insightful information on the formation of these compounds. However, these compounds were not detected in samples collected from cafeterias and student hostels, possibly due to differences in activities occurring in these areas.

TABLE 4. The FTIR spectral result analysis of the functional groups

Location	Origin	Group Frequency Wavenumber (cm^{-1})	Functional Groups
Senate Building	= N – H	3350 – 3320	Imino Compound (NH Stretch)
	C – N and N – H	1680 – 1630	Amide
	SiO ₃	1100 – 900	Silicate ion
	C – N	1090 – 1020	Primary amino (Primary amide, CN Stretch)
	C – S	715 – 670	Aryl thioethers, $\text{O} - \text{S}$ (C – S Stretch)
Library	C – H	3320 – 3310	Alkyne (C – H Stretch)
	-NCS	2150 – 1990	Isothiocyanate (-NCS)
	C – N and N – H	1680 – 1630	Amide
Worship Centre	= N – H	3350 – 3320	Imino Compound (NH Stretch)
	-O-C \equiv N	2285 – 1990	Cyanates, isocyanates, thiocyanates
	C – N and N – H	1680 – 1630	Amide
Offices	C – H and C = C – C	1355 – 1320	Aromatic nitro compounds
	-C=N-	1690 – 1590	Open – chain imino
	P – O – C	1100 – 1000	Aliphatic Phosphate
Cafeteria	C – H and C = C – C	1355 – 1320	Aromatic nitro compounds
	C \equiv C	2260 – 2100	Terminal Alkyne (mono substituted)
	-C = N -	1690 – 1590	Open – chain imino
Hostel	C – H and C = C – C	1355 – 1320	Aromatic nitro compounds
	-C = N -	1690 – 1590	Open – chain imino

The presence of silicate ions in the 1100–900 cm^{-1} region was also revealed by the results shown in Fig. 3. This has a wavenumber of 907.6 cm^{-1} and a transmittance of 72.789. This group demonstrates that silicates are saline in nature and contain silicon (Si) and oxygen anions, resulting in SiO_3 . This was not noticed in other places. The presence of SiO_3 in the Senate building indicates that salty activities are occurring there.

Furthermore, according to several writers, silicates constitute approximately 95% of the Earth's crust and upper mantle, making them the primary component of igneous rock. Silicates are also a major source of dust in Nigeria. Additionally, Fig. 3 shows evidence of primary amines in the sample. The C–N single bond stretch, which falls within the 1090–1020 cm^{-1} range, was detected at 1028.7 cm^{-1} with a transmittance of 70.871. However, tertiary amines were found to be more prevalent in the sample. The diagnostic data further reveal that only a single bond C–N vibration is present, and these amides were not detected in all studied locations.

The results also indicate the presence of aryl thioethers, identified by a wavenumber of 669.1 cm^{-1} with a transmittance of 39.169. This suggests the presence of aliphatic or aromatic (aryl) molecular fragments in the sample. Interestingly, aryl thioethers were not found in any other location, which could be attributed to activities specific to the Senate building, such as higher tourist traffic and increased environmental interactions in the surrounding area.

The results of the sample collected at the University library, as shown in Table 4, show that the group frequency ranges from 1680 to 1630 cm^{-1} , with the presence of the amide functional group, along with C–N and N–H single bonds. A wavenumber of 1638.2 cm^{-1} and a transmittance of 66.643 were detected. These findings suggest that compounds such as anhydrides and acid halides can react with water. Additionally, when these compounds interact with amines and alcohols, they may form amides and esters. Infrared spectroscopy further confirmed the presence of these compounds, indicating their significance in chemical processes. However, these compounds were not found in samples from the cafeteria and student

hostels, which could be attributed to differences in activities occurring in these locations.

Table 4 also shows the presence of amide in the sample. The C–N single bond stretch, occurring within the 1680–1630 cm^{-1} range, was observed at 1638.2 cm^{-1} with a transmittance of 66.643. Various researchers have noted that tertiary amines tend to be more significant than primary or secondary amines. However, the diagnostic data in this study indicate that the sample contains only a single bond C–N vibration. Notably, these amides were not detected in all the locations investigated.

Additionally, the results reveal the presence of isothiocyanate (–NCS) in the university library sample, identified at a wavenumber of 1992.3 cm^{-1} with a transmittance of 96.492. This suggests the presence of aliphatic molecular fragments. Isothiocyanate was absent in samples from other locations, which may be due to specific environmental activities and increased tourist presence around the university library.

Furthermore, the results in Table 4 for the worship center show the presence of =N–H at a wavenumber of 3322.9 cm^{-1} with a transmittance of 43.041, similar to what was observed in the Senate building. This corresponds to imino compounds, characterized by NH stretching in both single and double bonds. Imino and azo groups, which belong to the nitrogen double bond category, exhibit absorption similar to N–H single bonds. The Bowen University Senate building and worship center appear to contain examples of these frequency patterns, reflected in multiple single bonds and accumulated double-bonded sections. However, these compounds were not detected in other locations, likely due to dust transportation. This was not observed in any other study locations, while the sample's group frequency 1680–1630 cm^{-1} and amide functional group with C–N and N–H single bonds are said to be present in all locations. It does, however, show that compounds like anhydrides and acid halides react with water. When these compounds react with amines and alcohols, they can produce amides and esters. Furthermore, infrared spectroscopy revealed that the manufacturing of these chemicals is instructive. These compounds were not found in the cafeteria and student hostel samples, which

could be attributed to the activities that take place there.

Additionally, the origin of the $\text{-O-C}\equiv\text{N}$ broadband signal was observed only in the worship center, with a broadband range of $2285\text{--}1990\text{ cm}^{-1}$. This confirms the presence of cyanates, isocyanates, and thiocyanates in the sample, which were absent from all other locations.

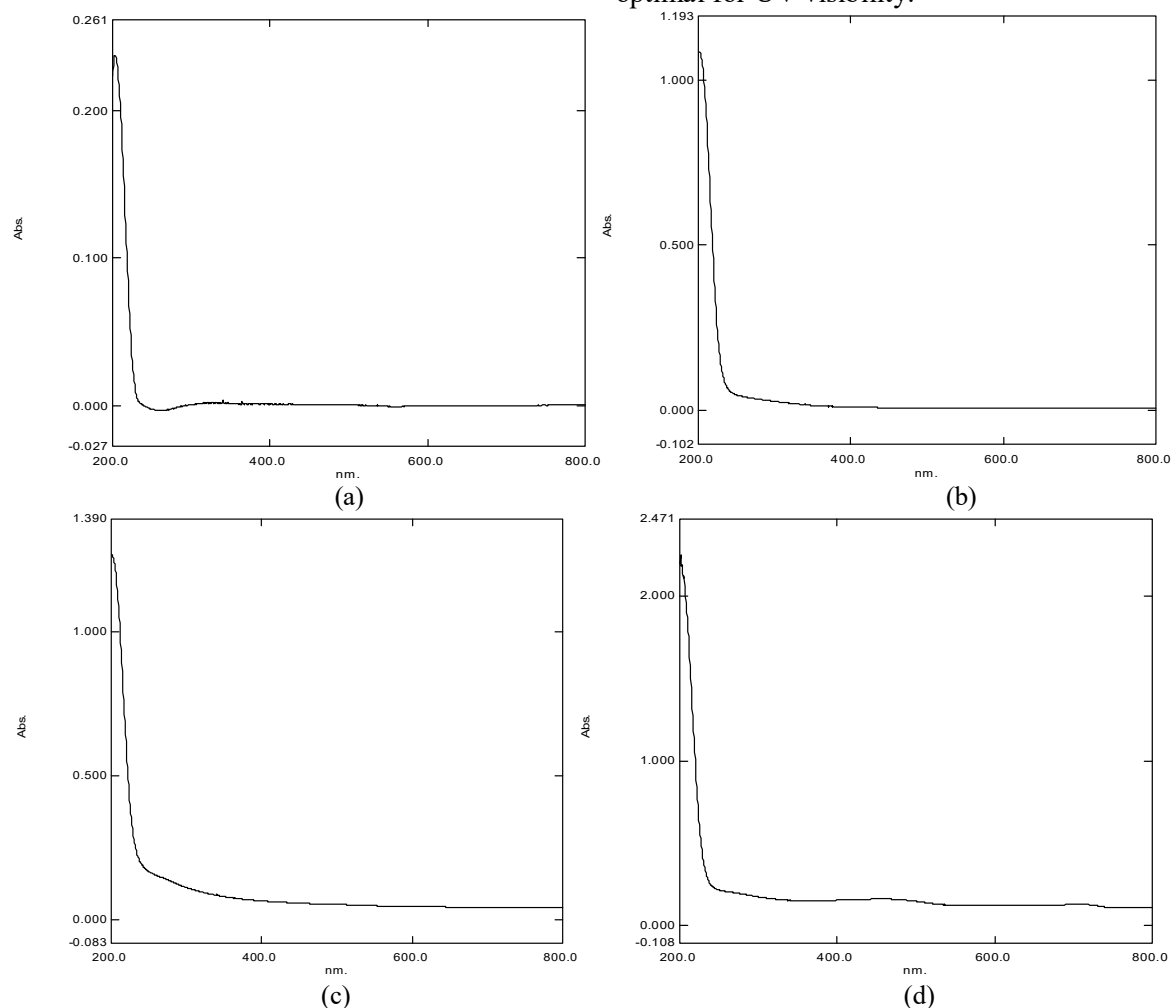
Table 4 further highlights the presence of aromatic compounds containing $\text{C}=\text{C}$ and $\text{C}\equiv\text{C}$ bonds. The samples from offices and the cafeteria exhibited both double and triple bonds. According to Cameron [57], Coates [58], and Coates [62], the triple bond carbon-to-carbon ($\text{C}\equiv\text{C}$) observed at 2120.7 cm^{-1} corresponds to a terminal alkyne of a mono-substituted compound. Additionally, saturated and unsaturated aromatic compounds exhibiting $\text{C}=\text{C}$ bonds were found in the cafeteria sample. Similarly, aromatic compounds with carbon-to-carbon double bonds ($\text{C}=\text{C}$) were identified in samples from offices and hostels. These

observations confirm the presence of aromatic molecular structures in the studied locations.

UV Characteristics of Bowen University

The ultraviolet (UV) characteristics of air conditioning (AC) dust collected at Bowen University were analyzed based on its exposure to the electromagnetic spectrum. The wavelength of the dust was found to be between 200 and 800 nm. However, according to Kealey and Haines [63], the visibility region of the spectrum is between 400 and 800 nm.

As shown in Figs. 9(a)-9(f), the absorption rate of UV light by the dust samples was weak, as revealed by the results. The absorbance spectra presented in Figs. 9(a)-9(f) indicate that the absorbance values ranged from 1.00 to 0.25 across all locations. Figure 9(a) has a value of 0.25, Fig. 9(b) has a value of 1.10, Fig. 9(c) has a value of 1.2, Fig. 9(d) has a value of 2.3, Fig. 9(e) has a value of 0.85, and Fig. 9(f) has a value of 1.0. According to Falaiye and Aweda [4], an absorbance value below 1.00 is considered optimal for UV visibility.



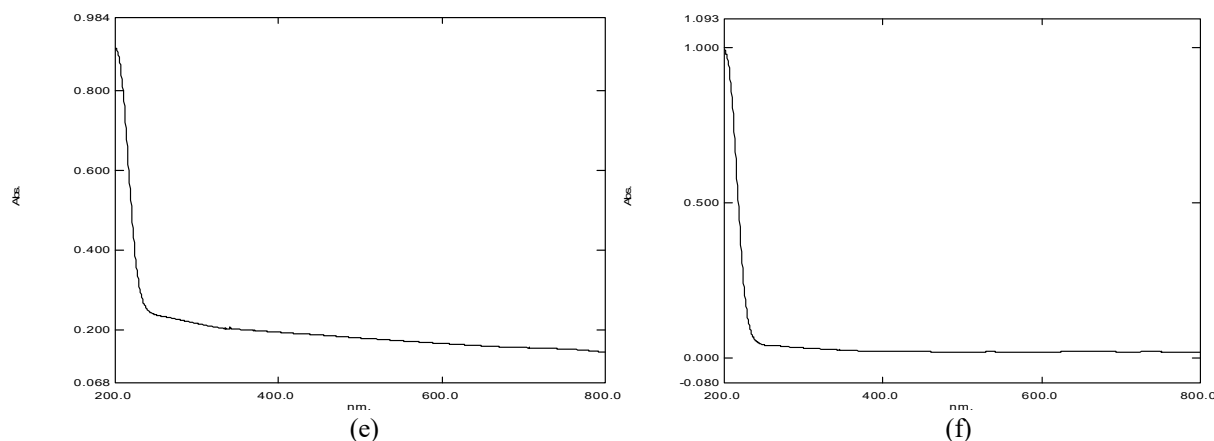


FIG. 9. UV characteristics of the samples collected at Bowen University

According to Aweda *et al.* [2] and Hemwech *et al.* [64], the visible spectrum for orange ranges between 600 and 700 nm, extending into the red region. Furthermore, the dust sample collected at Bowen University may have both minimum and maximum advantages in terms of the UV relationship. However, the orange to red spectrum indicates that dust may be trapped in the light visibility from solar radiation, which may have an effect on greenhouse radiation. Furthermore, this confirms the presence of greenhouse gases, which may have an effect on some of the chemicals present in the sample.

For each of the locations studied, it was discovered that the higher the incoming absorption in the ultraviolet (320 nm) absorption in the ultraviolet region (320 nm) corresponded with increased infrared wavelength emissions. This demonstrates that the particle has a lower UV concentration when compared to the dust collected at Bowen University. Furthermore, aerosol plays a significant role in the interaction of UV on dust particles across the spectrum transmittance. Furthermore, aerosol is primarily a dust particle that can transport trace metals and particulate matter, such as $PM_{2.5}$ or PM_{10} , throughout the Nigerian zone.

Conclusion

The dust samples collected from the AC filter at Bowen University contained ten elements: Na, K, Ca, Mg, Fe, Cd, Zn, Mn, Cu, and Cr. However, the elements present in the sample followed what was reported by [65, 66]. The functional group present in the sample identified that there are thirteen functional groups with origin ($=N-H$, $C-N$, $N-H$, SiO_3 , $C-S$, $C-H$, $-NCS$, $=N-H$, $-O-C\equiv N$, $C=C-C$, $-C=N-$,

$P-O-C$, $C\equiv C$). Maximum wavenumber peaks ranging from 3350 to 3320 cm^{-1} were observed. The transmittance ray's visibility showed the presence of orange to red within the $650-750\text{ nm}$ wavelength range. As a result, the study concludes that the presence of elements, functional groups, and UV rays in the dust collected from the air filter of the indoor air conditioning unit suggests that air conditioner filters should be cleaned and maintained regularly. Proper maintenance is essential to prevent the accumulation and inhalation of dust, which could lead to various nasal diseases in the community.

Recommendation

The authors wish to recommend to the management of Bowen University that adequate precautionary measures and policies should be made to help mitigate the effects of high elemental concentrations present in the filter of the air conditioner placed in different offices, classrooms, cafeterias, hostels, and other relaxation places in the University. However, for proper verification of air quality at the University, effect of dust on human health, both advantages and disadvantages as well as daily collection of the dust, is also recommended.

Acknowledgements

The authors would like to thank Bowen University's central laboratory for the opportunity to analyze the collected sample. Furthermore, we would like to thank the Bowen University administration for the grace extended during sample collection. We appreciate it.

References

- [1] Ferreira-Baptista, L. and De Miguel, E., *Atmos. Environ.*, 39 (25) (2005) 4501.
- [2] Aweda, F.O., Falaiye, O.A., and Oyewole, J.A., *Jordan J. Phys.*, 14 (1) (2021) 1.
- [3] Falaiye, O. and Aweda, F., *J. Appl. Sci. Envir. Manag.*, 22 (2) (2018) 281.
- [4] Falaiye, O.A. and Aweda, F.O., *Jordan J. Phys.*, 13 (1) (2020) 17.
- [5] Siddique, N., Majid, A., and Tufail, M., *J. Radioanal. Nucl. Chem.*, 290 (3) (2011) 691.
- [6] Abiye, O. et al., *Ife J. Sci.*, 16 (1) (2014) 107.
- [7] Ezech, G.C. et al., *Hum. Ecol. Risk Assess.*, 24 (4) (2018) 925.
- [8] Abiye, O.E. et al., *Environ. Sci. Pollut. Res.*, 27 (2020) 39317.
- [9] Falaiye, O.A. and Aweda, F.O., *arXiv preprint arXiv:1806.11557*, (2018).
- [10] Colbeck, I., Nasir, Z.A., and Ali, Z., *Environ. Sci. Pollut. Res.*, 17 (6) (2010) 1187.
- [11] Wasim, M., *Nucleus*, 47 (2) (2010) 149.
- [12] Manoli, E., Voutsas, D., and Samara, C., *Atmos. Environ.*, 36 (6) (2002) 949.
- [13] Kothai, P. et al., *Aerosol Air Qual. Res.*, 11 (5) (2011) 560.
- [14] Salim A.M. and Madany, I.M., *Water Air Soil Pollut.*, 66 (1) (1993) 111.
- [15] Aweda, F.O., Falaiye, O.A., and Babatunde, G.J., *J. Appl. Sci. Environ. Manag.*, 21 (7) (2017) 1313.
- [16] Sezgin, N. et al., *Environ. Int.*, 29 (7) (2004) 979.
- [17] Han, L. et al., *Atmos. Environ.*, 41 (35) (2007) 7485.
- [18] Martinez, T. et al., *J. Radioanal. Nucl. Chem.*, 276 (3) (2008) 799.
- [19] Jabeen, N. et al., *J. Radioanal. Nucl. Chem.*, 247 (1) (2001) 145.
- [20] Chung, Y.-S. et al., *J. Radioanal. Nucl. Chem.*, 278 (2) (2008) 441.
- [21] Waheed, S. et al., *J. Radioanal. Nucl. Chem.*, 285 (3) (2010) 723.
- [22] Okhravi, R., *J. Sci.*, 10 (1999) 706.
- [23] Zaidi, J. et al., *J. Radioanal. Nucl. Chem.*, 196 (1) (1995) 125.
- [24] Waheed, S. et al., *Toxicol. Environ. Chem.*, 83 (1-4) (2002) 13.
- [25] Pagotto, C. et al., *Environ. Technol.*, 22 (3) (2001) 307.
- [26] Elik, A., *Commun. Soil Sci. Plant Anal.*, 34 (1-2) (2003) 145.
- [27] Bryant, A.C., Painter, T.H., Deems, J.S., and Bender, S.M., *Geophys. Res. Lett.*, 40 (2013) 3945.
- [28] Su, J., Huang, J., Fu, Q., Minnis, P., Ge, J., and Bi, J., *Atmos. Chem. Phys.*, 8 (10) (2008) 2763.
- [29] Tegen, I., Heinold, B., Todd, M., Helmert, J., Washington, R., and Dubovik, O., *Atmos. Chem. Phys.*, 6 (2006) 4345.
- [30] Kalu, A. E., "The African dust plume: Its characteristics and propagation across West-Africa in winter". In: Ed. Morales, C., "Saharan Dust Mobilization Transport Deposit", SCOPE 14, (John Wiley, 1979), p. 95.
- [31] Falaiye, O.A., Yakubu, A.T., Aweda, F.O., and Abimbola, O.J., *Ife J. Sci.*, 15 (2013) 175.
- [32] Adimula, I.A., Falaiye, O.A., and Adindu, C.L., *Centrepont Sci. Ed.*, 16 (2008) 15.
- [33] Falaiye, O.A., Aweda, F.O., Yakubu, A.T., *FUTA J. Res. Sci.*, 13 (1) (2017) 158.
- [34] Resch, F., Sunnu, A., and Afeti, G., *Tellus B*, 60 (1) (2008) 98.
- [35] Sunnu, A., Afeti, G., and Resch, F., *Atmos. Res.*, 87 (1) (2008) 13.
- [36] Sunnu, A., Resch, F., and Afeti, G., *Aeolian Res.*, 9 (2013) 125.
- [37] Goudie, A.S., *Environ. Int.*, 63 (2014) 101.
- [38] de Longueville, F., Ozer, P., Doumbia, S., and Henry, S., *Int. J. Biometeorol.*, 57 (1) (2013) 1.
- [39] Sunnu, A.K., *J. Environ. Sci. Eng. A*, 1 (10A) (2012) 1203.

- [40] Ginoux, P., Prospero, J.M., Gill, T.E., Hsu, N.C., and Zhao, M., *Rev. Geophys.*, 50 (3) (2012) RG3005.
- [41] Rodríguez, S., Alastuey, A., and Querol, X., *Aeolian Res.*, 6 (2012) 55.
- [42] Ravi, S. et al., *Rev. Geophys.*, 49 (3) (2011) RG3001.
- [43] Okin, G.S. et al., *Eos Trans. Am. Geophys. Union*, 92 (29) (2011) 241.
- [44] Prospero, J.M., *Welcome to Bremen*, 10 (2011) 17.
- [45] He, C., Breuning-Madsen, H., and Awadzi, T.W., *Geogr. Tidsskr.-Danish J. Geogr.*, 107 (1) (2007) 9.
- [46] McFiggans, G. et al., *Atmos. Chem. Phys.*, 6 (9) (2006) 2593.
- [47] Breuning-Madsen, H. and Awadzi, T.W., *Catena*, 63 (1) (2005) 23.
- [48] von Schneidemesser, E. et al., *Sci. Total Environ.*, 408 (7) (2010) 1640.
- [49] Dybczynski, R. and Suschny, O., *Final Report on the Intercomparison Run SL-1 for the Determination of Trace Elements in a Lake Sediment Sample*, (IAEA Vienna, 1979).
- [50] Alaiyemola, S.R., Abbass, M., and Aweda, F.O., *Iran. J. Energy Environ.*, 15 (1) (2024) 38.
- [51] Chineke, T. and Chiemeka, I., *Afr. Rev. Phys.*, 3 (1) (2010) 125.
- [52] Temmerman, S. et al., *Nature*, 504 (7478) (2013) 79.
- [53] Gupta, T. and Mandariya, A., *Environ. Sci. Pollut. Res.*, 20 (8) (2013) 5615.
- [54] World Health Organization (WHO), *The World Health Report 2002: Reducing Risks, (Promoting healthy life, 2002)*.
- [55] Zdrowia, Ł.O., “Guidelines for Drinking-water Quality: Health Criteria and Other Supporting Information”, (World Health Organization, 1996).
- [56] Harrison, R.M. et al., *Atmos. Environ.*, 262 (2021) 118592.
- [57] Cameron, E.M., *Geochim. Cosmochim. Acta*, 45 (6) (1981) 997.
- [58] Coates, J., “Interpretation of Infrared Spectra, a Practical Approach”, (Citeseer 2000).
- [59] Workman J, Jr. and Springsteen, A., “Applied Spectroscopy: A Compact Reference for Practitioners”, (Academic Press, 1998).
- [60] Dey, S. and Ghose, J., *Mater. Res. Bull.*, 38 (11-12) (2003) 1653.
- [61] Alpert, N.L., Keiser, W.E., and Szymanski, H.A., “IR: Theory and Practice of Infrared Spectroscopy”, (Springer Science & Business Media, 2012).
- [62] Coates, J.P., *Appl. Spectrosc. Rev.*, 31 (1-2) (1996) 179.
- [63] Kealey, D. and Haines, P.J., “BIOS Instant Notes in Analytical Chemistry”, (Taylor & Francis, 2002).
- [64] Hemwech, P. et al., *SN Appl. Sci.*, 3 (12) (2021) 1.
- [65] Falaiye, O.A., Abiye, O.E., and Nwabachili, S.C., *Proc. Int. Acad. Ecol. Environ. Sci.*, 11 (1) (2021) 15.
- [66] Aweda, F.O., Falaiye, O.A., and Samson, T.K., *Jordan J. Phys.*, 16 (4) (2023) 413.

Field Emission Characteristics of Carbon Black Particles and Various Types of Carbon Nanotubes Using Glass Tubes

Hatem A. Al-Braikat^a, Samer I. Daradkeh^{b,c}, M-Ali H. Al-Akhras^a and Marwan S. Mousa^d

^a Department of Physics, Jordan University of Science and Technology, Irbid, Jordan.

^b Central European Institute of Technology, Brno University of Technology, Purkyňova 656/123, 612 00, Brno, Czech Republic.

^c Department of Physics, Faculty of Electrical Engineering and Communication, Brno University of Technology, Technická 2848/8, 616 00, Brno, Czech Republic.

^d Department of Renewable Energy, Jadara University, Irbid 21110, Jordan.

Doi: <https://doi.org/10.47011/18.1.4>

Received on: 12/07/2023;

Accepted on: 26/01/2024

Abstract: Carbon-based nanomaterials have gained considerable attention in recent decades owing to their exceptional structural and material characteristics, such as high thermal and electrical conductivity, chemical stability, and high aspect ratio. These remarkable properties make carbon-based nanomaterials highly desirable for various scientific and industrial applications. In this research, the field electron emission (FEE) properties of different materials were investigated using current-voltage (I-V) characteristics and the well-known Fowler-Nordheim (FN) plots. Specifically, four types of carbon-based nanomaterials were examined: single-walled carbon nanotubes (SWCNTs) synthesized through a high-pressure carbon monoxide process involving Fe particles, multi-walled carbon nanotubes (MWCNTs) with a carbon purity of 90% known as NanoclyTM NC 7000, carbon nanotube fibers (CNTFs) denoted as III PR-1, and carbon black (CB) referred to as Vulcan XC72. Field emission tips, also known as emitters, were fabricated using a glass-drawing technique, with the carbon material inserted until it protruded from the broken end. These emitters were then characterized using field emission microscopes (FEM) under ultra-high vacuum (UHV) conditions, with a cathode-to-screen (anode) separation of approximately 10 mm. The results obtained from the CB material exhibited satisfactory agreement with the linearity of the FN plots, while the other materials showed this agreement primarily at low applied voltages. The emission images appeared as a single-spot pattern at low voltages for SWCNTs and CNTFs, whereas CB and MWCNTs exhibited this characteristic pattern at higher voltages.

Keywords: Field emission, Fowler-Nordheim, Single-Walled carbon nanotubes, Multi-Walled carbon nanotubes, Carbon black, Carbon nanofibers.

1. Introduction

Electrons can be emitted from the surfaces of materials through several mechanisms, including thermionic emission, where the electrons gain sufficient thermal energy to overcome the potential barrier and extract into the vacuum or air. Photoelectric emission takes place when

incident photons transfer energy to electrons, enabling them to surpass the material's work function threshold and emit from the surface. [1]. Cold field electron emission (CFE) represents a quantum mechanical phenomenon operating at high electric field strengths and low

temperatures, wherein electrons with energies below the Fermi level are extracted through quantum tunneling across a narrowed potential barrier, without requiring the substantial energy input characteristic of other emission processes [2].

After 1922, CFE attracted more attention than thermionic emission due to its low energy spread, high brightness, and concentrated emission pattern [3]. Thermionic emission has a higher energy consumption, wider energy spread, and metal degradation caused by the high operating temperature [4]. Additionally, CFE can be operated at room temperature, which makes it more advantageous. CFE from cathodes can provide high current densities for a variety of applications, such as high-power microwave generation [5], vacuum electronics [6], X-ray generation [7], and space vehicle neutralization [8]. For electron extraction, the material must be subjected to a strong electric field, typically around $\sim 3 \text{ V/m}$ [9]. To achieve optimal field emission performance, emitters must be fabricated with high-curvature apices, as these geometrical features effectively concentrate the electric field at the tip region. This field enhancement phenomenon significantly reduces the required applied voltage for electron extraction, improving operational efficiency. The concentrated electric field at these sharp tips creates localized regions of intense field strength, facilitating quantum tunneling by narrowing the potential barrier at the emission surface.

Extensive experimentation has been conducted on various metals and metal oxide materials, employing different emitter fabrication methods such as zinc oxide (ZnO), tungsten (W) nanowires, liquid metal (gallium-Ga), and more, in the field of cold field emission. However, due to the active nature of metals, the presence of residual gases, and ion bombardment during the field emission process, limitations arise in terms of emitter lifetime and fluctuations in field emission current [10], hindering the advancement of field emission. Consequently, researchers are actively seeking alternative materials that exhibit favorable characteristics for utilization as field emitters [11].

In 1889, carbon nanotube fibers (CNTFs III PR-1) were first discovered. Studies have reported the growth of carbon filaments from

carbon-containing gases using a metallic crucible as the catalyst. Notably, Robertson [12] was among the first to observe that the interaction between methane and metal surfaces at relatively low temperatures resulted in the formation of graphitic carbon [13]. The accidental discovery of multiwalled carbon nanotubes (MWCNTs) occurred in 1991 when Iijima [14] was investigating the surfaces of a graphite electrode employed in electric arc discharge. Subsequently, in 1993, Iijima and his colleague discovered single-wall carbon nanotubes (SWCNTs) by identifying single-shell tubules within soot-like deposits formed in a carbon-arc chamber [15]. Carbon black (CB), similar to other colloidal materials generated in a flame, exists in the form of primary aggregates where the primary particles are fused [16]. It is well-established that carbon nanotubes (CNTs) can emit electrons at relatively low electric fields and can sustain a stable and intense current, aligning with the principles of the standard Fowler-Nordheim (FN) theory.

The unique structure of CNTs, including their high aspect ratio [17], high thermal and electrical properties [18], high chemical stability, and high melting point [19], are the reasons behind their superior performance in CFE from their surfaces. CFE, specifically from CNTs, is affected by a set of factors. These factors include ion bombardment (as mentioned before) and the existence of adsorbate on the surface, which sometimes can contribute to field emission, change emission current values, and could be identified as a sudden raise in the emission current value [20]. CNTs of different lengths and diameters with low vacuum can cause field emission fluctuations and the interaction between neighboring nanotubes [21], which can reduce the effective field enhancement factor [22]. Vacuum space charge can also lead to fluctuations in emission current [23]. Different techniques were conducted to mitigate the emission current fluctuation and improve overall field emission characteristics, for instance, high temperature annealing or heating of the tip by the extracted electron current for relatively long time can decrease defects of CNTs, thereby improving the efficiency of the emitter [24-25]. Additionally, the high aspect ratio can affect the field enhancement factor, thus improving the emitted current [26]. The existence of resistance in a CNT can cause the current to saturate [27], where the linear shape of the $(I - V)$

characteristics can denote the existence of resistance. There are two positions where resistance can exist: one along the carbon nanotube/nanofibers (CNs) and the other at the CN/substrate interface [28].

In this study, the emitters were fabricated using a glass puller apparatus, employing a drawing technique [29]. CNT tips show a deviation from the FN theory, but CBs follow it. Also, all types form a single-spot pattern at a relatively low applied voltage except for CB, which showed a single-spot pattern at a high applied voltage value as well [30-31]. However, the theory is often applied in other situations.

The elementary Fowler-Nordheim (FN) type equation can be written as:

$$i = A_n \{a\phi^{-1}(\beta_v V)^2\} \exp[-b\phi^{-3/2}/\beta_v V] \quad (1)$$

This equation is utilized to depict the phenomenon of field emission. The equation includes several variables: emission current (i), local work function (ϕ), applied voltage (V), local voltage-to-surface field conversion factor at a reference point (β_v), and notional emission area (A_n). The constants a and b are the first and second Fowler-Nordheim (FN) constants [32]. In the FN plot, $\ln(I/V^2)$ is plotted on the y-axis and $1/V$ on the x-axis [33]. Ideally, the FN plot should be a straight line; however, deviations can occur, as evidenced by the multilinear segments observed in SWCNTs, MWCNTs, and CNTFs III PR-1 in the results and discussion section.

Using Eq. (1) to describe the FN mechanism in CNTs presents challenges due to factors such as wave function structure, band structure, and the effect of screened potential. These factors are more pronounced in small-radius emitters like CNTs [34]. CNTs differ from bulk materials, such as metals, in several ways [35-36], including their energy band structure and the influence of impurities and defects on electron emission [37]. For example, the presence of impurities and defects can generate localized states near the Fermi energy, altering the emitter's energy band structure. Furthermore, in single-walled carbon nanotubes (SWCNTs), the density of states near and above the charge neutrality level is lower than in metals [38]. As a result, field penetration and band bending effects can occur, particularly near the emitter apex, leading to local dipole effects [39]. Therefore,

treating SWCNTs as bulk metals is not accurate [40-41].

This study investigates the field emission properties of carbon-based nanomaterials, emphasizing their potential for various scientific and industrial applications due to their distinctive structural and material characteristics. Additionally, it aims to contribute to ongoing research on identifying the optimal material and fabrication method for electron emitters by comparing the field electron emission (FEE) characteristics of several materials using common tools such as the I-V plot and the corresponding FN plot.

2. Materials and Methods

2.1 Materials

All materials were bought from specialized companies. The SWCNTs were produced via catalytic conversion of high-pressure CO over Fe particles (HiPCO) processed at CNI in Houston, TX. Individual SWCNTs have a length of approximately 1 – 3 μm , a mean diameter of 1 – 4 nm, and a surface area of 1040 m^2/g . MWCNTs (NanocylTM NC7000 S.A., Belgium) were produced via chemical vapor deposition, with a diameter of 9.5 nm and a high aspect ratio (> 150) [42]. The CNTFs Pyrograf III PR-1 have an average fiber diameter of 100 – 200 nm and a length of 30 – 100 μm . The CB Vulcan XC72 processed at CABOT Corporation has an average particle size of approximately 30 nm, with the mean size of primary aggregates ranging between 100 and 200 nm [43-44].

2.2 Methods

The emitters used in this study were fabricated using a glass puller device, employing a drawing technique as depicted in Fig. 1. In this process, carbon-based material was mechanically inserted into a glass tube, ensuring a consistent distribution along its length. The glass tube had an internal diameter of 0.1 mm and an external diameter of 1 mm, creating a controlled environment necessary for precise field emission measurements.



FIG. 1. Actual image of the glass puller, which heats and stretches glass tubes using gravity to create sharp emitter tips essential for producing the high electric field required in field emission.

The glass puller plays a pivotal role in this method by creating sharp emitter tips, which are essential for achieving the high electric field required for field emission. This technique allows for reproducible and well-defined tips that significantly influence the onset and behavior of the field emission. The precise geometry of the emitter tip is critical in reducing the threshold voltage and ensuring consistent emission characteristics. Further details on the emitter preparation and the operation of the glass puller can be found in prior works [45]. The uniformity of the emitter preparation ensures reliable and accurate measurements of the field emission properties, which are essential for understanding the performance of the materials being studied.

Field emission efficiency (FEE) measurements were conducted using a field emission microscope (FEM) within a high-vacuum chamber, which was evacuated to a base pressure of approximately 10^{-7} mbar. To remove any residual contaminants that might affect the measurements, the chamber was baked overnight at 180°C . The distance between the emitter and screen was maintained at approximately 10 mm, providing optimal conditions for accurate field emission measurements. The FEM system was connected to a 100 M Ω current-limiting resistor, which was

essential for protecting the system from excessive current during the emission process. The testing began by gradually increasing the applied voltage, at which point the "switch-on" phenomenon occurred. This was marked by a rapid increase in the emission current, transitioning from the nanoampere (nA) to the microampere (μA) range. At this point, the emission current, denoted as I_{SW} , and the corresponding voltage, V_{SW} , were recorded. The "switch-on" phenomenon is an important feature of field emission as it signifies the point at which emission begins. As the applied voltage decreased, a constant resistance regime was observed, during which the emission current remained stable until the voltage reached a specific value, V_{C} . The corresponding current in this regime, denoted as I_{C} , reflects the emitter's stable behavior under reduced voltage. Further reduction of the applied voltage led to a gradual decrease in emission current, eventually reaching a threshold voltage, V_{TH} , where the emission current fell to zero [46]. The current at this voltage, denoted I_{TH} , represents the point at which the emitter stops contributing to the current flow. This detailed characterization of the emission process, including the "switch-on" behavior, constant resistance regime, and threshold voltage, provides valuable insight into the emission properties and efficiency of the materials under investigation. Understanding these parameters is crucial for evaluating the potential of carbon-based materials in field emission applications [47].

3. Results and Discussion

The most common approach to presenting data from field emission experiments involves current-voltage (I-V) plots and their corresponding Fowler-Nordheim (FN) plots, where $\ln(1/V^2)$ is plotted on the y-axis and $1/V$ on the x-axis. During the experiments, emission current images were captured using a digital camera. All samples were tested under identical conditions of pressure and emitter-screen distance. Table 1 summarizes the switch-on voltage (V_{SW}) and threshold voltage (V_{TH}) values for all samples.

TABLE 1. The values of V_{SW} , I_{SW} ; V_{C} , I_{C} ; and V_{TH} , I_{TH} for all samples.

SWCNTs	$V_{\text{SW}}, I_{\text{SW}} = 700 \text{ V}, 3.05 \mu\text{A}$	$V_{\text{C}}, I_{\text{C}} = 450 \text{ V}, 1.1 \mu\text{A}$	$V_{\text{TH}}, I_{\text{TH}} = 140 \text{ V}, 4.2 \text{ pA}$
MWCNTs	$V_{\text{SW}}, I_{\text{SW}} = 3500 \text{ V}, 16 \mu\text{A}$	$V_{\text{SAT}}, I_{\text{SAT}} = 1600 \text{ V}, 2.9 \mu\text{A}$	$V_{\text{TH}}, I_{\text{TH}} = 600 \text{ V}, 9.6 \text{ pA}$
CNTFs	$V_{\text{SW}}, I_{\text{SW}} = 750 \text{ V}, 3.6 \mu\text{A}$	$V_{\text{C}}, I_{\text{C}} = 350 \text{ V}, 1.09 \mu\text{A}$	$V_{\text{TH}}, I_{\text{TH}} = 140 \text{ V}, 10 \text{ pA}$
CB	$V_{\text{SW}}, I_{\text{SW}} = 4450 \text{ V}, 1.1 \mu\text{A}$	$V_{\text{SAT}}, I_{\text{SAT}} = 4400 \text{ V}, 1.4 \mu\text{A}$	$V_{\text{TH}}, I_{\text{TH}} = 4000 \text{ V}, 6 \text{ pA}$

Field electron emission was initiated at relatively lower applied voltages for SWCNTs and CNTFs III PR-1 compared to CBs and MWCNTs. The latter materials demonstrated higher voltage requirements for comparable emission performance, indicating superior field enhancement characteristics in the SWCNT and CNTF structures. Additionally, SWCNTs exhibited a broader saturation region, extending to lower voltage values than MWCNTs and CBs. A similar trend was observed for the switch-on phenomenon, which occurred at lower voltages for SWCNTs.

The SWCNT emitter demonstrated the earliest "switch-on" phenomenon at the lowest applied voltage among all emitters, highlighting its superior performance in initiating electron emission. In contrast, the CNTFs III PR-1 emitter exhibited a saturation region extending to even lower voltage values than the SWCNT

emitter, indicating distinct differences in their emission characteristics.

For the SWCNTs emitter, as the applied voltage gradually increased, the emission current began at 320 V with 4.2 pA and rose steadily until the "switch-on" event occurred at 700 V, producing 3.05 μ A. The emission current continued to rise with increasing voltage, peaking at 6.2 μ A at 1050 V. Upon reducing the voltage, a constant-resistance regime persisted until 450 V, where a regime change occurred, corresponding to an emission current of 1.1 μ A. Further voltage reduction led to a gradual cessation of emission at 140 V and 4.2 pA. The linear current-voltage behavior can be attributed to significant resistance within the circuit, likely at the CNT interface, which also contributes to deviations in the FN plot's shape. Voltage drops in the circuit likely influence electron energy distribution, altering emission characteristics, as shown in Figs. 2(A) and 2(B).

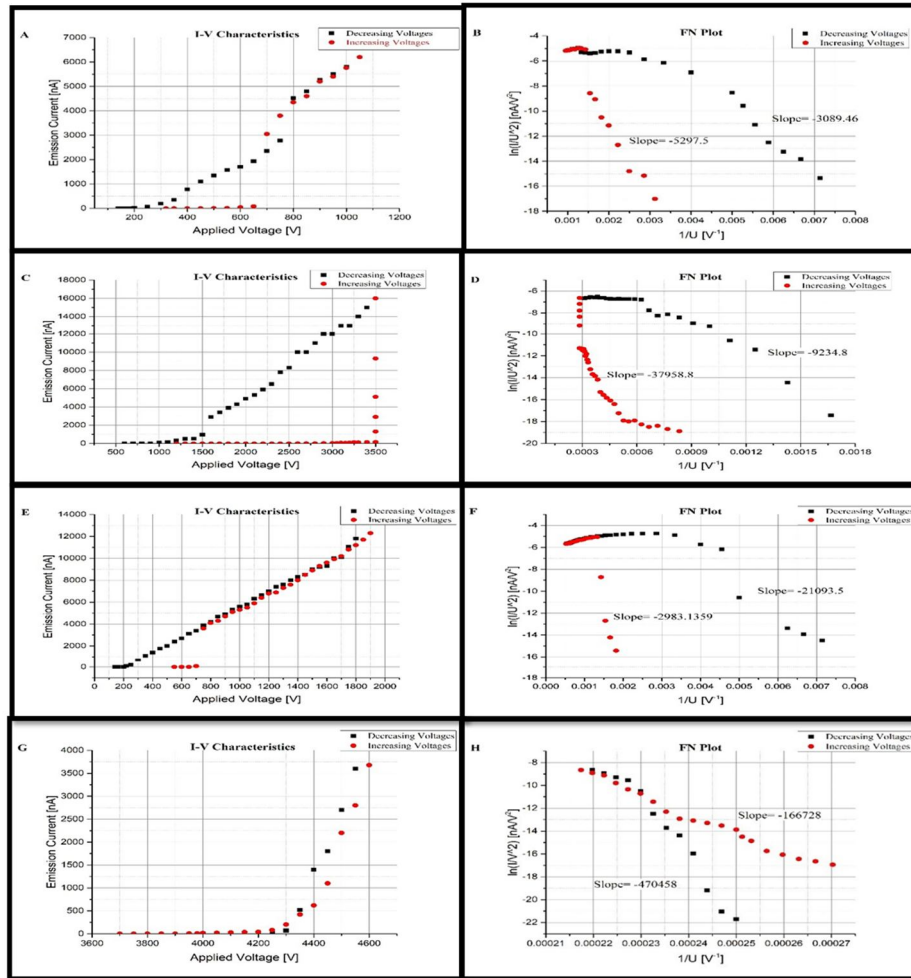


FIG. 2. the I-V characteristics for all the emitters employed in the experiment, with its related F-N plots, where (A) and (B) for the SWCNTs, (C) and (D) for MWCNTs, (E) and (F) for CNTFs III PR-1, and (G) and (H) for the CB. (B), (D), and (F): The non-linear shape of the FN plot for CNTs, where the slope in the high-field region is much lower than that in the low-field regime.

For the MWCNTs emitter, the voltage range spanned from 1200 to 3500 V, with emission currents from 9.1 pA to 1.3 μ A. The "switch-on" phenomenon occurred at 3500 V, yielding an emission current of 16 μ A. Notable jumps in current, potentially due to activation of new emission sites or adsorbate contributions, were observed as shown in Figs. 2(C) and 2(D). The saturation region extended down to 1600 V, with a saturation current of 2.9 μ A. Upon further voltage reduction, the emission current ceased at 600 V with 9.6 pA.

A comparison between the MWCNTs and CNTFs emitters revealed that CNTFs initiated emission at a much lower voltage (750 V vs. 3500 V for MWCNTs), with a consistent-resistance regime indicating stable performance, as shown in Figs. 2(E) and 2(F). However, MWCNTs demonstrated higher emission currents at higher applied voltages, reflecting their capacity for greater emission under optimal conditions.

For the CBs emitter [see Figs. 2(G) and 2(H)], electron emission began at 3700 V with a current of 600 pA, rising to 3.68 μ A at 4600 V. During voltage reduction, the emission current persisted in the microampere range down to

4400 V (1.4 μ A), then declined to zero at 4000 V (6 pA). Unlike the CNT-based emitters, the CB emitter showed minimal evidence of a constant-resistance regime and exhibited a smaller emission pattern, likely due to surface instability caused by weak intermolecular forces.

The FN plot for the CB emitter displayed linearity, whereas the CNT emitters showed deviations, likely due to contact resistance. Field enhancement factors are also influenced by preparation methods. Vertically aligned CNTs exhibit higher field enhancement factors due to their optimal geometry, while randomly oriented CNTs experience screening effects and lower efficiency [48].

The emission current profile for all samples formed relatively focused spatial distributions, as shown in Figs. 3 and 4. Among the samples, CB emitters exhibited the smallest emission pattern, likely due to their spherical morphology.

These findings highlight the importance of emitter structure and preparation in optimizing field emission performance. Further investigations aim to leverage these properties for developing reliable electron sources.

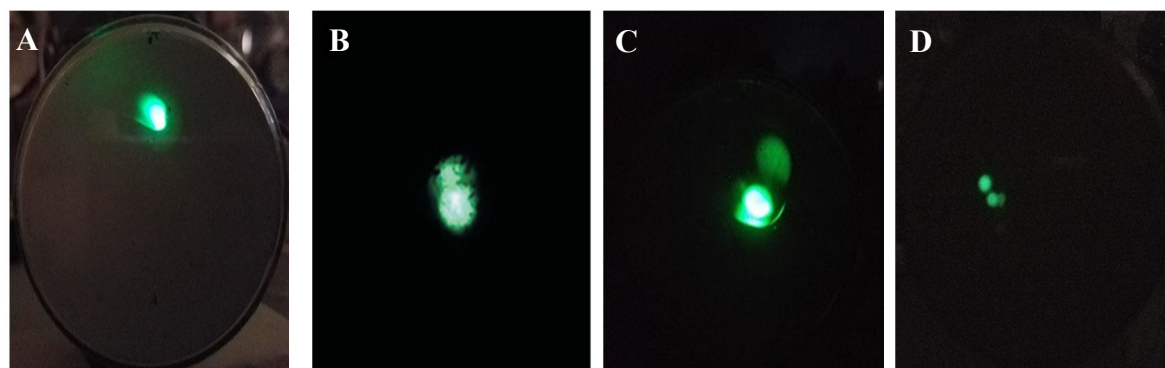


FIG. 3. Emission current images for (A) SWCNTs at 700 V, 2.35 μ A. (B) MWCNTs at 3500 V, 0.15 μ A. (C) CNTFs at 1300 V, 7.3 μ A. (D) CB at 4600 V, 3.68 μ A.

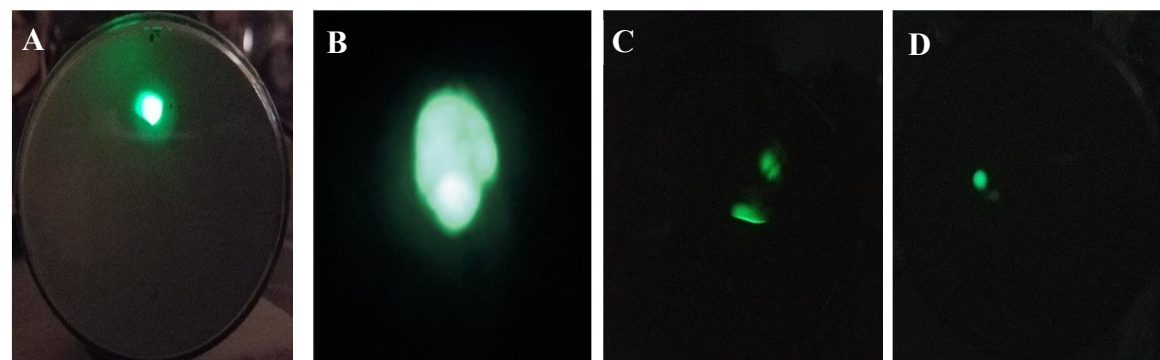


FIG. 4. Emission current for (A) SWCNTs at 900 V, 5.26 μ A. (B) MWCNTs at 3500 V, 2.9 μ A. (C) CNTFs at 950 V, 5.1 μ A. (D) CBs at 4400 V, 1.4 μ A.

4. Conclusions

The emitters were prepared using a drawing technique with a glass puller. The CB emitter exhibits linear behavior in the FN plot and shows no obvious signs of series resistance, whereas such resistance was observed in the (I-V) plots for SWCNTs, MWCNTs, and CNTFs. The CNT emitters deviate from the linearity of the FN plot, possibly due to contact resistance, as indicated by the linear behavior of the (I-V) plot.

The emission current was initiated at a relatively low applied voltage for SWCNTs and CNTFs III PR-1, while CBs and MWCNTs required a higher applied voltage. Additionally, a saturation region was reported for the SWCNTs, extending to a lower voltage value than MWCNTs and CBs. The same situation has been recorded with the switch-on phenomenon, which occurs at lower applied voltage values. The emission current spatial pattern for all samples

was approximately focused. CB emitters exhibited the smallest emitted current pattern, possibly due to the spherical structure of their particles.

This study focused on understanding the field emission behavior of different carbon-based materials—SWCNTs, MWCNTs, CNTFs, and CBs—to explore their potential as advanced electron sources. By comparing their performance under identical experimental conditions, we aimed to reveal how factors such as material properties, structure, and preparation methods influence key emission parameters, including switch-on voltage and saturation behavior. This research is driven by the need to optimize field emission performance and harness the unique properties of these materials to develop efficient and reliable electron sources for a wide range of applications in science and industry.

References

- [1] Fischer, T.E., *Phys. Rev.*, 142 (2) (1966) 519.
- [2] Lu, X., Yang, Q., Xiao, C., and Hirose, A., *J. Phys. D Appl. Phys.*, 39 (15) (2006) 3375.
- [3] Shao, X. and Khurshed, A., *Appl. Sci.*, 8 (6) (2008) 15.
- [4] Giubileo, F., Di Bartolomeo, A., Iemmo, L., Luongo, G., and Urban, F., *Appl. Sci.*, 8 (4) (2018) 526.
- [5] Booske, J.H., He, X., Miller, R.L., Morgan, D., Scharer, J.E., Vlahos, V., Gilgenbach, R.M., Jordan, N.M., Lau, Y.Y., Feng, Y., and Verboncoeur, J., *IEEE 34th International Conference on Plasma Science (ICOPS)*, (2007), 481.
- [6] Gaertner, G., *J. Vac. Sci. Technol. B*, 30 (6) (2012) 060801.
- [7] Yue, G.Z., Qiu, Q., Gao, B., Cheng, Y., Zhang, J., Shimoda, H., Chang, S., Lu, J.P., and Zhou, O., *Appl. Phys. Lett.*, 81 (2) (2002) 355.
- [8] Grandal, B. and North, A., "Artificial Particle Beams in Space Plasma Studies" (Springer US, 2012).
- [9] de Heer, W.A., Châtelain, A., and Ugarte, D., *Science*, 270 (5239) (1995) 1179.
- [10] Hideo, T., Norio, S., and Shigehiko, Y., *Jpn. J. Appl. Phys.*, 21 (10R) (1982) 1513.
- [11] Yunhan, L., Yonghai, S., and Yeow, J.T.W., *Nanotechnology*, 26 (24) (2015) 242001.
- [12] Robertson, S.D., *Nature*, 221 (1969) 1044.
- [13] De Jong, K.P. and Geus, J.W., *Catal. Rev.*, 42 (4) (2000) 481.
- [14] Iijima, S., *Nature*, 354 (6348) (1991) 56.
- [15] Iijima, S. and Ichihashi, T., *Nature*, 363 (6430) (1993) 603.
- [16] Medalia, A.I. and Heckman, F.A., *Carbon*, 7 (5) (1969) 567.
- [17] Harris, P.J.F., "Carbon Nanotube Science: Synthesis, Properties and Applications" (Cambridge University Press, 2009).
- [18] Hone, J., Llaguno, M.C., Nemes, N.M., Johnson, A.T., Fischer, J.E., Walters, D.A., Casavant, M.J., Schmidt, J., and Smalley, R.E., *Appl. Phys. Lett.*, 77 (5) (2000) 666.
- [19] Wei, X., Wang, M.-S., Bando, Y., and Golberg, D., *Sci. Technol. Adv. Mat.*, 12 (4) (2011) 044605.
- [20] de Jonge, N., Allieux, M., Oostveen, J.T., Teo, K.B.K., and Milne, W.I., *Appl. Phys. Lett.*, 87 (13) (2005) 133118.

- [21] Collins, P.G. and Zetl, A., *Phys. Rev. B*, 55 (15) (1997) 9391.
- [22] Bonard, J.-M., Dean, K.A., Coll, B.F., and Klinke, C., *Phys. Rev. Lett.*, 89 (19) (2002) 197602.
- [23] Barbour, J.P., Dolan, W.W., Trolan, J.K., Martin, E.E., and Dyke, W.P., *Phys. Rev.*, 92 (1) (1953) 45.
- [24] Sun, Y., Shin, D.H., Yun, K.N., Hwang, Y.M., Song, Y., Leti, G., Jeon, S.-G., Kim, J.-I., Saito, Y., and Lee, C.J., *AIP Adv.*, 4 (7) (2014) 077110.
- [25] Schwoebel, P.R., Spindt, C.A., Holland, C.E., and Panitz, J.A., *J. Vac. Sci. Technol.*, 19 (3) (2001) 980.
- [26] Edgcombe, C.J. and Valdrè, U., *J. Microsc.*, 203 (2) (2001) 188.
- [27] Jo, S.H., Tu, Y., Huang, Z.P., Carnahan, D.L., Huang, J.Y., Wang, D.Z., and Ren, Z.F., *Appl. Phys. Lett.*, 84 (3) (2004) 413.
- [28] Minoux, E., Groening, O., Teo, K.B.K., Dalal, S.H., Gangloff, L., Schnell, J.-P., Hudanski, L., Bu, I.Y.Y., Vincent, P., Legagneux, P., Amaratunga, G.A.J., and Milne, W.I., *Nano Lett.*, 5 (11) (2005) 2135.
- [29] Mousa, M.S., *J. Phys. Conf. Ser.*, 305 (1) (2018) 012025.
- [30] Kleshch, V.I., Purcell, S.T., and Obraztsov, A.N., *Sci. Rep.*, 6 (2016) 35260.
- [31] Baskin, L.M., Lvov, O I., and Fursey, G.N., *Phys. Status Solidi B*, 47 (1) (1971) 49.
- [32] Peng, J., Li, Z., He, C., Chen, G., Wang, W., Deng, S., Xu, N., Zheng, X., Chen, G., Edgcombe, C.J., and Forbes, R.G., *J. Appl. Phys.*, 104 (1) (2008) 014310.
- [33] Forbes, R.G., Deane, J.H.B., Fischer, A., and Mousa, M.S., *Jordan J. Phys.*, 8 (3) (2015) 125.
- [34] Forbes, R.G., *J. Vac. Sci. Technol. B*, 28 (2) (2010) C2A43.
- [35] Abuamr, A.M., Mousa, M.S., Al-Bashaish, S.R., Madanat, M.A., AlSoud, A., MD, A., and Sobola, D., *Physica Scripta*, 99 (10) (2024) 105029.
- [36] Mousa, M. and Abuamr, A., *Jordan J. Phys.*, 16 (2) (2023) 247.
- [37] Chen, L.F., Song, H., Cao, L.Z., Jiang, H., Li, D.B., Guo, W.G., Liu, X., Zhao, H.F., and Li, Z.M., *J. Appl. Phys.*, 106 (3) (2009) 033703.
- [38] Liang, S.-D., "Quantum Tunneling and Field Electron Emission Theories" (World Scientific Publishign Co. Pte Ltd Singapore, 2014).
- [39] Peng, J., Li, Z., He, C., Chen, G., Wang, W., Deng, S., Xu, N., Zheng, X., Chen, G., Edgcombe, C.J., and Forbes, R.G., *J. Appl. Phys.*, 104 (1) (2008) 014310.
- [40] Chen, Y., Shaw, D.T., and Guo, L., *Appl. Phys. Lett.*, 76 (17) (2000) 2469.
- [41] Wang, Y.H., Lin, J., and Huan, C.H.A., *Thin Solid Films*, 405 (1) (2002) 243.
- [42] Wang, X.Q., Wang, M., Li, Z.H., Xu, Y.B., and He, P.M., *Ultramicroscopy*, 102 (3) (2005) 181.
- [43] Hom, S., Bhattacharyya, A.R., Khare, R.A., Kulkarni, A.R., Saroop, M., and Biswas, A., *J. Appl. Polym. Sci.*, 112 (2) (2009) 998.
- [44] Mdarhri, A., Brosseau, C., and Carmona, F., *J. Appl. Phys.*, 101 (8) (2007) 084111.
- [45] Daradkeh, S.I. and Mousa, M.S., *Appl. Microsc.*, 47 (3) (2017) 86.
- [46] Al-Qudah, A.A., Mousa, M., and Fischer, A., *IOP Conf. Ser., Mater. Sci. Eng.*, 92 (1) (2015) 012021.
- [47] Yeong, K.S. and Thong, J.T.L., *Appl. Surf.*, 233 (1-4) (2004) 20.
- [48] Li, N., Yan, F., Pang, S., Chen, L., Jin, D., Xiang, W., Zhang, D., Dai, J., and Zeng, B., *J. Korean Phys. Soc.*, 66 (2015) 1186.4.

Negative Ion Formation in H + H Collisions at Low- to High-Energies

Saed J. Al Atawneh

Department of Physics, Zarqa University, Zarqa 13110, Jordan.

Doi: <https://doi.org/10.47011/18.1.5>

Received on: 03/07/2023;

Accepted on: 09/10/2023

Abstract: For various branches of science, it is essential to determine all possible reactions and collisional cross-sections. Despite extensive large-scale studies conducted over the past decades to provide such data, many fundamental atomic and molecular cross-section values remain unknown, and the accuracy of the available data still requires verification.

In this paper, we present cross-section calculations for negative ion formation (ion-pair formation) in hydrogen-hydrogen atom collisions based on the classical trajectory and quasi-classical trajectory Monte Carlo models. By comparing our results with available experimental data and theoretical predictions, we find that the QCTMC calculations align well with previous studies. However, the negative ion formation cross-sections obtained using the CTMC model underestimate all previously reported theoretical and experimental values. Nonetheless, the CTMC results show good agreement with the Q -, P -series approximation in the energy range of 1–10 keV. We present negative ion formation cross-sections for impact energies ranging from 1 keV to 100 keV, which are relevant to applications in astronomy, atmospheric sciences, plasma laboratories, and fusion research.

Keywords: Atom-atom collision, Negative ion formation, Classical Trajectory Monte Carlo method, Quasi-classical Trajectory Monte Carlo method.

1. Introduction

Recently, the search for new energy sources has become increasingly urgent [1]. In contrast to nuclear fission energy, which creates massive amounts of nuclear waste that are damaging to the environment and humans [2], the current tendency is to employ clean fusion energy, which does not release or leave any dangerous radioactive material [1]. Therefore, the development of nuclear fusion reactors such as tokamak has attracted attention as a clean energy source [3, 4].

In fusion reactors, the limiter and divertor regions contain plenty of neutrals, such as hydrogen atoms [5-8]. These regions, characterized by lower temperatures and high particle densities, serve as sites for numerous atomic, ionic, and molecular collisions [5-8].

Plasma-neutral interactions involving hydrogen play a crucial role in plasma diagnostics, as the cross-sections of elastic and inelastic collisions provide essential data for diagnostic tools such as Beam Emission Spectroscopy (BES) [5-10]. Consequently, many studies have focused on plasma-neutral interactions in divertor and limiter regions [5-18].

In this study, we investigate the cross-sections of negative ions formation (ion-pair formation) resulting from collisions between ions and atoms or between two atoms. Specifically, we examine the production of negative ions in collisions between two ground-state hydrogen atoms over an energy range of 1 keV to 100 keV. These cross sections are not only fundamental to fusion research but also play

a significant role in energy balance studies in astrophysics [19] and atmospheric sciences [20].

Negative ions also play an essential role in various industries, including their application in etching processes (NBIs) [21]. Even in biological sciences, negative ions play an essential role as antioxidants against free radicals that are hazardous to the human body. However, no significant efforts have been made to coordinate experiments and theory, basic science, and applications to understand the structure and formation dynamics of negative ions.

In this study, we are specifically interested in ion-pair cross-sections in atom-atom collisions, as described by:



The four-body classical (CTMC) and quasi-classical (QCTMC) Monte Carlo simulations were performed [5-15] to calculate the negative ion formation cross-sections. The QCTMC is just a modified version of the standard model that adds a quantum feature to the model potential, such as the Heisenberg correction term to the pure Coulomb inter-particle potential. This modification accounts for nonclassical effects, enhancing the stability of classical hydrogen atoms [22, 23]. In traditional CTMC simulations, the absence of lower energy bounds imposed by quantum mechanics often leads to autoionization or collapse of classical hydrogen atoms, potentially affecting the accuracy of cross-section calculations.

In this work, we present cross-section data for negative ion formation obtained using both the standard and modified CTMC methods. To the best of our knowledge, such data have not been previously reported. Our calculations span an energy range of 1 to 100 keV, which is particularly relevant to applications in astronomy, atmospheric sciences, plasma laboratories, and fusion research. Unless otherwise stated, all results are presented in atomic units.

2. Theory

2.1. The CTMC Models

As is well-known, classical descriptions of collision processes work extremely well [5-10, 16-18]. In this model, the H atom is represented by two particles: the ionic core of H and one active electron. All particles can be described by their masses and charges [9, 23]. Let P represent the ionic core of the projectile, P_e the electron of the projectile, T the ionic core of the target, and T_e the electron of the target [9]. Interactions between electrons are explicitly included in our four-body calculations. At time $t = -\infty$, we assume that the four-body collision system is made up of two isolated atoms: a projectile atom (P, P_e), marked as particles (1, 4), and a target atom (T, T_e), marked as particles (2, 3), as shown in Fig. 1 [8]. At the beginning, both particles are in the ground state ($n=1, 0$) [8]. We used the Coulomb potential to describe all interactions [8, 9]. Figure 1 depicts the relative position vectors for the four-body collision systems.

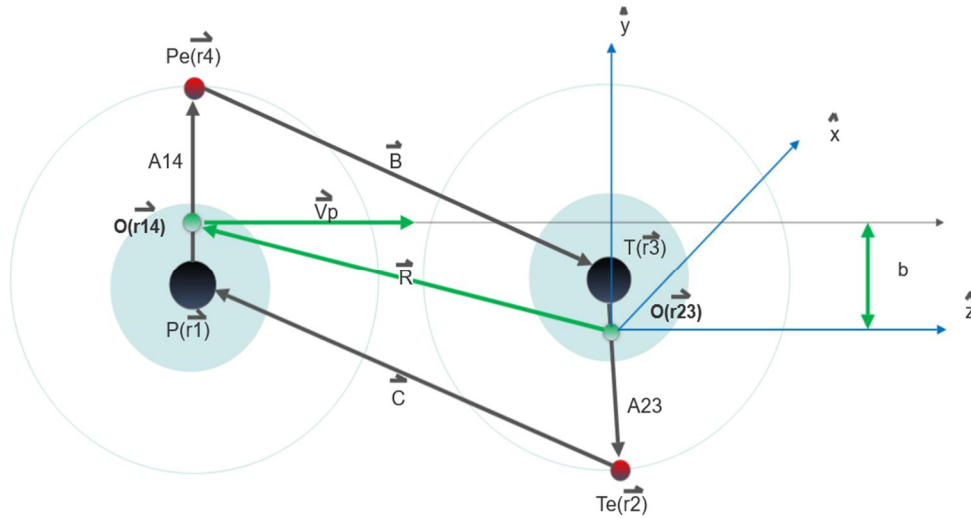


FIG. 1. The schematic diagram represents the relative position vectors for particles involved in our 4-body collision systems. $\vec{A}_{14} = \vec{r}_4 - \vec{r}_1$, $\vec{B} = \vec{r}_4 - \vec{r}_3$, $\vec{A}_{23} = \vec{r}_3 - \vec{r}_2$, and $\vec{C} = \vec{r}_2 - \vec{r}_1$, in such way that $\vec{A}_{14} + \vec{A}_{23} + \vec{B} + \vec{C} = 0$. Where $O(\vec{r}_{14})$ and $O(\vec{r}_{23})$ represent centre-of-mass vectors for target and projectile systems respectively, with b as their impact parameter.

The initial electronic states can be determined by means of a microcanonical distribution. A microcanonical set represents the initial state of the target and projectile, compelled by their binding energy in any given shell, and can be described as follows:

$$\rho_{E_0}(\vec{A}, \dot{\vec{A}}) = K_1 \delta(E_0 - E) = \delta \left(E_0 - \frac{1}{2} \mu_{T,Te,P,Pe} \dot{\vec{A}}^2 - V(A) \right). \quad (2)$$

Here, K_1 is a normalization constant, E_0 is the ionization energy of the active electron, $V(A)$ represents the electron and ionic-core potential, A is the length of the vector \vec{A} , and $\mu_{T,Te,P,Pe}$ is the reduced mass of particles ("T", "Te", "P", and "Pe") [5-10]. According to Eq. (2), the electronic coordinates are restricted within intervals where Eq. (3) holds:

$$\frac{1}{2} \mu_{Te} \dot{\vec{A}}^2 = E_0 - V(A) > 0. \quad (3)$$

Hamilton equation is given by:

$$H_0 = T + V_{coul}, \quad (4)$$

where

$$T = \frac{\vec{P}_P^2}{2m_P} + \frac{\vec{P}_{Pe}^2}{2m_{Pe}} + \frac{\vec{P}_T^2}{2m_T} + \frac{\vec{P}_{Te}^2}{2m_{Te}}, \quad (5)$$

and

$$V_{coul} = \frac{Z_P Z_{Pe}}{|\vec{r}_P - \vec{r}_{Pe}|} + \frac{Z_P Z_T}{|\vec{r}_P - \vec{r}_T|} + \frac{Z_P Z_{Te}}{|\vec{r}_P - \vec{r}_{Te}|} + \frac{Z_{Pe} Z_T}{|\vec{r}_{Pe} - \vec{r}_T|} + \frac{Z_{Pe} Z_{Te}}{|\vec{r}_{Pe} - \vec{r}_{Te}|} + \frac{Z_T Z_{Te}}{|\vec{r}_T - \vec{r}_{Te}|}. \quad (6)$$

Here, T and V_{coul} stand for total kinetic energy and Coulomb potential term, respectively [5-10]. \vec{P} , Z , \vec{r} , and m stand for momentum vector, charge, position vector, and mass of each particle, respectively [5-10]. Here are the equations of motion according to Hamiltonian mechanics:

$$\dot{\vec{P}}_P = -\frac{\delta H_0}{\delta \vec{r}_P} = \frac{Z_P Z_{Pe}}{|\vec{r}_P - \vec{r}_{Pe}|^3} (\vec{r}_P - \vec{r}_{Pe}) + \frac{Z_P Z_T}{|\vec{r}_P - \vec{r}_T|^3} (\vec{r}_P - \vec{r}_T) + \frac{Z_P Z_{Te}}{|\vec{r}_P - \vec{r}_{Te}|^3} (\vec{r}_P - \vec{r}_{Te}), \quad (7)$$

$$\dot{\vec{P}}_{Pe} = -\frac{\delta H_0}{\delta \vec{r}_{Pe}} = -\frac{Z_P Z_{Pe}}{|\vec{r}_P - \vec{r}_{Pe}|^3} (\vec{r}_P - \vec{r}_{Pe}) - \frac{Z_T Z_{Pe}}{|\vec{r}_T - \vec{r}_{Pe}|^3} (\vec{r}_T - \vec{r}_{Pe}) - \frac{Z_{Te} Z_{Pe}}{|\vec{r}_{Te} - \vec{r}_{Pe}|^3} (\vec{r}_{Te} - \vec{r}_{Pe}), \quad (8)$$

$$\dot{\vec{P}}_T = -\frac{\delta H_0}{\delta \vec{r}_T} = -\frac{Z_P Z_T}{|\vec{r}_P - \vec{r}_T|^3} (\vec{r}_P - \vec{r}_T) - \frac{Z_{Te} Z_T}{|\vec{r}_{Te} - \vec{r}_T|^3} (\vec{r}_{Te} - \vec{r}_T) + \frac{Z_T Z_{Pe}}{|\vec{r}_T - \vec{r}_{Pe}|^3} (\vec{r}_T - \vec{r}_{Pe}), \quad (9)$$

$$\dot{\vec{P}}_{Te} = -\frac{\delta H_0}{\delta \vec{r}_{Te}} = -\frac{Z_P Z_{Te}}{|\vec{r}_P - \vec{r}_{Te}|^3} (\vec{r}_P - \vec{r}_{Te}) - \frac{Z_{Te} Z_T}{|\vec{r}_{Te} - \vec{r}_T|^3} (\vec{r}_{Te} - \vec{r}_T) - \frac{Z_{Te} Z_{Pe}}{|\vec{r}_{Te} - \vec{r}_{Pe}|^3} (\vec{r}_{Te} - \vec{r}_{Pe}). \quad (10)$$

The Runge-Kutta method is typically utilized to numerically integrate equations of motion using an ensemble of approximately 5×10^6 primary trajectories per energy [5-10]. Such an ensemble typically is required in order to ensure statistical uncertainties of less than 5% [5-10]. The negative ion formation cross-section is given by:

$$\sigma = \frac{2\pi b_{max}}{N} \sum_j b_j, \quad (11)$$

where b_j is the impact parameter corresponding to the trajectory associated with a negative ion formation process, N is the total number of calculated trajectories, and b_{max} is the maximum value for the impact parameter where the described processes can occur. The statistical uncertainty of the cross-section can be calculated by:

$$\Delta\sigma = \sigma \left[\frac{N - N_P}{N N_P} \right]^{1/2}. \quad (12)$$

Here, N_P is the number of trajectories that satisfy the criteria for the negative ion formation process.

2.2. The QCTMC Model

The QCTMC model improves on the CTMC model by including a quantum correction term [6, 9, 10, 22, 23]. To simulate the Heisenberg uncertainty and Pauli principle, a modified Hamiltonian effective potential (V_H for Heisenberg and V_P for Pauli) is added to the pure Coulomb inter-particle potentials to represent a non-classical effect [22, 23]. As a result, inter-particle interactions are enhanced. Thus:

$$H_{QCTMC} = H_0 + V_H + V_P, \quad (13)$$

where H_0 is the standard Hamiltonian [see Eq. (4)], and the correction terms for H_0 include:

$$V_H = \sum_{i=1}^N \frac{1}{mr_i^2} f(\vec{r}_i, \vec{p}_i; \xi_H; \alpha_H), \quad (14)$$

and

$$V_P = \sum_{i=1}^N \sum_{j=i+1}^N \frac{2}{mr_{ij}^2} f(\vec{r}_{ij}, \vec{p}_{ij}; \xi_P; \alpha_P) \delta_{s_i s_j}. \quad (15)$$

Here, i and j refer to the electron indices. Additionally, $r_{ij} = r_j - r_i$, and the relative momentum is determined as follows:

$$\vec{p}_{ij} = \frac{m_i \vec{p}_j - m_j \vec{p}_i}{m_i + m_j}, \quad (16)$$

where $\delta_{s_i, s_j} = 1$ if the i th and j th electrons have the same spin, and 0 if they are different [9, 10]. Finally, the constraining potential is chosen as:

$$f(\vec{r}_{\lambda\nu}, \vec{p}_{\lambda\nu}; \xi, \alpha) = \frac{\xi^2}{4\alpha r_{\lambda\nu}^2 \mu_{\lambda\nu}} \exp\left\{\alpha \left[1 - \left(\frac{\vec{r}_{\lambda\nu} \vec{p}_{\lambda\nu}}{\xi}\right)^4\right]\right\}. \quad (17)$$

Since a hydrogen atom consists of one electron and one proton, Heisenberg constraints with a specific scale parameter, a hardness parameter ($\alpha_H = 3.0$), and a dimensionless constant ($\xi_H = 0.9258$) are applied to the four-body QCTMC model. As illustrated in the following equation:

$$f(\vec{r}_{T,Te}, \vec{p}_{T,Te}; \varepsilon_H, \alpha_H) = \frac{\xi_H^2}{4\alpha_H \vec{r}_{T,Te}^2 \mu_{T,Te}} \exp\left\{\alpha_H \left[1 - \left(\frac{\vec{r}_{T,Te} \vec{p}_{T,Te}}{\xi_H}\right)^4\right]\right\}. \quad (18)$$

Similar to the target atom, the correction term should also be added to the projectile atom as follows:

$$f(\vec{r}_{P,Pe}, \vec{p}_{P,Pe}; \varepsilon_H, \alpha_H) = \frac{\xi_H^2}{4\alpha_H \vec{r}_{P,Pe}^2 \mu_{P,Pe}} \exp\left\{\alpha_H \left[1 - \left(\frac{\vec{r}_{P,Pe} \vec{p}_{P,Pe}}{\xi_H}\right)^4\right]\right\}. \quad (19)$$

As shown in Fig. 1, the equations of motion, which incorporate Hamiltonian mechanics as well as correction terms for cross-section calculations, can be expressed as:

$$\begin{aligned} \dot{\vec{p}}_P = -\frac{\delta H_{QCTMC}}{\delta \vec{r}_P} = & \left[\frac{Z_P Z_{Pe}}{|\vec{r}_P - \vec{r}_{Pe}|^3} (\vec{r}_P - \vec{r}_{Pe}) - \left(-\frac{\xi_H^2}{2\alpha_H \vec{r}_{P,Pe}^4 \mu_{P,Pe}} - \frac{(\vec{p}_{P,Pe})^4}{\mu_{P,Pe} \xi_H^2} \right) \exp\left\{\alpha_H \left[1 - \left(\frac{\vec{r}_{P,Pe} \vec{p}_{P,Pe}}{\xi_H}\right)^4\right]\right\} \right] \\ & + \frac{Z_P Z_T}{|\vec{r}_P - \vec{r}_T|^3} (\vec{r}_P - \vec{r}_T) + \frac{Z_P Z_{Te}}{|\vec{r}_P - \vec{r}_{Te}|^3} (\vec{r}_P - \vec{r}_{Te}), \end{aligned} \quad (20)$$

$$\begin{aligned} \dot{\vec{p}}_{Pe} = -\frac{\delta H_{QCTMC}}{\delta \vec{r}_{Pe}} = & -\left[\frac{Z_P Z_{Pe}}{|\vec{r}_P - \vec{r}_{Pe}|^3} (\vec{r}_P - \vec{r}_{Pe}) + \left(-\frac{\xi_H^2}{2\alpha_H \vec{r}_{P,Pe}^4 \mu_{P,Pe}} - \frac{(\vec{p}_{P,Pe})^4}{\mu_{P,Pe} \xi_H^2} \right) \exp\left\{\alpha_H \left[1 - \left(\frac{\vec{r}_{P,Pe} \vec{p}_{P,Pe}}{\xi_H}\right)^4\right]\right\} \right] \\ & - \frac{Z_T Z_{Pe}}{|\vec{r}_T - \vec{r}_{Pe}|^3} (\vec{r}_T - \vec{r}_{Pe}) - \left[\frac{Z_{Te} Z_{Pe}}{|\vec{r}_{Te} - \vec{r}_{Pe}|^3} (\vec{r}_{Te} - \vec{r}_{Pe}) - \left(-\frac{\xi_P^2}{2\alpha_P \vec{r}_{Te,Pe}^4 \mu_{Te,Pe}} - \frac{(\vec{p}_{Te,Pe})^4}{\mu_{Te,Pe} \xi_H^2} \right) \exp\left\{\alpha_P \left[1 - \left(\frac{\vec{r}_{Te,Pe} \vec{p}_{Te,Pe}}{\xi_P}\right)^4\right]\right\} \right], \end{aligned} \quad (21)$$

$$\begin{aligned} \dot{\vec{p}}_T = -\frac{\delta H_{QCTMC}}{\delta \vec{r}_T} = & -\frac{Z_P Z_T}{|\vec{r}_P - \vec{r}_T|^3} (\vec{r}_P - \vec{r}_T) - \left[\frac{Z_{Te} Z_T}{|\vec{r}_{Te} - \vec{r}_T|^3} (\vec{r}_{Te} - \vec{r}_T) + \left(-\frac{\xi_H^2}{2\alpha_H \vec{r}_{T,Te}^4 \mu_{T,Te}} - \frac{(\vec{p}_{T,Te})^4}{\mu_{T,Te} \xi_H^2} \right) \exp\left\{\alpha_H \left[1 - \left(\frac{\vec{r}_{T,Te} \vec{p}_{T,Te}}{\xi_H}\right)^4\right]\right\} \right] \\ & + \frac{Z_T Z_{Pe}}{|\vec{r}_T - \vec{r}_{Pe}|^3} (\vec{r}_T - \vec{r}_{Pe}), \end{aligned} \quad (22)$$

$$\begin{aligned} \dot{\vec{p}}_{Te} = -\frac{\delta H_{QCTMC}}{\delta \vec{r}_{Te}} = & -\frac{Z_P Z_{Te}}{|\vec{r}_P - \vec{r}_{Te}|^3} (\vec{r}_P - \vec{r}_{Te}) - \left[\frac{Z_{Te} Z_T}{|\vec{r}_{Te} - \vec{r}_T|^3} (\vec{r}_{Te} - \vec{r}_T) + \left(-\frac{\xi_H^2}{2\alpha_H \vec{r}_{T,Te}^4 \mu_{T,Te}} - \frac{(\vec{p}_{T,Te})^4}{\mu_{T,Te} \xi_H^2} \right) \exp\left\{\alpha_H \left[1 - \left(\frac{\vec{r}_{T,Te} \vec{p}_{T,Te}}{\xi_H}\right)^4\right]\right\} \right] \\ & - \left[\frac{Z_{Te} Z_{Pe}}{|\vec{r}_{Te} - \vec{r}_{Pe}|^3} (\vec{r}_{Te} - \vec{r}_{Pe}) - \left(-\frac{\xi_P^2}{2\alpha_P \vec{r}_{Te,Pe}^4 \mu_{Te,Pe}} - \frac{(\vec{p}_{Te,Pe})^4}{\mu_{Te,Pe} \xi_H^2} \right) \exp\left\{\alpha_P \left[1 - \left(\frac{\vec{r}_{Te,Pe} \vec{p}_{Te,Pe}}{\xi_P}\right)^4\right]\right\} \right]. \end{aligned} \quad (23)$$

3. Results and Discussion

Despite the importance of negative ion production in several scientific fields, no substantial efforts have been made to coordinate experiments and theories, fundamental science, and applications to better understand the structure and formation dynamics of negative ions. In the present paper, the production of negative ions can be described qualitatively using a simple kinematics picture as follows: A second electron approaches a hydrogen atom, which consists of a proton and an electron. The electric field of the second electron (which decreases with distance as r^{-2}) creates a dipole moment in the neutral hydrogen atom, and then. As a result, the two electrons position themselves on opposite sides of the proton, forming a stable negative ion, as illustrated in Fig. 2.

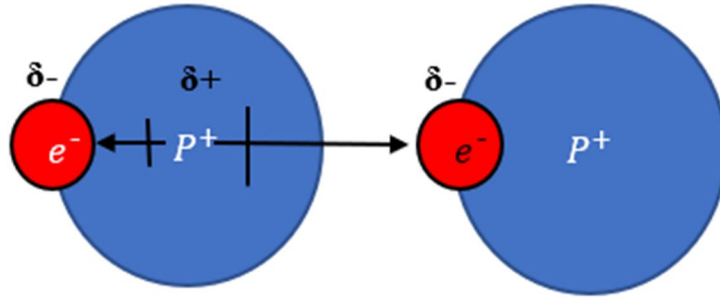


FIG. 2. The dipole moment induced by the second electron in H+H collisions.

The induced dipole moment is proportional to the polarizing electron's electric field and, consequently, to r^{-2} . The second electron is now surrounded by the electric field of the dipole it has created in the neutral H atom, allowing it to be captured. In general, the initial stage of the negative ion formation process is governed by a weak polarization interaction between two neutral species, exhibiting a relatively weak dependence on the interatomic distance (R). In contrast, the final ion-pair formation stage is strongly dominated by Coulomb interactions, which scale as $1/R$.

Classically, the negative ion formation channel can be categorized into two channels. The first is the target capture channel, as described by Eq. (24):



The second is the projectile capture channel, as represented by Eq. (25):



As discussed in previous reviews [5, 9], the collision system ($H+H$) is symmetrical. Consequently, the negative ion formation cross-section in this study is identical for both the target and projectile atoms.

Figure 3 illustrates the probability of negative ion formation, as determined by CTMC and QCTMC computational approaches, as a function of the impact parameter for projectile impact energies of 20, 60, and 100 keV. The probability distributions were fitted using Gaussian functions, with the peak maxima also shown in Fig. 3. Significant variations in the

peak maxima were observed, with lower impact energies corresponding to higher maximum values of the impact parameter.

This behavior can be understood using a simple kinematic picture: at low impact energies, the projectile remains in close proximity to the target for an extended period during the collision, increasing the likelihood of negative ion formation due to prolonged interactions among ionic cores and electrons (slow-collision scenario). This suggests that as the impact parameter increases, the probability of negative ion formation also rises [7, 8].

Conversely, at higher impact energies, the probability of negative ion formation is inversely proportional to the impact parameter. This indicates that negative ion formation predominantly occurs in short-range (close) collisions. The impact parameter analysis in Fig. 3 confirms this, showing that projectiles with higher impact energies exhibit a much narrower impact parameter range compared to those with lower impact energies.

Once again, this underscores that the underlying mechanism of negative ion formation is governed by weak polarization interactions between two neutral atoms. Similar to the CTMC results, the probability of negative ion formation as a function of the impact parameter in the QCTMC model follows the same trend (see Fig. 3). However, the QCTMC calculations predict systematically higher probabilities than the standard CTMC model, emphasizing the significance of the Heisenberg correction term.

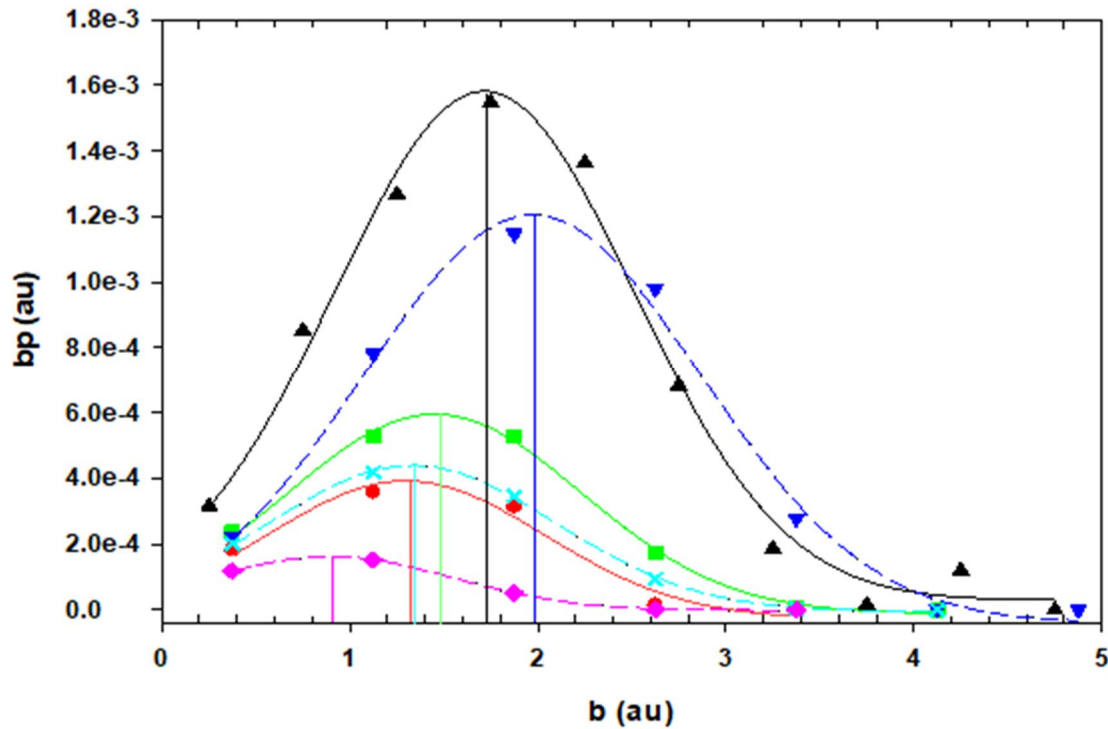


FIG. 3. Negative ion formation probability in H+H collisions using the CTMC and QCTMC methods as a function of impact parameters. Blue triangles down: the CTMC results for 20 keV. Cyan crosses: the CTMC results for 60 keV. Pink diamonds: the CTMC results for 100 keV. Black triangles up: the QCTMC results for 20 keV. Green squares: the QCTMC results for 60 keV. Red circles: the QCTMC results for 100 keV.

Figure 4 displays the cross-sections of present negative ion formation in H+H collisions as a function of impact energy, along with the experimental data from Gealy and Van Zyl [24] and McClure [25]. Figure 4 also displays the earlier theoretical cross-section results from Ovchinnikov [26], who showed a mechanism for the formation of negative ions in the slow-collision regime using a Q -, P -series method. Q -, P -series establishes a connection between the ground singlet $H + H$ state and the ground $H^+ + H^-$ state. As noted, the findings of Gealy and Van Zyl [24] at low energies below 1 keV are somewhat inconsistent with previous and contemporary studies. The present QCTMC results for negative ion formation cross sections in the energy range of 1 keV to 20 keV are in excellent agreement with the experimental and theoretical data of McClure [25] and Ovchinnikov [26]. In contrast, the current

CTMC approaches underestimate all prior theoretical and experimental results. Additionally, in the high-energy range above 80 keV, when the projectile's energy (velocity) exceeds that of an orbital electron velocity ($v_p \gg v_e$), the Heisenberg correction component is minimal (see Fig. 4). This means that the CTMC and QCTMC calculations yield roughly similar results, which can be explained by two factors: 1) The Heisenberg potential has less influence as the projectile momentum increases, and 2) The Heisenberg potential is inversely proportional to the square of the relative distance between colliders ($V_H \propto 1/r_{ij}^2$), see Eq. (17). As

a result, the $V_H(r, p, \alpha)$ potential contributes in the low-to-medium energy region but is negligible in the high-energy region.

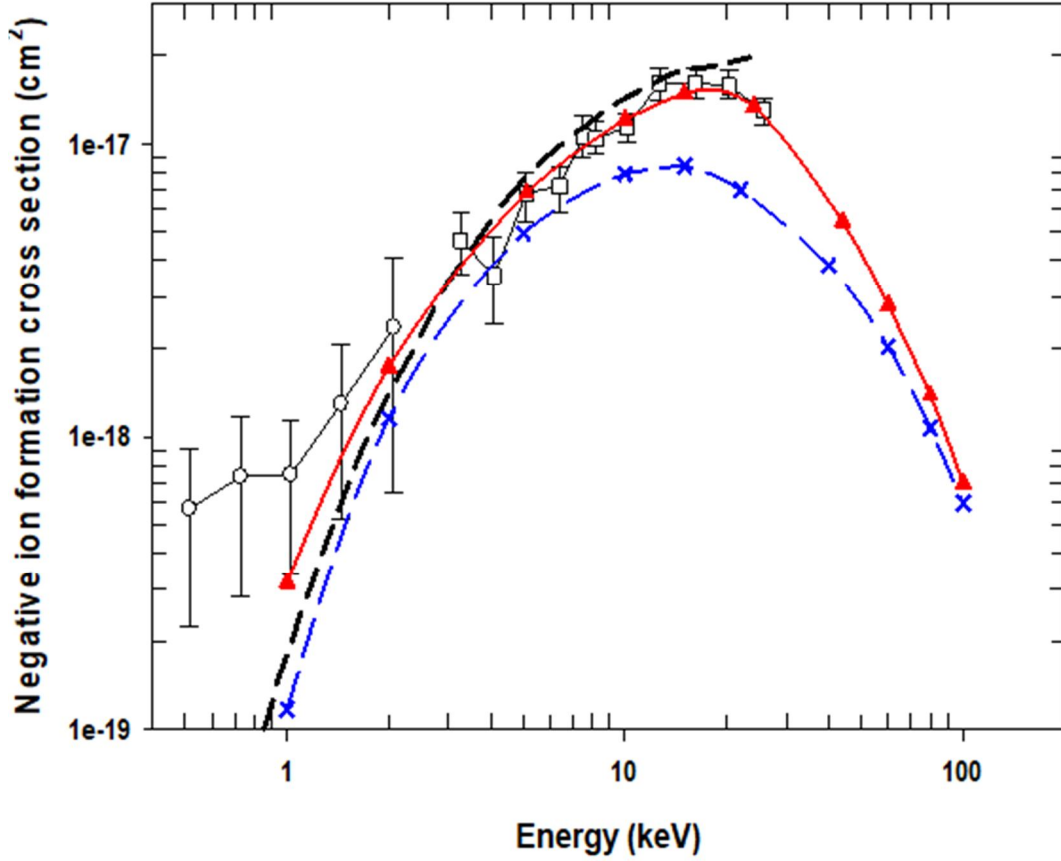


FIG. 4. Negative ion formation cross-section in H+H collision as a function of impact energy. Red triangles-solid line: presents QCTMC results. Blue crosses-dashed line: presents CTMC results. Open circles-solid line: measured data by Gealy and Van Zyl [24]. Open squares-solid line: measured data by McClure [25]. Black dashed line: Q-, P-series results by Ovchinnikov *et al.* [26].

4. Conclusion

We have presented negative ion formation cross-sections for H+H collisions using both four-body CTMC and four-body QCTMC calculation methods. Our calculations were performed for impact energies ranging from 1 to 100 keV, where the cross sections are expected to be significant to astronomy, atmospheric sciences, plasma laboratories, and fusion research. We found a consistent pattern in the maximum impact parameter for negative ion formation probability as a function of impact energy in both the CTMC and QCTMC approaches. Specifically, the maximum impact parameter was found to be larger at lower

energies. Furthermore, the QCTMC results showed good agreement with previously reported experimental and theoretical data. In contrast, our CTMC calculations slightly underestimated previous results. However, at impact energies between 1 and 10 keV, the CTMC data aligned well with *Q*- and *P*-series approximation data. In conclusion, we found that the QCTMC approach accurately calculates the cross-sections of negative ion formation.

Acknowledgment

This work has no funding.

References

- [1] Dunlap, R.A., “Energy from Nuclear Fusion” (IOP Publishing, 2021).
- [2] Tikhomirov, G.V. and Gerasimov, A.S., J. Phys. Conf. Ser., 1689 (1) (2020) 012032.
- [3] Ikeda, K., Nucl. Fusion, 47 (6) (2007) E01.
- [4] Janev, R.K., Langer, W.D., Evans, K., and Post, D.E., “Atomic and Molecular Processes in Hydrogen–Helium Plasma” (Springer-Verlag, Berlin, 1985).
- [5] Atawneh, S.J.A., Asztalos, Ö., Szondy, B., Pokol, G.I., and Tőkési, K., Atoms, 8 (2020) 31.
- [6] Atawneh, S.J.A. and Tőkési, K., Atomic Data Nucl. Data, 146 (2022) 101513.
- [7] Atawneh, S.J.A. and Tőkési, K., J. Phys. B: At. Mol. Opt. Phys., 54 (2021) 065202.
- [8] Atawneh, S.J.A., PhD dissertation, Debrecen U, ProQuest, <http://hdl.handle.net/2437/329082>.
- [9] Atawneh, S.J.A. and Tőkési, K., Phys. Chem. Chem. Phys., 24 (2022) 15280.
- [10] Atawneh, S.J.A. and Tőkési, K., Nucl. Fusion., 62 (2021) 026009.
- [11] Shipsey, E.J., Browne, J.C., and Olson, R.E., J. Phys. B: At. Mol. Opt. Phys., 14 (1981) 869.
- [12] McCullough, R.W., Phys. Scr., T92 (2001) 76.
- [13] Olson, R.E., Reinhold, C.O., and Schultz, D.R., Proc. 4th Workshop on High-Energy Ion-Atom Collision Processes, Debrecen, Hungary (1990).
- [14] Abrines, R. and Percival, I.C., Proc. Phys. Soc., 88 (1966) 861.
- [15] Janev, R.K. and McDowell, M.R.C., Phys. Lett. A, 102 (1984) 405.
- [16] Velayati, A. and Ghanbari-Adivi, E., Eur. Phys. J. D, 72 (2018) 100.
- [17] Velayati, A., Ghanbari-Adivi, E., and Ghorbani, O., J. Phys. B: At. Mol. Opt. Phys., 51 (2018) 185201.
- [18] Ghavaminia, H. and Ghanbari-Adivi, E., Chinese Phys. B, 24 (2015) 073401.
- [19] Hartquist, T.W., “Molecular Astrophysics” (Cambridge University Press, 1994).
- [20] Wayne, R.P., “Atmospheric Chemistry” (Oxford University Press, 1991).
- [21] Makabe, T. and Petrovic, Z.L., Appl. Surf. Sci., 192 (2002) 88.
- [22] Wilets, L. and Cohen, J.S., Cont. Phys., 39 (1998) 163.
- [23] Kirschbaum, C.L. and Wilets, L., Phys. Rev. A, 21 (1980) 834.
- [24] Gealy, M.W. and Zyl, B.V., Phys. Rev. A, 36 (1987) 3100.
- [25] McClure, G.W., Phys. Rev., 166 (1968) 22.
- [26] Yu Ovchinnikov, S., Kamyshev, Y., Zaman, T., and Schultz, D.R., J. Phys. B: At. Mol. Opt. Phys., 50 (2017) 085204.

Soliton Type Solutions for Electromagnetic Wiggler Free Electron Laser

Mustafa Abu Safa

*Department of Applied Physics, Palestine Polytechnic University, Hebron, P. O. Box198,
Palestine.*

Doi: <https://doi.org/10.47011/18.1.6>

Received on: 11/08/2023;

Accepted on: 20/11/2023

Abstract: The nonlinear electromagnetic wave propagation in a system consisting of a relativistic cold-electron beam propagating through an electromagnetic wiggler is solved. A set of coupled nonlinear ordinary differential equations is derived by coordinate transformation to the wiggler coordinates. Soliton-type solutions in the form of coupled electromagnetic and plasma waves are presented numerically, which may represent possible nonlinear saturated states of the electromagnetic wiggler free-electron laser instability. It is shown that the soliton solutions become an eigenvalue problem in the wiggler frequency $\hat{\omega}_w$, given a fixed set of parameters $\hat{\omega}_c$, γ_0 , β , and $\hat{\omega}_p$.

Keywords: Solitons, Wiggler, Free Electron Laser, FEL, Undulators.

Introduction

A significant source of mathematical inspiration has been and remains the study of the dynamical behavior of physical systems. In the 20th century, a thorough investigation into many non-linear systems and their commonalities began [1]. Two opposites on the dynamics spectrum have drawn a lot of attention: chaos and solitons. Due to the extremely rich behavior that partial and ordinary differential equations can display, as shown by chaos theory, some deterministic systems can become exponentially unpredictable over time. The soliton hypothesis [2], on the other hand, offers a number of significant instances of non-linear systems behaving in a stable, quasi-linear manner. J. Scott Russell, riding a horse, chased a one-foot-high, thirty-foot-long wave produced by a stopping canal boat traveling at eight to nine miles per hour for nearly two miles in its original form. This was the first experimental demonstration of stable "solitary waves"—the precursors of the term "soliton"—in 1834. In 1895, the KdV problem was solved using this

single wave solution [3]. Since then, numerous more nonlinear partial differential equations (PDEs) have featured stable solitary wave solutions prominently, and the techniques for producing soliton solutions have led to numerous profound concepts in both mathematics and science [2, 4].

The free-electron laser, often known as a FEL [5], is a type of laser that, while using some quite different operating principles to create the beam, exhibits many of the same optical characteristics as conventional lasers, including the ability to emit coherent electromagnetic radiation beams with high strength. The lasing medium in free electron lasers is a relativistic electron beam that is free to flow through a wiggler, or transverse periodic magnetic field. The free-electron laser has the broadest frequency range and is the most widely tunable of all laser types. Numerous investigations, including both practical and theoretical ones, have been conducted in recent years on free-electron lasers (FEL) [6]. Various successful findings have been obtained through

experimental and theoretical work at labs and research facilities all around the world [7]. FEL is notable for its unique characteristics, which include its high frequency, high power, and wide bandwidth. Different medical, industrial, and military applications find these properties appealing [8]. A magnetic device called an "undulator" or "wiggler" is typically utilized for passing an electron down, forcing it to follow a periodic oscillatory path in space. This produces the FEL radiation. There are several possible configurations for the wiggler field's precise shape, and both helically and linearly polarized wiggler fields have been used to build FELs [9].

This paper solves the nonlinear electromagnetic wave propagation in a system with a relativistic cold-electron beam moving through an electromagnetic field. A system of coupled nonlinear ODEs has been generated by transforming the coordinates to wiggler coordinates. Numerical solutions of the soliton type, which may reflect potential nonlinear saturated states of the free-electron-laser instability, are shown as coupled electromagnetic and plasma waves.

2. The Electromagnetic Wiggler Field

We start with a relativistic cold fluid to describe the nonlinear evolution of the free electron laser instability [10], [11]. This applies to a relativistic cold electron beam of uniform density propagating in the z -direction through an electromagnetic wiggler field. The electromagnetic wiggler is given by [12], [13]:

$$\vec{E}_w(z, t) = \tilde{E}_w [-\hat{e}_x \sin(k_w z + w_w t) + \hat{e}_y \cos(k_w z + w_w t)] \quad (1)$$

$$\vec{B}_w(z, t) = -\tilde{B}_w [\hat{e}_x \cos(k_w z + w_w t) + \hat{e}_y \sin(k_w z + w_w t)], \quad (2)$$

where $\tilde{B}_w = \text{constant}$, $\tilde{E}_w = \frac{w_w \tilde{B}_w}{k_w c}$, and $\lambda_w = \frac{2\pi}{k_w}$ is the wave length, which are derived from the following vector potential:

$$\vec{A}_w(z, t) = A_w [\hat{e}_x \cos(k_w z + w_w t) + \hat{e}_y \sin(k_w z + w_w t)] \quad (3)$$

where $A_w = \frac{\tilde{B}_w}{k_w}$.

The beam density is assumed to be sufficiently small so that the equilibrium space-

charge effects are negligible, and the equilibrium self-magnetic field (B_s) is neglected. Therefore;

$$\vec{E}^0(\vec{r}) = \vec{E}_w(z, t), \quad \vec{B}^0(\vec{r}) = \vec{B}_w(z, t), \quad \text{and} \quad \vec{A}^0(\vec{r}) = \vec{A}_w(z, t).$$

We consider perturbations in which the spatial variations are one-dimensional in nature with $\frac{\partial}{\partial_x} = \frac{\partial}{\partial_y} = 0$, and $\frac{\partial}{\partial_z}$ is generally nonzero. The perturbed potentials and fields are:

$$\phi(z, t) = \delta\phi(z, t) \quad (4)$$

$$\delta\vec{A}(z, t) = \delta A_x(z, t) \hat{e}_x + \delta A_y(z, t) \hat{e}_y \quad (5)$$

$$\begin{aligned} \delta\vec{E}(z, t) = & -\frac{1}{c} \frac{\partial}{\partial_z} \delta\phi(z, t) \hat{e}_z - \frac{1}{c} \frac{\partial}{\partial_t} \delta A_x(z, t) \hat{e}_x - \\ & \frac{1}{c} \frac{\partial}{\partial_t} \delta A_y(z, t) \hat{e}_y \end{aligned} \quad (6)$$

$$\delta\vec{B}(z, t) = -\frac{\partial}{\partial_z} \delta A_y(z, t) \hat{e}_x + \frac{\partial}{\partial_z} \delta A_x(z, t) \hat{e}_y \quad (7)$$

Thus, the fields become:

$$\vec{E}(\vec{r}, t) = \vec{E}^0(z, t) + \delta\vec{E}(z, t) \quad (8)$$

$$\vec{B}(\vec{r}, t) = \vec{B}^0(z, t) + \delta\vec{B}(z, t) \quad (9)$$

The vector potential is:

$$\vec{A}(z, t) = \vec{A}^0(z, t) + \delta\vec{A}(z, t) \quad (10)$$

The relativistic momentum and the velocity are related by:

$\vec{p}(\vec{r}, t) = \gamma m \vec{v}$, where $\gamma = (1 + \frac{p^2}{m^2 c^2})^{1/2}$ is the relativistic factor and $\vec{v}(\vec{r}, t)$ is the flow velocity.

The continuity equation is given by:

$$\frac{\partial n}{\partial t} + \frac{\partial(nv_z)}{\partial z} = 0,$$

where $n(z, t)$ is the number density.

The equation of motion for a fluid element is:

$$\frac{d\vec{p}}{dt} = -e \left[\vec{E} + \frac{1}{c} \vec{v} \times \vec{B} \right], \quad (11)$$

where the convective derivative is: $\frac{d}{dt} = \frac{\partial}{\partial t} + v_z \frac{\partial}{\partial z}$.

$$\vec{E} = -\frac{\partial}{\partial z} \delta\phi(z, t) \hat{e}_z - \frac{1}{c} \frac{\partial}{\partial t} \delta\vec{A} \quad (12)$$

Substituting into Eq. (11) gives:

$$\frac{d\vec{p}_\perp}{dt} = -e \left[-\frac{1}{c} \frac{\partial}{\partial t} \vec{A}_\perp + \frac{1}{c} \{ \vec{v} \times (\nabla \times \vec{A}) \}_\perp \right] \quad (13)$$

$$\{ \vec{v} \times (\nabla \times \vec{A}) \}_\perp = -v_z \frac{\partial}{\partial z} \vec{A}_\perp \quad (14)$$

$$\frac{d\vec{P}_\perp}{dt} = \frac{e}{c} \left[\frac{\partial}{\partial t} \vec{A}_\perp + v_z \frac{\partial}{\partial z} \vec{A}_\perp \right] = \frac{e}{c} \frac{d\vec{A}}{dt} \quad (15)$$

$$\text{Or, } \frac{d}{dt} \left[\vec{P}_\perp - \frac{e}{c} \vec{A} \right] = 0 \quad (16)$$

Now, integrating yields:

$$\int \frac{d}{dt} \left[\vec{P}_\perp - \frac{e}{c} \vec{A} \right] = \text{constant} \quad (17)$$

Assuming the constant to be zero, we conclude:

$$\left[\vec{P}_\perp - \frac{e}{c} \vec{A} \right] = 0 \Rightarrow \vec{P}_\perp = \frac{e}{c} \vec{A} \quad (18)$$

The wave equation for \vec{A} (choosing Coulomb's gauge) is written as:

$$\nabla^2 \vec{A} - \frac{1}{c^2} \frac{\partial^2}{\partial t^2} \vec{A} = -\frac{4\pi}{c} \vec{J}_\perp \quad (19)$$

$$\vec{J}_\perp = -ne \vec{v}_\perp = \frac{-ne \vec{P}_\perp}{m\gamma} = \frac{-ne^2 \vec{A}}{m\gamma c} \quad (20)$$

$$\left[\frac{\partial^2}{\partial z^2} - \frac{1}{c^2} \frac{\partial^2}{\partial t^2} \right] \delta \vec{A} = \frac{4\pi e^2}{mc^2} \left[\frac{n}{\gamma} \vec{A} - \frac{n_0}{\gamma_0} \vec{A}^0 \right] = \frac{\omega_{p0}^2}{c^2} \left[\frac{n}{n_0 \gamma} \vec{A} - \frac{\vec{A}^0}{\gamma_0} \right] \quad (21)$$

Back to the equation of motion with its z-component:

$$\frac{\partial p_z}{\partial t} + v_z \frac{\partial p_z}{\partial z} = -e \left[E_z + \frac{1}{c} (\vec{v} \times \vec{B})_z \right] \quad (22)$$

while the $E_z = -\frac{\partial}{\partial z} \phi(z, t)$ and

$$\begin{aligned} (\vec{v} \times \vec{B})_z &= (v_x B_y - v_y B_x) = v_x \frac{\partial}{\partial z} A_x - v_y \frac{\partial}{\partial z} A_y \\ &= \frac{c}{e} v_x \frac{\partial}{\partial z} p_x + \frac{c}{e} v_y \frac{\partial}{\partial z} p_y \end{aligned} \quad (23)$$

Then,

$$\begin{aligned} \frac{\partial p_z}{\partial t} &= e \frac{\partial}{\partial z} \phi - \left[\frac{p_x}{m\gamma} \frac{\partial}{\partial z} p_x + \frac{p_y}{m\gamma} \frac{\partial}{\partial z} p_y + \frac{p_z}{m\gamma} \frac{\partial}{\partial z} p_z \right] \\ &= e \frac{\partial}{\partial z} \phi - mc^2 \frac{\partial}{\partial z} \gamma \end{aligned} \quad (24)$$

Differentiation with respect to t:

$$\frac{\partial^2 p_z}{\partial t^2} = e \frac{\partial^2}{\partial t \partial z} \phi - mc^2 \frac{\partial^2}{\partial t \partial z} \gamma \quad (25)$$

Now, using the axial components of Maxwell's equations:

$$\nabla \times \delta \vec{B} = \frac{4\pi}{c} \delta \vec{J} + \frac{1}{c} \frac{\partial}{\partial t} \delta \vec{E} \quad (26)$$

But, $(\nabla \times \delta \vec{B})_z = (\partial_x \delta B_y - \partial_y \delta B_x) = 0 - 0 = 0$.

Then, $\frac{\partial}{\partial t} \delta E_z = -4\pi(J_z - J_{0z}) = 4\pi e(nv_z - n_0 v_{0z})$.

$$\frac{\partial}{\partial t} \left(-\frac{\partial}{\partial z} \delta \phi \right) = -\frac{\partial}{\partial t} \left(\frac{\partial}{\partial z} \phi \right) = -\left(\frac{\partial^2}{\partial t \partial z} \phi \right) = \frac{4\pi e(nv_z - n_0 v_{0z})}{\gamma} \quad (27)$$

Using $\vec{p} = \gamma m \vec{v}$ and substituting into Eq. (27), we get:

$$e \frac{\partial^2}{\partial t \partial z} \phi = -\frac{4\pi e^2 n_0}{m} \left[\frac{n}{n_0} \frac{p_z}{\gamma} - \frac{p_{0z}}{\gamma_0} \right] \quad (28)$$

Substituting into Eq. (25) gives:

$$\frac{\partial^2 p_z}{\partial t^2} = -mc^2 \frac{\partial^2 \gamma}{\partial t \partial z} - \omega_{p0}^2 \left[\frac{n}{n_0} \frac{p_z}{\gamma} - \frac{p_{0z}}{\gamma_0} \right] \quad (29)$$

3. Transforming to the Wiggler Coordinates Frame

$$\hat{e}_1 = \hat{e}_x \cos(k_w z + w_w t) + \hat{e}_y \sin(k_w z + w_w t),$$

$$\hat{e}_2 = -\hat{e}_x \sin(k_w z + w_w t) + \hat{e}_y \cos(k_w z + w_w t), \quad \hat{e}_3 = \hat{e}_z$$

Equation (3) becomes:

$$A_x = A_1 \cos(k_w z + w_w t) - A_2 \sin(k_w z + w_w t) \quad (30)$$

$$A_y = A_1 \sin(k_w z + w_w t) + A_2 \cos(k_w z + w_w t) \quad (31)$$

$$A_z = A_3 \quad (32)$$

Substituting into the wave equation, we get:

$$\left[\frac{\partial^2}{\partial z^2} - \left(k_w^2 - \frac{w_w^2}{c^2} \right) - \frac{1}{c^2} \frac{\partial^2}{\partial t^2} \right] \delta A_1 - 2 \left[k_w \frac{\partial}{\partial z} - \frac{w_w}{c} \frac{1}{c} \frac{\partial}{\partial t} \right] \delta A_2 = \frac{\omega_{p0}^2}{c^2} \left[\frac{n}{n_0} \frac{A_1}{\gamma} - \frac{A_1^0}{\gamma_0} \right] \quad (33)$$

$$\left[\frac{\partial^2}{\partial z^2} - \left(k_w^2 - \frac{w_w^2}{c^2} \right) - \frac{1}{c^2} \frac{\partial^2}{\partial t^2} \right] \delta A_2 + 2 \left[k_w \frac{\partial}{\partial z} - \frac{w_w}{c} \frac{1}{c} \frac{\partial}{\partial t} \right] \delta A_1 = \frac{\omega_{p0}^2}{c^2} \left[\frac{n}{n_0} \frac{A_2}{\gamma} \right] \quad (34)$$

Making the traveling wave ansatz, where all the dynamical quantities depend on z and t by the combination $\xi = z - ut$, so $\frac{\partial}{\partial z} = \frac{d}{d\xi}$, and $\frac{\partial}{\partial t} = -u \frac{d}{d\xi}$.

Substituting into the wave equation, we obtain the following form in the wave frame:

$$\begin{aligned} \frac{\partial}{\partial t} n + \frac{\partial}{\partial z} (nv_z) &= 0 \\ -u \frac{dn}{d\xi} + n \frac{dv_z}{d\xi} + v_z \frac{dn}{d\xi} &= 0 \\ (v_z - u) \frac{dn}{d\xi} &= -n \frac{dv_z}{d\xi} \\ -\frac{dn}{n} &= \frac{dv_z}{(v_z - u)} \end{aligned} \quad (35)$$

Integrating:

$$\ln\left(\frac{n}{n_0}\right) = -\ln\left(\frac{v_z - u}{v_{0z} - u}\right) \quad (36)$$

Normalizing as follows: $\beta \equiv \frac{u}{c}$, $\beta_b \equiv \frac{v_0}{c}$, $q_3 \equiv \frac{p_z}{mc}$:

$$\frac{n}{n_0} = \frac{v_{0z}/c - u/c}{v_z/c - u/c} = \gamma \left(\frac{\beta_b - \beta}{\gamma \left(\frac{mv_z}{mc} \right) - \gamma \beta} \right) \quad (37)$$

$$\frac{n}{n_0} = \gamma \left(\frac{\beta - \beta_b}{\gamma \beta - q_3} \right) \quad (38)$$

Equation (33) can be reduced to the following form:

$$u^2 \frac{d^2 p_z}{d\xi^2} = mc^2 u \frac{d^2 \gamma}{d\xi^2} - \omega_{p0}^2 \left[\frac{n}{n_0} \frac{p_z}{\gamma} - \frac{p_{0z}}{\gamma_0} \right] \quad (39)$$

$$\beta \frac{d^2 (\beta q_3 - \gamma)}{d\eta^2} + \hat{\omega}_p^2 \left[\frac{n}{n_0} \frac{q_3}{\gamma} - \frac{q_{03}}{\gamma_0} \right] = 0 \quad (40)$$

where $\xi = \eta/k_w$, $p_z = q_3 mc$, $\omega_{p0}^2 = \hat{\omega}_p^2 c k_w$.

And in terms of q_1 , q_2 and $Z = (\beta q_3 - \gamma)$:

$$(\gamma \beta - q_3) = \sqrt{(\beta^2 - 1)(1 + q_1^2 + q_2^2) + Z^2} \quad (41)$$

We can rewrite Eq. (38) as follows:

$$\frac{n}{n_0 \gamma} = \frac{|\beta - \beta_b|}{\sqrt{(\beta^2 - 1)(1 + q_1^2 + q_2^2) + Z^2}} \quad (42)$$

$$\text{Or, } \frac{n q_3}{n_0 \gamma} = \left(\frac{\beta - \beta_b}{\beta^2 - 1} \right) + \frac{n}{n_0 \gamma} \left(\frac{\beta Z}{\beta^2 - 1} \right) \quad (43)$$

Hence,

$$\frac{n q_3}{n_0 \gamma} = \left(\frac{\beta - \beta_b}{\beta^2 - 1} \right) + \left(\frac{\beta |\beta - \beta_b| Z}{(\beta^2 - 1) \sqrt{(\beta^2 - 1)(1 + q_1^2 + q_2^2) + Z^2}} \right) \quad (44)$$

Substitution into Eq. (40) gives:

$$\beta \frac{d^2 Z}{d\eta^2} + \hat{\omega}_p^2 \left[\left(\frac{\beta - \beta_b}{\beta^2 - 1} \right) + \left(\frac{\beta |\beta - \beta_b| Z}{(\beta^2 - 1) \sqrt{(\beta^2 - 1)(1 + q_1^2 + q_2^2) + Z^2}} \right) - \frac{q_{03}}{\gamma_0} \right] = 0$$

Finally, the differential equation of Z is:

$$Z'' + \frac{\hat{\omega}_p^2 \gamma_0 |\beta - \beta_b| Z}{(\beta^2 - 1) \sqrt{(\beta^2 - 1)(1 + q_1^2 + q_2^2) + Z^2}} + \frac{\hat{\omega}_p^2 \gamma_0 (1 - \beta_b \beta)}{(\beta^2 - 1)} = 0 \quad (45)$$

where the over prime denotes $\frac{d}{d\eta}$.

Again, using the combination of the variables z and t by $\xi = z - ut$, where $u = \text{constant}$ is the

signal speed, $\frac{\partial}{\partial z} = \frac{d}{d\xi}$, and $\frac{\partial}{\partial t} = -u \frac{d}{d\xi}$. Substituting into and simplifying Eq. (33), we get:

$$\frac{d^2 \delta A_1}{d\xi^2} - \frac{u^2}{c^2} \frac{d^2 \delta A_1}{d\xi^2} - \left(k_w^2 - \frac{w_w^2}{c^2} \right) \delta A_1 - 2 \left(k_w \frac{d \delta A_2}{d\xi} + \frac{w_w u}{c} \frac{d \delta A_2}{d\xi} \right) = \frac{\omega_{p0}^2}{c^2} \left[\frac{n}{n_0} \frac{A_1}{\gamma} - \frac{A_1^0}{\gamma_0} \right] \quad (46)$$

Using $\xi = \frac{\eta}{k_w}$, $\delta A_1 = \frac{mc^2}{e} \delta q_1$, $\delta A_2 = \frac{mc^2}{e} \delta q_2$, $\hat{\omega}_{p0}^2 = \hat{\omega}_p^2 \gamma_0$, $\hat{w}_w = \frac{w_w}{c k_w}$ and in terms of q_1 , q_2 and $Z = (\beta q_3 - \gamma)$, Eq. (46) can be reduced to the following form:

$$(1 - \beta^2) \delta q_1'' - (1 - \hat{w}_w^2) \delta q_1 - 2(1 + \beta \hat{w}_w) \delta q_2' = \hat{\omega}_p^2 \gamma_0 \left[\frac{n}{n_0} \frac{q_1}{\gamma} - \frac{q_{01}}{\gamma_0} \right] \quad (47)$$

We can reduce the above equation using: $\delta q_1 = q_1 - q_{01}$, $\delta q_1' = q_1' - q_{01}'$, $\delta q_1'' = q_1'' - q_{01}''$, and $\delta q_2 = q_2 - q_{02}$, $\delta q_2' = q_2' - q_{02}'$, $\delta q_2'' = q_2'' - q_{02}''$, since $q_{01} = \frac{P_1}{mc} = \frac{e \hat{B}}{mc^2 k_w}$ then, $q_{01}' = q_{01}'' = 0$,

$$(1 - \beta^2) q_1'' - \left[(1 - \hat{w}_w^2) + \hat{\omega}_p^2 \gamma_0 \frac{n}{n_0 \gamma} \right] q_1 - 2(1 + \beta \hat{w}_w) q_2' = -\hat{\omega}_p^2 \gamma_0 \frac{q_{01}}{\gamma_0}.$$

Now substituting $\frac{q_{01}}{\gamma_0} = \frac{P_1}{mc \gamma_0} = \frac{e \hat{B}}{mc^2 k_w \gamma_0} = \hat{w}_c$, and $\frac{n}{n_0 \gamma} = \frac{|\beta - \beta_b|}{\sqrt{(\beta^2 - 1)(1 + q_1^2 + q_2^2) + Z^2}}$ yields:

$$(1 - \beta^2) q_1'' - \left[(1 - \hat{w}_w^2) + \hat{\omega}_p^2 \gamma_0 \frac{|\beta - \beta_b|}{\sqrt{(\beta^2 - 1)(1 + q_1^2 + q_2^2) + Z^2}} \right] q_1 - 2(1 + \beta \hat{w}_w) q_2' = -\hat{\omega}_p^2 \gamma_0 \hat{w}_c \quad (48)$$

Similarly, Eq. (41) becomes:

$$(1 - \beta^2) q_2'' - \left[(1 - \hat{w}_w^2) + \hat{\omega}_p^2 \gamma_0 \frac{|\beta - \beta_b|}{\sqrt{(\beta^2 - 1)(1 + q_1^2 + q_2^2) + Z^2}} \right] q_2 + 2(1 + \beta \hat{w}_w) q_1' = 0 \quad (49)$$

4. Results and Discussion

Equations (45), (47), and (48) are the final set of nonlinear coupled equations that we will solve to study the nonlinear evolution of the electromagnetic wiggler FEL.

The equilibrium solutions ($\frac{d}{d\eta} = 0$) are given for Eqs. (45), (47), and (48) as:

$$\varrho_{01} = \frac{\gamma_0 \hat{\omega}_c (1 + \hat{\omega}_p^2)}{(1 + \hat{\omega}_p^2) - \hat{\omega}_w^2}, \quad \varrho_{02} = 0, \quad \text{and} \quad Z_0 = \gamma_0 (\beta_b \beta - 1).$$

The small-signal analysis around the equilibrium [10] yields a traveling wave dispersion relation, which can be related formally to the familiar cold fluid mode dispersion relation for an electromagnetic wiggler free electron laser. It was shown by Davidson, Johnston, and Sen [10] that the free electron laser instability corresponds to the condition $\beta < \beta_b < 1$.

The solutions can be infinite wave trains, solitons, or periodic chaotic. In our case, we are addressing the soliton solutions for which we solved Eqs. (45), (47), and (48) numerically.

Such solutions for the electromagnetic wiggler FEL are evident in the profiles of $\delta \varrho_1$, $\delta \varrho_2$, δZ , and $\frac{n}{n_0 \gamma}$.

Figure 1(a) shows a soliton-type solution for $\hat{\omega}_c = 0.50$, $\gamma_0 = 10.0$, $\beta = 0.50$, $\hat{\omega}_p = 0.501935$, and $\hat{\omega}_w = 0.00$, representing the case without an electromagnetic wiggler. The $\delta Z = Z - Z_0$ profile is bell-shaped, while the other profiles ($\delta \varrho_1$, $\delta \varrho_2$, and $\frac{n}{n_0 \gamma}$) have a number of nodes, as seen in Figs. 1(b), 1(c), and 1(d). The δZ profile has a maximum amplitude of about -6.0, whereas the $\frac{n}{n_0 \gamma}$ profile remains positive, as expected, with density reduced across most of the region but sharply increasing at the edges.

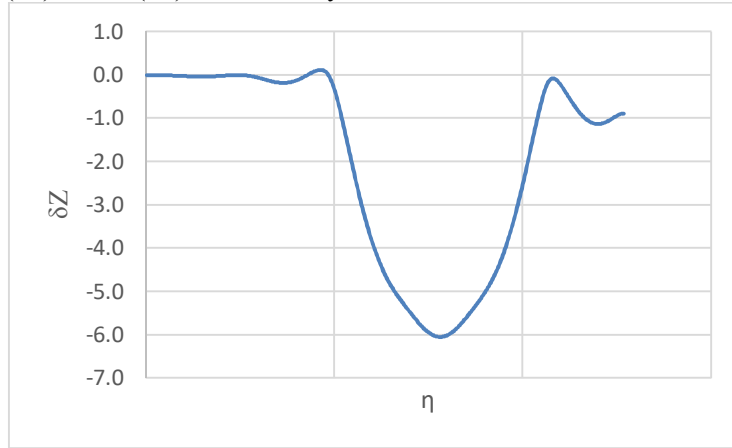


FIG. 1(a). Profile of δZ for a soliton pulse with $\hat{\omega}_w = 0.00$, $\hat{\omega}_c = 0.50$, $\gamma_0 = 10.0$, $\beta = 0.50$, and $\hat{\omega}_p = 0.501935$.

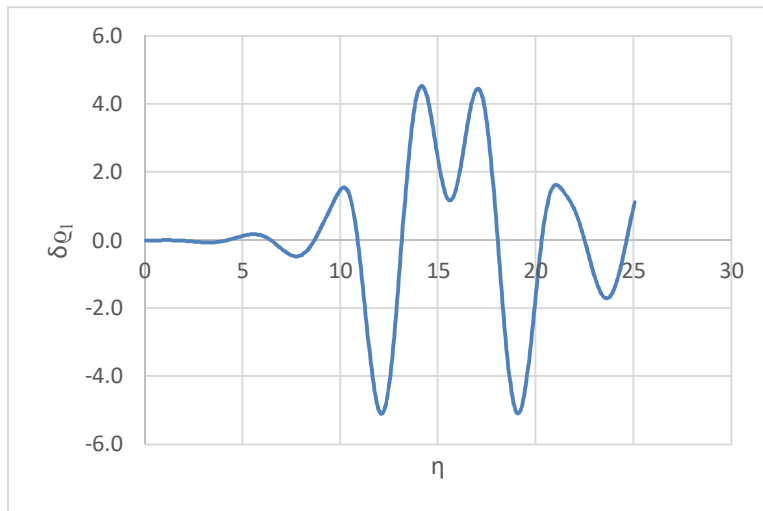


FIG. 1(b). Profile of $\delta \varrho_1$ for a soliton pulse with $\hat{\omega}_w = 0.00$, $\hat{\omega}_c = 0.50$, $\gamma_0 = 10.0$, $\beta = 0.50$, and $\hat{\omega}_p = 0.501935$.

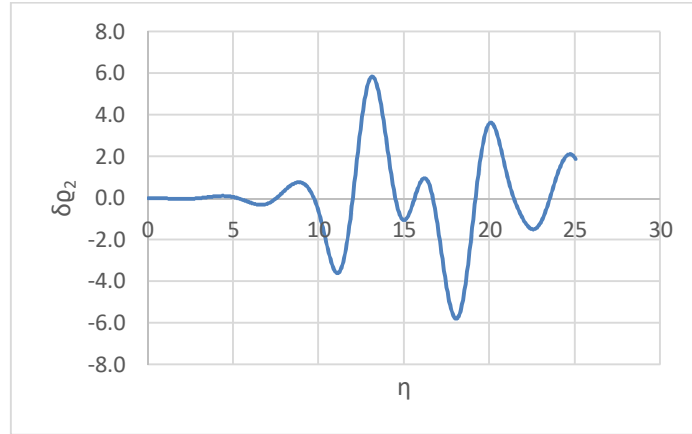


FIG. 1(c). Profile of δq_2 for a soliton pulse with $\hat{w}_w = 0.00$, $\hat{w}_c = 0.50$, $\gamma_0 = 10.0$, $\beta = 0.50$, and $\hat{w}_p = 0.501935$.

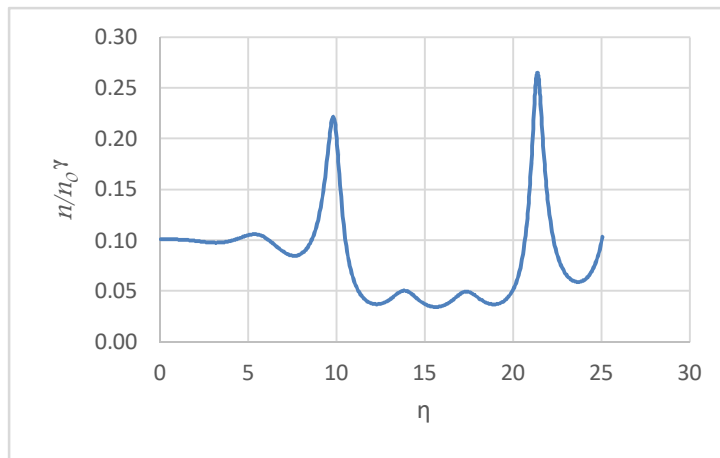


FIG. 1(d). Profile of $\frac{n}{n_0 \gamma}$ for a soliton pulse with $\hat{w}_w = 0.00$, $\hat{w}_c = 0.50$, $\gamma_0 = 10.0$, $\beta = 0.50$, and $\hat{w}_p = 0.501935$.

Figures 2(a), 2(b), 2(c), and 2(d) show a soliton-type solution for $\hat{w}_c = 0.50$, $\gamma_0 = 10.0$, $\beta = 0.50$, $\hat{w}_p = 0.501935$, and $\hat{w}_w = 0.50$ (in the presence of the electromagnetic wiggler). The $\delta Z = Z - Z_0$ profile retains its bell shape, while the other profiles (δq_1 , δq_2 , and $\frac{n}{n_0 \gamma}$) exhibit multiple nodes. The δZ profile has a

maximum amplitude of about -5.0 but is shifted to the left, as seen in the figure (appears earlier). Meanwhile, the $\frac{n}{n_0 \gamma}$ profile remains positive, showing a reduction in density over most of the region, though the depleted region is wider in this case.

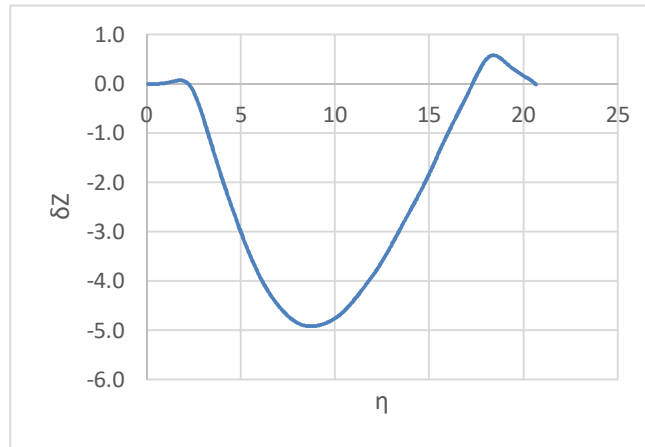


FIG. 2(a). Profile of δZ for a soliton pulse with $\hat{w}_w = 0.50$, $\hat{w}_c = 0.50$, $\gamma_0 = 10.0$, $\beta = 0.50$, and $\hat{w}_p = 0.501935$.

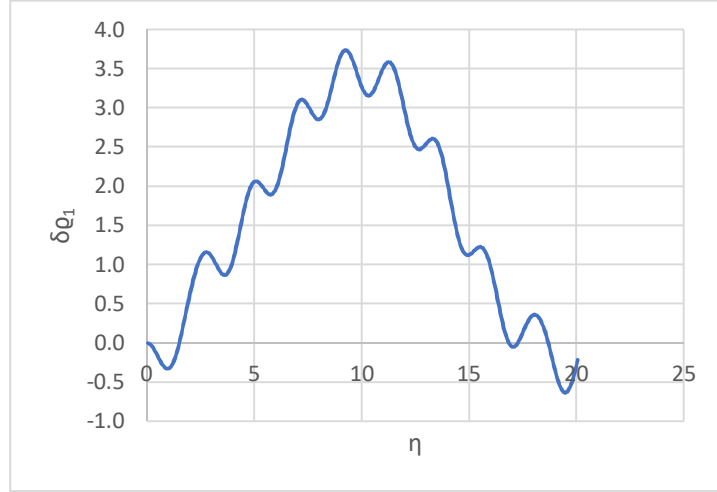


FIG. 2(b). Profile of δq_1 for a soliton pulse with $\hat{\omega}_w = 0.50$, $\hat{\omega}_c = 0.50$, $\gamma_0 = 10.0$, $\beta = 0.50$, and $\hat{\omega}_p = 0.501935$.

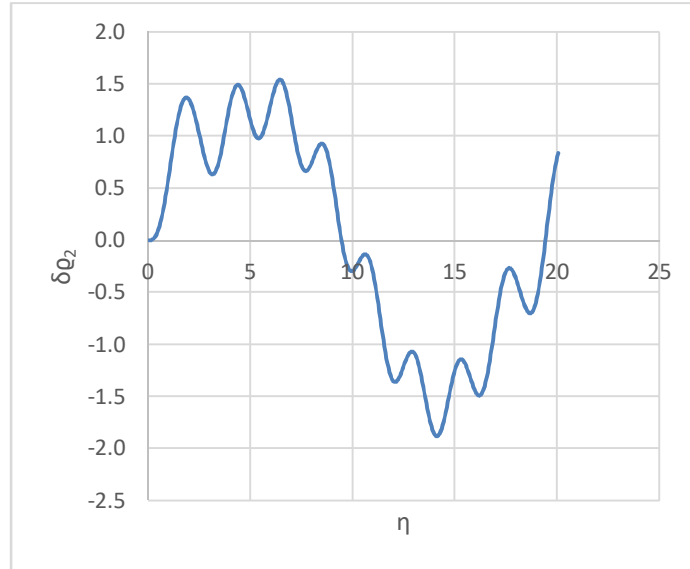


FIG. 2(c). Profile of δq_2 for a soliton pulse with $\hat{\omega}_w = 0.50$, $\hat{\omega}_c = 0.50$, $\gamma_0 = 10.0$, $\beta = 0.50$, and $\hat{\omega}_p = 0.501935$.

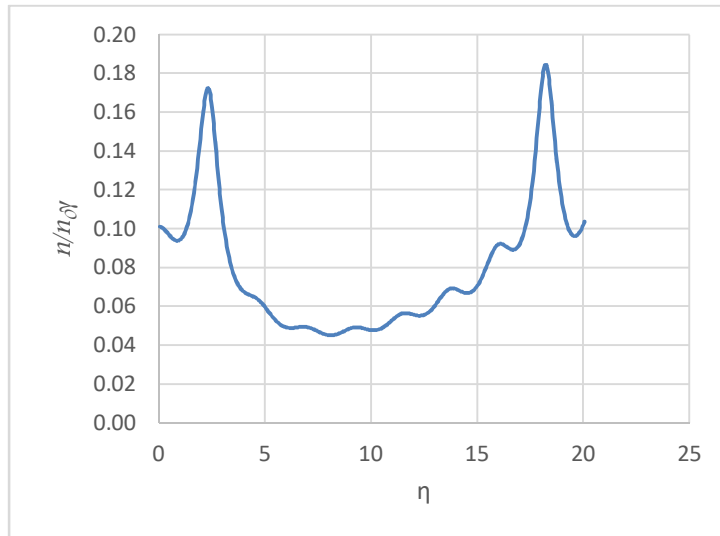


FIG. 2(d). Profile of $\frac{n}{n_0 \gamma}$ for a soliton pulse with $\hat{\omega}_w = 0.50$, $\hat{\omega}_c = 0.50$, $\gamma_0 = 10.0$, $\beta = 0.50$, and $\hat{\omega}_p = 0.501935$.

Figures 3(a), 3(b), 3(c), and 3(d) show the soliton solution for $\hat{w}_c = 0.60$, $\gamma_0 = 10.0$, $\beta = 0.50$, $\hat{\omega}_p = 0.501935$, and $\hat{w}_w = 0.60$ (in the presence of the electromagnetic wiggler). The $\delta Z = Z - Z_0$ is still bell-shaped, while the other

profiles ($\delta \varrho_1$, $\delta \varrho_2$, and $\frac{n}{n_0 \gamma}$) have a number of nodes. The δZ profile has a maximum amplitude of about -7.0, which is greater than that observed for $\hat{w}_w = 0.50$, while the $\frac{n}{n_0 \gamma}$ profile behaves almost identically.

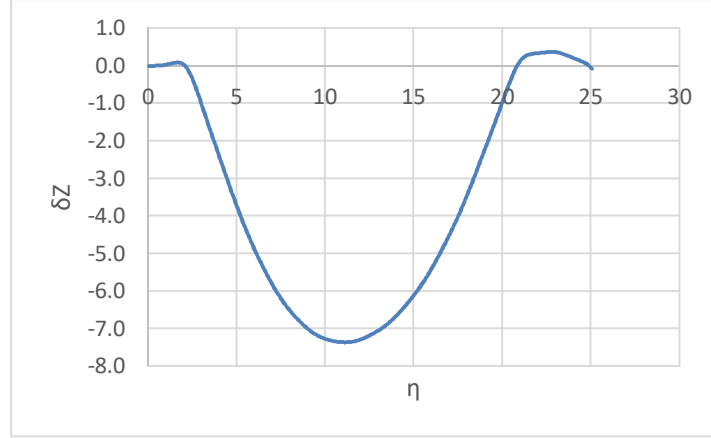


FIG. 3(a). Profile of δZ for a soliton pulse with $\hat{w}_w = 0.60$, $\hat{w}_c = 0.50$, $\gamma_0 = 10.0$, $\beta = 0.50$, and $\hat{\omega}_p = 0.501935$.

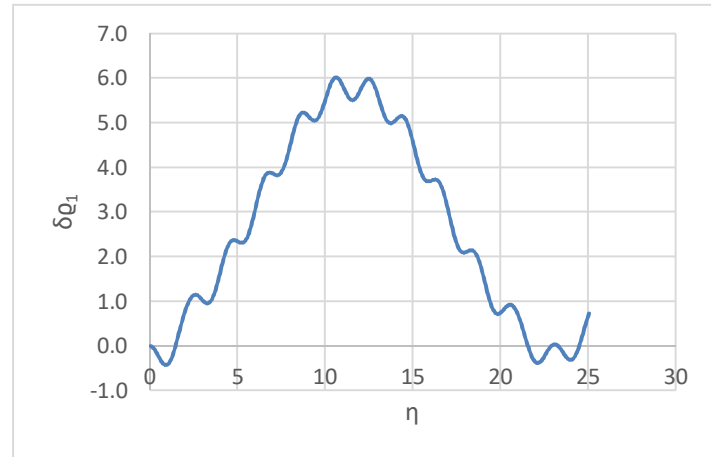


FIG. 3(b). Profile of $\delta \varrho_1$ for a soliton pulse with $\hat{w}_w = 0.60$, $\hat{w}_c = 0.50$, $\gamma_0 = 10.0$, $\beta = 0.50$, and $\hat{\omega}_p = 0.501935$.

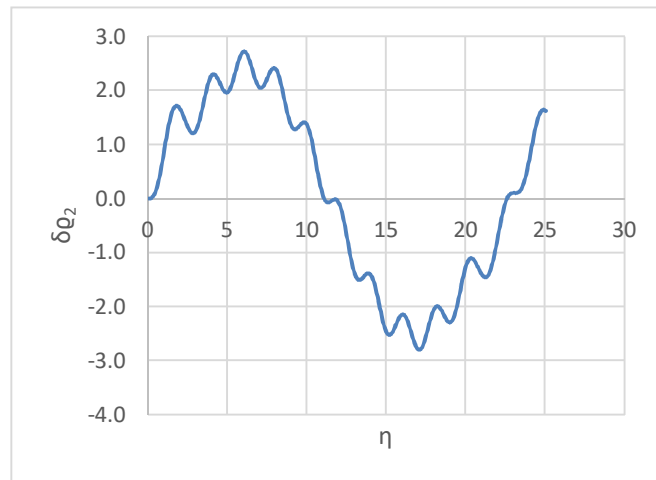


FIG. 3(c). Profile of $\delta \varrho_2$ for a soliton pulse with $\hat{w}_w = 0.60$, $\hat{w}_c = 0.50$, $\gamma_0 = 10.0$, $\beta = 0.50$, and $\hat{\omega}_p = 0.501935$.

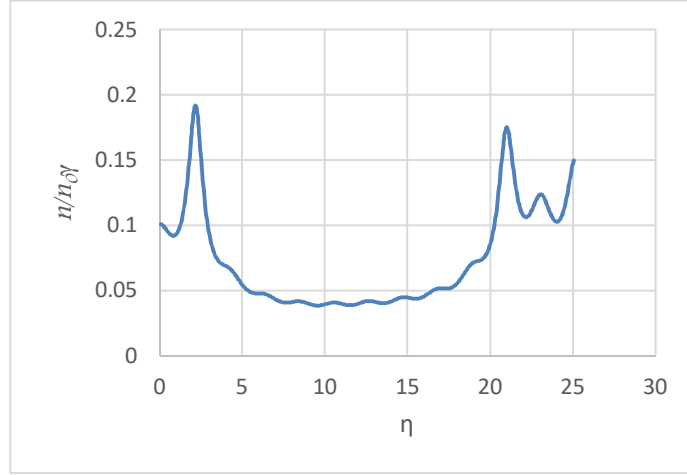


FIG. 3(d). Profile of $\frac{n}{n_0\gamma}$ for a soliton pulse with $\hat{w}_w = 0.60$, $\hat{w}_c = 0.50$, $\gamma_0 = 10.0$, $\beta = 0.50$, and $\hat{w}_p = 0.501935$.

Finally, Figs. 4(a), 4(b), 4(c), and 4(d) show the soliton solution for $\hat{w}_c = 0.60$, $\gamma_0 = 10.0$, $\beta = 0.50$, $\hat{w}_p = 0.501935$, and $\hat{w}_w = 0.70$, (in the presence of the electromagnetic wiggler). The $\delta Z = Z - Z_0$ profile remains bell-shaped,

while the other profiles ($\delta \varrho_1$, $\delta \varrho_2$, and $\frac{n}{n_0\gamma}$) exhibit multiple nodes. The δZ profile has a maximum amplitude of about -12.0, which is greater than that observed for $\hat{w}_w = 0.60$.

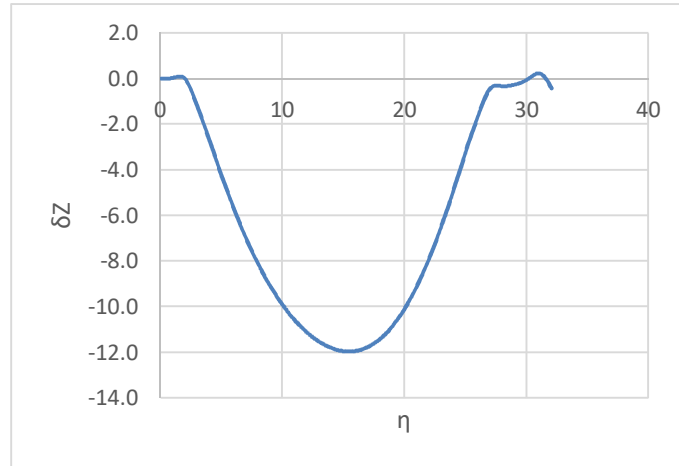


FIG. 4(a). Profile of δZ for a soliton pulse with $\hat{w}_w = 0.70$, $\hat{w}_c = 0.50$, $\gamma_0 = 10.0$, $\beta = 0.50$, and $\hat{w}_p = 0.501935$.

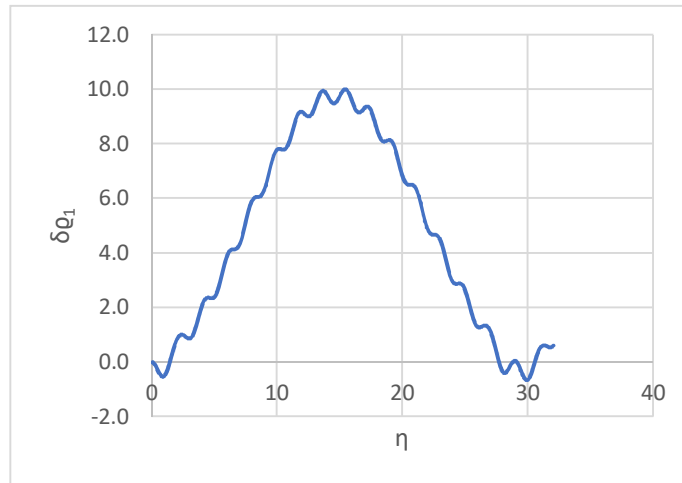


FIG. 4(b). Profile of $\delta \varrho_1$ for a soliton pulse with $\hat{w}_w = 0.70$, $\hat{w}_c = 0.50$, $\gamma_0 = 10.0$, $\beta = 0.50$, and $\hat{w}_p = 0.501935$.

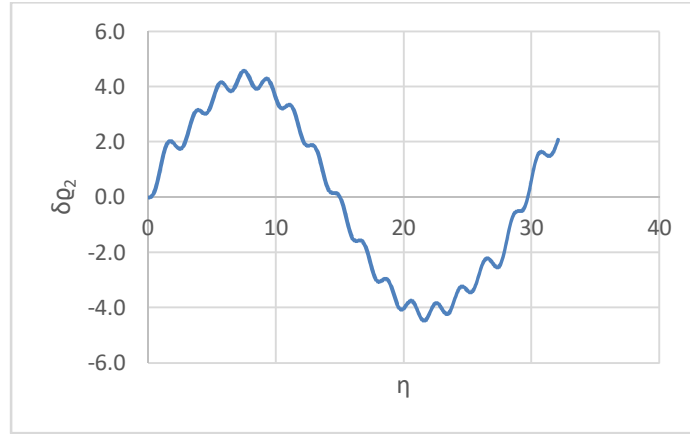


FIG. 4(c). Profile of δq_2 for a soliton pulse with $\hat{\omega}_w = 0.70$, $\hat{\omega}_c = 0.50$, $\gamma_0 = 10.0$, $\beta = 0.50$, and $\hat{\omega}_p = 0.501935$.

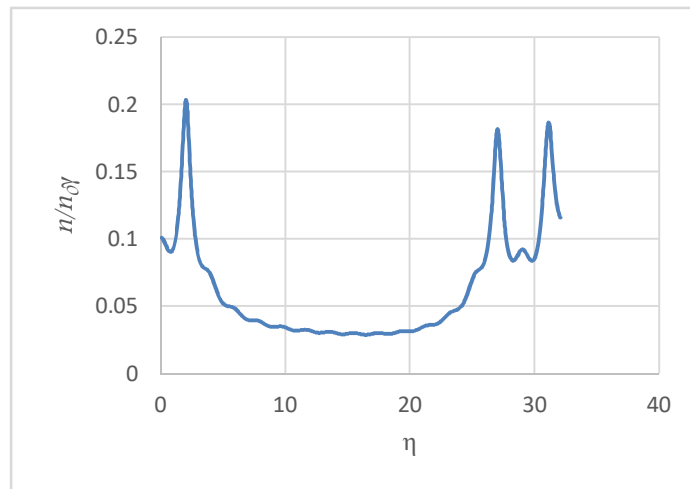


FIG. 4(d). Profile of $\frac{n}{n_0 \gamma}$ for a soliton pulse with $\hat{\omega}_w = 0.70$, $\hat{\omega}_c = 0.50$, $\gamma_0 = 10.0$, $\beta = 0.50$, and $\hat{\omega}_p = 0.501935$.

5. Conclusion

To conclude, I have obtained a soliton solution for the electromagnetic wiggler free-electron laser. The one-dimensional nonlinear traveling wave solutions were obtained by a numerical solution of the relativistic equations in the form of isolated pulses of coupled electromagnetic and plasma waves. It is shown that the soliton solutions became an eigenvalue

problem in the wiggler frequency $\hat{\omega}_w$ for a fixed set of parameters $\hat{\omega}_c$, γ_0 , β , and $\hat{\omega}_p$. This new class of solutions has a variety of potential applications and may represent nonlinear saturated states of the electromagnetic wiggler free-electron-laser instability.

References:

- [1] Hirota, R., "The Direct Method in Soliton Theory", (Cambridge University Press, 2004).
- [2] Manukure, S. and Booker, T., Partial Differ. Equ. Appl. Math., 4 (2021) 100140.
- [3] Drazin, P.G. and Johnson, R.S., "Solitons: An Introduction", (Cambridge University Press, 1989).
- [4] Al-Ghafri, K.S., Waves Random Complex Media, 28 (2) (2018) 261.
- [5] Udholm, P., Willett, J.E., and Bilikmen, S., J. Phys. D, 24 (1991) 1278.
- [6] Marshall, T.C., "Free Electron Laser", (New York, Macmillan, 1985).
- [7] Bilikmen, S. and Abu Safa, M., Tr. J. Phys., (16) (1992) 537.
- [8] Schmitt, W.J. and Elliott, C.J., Phys. Rev. A, 41 (1990) 3853.
- [9] Abu Safa, M., Int. J. Phys. Sci., 9 (21) (2014) 459.
- [10] Davidson, R.C., Johnston, G.L., and Sen, A., Phys. Rev. A, 34 (1986) 392.
- [11] Sen, A. and Johnston, G.L., Phys. Rev. Lett., (70) (1993) 786.
- [12] Fruend, H.P., Kehs, R.A., and Granatstein, V.L., Phys. Rev. A, 34 (1986) 2007.
- [13] Fruend, H.P. et al., IEEE J. Quantum Electron., QE 21 (7) (1985) 1080.

The Influence of Multiwall Carbon Nanotubes Additives on the Structural and Mechanical Properties of Alumina Composites

Abdulsattar K. Hasan^a, Thamir A. Jumah^a and Kassim M. Wadi^b

^a Department of Physics, College of Science, Al-Nahrain University, Jadiriya, Baghdad, Iraq.

^b Almamon College, Bagdad, Iraq.

Doi: <https://doi.org/10.47011/18.1.7>

Received on: 16/09/2023;

Accepted on: 26/11/2023

Abstract: Monolithic Al₂O₃ / multi-walled carbon nanotube (MWCNT) composites were generated in three categories through ratios by conventional sintering method. The microstructure and mechanical properties were studied. After being prepared and pressed, the specimens were sintered. The as-synthesized specimens were characterized through XRD, SEM, particle size distribution, and porosity measurements. The mechanical property evaluations included measuring the compression, Vickers hardness, and Charpy impact testing. The absorbed energy and toughness were calculated for each sample. The XRD patterns were used to identify the structural parameters of the samples and identify the phases present. The SEM images were used to investigate the dispersion characteristics of the MWCNTs in addition to the nature of the fractured areas. The results show the possibility of enhancing the mechanical properties of the composite material by varying the composition ratio of the MWCNTs. The mechanical properties are also varying with the porosity character of the samples. The present analysis of the mechanical and structural properties of the fabricated samples is believed to assist the development of the composite material for armor applications.

Keywords: Ceramics composites, MWCNTs, Microstructure, Armors, Mechanical properties.

1. Introduction

The number of fields in which ceramics can be used is increasing significantly due to advancements in ceramic-based nanocomposites (CMNCs) [1]. Alumina (Al₂O₃)-based compounds are prospective engineering materials with exceptional mechanical and tribological characteristics. Due to their chemical inertness and hardness, ceramics are now widely used in applications such as armor, dental implants, high-speed cutting tools, electrical and chemical insulators, wear-resistant parts, and various coatings. Ceramics are known to have excellent thermal and electrical insulating qualities [2-6]. Monolithic porcelain has low

fracture toughness, weak creep resistance, and intrinsic brittleness. Over the past few decades, numerous attempts have been made to create ceramic matrix composites (CMCs), which possess superior mechanical properties over monolithic ceramics [7]. Due to their light weight, excellent toughness, and exceptional thermal and chemical resistance, CMCs have recently been a popular choice for a variety of applications [8]. The use of nano-fillers as a reinforcing phase is an important and promising strategy for improving the mechanical characteristics of CMNCs [1]. As prospective nano-fillers for CMNCs, carbon nanotubes

(CNTs) have come to light [9-13]. The reinforced alumina composites cannot, however, be guaranteed to perform as envisaged despite the remarkable characteristics of CNTs. The primary explanation is that the mechanical properties of CNTs and their reinforced composites are significantly influenced by interfacial features [14, 15]. In the present study, Al₂O₃-MWCNT composites are developed with the use of multi-walled carbon nanotubes (MWCNTs). MWCNTs have an approximate density of 2.6 g/cm³ and a specific surface area of 200–400 m²/g. MWCNTs have compression strength between 10 and 60 GPa and a modulus between 0.3 and 1 TPa. Additionally, MWCNTs possess a high thermal conductivity of up to 3000 W/m and a noteworthy electrical conductivity in the range of 106-107 S/m [16, 17].

As a result of its striking high hardness (15-22 GPa), chemical inertness, and strong oxidation resistance, Al₂O₃ ceramics is one of the important, widely used ceramic materials [18]. Al₂O₃ ceramics is one of the cheapest and commercially viable options used in material engineering. Al₂O₃ has a density between 3.75 and 3.95 gm/cm³ and a melting point of 2071 °C [19]. In addition to these characteristics, the material has a bulk modulus of 324 GPa, a Young's modulus of 413 GPa, and a compressive strength between 2000 and 4000 MPa. Al₂O₃ has a 5 MPa/m fracture toughness and a 10.9 10⁻⁶/K thermal expansion coefficient [19]. Despite having a number of exceptional functional qualities, Al₂O₃'s applications are restricted due to its low fracture toughness. To overcome this limitation, significant efforts have been made to enhance the fracture toughness of Al₂O₃ using advanced sintering techniques such as spark plasma sintering (SPS) and the incorporation of nano-fillers. [20, 21]. The target of this project is to study the structural variations and mechanical properties of composites reinforced with carbon nanotubes, aiming to improve their performance for armor applications.

2. Materials and Methods

2.1. Preparation of Alumina-MWCNT Composites

Due to their high tendency to agglomerate, MWCNTs are not easily distributed homogeneously in the matrix material of the reinforced composite. This challenge arises from

the morphological and structural aspects of the CNTs. Accordingly, the interface between the MWCNTs and the matrix may not be well constructed. To transfer/generate the appropriate mechanical and structural properties to the compounds, the dispersion of MWCNTs inside the matrix must be as homogenous as feasible.

The starting materials were initially weighed accurately and added to the ball mill container. The ball milling was achieved in a wet medium in the presence of ethanol. Materials are constantly ground by a motor-driven mill with atria-stabilized zirconia balls as grinding media for the homogeneous mixing of powders for 24 hours. Then, the mixture was dried for 30 minutes at 100°C in a vacuum oven. 2wt% PVA and polyvinyl alcohol were added as binders to the dried material and crushed using a mortar and pestle for further mixing. Before sintering, the combined mixture was pressed unidirectional into 12 mm diameter discs at 350 MPa for 10 minutes. The pressed samples were placed in a furnace for sintering at an elevated temperature of 1500°C for two hours with a heating rate of 10°C/min. The group samples were then gradually cooled until they reached the laboratory temperature; the cooling rate of the sample was 10 °C/min. After the green samples were dried, the density of the calcified body was determined using Archimedes' principle by immersion in distilled water. To estimate the density of any sort of sintered sample and the change in density, at least six samples were taken into account.

Using Archimedes' principle, the density of the calcified body was determined in this experiment by immersion in distilled water. According to Eq. (1), the link between apparent density and theoretical density was used to calculate the relative density (r), whereas porosity (ϵ) was calculated using Eq. (2):

$$pr = \rho_{ab}/\rho_t \quad (1)$$

$$\epsilon = 1 - pr \quad (2)$$

TABLE 1. Composition ratios of samples.

Samples	Al ₂ O ₃	MWCNTs
A (pure)	100 wt.%	0 wt.%
A3	97 wt.%	3 wt.%
A5	95 wt.%	5 wt.%

2.2. Sample Consolidation and Sintering

Al₂O₃-MWCNT composites were chosen for consolidation using pressure-free sintering

methods. The samples included pure Al_2O_3 as well as Al_2O_3 3wt. %, and 5wt. % MWCNT composites. Green pellets were prepared for the traditional sintering process in a uniaxial pressing machine with a load of 395 MPa. Samples were fired to a temperature of 1500°C for 10 minutes at a rate of $10^\circ\text{C}/\text{min}$, then allowed to cool naturally in the furnace until they reached laboratory temperature.

Using Archimedes' approach, the bulk density of the different composites was determined. Al_2O_3 was supposed to have a density of 3.95 g/cm^3 , while MWCNT was believed to have a density of 2.6 g/cm^3 . The morphology of the fabricated composite samples was examined using SEM.

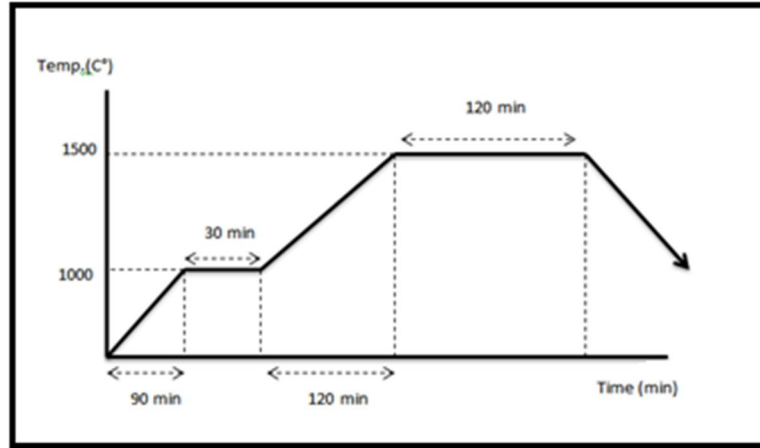


FIG. 1. Sintering furnace program cycle.

2.3. Characterization Techniques

The Al_2O_3 and Al_2O_3 -MWCNT powder mixtures, as well as the produced composites, were characterized using X-ray diffraction (XRD) and an electron microscope with field emission scanning (FESEM). The morphologies of the blended powder mixtures were examined using a scanning electron microscope (SEM).

2.4. Mechanical Tests

Hardness measurements of the sintered samples - A (pure Al_2O_3), A3 (3wt% MWCNTs), and A5 (5wt% MWCNTs) - were conducted on polished cross-sections using a Vickers hardness tester, with a 500-gram load applied for 10 seconds. Five indentations were made on each sample to obtain average hardness values. The sintered samples typically had dimensions of $10 \text{ mm} \times 10 \text{ mm} \times 55 \text{ mm}$.

To assess the fracture toughness of the composite materials, the single-edge notched beam method was used. Each sample had a grooved incision, and the absorbed energy was measured through an impact test. Toughness values were then calculated using the following equations [22]:

$$IE = l * \omega [\cos(\alpha) - \cos(\beta)] \quad (3)$$

where IE is impact energy absorbed by damage sample, $l = 0.75\text{m}$ is length of the arm, $\omega = 25.81 \text{ kg}$ is the weight of the mass, $\alpha = 141.5^\circ$, and β is computed angle from test.

The toughness was then determined using the equation:

$$\text{Toughness} = IE/a \quad (4)$$

where a represents the cross-sectional area of the sample.

3. Results and Discussion

3.1. Structural Characterization

The XRD patterns are shown in Fig. 2. The majority of the sintered samples consisted of α - Al_2O_3 . All samples had high-intensity patterns. The high-intensity peaks of the XRD patterns show that the powder had a high degree of crystallinity. For each prepared sample, the peaks correspond to a single-phase hexagonal lattice (R-3c space group, space group number 167). Specifically, the reference sample (A) matches ICSD: 31546 (Ref. Code 98-003-1546) [23], sample A3 corresponds to ICSD: 75560 (Ref. Code 98-007-5560) [24], and sample A5 aligns with ICSD: 160604 (Ref. Code 98-016-0604) [25]. These peaks confirm the presence of a single phase in each prepared sample, with no

additional minor phases detected, suggesting that the milling process did not introduce any unwanted phase transformations.

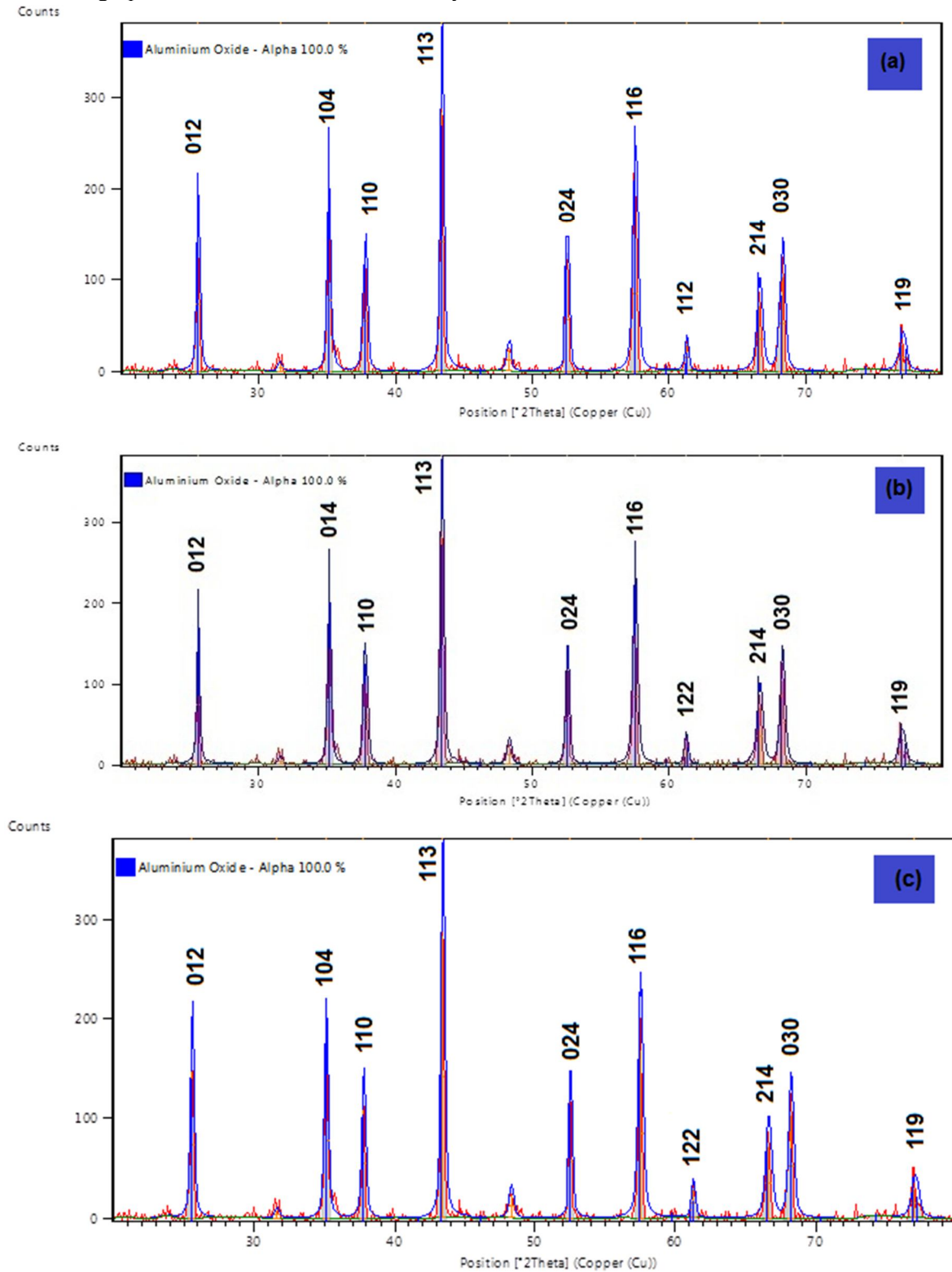


FIG. 2. XRD patterns of the manufactured compositions: (a) A, (b) A3, and (c) A5.

3.2 Analysis of sample morphology

Figures 3(a)-3(b) show the morphology of the multi-walled carbon nanotubes (MWCNTs) reinforcement phase and the alumina (Al_2O_3)

matrix phase. Figure 3(a) presents an SEM image of carbon tubes with diameters ranging from approximately 20 to 26 nm. Figure 3(b) illustrates a homogeneous alumina ceramic. It demonstrates consistency in the structure of the

ceramic particles, which are mostly uniform, with an average grain size of 6 μm , while

discernible porosity between the grains is also observed.

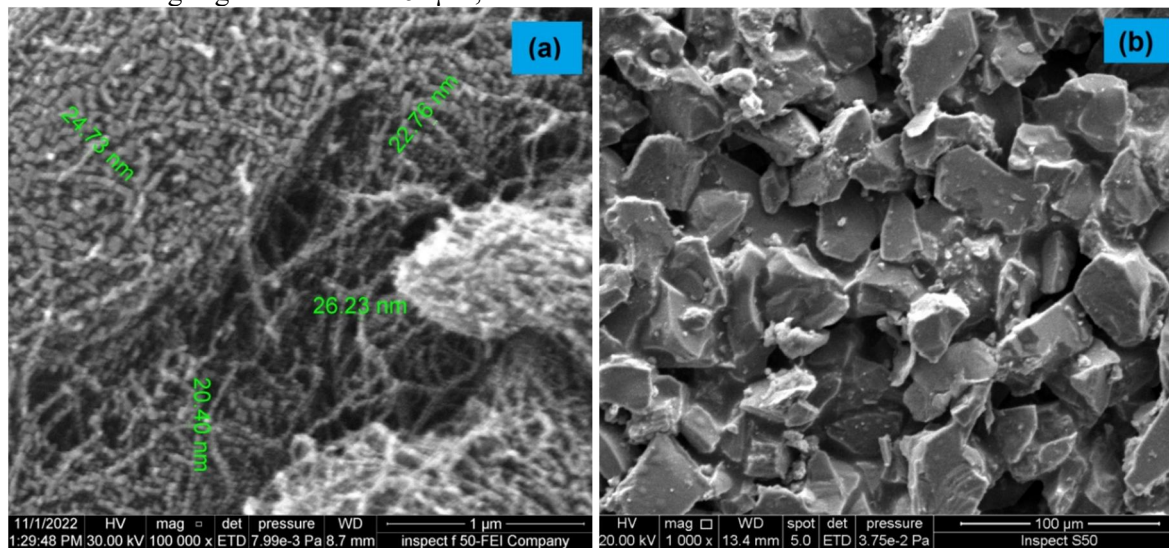


FIG. 3. SEM images of (a) MWCNTs and (b) Al₂O₃.

Figures 4(a) and 4(b) show the microstructures of monolithic alumina ceramics. Image (a) corresponds to the pure sample. The particle size analysis of the monolithic sample (A) indicates that the ceramic grain sizes are mostly equivalent, with an average grain size of 6 μm . Figure 4 presents SEM images of the surfaces of particles smaller than 6 μm in size for (a) the pure sample (0.0 wt.% MWCNTs). The images in (a) and (b) reveal surface morphologies associated with intergranular fracture, transgranular fracture, and plastic deformation. Alumina fragments with a size of less than 6 μm were discovered to have a faceted

structure with sundry sharp corners, as seen in Figs. 4(a) and 4(b). These fragments had rough surfaces and a morphology that was primarily broken. According to the FESEM images in Figure 4(b), the observed fractures are primarily intergranular, with localized transgranular fractures [26]. Quasi-static Vickers indentation tests confirm the mixed-mode nature of crack propagation in ceramics under ballistic conditions [21]. Additionally, fragmented regions within the ceramics show traces of minute smearing, indicating significant underlying plastic deformation.

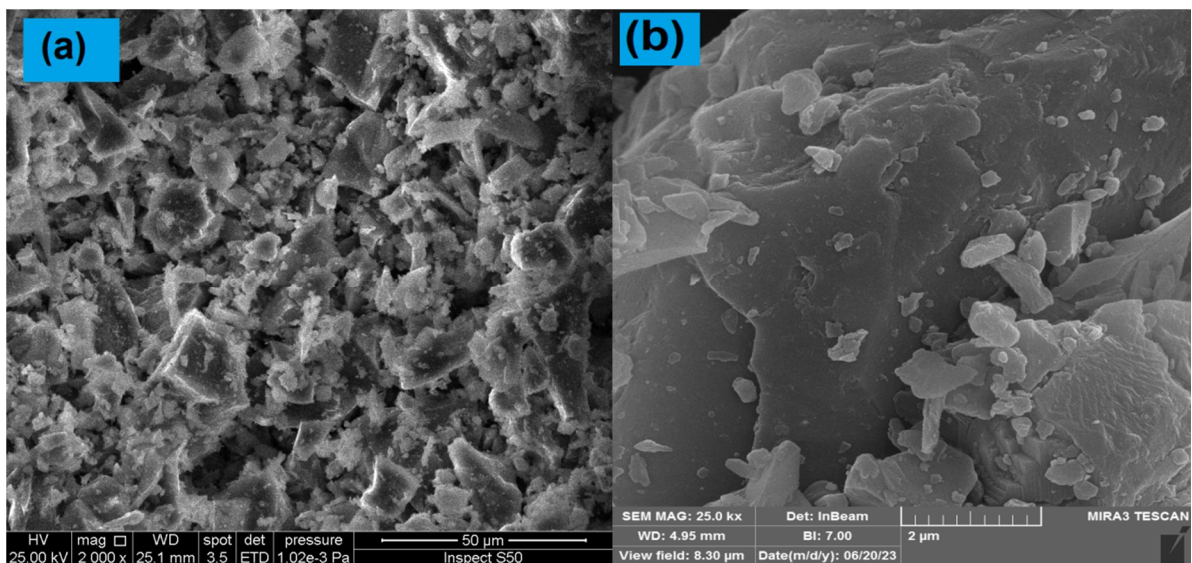


FIG.4. FESEM and SEM micrographs of fracture surfaces: (a) SEM of A sample, (b) FESEM of A sample.

The micrographs of fractured surfaces for the nanocomposite A3 (alumina with a 3 wt.% MWCNT addition) acquired by SEM and

sintered at 1500°C are shown in Fig. 5. The sample had good carbon nanotube dispersion, but it was also possible to see that the A3 sample

developed a nonhomogeneous morphology. Compared to the A5 samples, the MWCNT in the samples appear to be more evenly distributed. This improved dispersion may contribute to the enhanced mechanical properties of the nanocomposite [27]. The presence of MWCNTs at the grain boundaries is indicated by black arrows in the micrographs. Micrographs of the composition A3 ($\text{Al}_2\text{O}_3 + 3 \text{ wt. \% MWCNT}$) sintered at 1500°C are shown in the figures. Although the sample had low densification and a lower density than the previous sample after sintering at 1500°C , carbon nanotubes are still visible at the grain boundaries. Figure 5 shows SEM images of the fracture surface for sample A3, where all specimens exhibit highly textured fracture surfaces with numerous dimpled

patterns [28]. The average dimple size remained relatively unchanged with increasing nanotube concentration.

Although minor local agglomerates of MWCNTs are observed in some regions, the majority of the fracture surface is covered with well-dispersed individual nanotubes. As the MWCNT concentration increased, so did the presence of individual nanotubes on the fracture surface. Most MWCNTs appear as fractured segments, indicating that they ruptured during the fracture process. Additionally, increased surface roughness is evident due to the formation of several "bulge" regions. These bulges consist of a few broken MWCNTs that are fully embedded within the surrounding matrix [29].

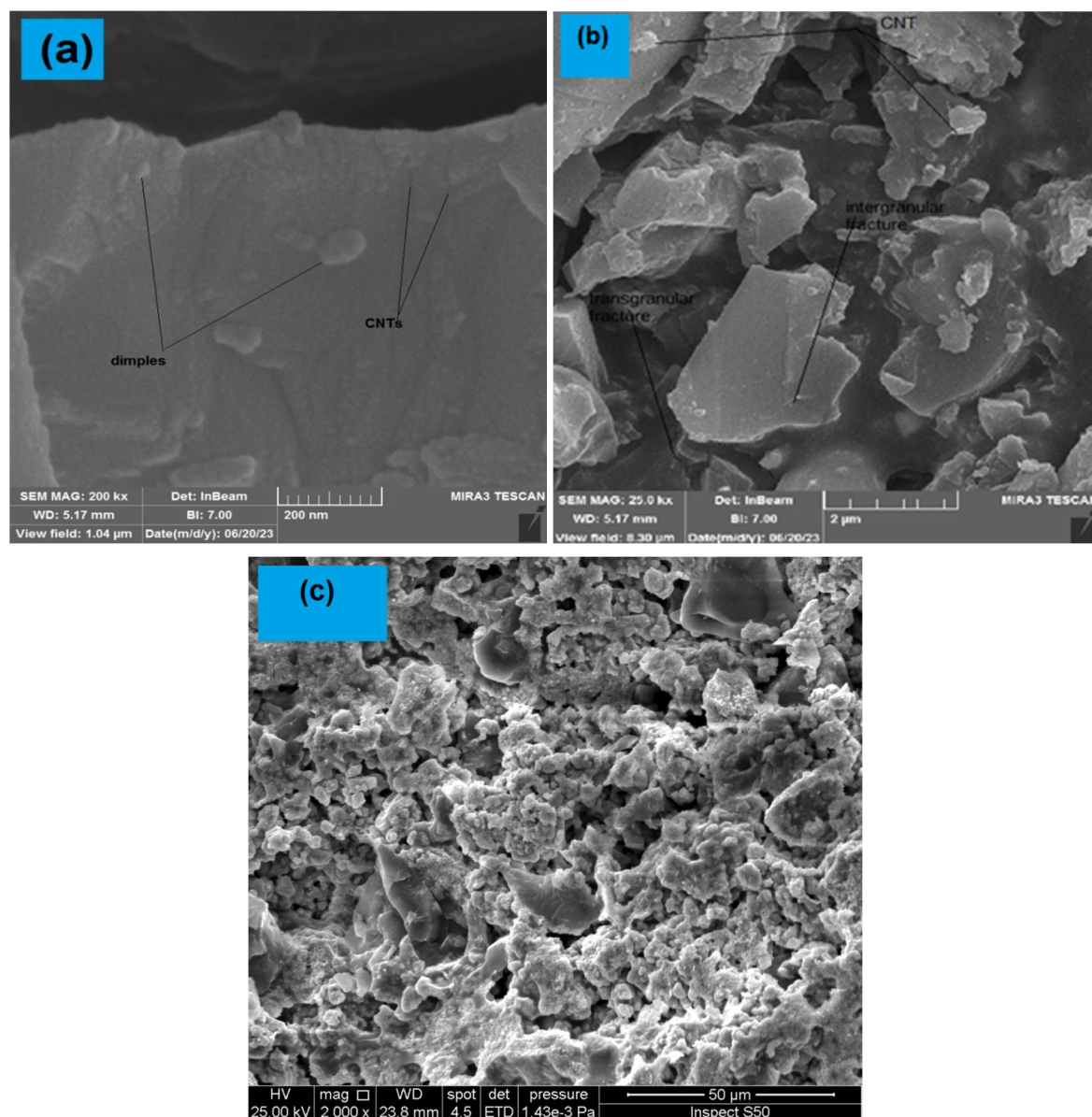


FIG. 5. FESEM and SEM micrographs of fracture surfaces: (a) and (b) FESEM of A3 sample, (c) SEM of the same sample.

The micrographs of the composition A5 ($\text{Al}_2\text{O}_3 + 5 \text{ wt.}\% \text{ MWCNT}$) sintered at 1500°C are shown in Figs. 6(a), 6(b), and 6(c). A relative increase in porosity is observed due to the increase in the amount of CNTs in the matrix. When MWCNT was added, the grain development was stopped, leading to isolated concentrations of carbon nanotubes in the microstructure. Compared to the A3 sample, MWCNTs are found to agglomerate. The observed decrease in the hardness and toughness of this nanocomposite could be attributed to this non-uniform dispersion.

Furthermore, the densification of alumina nanocomposites was significantly affected by the addition of MWCNTs within a tolerable range. The more even distribution of MWCNTs in alumina nanocomposites helped hinder the carbothermal reduction of alumina. Most MWCNTs exhibited broken segments, indicating that they ruptured during the fracture. The micrographs also reveal increased surface roughness due to the formation of multiple newly formed "bulge" regions [29].

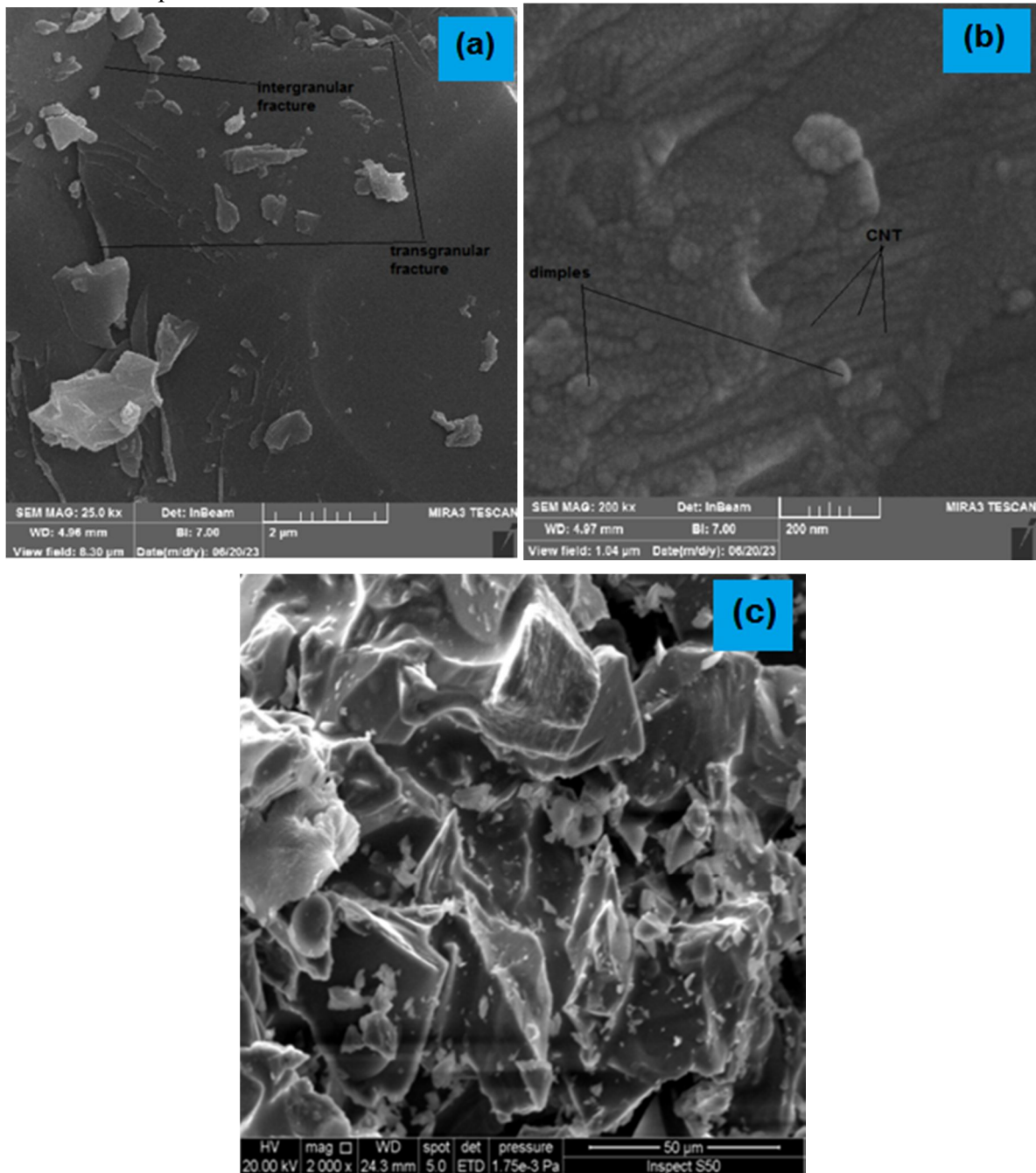


FIG. 6. FESEM and SEM micrographs of fracture surfaces: (a) and (b) FESEM of A5 sample, (c) SEM of the same sample.

In the context of ceramics composites for armor applications, "bulge" locations refer to specific regions on the surface of the alumina matrix where a noticeable deformation or protrusion occurs. These bulges can appear when high ratios of MWCNTs are incorporated into the ceramic composite.

The formation of these bulges is typically associated with localized changes in the microstructure or mechanical properties of the composite. When MWCNTs are added to the ceramic matrix, especially at high concentrations, they can interact with the surrounding material in a way that leads to the development of these bulging regions. Several factors may contribute to their formation:

1. Entanglement and Clustering: MWCNTs have a tendency to entangle and cluster together due to strong van der Waals forces and their unique sp² bonding. When these clusters are embedded within the ceramic matrix, they can create regions of increased volume or

local strain, which can lead to bulges on the surface [29].

2. Differential Stress: The incorporation of MWCNTs can introduce areas of differential stress within the composite. Depending on the distribution and orientation of MWCNTs, certain regions may experience more stress than others, resulting in localized deformation and bulging [31].
3. Interfacial Effects: The interaction between MWCNTs and the ceramic matrix can influence how stresses are distributed. Variations in the strength of the interfacial bonding between the MWCNTs and the matrix can lead to uneven mechanical responses, potentially causing bulging [32].
4. Thermal Effects: During processing or post-processing, variations in temperature or differences in thermal expansion coefficients between MWCNTs and the ceramic matrix can create localized thermal stress, which may contribute to the formation of bulges [33].

TABLE 2: Apparent density, theoretical density, relative density, porosity, and mean pore diameter of the sintered samples.

Composition	A	A3	A5
Apparent density ($\rho_{ab}, \text{g.cm}^{-3}$)	3.75	3.78	3.8
Theoretical density ($\rho_t, \text{g.cm}^{-3}$)	3.99	3.98	3.96
Relative density ($\rho_r, \%$)	93.98	94.97	95.95
Porosity ($\epsilon, \%$)	0.74	0.51	0.43
Mean pore diameter (nm)	8.72	8.26	4.76

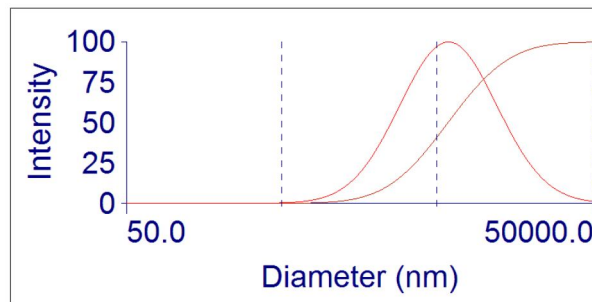


FIG. 7. Particle size distributions (PSDs).

Using dynamic laser scattering, the particle size distribution (PSD) of pure Al₂O₃ powder mixtures was determined, and the zeta potential was utilized to assess the dispersion state. The average particle size of the different powder mixtures was ascertained by calculating the PSD of Al₂O₃ powder mixtures. The average size of the Al₂O₃ particles is approximately 5.8 μm , as indicated by the PSD of pure Al₂O₃ shown in Fig. 6. It is noteworthy that the pure Al₂O₃ obtained had a particle size of around 25 μm .

This demonstrates that Al₂O₃ particles can be ground to an extremely fine size in a short amount of time during milling.

The analysis of Fig. 7 relates to several aspects of the composite, where the distribution of particle sizes, especially in composite materials, is a critical factor that affects the overall material properties and performance. A well-controlled, narrow distribution can lead to more uniform and enhanced properties, making

it an important consideration in materials science and engineering.

1. The size distribution: The average particle size of 5.887 μm refers to the average Al_2O_3 particle size, and the actual particle sizes can vary [34].
2. The width of distribution: The width of the particle size distribution is a key factor. A narrow distribution means that most particles are close in size to the average. In contrast, a broad distribution means that particles can vary greatly in size. The distribution width can affect properties such as packing density, sintering behavior, and mechanical properties of the composite [34].
3. Effect on composite properties: When Al_2O_3 particles are combined with carbon nanotubes (MWCNTs), the particle size distribution of both components is critical. A narrow distribution can help ensure more consistent and predictable properties in the composite. If both Al_2O_3 and MWCNT have narrow size distributions, it could lead to better particle packing, uniform dispersion, and possibly improved mechanical properties [35].
4. Effect on sintering: During the sintering process, the particle size distribution can affect how the particles pack together. A tighter distribution may result in more efficient packing and improved sintering, leading to a denser and stronger composite [36].
5. Homogeneity: In composite materials, achieving a homogeneous distribution of components is essential. A tight particle size distribution can help achieve this uniformity, preventing issues such as phase separation and particle aggregation during mixing and processing [37].

After consolidation by traditional sintering, Table 2 displays the relative density and porosity of monolithic alumina and MWNT/ Al_2O_3 composites. The relative densities were discovered to be between 93% and 95%. It is implied that MWNTs encourage densification in these materials by the rise in relative density of MWNT/ Al_2O_3 composites with increasing carbon nanotube concentration. As expected, the relative density decreased with increasing Al_2O_3 content under the same sintering temperature and holding time. Additionally, sample A (pure) had larger particles than the other samples, which prevented the particles from fitting as well and

resulted in higher porosity in the compact. The enhanced sintering ability may be attributed to the efficient diffusion layer that connects the MWCNTs and the alumina grains. Depending on the sintering temperature, an aluminum oxy-carbide phase (Al-O-C interphase between MWNTs and Al_2O_3 grains) may form [38,39].

3.3. Mechanical Tests

Vickers hardness values for sintered samples are shown in Table 3. Despite variations in porosity, the compositions of the samples under investigation were in good agreement with Karandikar's measurements [40]. For ballistic applications, where it is anticipated that the projectile will be ruptured by the ballistic tile, the hardness attribute is crucial. The MWCNT particles in the Al_2O_3 matrix, as shown by the experimental results, enhanced the mechanical strength of the nanocomposite, as shown by the hardness and toughness results. The hardness and toughness of the nanocomposites were improved by adding up to 3 wt.% more MWCNT to the alumina matrix (Al_2O_3) [41]. A higher MWCNT cluster content in the nanocomposite structure may explain why exceeding this content did not significantly improve hardness and toughness [42].

TABLE 3. Vickers hardness of sintered compositions.

Compositions	HV
A	370.3
A3	763.8
A5	661.6

Table 4 presents the impact energy of the damaged core for each of the synthesized samples, revealing that sample A3 (3wt% MWCNTs) exhibited the highest average absorption energy compared to samples A (pure Al_2O_3) and A5 (5wt% MWCNTs).

TABLE 4. Impact energy (Kg.m)

Compositions	I.E (impact energy for all synthesized samples)
A	1.43
A3	1.94
A5	1.64

TABLE 5. Toughness (impact energy absorbed per unit damage area) (kg.m/cm^2)

Compositions	Toughness
A	1.4721
A3	2.08
A5	1.2632

The toughness values for the examined samples are shown in Table 5. The toughness and strength values of each composition varied. However, compared to composition samples A (pure) and A5, composition sample A3 showed nearly the greatest average values of toughness strength. Due to cracks and effective MWCNT dispersion in the Al_2O_3 matrix, the addition of carbon nanotube MWCNTs to the Al_2O_3 ceramic significantly improved its toughness and, consequently, Al_2O_3 matrix composites fracture toughness.

4. Conclusions

In this work, three commercial alumina compositions—designated A3, A5, and A—were examined as ballistic ceramics. These compositions consisted of Al_2O_3 with 3 wt.%, 5 wt.%, and 0 wt.% MWCNTs, respectively. Compositions were examined using X-ray diffraction (XRD), scanning electron microscope (SEM), and mechanical testing. Vickers hardness

measurements and the Charpy impact test were used to assess the toughness of the samples.

Among the compositions, A3 was selected for ballistic testing due to its superior hardness and toughness. The addition of MWCNTs significantly improved the mechanical properties of the A3 alumina nanocomposite by enhancing densification, inhibiting excessive grain growth, reinforcing the matrix, and increasing both hardness and fracture toughness. Among the investigated nanocomposites, the Al_2O_3 /3 wt.% MWCNT nanocomposite exhibited the lowest porosity, the smallest grain size, and the highest mechanical performance in terms of flexural strength and fracture toughness. It was also sintered at 1500 °C.

The conventional ceramic processing method used to fabricate alumina nanocomposites with 3 wt.% MWCNTs demonstrated significant potential for ballistic shielding applications.

References

- [1] Sharma, N., Saxena, T., Alam, S.N., Ray, B.C., Biswas, K., and Jha, S.K., *Mater. Today Commun.*, 31 (2022) 103764.
- [2] Ighodaro, O.L. and Okoli, O.I., *Int. J. Appl. Ceram. Technol.*, 5 (3) (2008) 313.
- [3] Rathinavel, S., Priyadarshini, K., and Panda, D., *Mater. Sci. Eng. B*, 268 (2021) 115095.
- [4] Fang, H., Gao, J.F., Wang, H.T., and Chen, C.S., *J. Memb. Sci.*, 403 (2012) 41.
- [5] Mondal, K., Nuñez III, L., Downey, C.M., and Van Rooyen, I.J., *Ind. Eng. Chem. Res.*, 60 (17) (2021) 6061.
- [6] Zuccarini, C., Ramachandran, K., Russo, S., Jayakody, Y.C., and Jayaseelan, D.D., *Int. J. Ceram. Eng. Sci.*, 5 (1) (2023) e10168.
- [7] Palmero, P., *Nanomaterials*, 5 (2) (2015) 656.
- [8] Heimann, R.B., "Classic and Advanced Ceramics: From Fundamentals to Applications". (John Wiley & Sons, 2010).
- [9] Gao, C., Feng, P., Peng, S., and Shuai, C., *Acta Biomater.*, 61 (2017) 1.
- [10] Mu, X. N. et al., *Mater. Sci. Eng. A*, 687 (2017) 164.
- [11] Thirugnanasabandam, A., Ramachandran, K., Mariadas, A., Jayaraman, J.T., Boddula, R., and Jagannathan, M., *Curr. Anal. Chem.*, 17 (6) (2021) 849.
- [12] Sharma, N., Syed, A.N., Ray, B.C., Yadav, S., and Biswas, K., *J. Asian Ceram. Soc.*, 7 (1) (2019) 1.
- [13] Cho, S. et al., *Compos. Part A Appl. Sci. Manuf.*, 139 (2020) 106138.
- [14] Chen, B., Kondoh, K., Umeda, J., Li, S., Jia, L., and Li, J., *J. Alloys Compd.*, 789 (2019) 25.
- [15] He, P. et al., *J. Alloys Compd.*, 819 (2020) 153009.
- [16] Vasiliev, A.L. and Padture, N.P., *Scr. Mater.*, 56 (6) (2007) 461.
- [17] Choudhary, M., Sharma, A., Aravind Raj, S., Sultan, M.T.H., Hui, D., and Shah, A.U.M., *Nanotechnol. Rev.*, 11 (1) (2022) 2632.
- [18] Cygan, T. et al., *Ceram. Int.*, 46 (6) (2020) 7170.
- [19] Silva, M.V., Stainer, D., Al-Qureshi, H.A., Montedo, O.R.K., and Hotza, D., *J. Ceram.*, 2014 (2014) 1.

- [20] Wei, T., Fan, Z., Luo, G., and Wei, F., *Mater. Lett.*, 62 (4–5) (2008) 641.
- [21] Zhu, Y., “Development of Alumina-based Ceramic Nanocomposites for Armour Applications”, (Loughborough University, 2017).
- [22] González-Velázquez, J.L., "Mechanical Behavior and Fracture of Engineering Materials", (Springer, 2020).
- [23] Cox, D.E., Moodenbaugh, A.E., Sleight, A.W., and Chen, H.Y., *Spec. Publ.*, 567 (1980) 189e201.
- [24] Sawada, H., *Mater. Res. Bull.*, 29 (2) (1994) 127.
- [25] Kondo, S., Tateishi, K., and Ishizawa, N., *Jpn. J. Appl. Phys.*, 47 (1S) (2008) 616.
- [26] Huang, L., Yao, W., Mukherjee, A.K., and Schoenung, J.M., *J. Am. Ceram. Soc.*, 95 (1) (2012) 379.
- [27] Ahmad, I. et al., *Compos. Sci. Technol.*, 70 (8) (2010) 1199.
- [28] Nasresfahani, M.R. and Shamanian, M., *J. Mater. Sci.*, 53 (15) (2018) 10812.
- [29] Sharma, N., Syed, A.N., Ray, B.C., Yadav, S., and Biswas, K., *J. Asian Ceram. Soc.*, 7 (1) (2019) 1.
- [31] Sharma, N., Saxena, T., Alam, S.N., Ray, B.C., Biswas, K., and Jha, S.K., *Mater. Today Commun.*, 31 (2022) 103764.
- [32] Liu, Y. et al., *Nanotechnol. Rev.*, 9 (1) (2020) 190.
- [33] Yang, Q., Kalathiparambil, K., Elg, D.T., Ruzic, D., and Kriven, W.M., *Acta Mater.*, 132 (2017) 479.
- [34] Krause, B. et al., *Carbon*, 48 (10) (2010) 2746.
- [35] Sharma, N., Syed, A.N., Ray, B.C., Yadav, S., and Biswas, K., *J. Asian Ceram. Soc.*, 7 (1) (2019) 1.
- [36] Hanzel, O. et al., *J. Eur. Ceram. Soc.*, 35 (5) (2015) 1559.
- [37] Sarkar, S. and Das, P.K., *Ceram. Int.*, 40 (2014) 7449.
- [38] Sarkar, S. and Das, P.K., *Mater. Chem. Phys.*, 137 (2012) 511.
- [39] Sheikh, S. et al., *Int. J. Ref. Metals. Hard Mater.*, 49 (2015) 153.
- [40] Heimann, “Classic and Advanced Ceramics: From Fundamentals to Applications”, (Wiley-VCH, New York, NY, USA, 2010).
- [41] Ramachandran, K. et al., *J. Mater. Res. Technol.*, 24 (2023) 6595.
- [42] Ghahramani, P., Behdinin, K., Moradi-Dastjerdi, R., and Naguib, H.E., *Nanotechnol. Rev.*, 11 (1) (2021) 55.

Application of the Matrix Mechanics Method to Solve the Schrodinger Equation of the Bottomonium System

Aissa Belhouari

National Higher School of Mathematics, Scientific and Technology Hub of Sidi Abdellah,
P.O. Box 75, Algiers 16093. Algeria.

Doi: <https://doi.org/10.47011/18.1.8>

Received on: 06/10/2023;

Accepted on: 27/11/2023

Abstract: The matrix mechanics technique [1, 2] was used to analyze the charmonium ($c\bar{c}$ bound state system) in our most recent study [3], and the results showed that it works admirably. In this paper, we attempt to solve the Schrödinger equation for the bottomonium system ($b\bar{b}$ bound state) using the same technique. The results (the masses of the various states and the associated radial wave function) are consistent with experimental and other theoretical results obtained using other methods.

Keywords: Quarkonium, Bottomonium, Non-relativistic potential models, Radial Schrodinger equation.

PACS: 14.40.Pq; 14.65.Fy; 12.39.Jh; 12.39.Pn.

1. Introduction

The term "quarkonium" often refers to a system made up of a heavy quark Q and an antiquark \bar{Q} linked together by a strong interaction. The term "quarkonium" originated from the similarity between the quarkonium

system and the positronium system (e^+e^- bound state). The gluon mediates the interaction between quarks just as the photon mediates the electromagnetic interaction between charged particles.

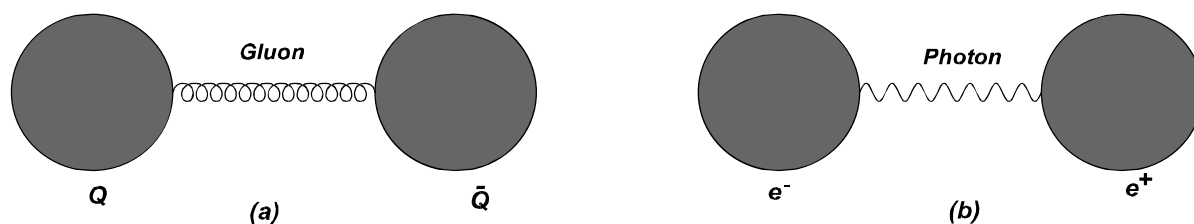


FIG. 1. (a) Strong interaction via one gluon exchange (quarkonium) and (b) electromagnetic interaction via one photon exchange (positronium)

Bottomonium is a quarkonium system made up of a bottom (b) and anti-bottom (\bar{b}) quark pair. A team at Fermilab made the first experimental observation of the first bottomonium state $Y(1S)$ (Epsilon) in 1977 [4].

The bottomonium states are produced in hadron colliders such as the Large Hadronic Collider (LHC) and Tevatron, as well as in leptonic colliders like e^+e^- colliders.

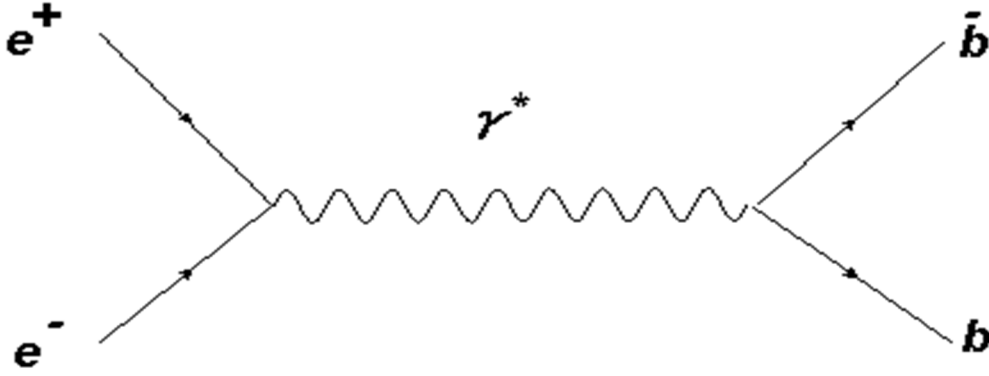


FIG. 2. Example of bottomonium production in an e^+e^- collider.

Because charm and bottom quarks have large masses, it was thought that the bound states of heavy quarks could be characterized by a non-relativistic potential model analogous to positronium [5]. The treatment within the context of non-relativistic quantum mechanics is based on the solution of the Schrödinger equation for the quarkonium system [6]. Numerov algorithm [7], shooting method [8], lattice QCD [9], and the Fourier grid Hamiltonian method [10] are just a few of the numerical methods that have been used to solve this equation. In this work, we use the matrix mechanics method. This method is briefly described in the subsequent section. For further details, see the Refs. [1] and [2].

2. Application of Matrix Mechanics Method to the Radial Schrodinger Equation

In quantum mechanics, the resolution of the equation consists of determining the energy levels and associated eigenfunctions $\psi_{nlm}(r, \theta, \varphi)$. The Hamiltonian exhibits spherical symmetry since the potential solely depends on the separation from the origin. The Schrödinger equation can, therefore, be written in terms of the common spherical coordinate system [11].

$$\Rightarrow \left[-\frac{\hbar^2}{2m} \frac{1}{r} \frac{\partial^2}{\partial r^2} r + \frac{L^2}{2mr^2} + V(r) \right] \psi_{nlm}(r, \theta, \varphi) = E_n \psi_{nlm}(r, \theta, \varphi) \quad (1)$$

where:

$$L^2 = -\hbar^2 \left[\frac{1}{\sin \theta} \frac{\partial}{\partial \theta} \left(\sin \theta \frac{\partial}{\partial \theta} \right) + \frac{1}{\sin^2 \theta} \frac{\partial^2}{\partial \varphi^2} \right] \quad (2)$$

is the modulus squared operator of the orbital angular momentum:

$$\vec{L} = \vec{r} \times \vec{p} = -i\hbar \vec{r} \times \vec{\nabla} \quad (3)$$

The standard approach to solving partial differential equations is the separation of variables. Here, we assume that the wave function is a product of two functions: one dependent on r (the radial part) and the other on θ and φ (the angular part)

$$\psi_{nlm}(r, \theta, \varphi) = R_{nl}(r) Y_l^m(\theta, \varphi) \quad (4)$$

The angular part $Y_l^m(\theta, \varphi)$ (the spherical harmonics) are the eigenfunctions of L^2 and L_z

$$L^2 Y_l^m(\theta, \varphi) = \hbar^2 l(l+1) Y_l^m(\theta, \varphi) \quad (5)$$

$$L_z Y_l^m(\theta, \varphi) = \hbar m Y_l^m(\theta, \varphi) \quad (6)$$

The three-dimensional problem is transformed into a one-dimensional radial equation [11]:

$$-\frac{\hbar^2}{2m} \frac{d^2}{dr^2} (r R_{nl}(r)) + \left[\frac{\hbar^2 l(l+1)}{2mr^2} + V(r) \right] (r R_{nl}(r)) = E_n (r R_{nl}(r)) \quad (7)$$

With $U_{nl}(r) = r R_{nl}(r)$ the equation becomes:

$$-\frac{\hbar^2}{2m} \frac{d^2 U_{nl}(r)}{dr^2} + V_{eff}(r) U_{nl}(r) = E_n U_{nl}(r) \quad (8)$$

where

$$V_{eff}(r) = V(r) + \frac{\hbar^2 l(l+1)}{2m r^2} \quad (9)$$

In Ref. [2], it is shown that the matrix mechanic method works perfectly for the problem of the hydrogen atom (a problem with central potential). The matrix mechanics method is based on choosing a simple set of basis states:

$$\psi_n(r) = \sqrt{\frac{2}{a}} \sin\left(\frac{n\pi r}{a}\right) \quad (10)$$

which are simply the eigenfunctions of the infinite potential well with eigenvalues:

$$E_n = \frac{\pi^2 \hbar^2 n^2}{2ma^2}; \quad n \geq 1 \quad (11)$$

The corresponding Hamiltonian is given by: where:

$$H_0 = -\frac{\hbar^2}{2m} \frac{d^2}{dr^2} + V_{inf}(r) \quad (12) \quad V_{inf}(r) = \begin{cases} 0 & \text{if } 0 < r < a \\ +\infty & \text{otherwise} \end{cases} \quad (13)$$

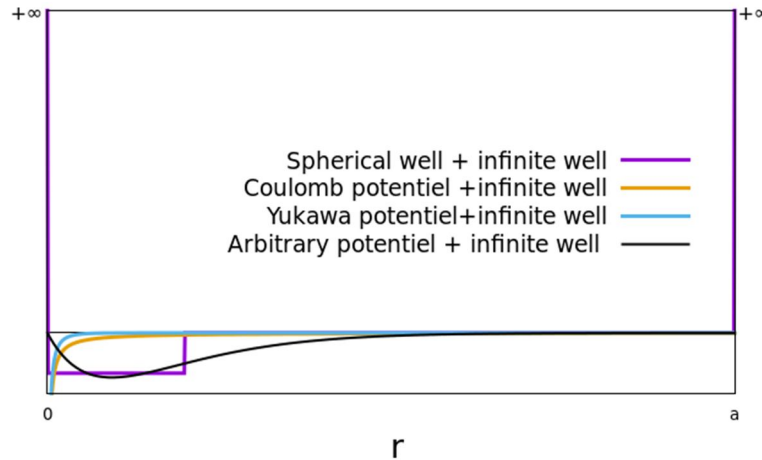


FIG. 3. Examples of potentials plotted along with the infinite square well “embedding” potential of width a .

The infinite well potential model describes a situation where a system is confined or trapped in a certain region. For example, this can represent a gas of molecules inside a container. The model of a particle in a one-dimensional infinite well is a reasonable approximation for an electron moving in a thin metal wire. The potential inside the wire is constant on average but rises sharply at each end.

By embedding the potential of the system in an infinite spherical well of width a , Eq. (8) becomes in the region $0 < r < a$.

$$\left(H_0 + \left[\frac{\hbar^2 l(l+1)}{2mr^2} + V(r) \right] \right) (U_{nl}(r)) = E_n U_{nl}(r) \quad (14)$$

The function $\psi_n(r) = \sqrt{\frac{2}{a}} \sin\left(\frac{n\pi r}{a}\right)$ is used to expand the radial function $U(r)$ and to construct the matrix H_{nm} of the Hamiltonian $H = H_0 + V_{eff}(r)$:

$$U(r) = \sum_n c_n \psi_n(r) \quad (15)$$

$$H_{nm} = \langle \psi_n | H | \psi_m \rangle \quad (16)$$

The eigenvalue problem in Eq. (14) becomes now:

$$\sum_{m=1}^{\infty} H_{nm} c_m = E c_n \quad (17)$$

Thus, the problem is transformed from a differential equation to a matrix form problem.

3. Application to the Bottomonium State

The $b\bar{b}$ system interacts via a central potential depending on the relative distance only, $V(|\vec{r}_1 - \vec{r}_2|) = V(r)$. In the center-of-mass system frame, this two-particle system problem is equivalent to a one-particle problem of mass $\mu = m_b/2$ (the reduced mass of the system) subject to the potential $V(r)$. As a consequence of the spherical symmetry, only the resolution of the radial equation is required in this case:

$$-\frac{\hbar^2}{2\mu} \frac{d^2 U_{nl}(r)}{dr^2} + V_{eff}(r) U_{nl}(r) = E_n U_{nl}(r) \quad (18)$$

Motivated by our results [3] and those of [2], we applied the matrix mechanics method to solve the radial equation of the bottomonium system. In this work, a non-relativistic potential model, known in the literature as the Song-Lin (SL) potential [12], is used:

$$V_{SL}(r) = -\frac{d}{\sqrt{r}} + b\sqrt{r}, \quad (19)$$

where d and b are parameters. The potential $V_{SL}(r)$ consists of an attractive Coulomb-like term plus a confining linear term. The Song-Lin potential has been theoretically derived from the fundamental features of Quantum Chromodynamics (QCD) [13]. In [14] and [15], it was pointed out that the SL potential exhibits a number of appealing features that make it a better model than the usual Cornell potential [16, 17]. Other types of potentials, such as the Hulthén-Hellmann potential [19] or the harmonic potential [20], have also been used.

The resolution of the radial Schrödinger equation is carried out following the same strategy used in [2], beginning by constructing the Hamiltonian matrix

H matrix with a specific dimension n_{\max} :

$$H_{nm} = \langle \psi_n | H | \psi_m \rangle = \langle \psi_n | H_0 | \psi_m \rangle + \langle \psi_n | V_{eff}(r) | \psi_m \rangle, \quad (20)$$

where the matrix element of H_0 is:

$$\langle \psi_n | H_0 | \psi_m \rangle = E_n^0 \delta_{nm} = \frac{\pi^2 \hbar^2 n^2}{2\mu a^2} \delta_{nm} \quad (21)$$

and the one of $V_{eff}(r)$ is expressed by the integral:

$$\langle \psi_n | V_{eff}(r) | \psi_m \rangle = \frac{2}{a} \int_0^a \sin\left(\frac{n\pi r}{a}\right) V_{eff}(r) \sin\left(\frac{m\pi r}{a}\right) dr \quad (22)$$

Where, in our case:

$$V_{eff}(r) = V_{SL}(r) + \frac{\hbar^2}{2\mu} \frac{l(l+1)}{r^2} \quad (23)$$

is composed of the SL potential term $V_{SL}(r)$ plus the centrifugal term. Using the useful trigonometric relation $\sin(\theta) \sin(\varphi) = \frac{1}{2}(\cos(\theta - \varphi) - \cos(\theta + \varphi))$ with the change of variable $= \frac{r}{a}$, one can write the integral:

$$\int_0^a \sin\left(\frac{n\pi r}{a}\right) V_{eff}(r) \sin\left(\frac{m\pi r}{a}\right) dr = \{(L_1(n+m) - L_1(n-m)) + (L_2(n+m) - L_2(n-m))\} \quad (24)$$

where:

$$L_1(k) = \frac{\hbar^2 l(l+1)}{4\mu a} \int_0^1 \frac{(1 - \cos(k\pi x))}{x^2} dx \quad (25)$$

$$L_2(k) = \frac{a}{2} \int_0^1 V_{SL}(ax) (1 - \cos(k\pi x)) dx \quad (26)$$

Once the matrix H of dimension $n_{\max} \times n_{\max}$ is constructed, it is diagonalized to obtain the eigenvalues and the corresponding wavefunctions.

4. Results and Analysis

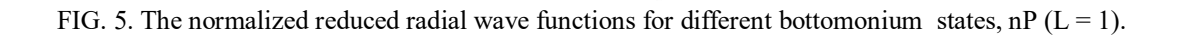
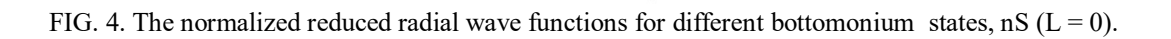
In this work, we use the same potential parameters as those in Ref. [21]: $d = -0.7011 \text{ GeV}^{3/2}$ (denoted as “a” in Ref. [21], while “a” in this work refers to the width of the infinite square well), $b = 0.8912 \text{ GeV}^{1/2}$, and $m_b = 4.668 \text{ GeV}$ to compare the results. We adopted the natural energy units in the problem, with $\hbar = c = 1$.

We numerically computed the integrals after changing the variable to $x = r/a$. The matrix H was then diagonalized using the Jacobi routine [22] (see the corresponding Fortran code in the Appendix). The mass spectra $M_{b\bar{b}}$ of the bottomonium system are related to the eigenvalue E by the relation: $M_{b\bar{b}} = E + 2m_b$. Table 1 displays the results of our calculation for the mass spectra of the bottomonium system (column 2) using an infinite square well width of $a = 5 \text{ fermi}$ and $n_{\max} = 300$. The states (first column) are denoted by the spectroscopic notation (nL), where L is the total orbital angular momentum $\vec{L} = \vec{L}_b + \vec{L}_{\bar{b}}$ of the $b\bar{b}$ system. The integer n is the principal quantum number corresponding to the different bottomonium states.

Our results in column 2 are compared with theoretical results in Refs. [21] and [23] (columns 3 and 4), as well as with experimental values (last column). The normalized reduced radial wave functions $U_{nl}(r)$ for different bottomonium states nS ($L = 0$), nP ($L = 1$), and nD ($L = 2$) for $n = 1, 2, 3, 4, 5$ are illustrated in Figs. 4, 5, and 6, respectively.

TABLE 1. Results of the bottomonium mass spectra (our numbers are rounded to 5 digits)

State nL	Our results	Results of Ref. [21]	Results of Ref. [23]	Experimental results [24]
1S	9.4390	9.444	9.473	9.444
2S	10.095	10.098	10.024	10.023
3S	10.480	10.482	10.327	10.355
4S	10.765	10.766	10.593	10.579
5S	10.997	10.998	10.788	10.865
1P	9.9308	9.930	9.912	9.900
2P	10.359	10.358	10.275	9.900
3P	10.666	10.665	10.580	-----
4P	10.912	10.911	10.703	-----
5P	11.120	11.119	-----	-----
1D	10.235	10.234	10.156	10.161
2D	10.566	10.565	10.434	-----
3D	10.826	10.825	10.625	-----
4D	11.044	11.043	-----	-----
5D	11.233	11.232	-----	-----



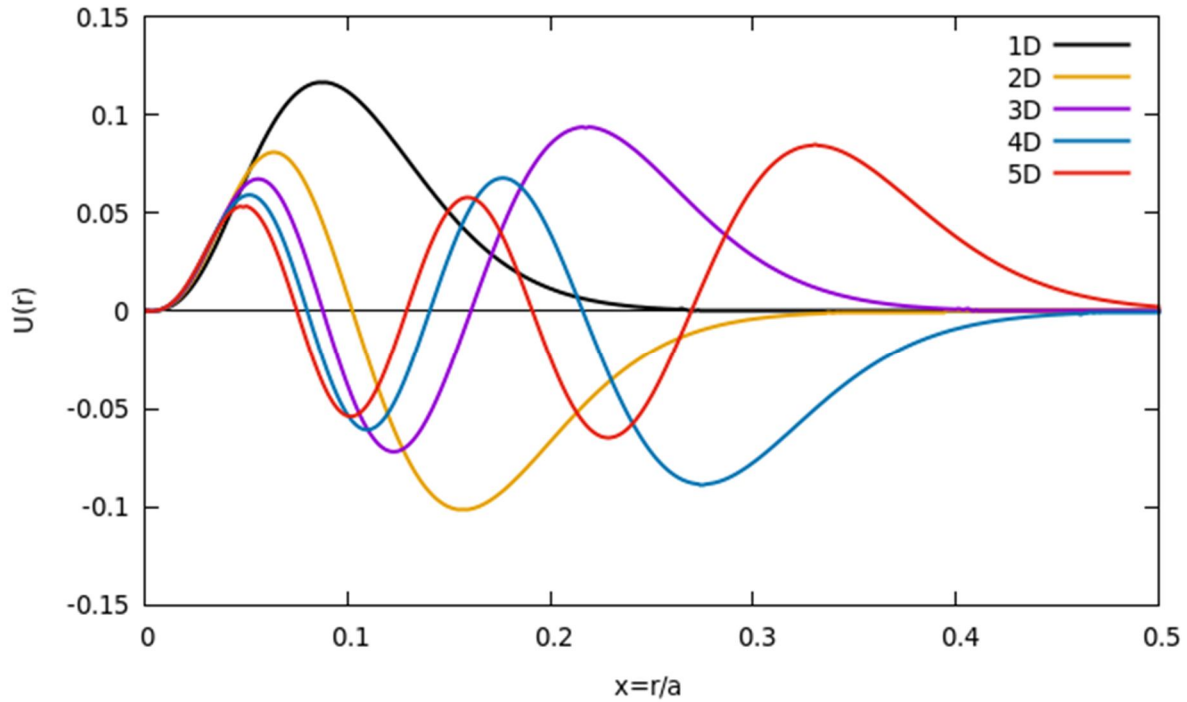


FIG. 6. The normalized reduced radial wave functions for different bottomonium states, nD ($L = 2$).

5. Conclusion

In the present work, the quarkonium systems have been treated in a non-relativistic framework by solving the corresponding Schrödinger equation. The potential models have a simple form that correctly describes the overall properties of quark-antiquark pairs. Our numerical strategy relies on the matrix mechanics method to compute the full mass spectra and the associated wave functions. This method is based on a specific choice of the basis state vectors in the Hilbert space of the system.

In this paper, we compare our approach with two distinct techniques. We observe that the results are in good agreement with those of [21], where the Numerov method algorithm was used to solve the radial equation, yielding satisfactory agreement with experiments [24]. The agreement is also strong with the results obtained using the asymptotic iteration method [23]. This work serves as the first step toward more complex studies in the near future.

Appendix: Fortran Code

This is the main program of the Fortran code, written in Fortran 90 and compiled with the gfortran compiler under Linux Ubuntu. Lines preceded by “!” are comments intended to clarify the program.

```

IMPLICIT NONE
INTEGER, PARAMETER:: np=300!np should be greater or equal to Nmax
INTEGER:: i,n,m,Nmax,j, nrot,leveln
DOUBLE PRECISION, DIMENSION(np):: d
DOUBLE PRECISION, DIMENSION(0:10000):: x
DOUBLE PRECISION, DIMENSION(np,np)::
s1,s3,s4, sum1,sum2 sum3,sum4 DOUBLE
PRECISION, DIMENSION(np,np)::
delta,integral,a,v
DOUBLE PRECISION:: pi, mb, pas, aa, L1_0,
L2_0, L3_0, factor, L
DOUBLE PRECISION:: L1,L2
INTEGER, PARAMETER:: nbrpt=1000
!number of point used in the !integration
COMMON /DATA/aa,pi,mb,L
pi=3.141592653d0
mb=4.668d0 !MASSE OF THE BOTTOM QUARK
!INPUTS Nmax: H DIMENSION, aa: VALUE OF THE DEPTH a IN FERMI, !L: ORBITAL MOMENTUM,
READ(*,*) Nmax,aa,L
factor=5.076142132d0 !CONVERSION FACTOR: from fermi to Gev-1 unit
aa=factor*aa ! aa=a the VALUE OF THE DEPTH OF THE INFINITE SQUARE WELL
!STARTING CONTRUCTING Hnm
DO n=1,Nmax
DO m=1,Nmax
IF(n/=m) THEN

```

```

delta(n,m)=0.0d0
ELSE
delta(n,m)=(pi*n/aa)**2/mb +2*mb ! E^0 +2mb
END IF
!COMPUTATION OF THE INTEGRANDS AT
THE PROBLEMATIC POINT r=0
x(0)=0.0d0
pas=1.d0/nbrpt
x(1)=0.0d0+pas
L2_0=0.0d0
L1_0=2*n*m*pi**2/(mb*aa)
L3_0=0.0d0
s1(n,m)=s1(n,m)+(L2(x(1),n+m)+L2_0)*pas/2.
s2(n,m)=s2(n,m)+(L2(x(1),n-m)+L2_0)*pas/2.
s3(n,m)=s3(n,m)+(L1(x(1),n+m)+L1_0)*pas/2.
s4(n,m)=s4(n,m)+(L1(x(1),n-m)+L1_0)*pas/2.
s5(n,m)=s5(n,m)+(L3(x(1),n+m)+L3_0)*pas/2.
s6(n,m)=s6(n,m)+(L3(x(1),n-m)+L3_0)*pas/2.
!STARTING INTEGRATION FROM x(2) to
x(n)=1
DO i=2,nbrpt
x(i)=x(0)+i*pas
!CENTRIFUGAL TERM
s1(n,m)=s1(n,m)+(L1(x(i),n+m)+L1(x(i-1),n+m))*pas/2.
s2(n,m)=s2(n,m)+(L1(x(i),n-m)+L1(x(i-1),n-m))*pas/2.
!COULOMB LIKE ATTRACTIVE TERM +
LINEAR TERM (SL potential)
s3(n,m)=s3(n,m)+(L2(x(i),n+m)+L2(x(i-1),n+m))*pas/2.
s4(n,m)=s4(n,m)+(L2(x(i),n-m)+L2(x(i-1),n-m))*pas/2.
END DO
END DO
END DO
!COMPUTING Li(n+m)-Li(n-m) i=1,2
sum1=s1-s2
sum2=s3-s4
!COMPUTING {L1(n+m)-L1(n-m)}+{L2(n+m)-L2(n-m)}
integral=(2./aa)*(sum1+sum2)
!HAMILTONIAN MATRIX a(n,m)=H(n,m)
a=delta+integral
!DIAGONALIZATION
n=Nmax
CALL jacobi(a,n,np,d,v,nrot)
CALL eigsrt(d,v,n,np)
! NUMBER OF THE LEVELS TO PRINT THE
MASS VALUE
nlevel=5
DO j=0, nlevel
WRITE(*,*) 'level', j, ' ', 'mass', d(nmax-j)
ENDDO

```

```

END
! STARTING COMPUTING THE VALUES OF
THE RADIALE FUNCTION U(R)
open(3,file='values_of_u1_0.txt',status='new')
open(4,file='values_of_u2_0.txt',status='new')
open(5,file='values_of_u3_0.txt',status='new')
open(6,file='values_of_u4_0.txt',status='new')
open(7,file='values_of_u5_0.txt',status='new')
do i=1,nbrpt
u(1,i)=0.d0
u(2,i)=0.d0
u(3,i)=0.d0
u(4,i)=0.d0
u(5,i)=0.d0
do m=1,Nmax
u(1,i)=u(1,i)+dsqrt(2.d0)*dsin(m*pi*x(i))*v(m,nmax)
u(2,i)=u(2,i)+dsqrt(2.d0)*dsin(m*pi*x(i))*v(m,nmax-1)
u(3,i)=u(3,i)+sqrt(2.d0)*dsin(m*pi*x(i))*v(m,nmax-2)
u(4,i)=u(4,i)+dsqrt(2.d0)*dsin(m*pi*x(i))*v(m,nmax-3)
u(5,i)=u(5,i)+sqrt(2.d0)*dsin(m*pi*x(i))*v(m,nmax-4)
enddo
enddo
norme1=0.d0
norme2=0.d0
norme3=0.d0
norme4=0.d0
norme5=0.d0
do i=1,nbrpt
norme1=norme1+u(1,i)**2
norme2=norme2+u(2,i)**2
norme3=norme3+u(3,i)**2
norme4=norme4+u(4,i)**2
norme5=norme5+u(5,i)**2
enddo
do i=1,nbrpt
write(3,*) x(i),u(1,i)/dsqrt(norme1)
write(4,*) x(i),u(2,i)/dsqrt(norme2)
write(5,*) x(i),u(3,i)/dsqrt(norme3)
write(6,*) x(i),u(4,i)/dsqrt(norme4)
write(7,*) x(i),u(5,i)/dsqrt(norme5)
enddo
! THIS FUNCTION COMPUTES THE
INTEGRAND OF THE CENTRIFUGAL TERM
DOUBLE PRECISION FUNCTION L1(x,k)
INTEGER k
DOUBLE PRECISION pi,aa,mb,x,L
COMMON /DATA/aa,pi,mb,L
L1=(1*(1+1)/mb)*(1-dcos(k*pi*x))/(2.*aa*x**2)
RETURN

```

```

END FUNCTION
! THIS FUNCTION COMPUTES THE
INTEGRAND OF THE COULOMBIEN LIKE
!TERM+LINEAR CONFINING TERM (SL
POTENTIEL)
DOUBLE PRECISION FUNCTION L2(x,k)
INTEGER k
DOUBLE PRECISION x,pi,mb,aa,b,L
COMMON /DATA/aa,pi,mb,L
a1=-0.7011d0
b=0.8912d0
L2=(1-
dcos(k*pi*x))*(a1*dsqrt(aa)/dsqrt(x)+(aa*dsqrt(
aa))*b*dsqrt(x))/2

```

```

RETURN
END FUNCTION

```

6. Acknowledgments

The author would like to thank the Theoretical Physics Group at CERN (Centre Européen de Recherche Nucléaire) in Geneva, Switzerland, and the High Energy Physics and Cosmology Division at ICTP (International Center of Theoretical Physics) in Trieste, Italy, for their help and warm hospitality during my visits.

References

- [1] Marsiglio, F., Am. J. Phys., 77 (2009) 253.
- [2] Jugdutt, B.A. and Marsiglio, F., Am. J. Phys., 81 (2013) 343.
- [3] Belhouari, A., Am. J. Phys., 91 (2023) 34.
- [4] Herb, S.W. et al., Phys. Rev. Lett., 39 (1977) 252.
- [5] Lucha, W. and Schoberl., F.F., HEPHY/PUB-527., UWThPh (1989) 71.
- [6] Quigg, C. and Rosner, J.L., Phys. Rep., 56 (4) (1979) 167.
- [7] Segovia, J., Yasser, A.M., Entem, D.R., and Fernandez, F., Phys. Rev. D, 78 (114033) (2008) 1.
- [8] Pillai, M., Goglio, J., and Walker, T.G., Am. J. Phys., 80 (2012) 1017.
- [9] Killingbeck, J., J. Phys. A: Math. Gen., 20 (1987) 1411.
- [10] Marston, C.C. and Balint-Kurti, G.G., J. Chem. Phys., 91 (6) (1989) 3571.
- [11] Griffiths, D.J., "Introduction to Quantum Mechanics", (Pearson Education, 1995).
- [12] Song, X. and Lin, H., Z. Phys. C, 34 (1987) 223.
- [13] Chabab, M. and Sanhaji, L., Int. J. Mod. Phys. A, 20 (2005) 1863.
- [14] Wang, J.Z., Qian, R.Q., Liu, X. and Matsuki, T., Phys. Rev. D, 101 (2020) 034001.
- [15] Bazavov, A. and Weber, J.H., Prog. Part. Nucl. Phys., 116 (2021) 103823.
- [16] Eichten, E., Gottfried, K., Kinoshita, T., Lane, K., and Yan, T.-M., Phys. Rev. D, 17 3090 (1978).
- [17] Sonia, N.R., Joshi, B.R., Shah, R.P., Chauhan, H.R., and Pandya, J.N., Eur. Phys. J. C, 78 (2018) 592.
- [18] Al-Jamel, A., Mod. Phys. Lett. A, 34 (37) (2018).
- [19] Akpan, I.O., Inyang, E.P., Inyang, E.P., and William, E.S., Rev. Mex. Fis., 67 (1) (2021).
- [20] Cuervo-Reyes, E., Rigol, M., and Rubayo-Soneira, J., Rev. Bras. Ensino Fis., 25 (1) (2003).
- [21] Manzoor, R., Ahmed, J., and Raya, A., Rev. Mex. Fis., 67 (1) (2021) 33.
- [22] Press, W.H., Flannery, B.P., Teukolsky, S.A., and Vetterling, W.T., "Numerical Recipes: The Art of Scientific Computing", (Cambridge University Press, Cambridge, 1986).
- [23] Mutuk, H., Can. J. Phys., 97 (2019) 1342.
- [24] Workman, R.L. et al. (Particle Data Group), Prog. Theor. Exp. Phys., 2022 (2022) 083C01.

Performance of a Thin Layer of Plastic Scintillator Material to be Used as a Charged Particle Detector Using Geant4

K. Al-Khasawneh^a, B. Brückner^b, P. Erbacher^b, S. Fiebiger^b, K. Göbel^b, T. Heftrich^b, Kisselbach^b, D. Kurtulgil^b, C. Langer^b, M. Reich^b, R. Reifarth^b, M. Volknandt^b and M. Weigand^b

^a Jordan Atomic Energy Commission, Jordan Research and Training Reactor (JRTR), Amman, Jordan.

^b Goethe University Frankfurt, Frankfurt, Germany.

Doi: <https://doi.org/10.47011/18.1.9>

Received on: 11/10/2023;

Accepted on: 02/01/2024

Abstract: The performance of a thin layer of plastic scintillator is investigated for use as a charged particle detector in various applications, including neutron-induced reactions with a charged particle in the exit channel. The detection efficiency for alpha particles and background radiation, including γ -radiation, electrons, and neutrons, was investigated using the Geant4 simulation toolkit. The results show that a thin layer of plastic scintillator can measure the alpha particles with a high efficiency of 50% for isotropic sources while keeping background radiation (with a very low detection efficiency) below 10%.

Keywords: Plastic Scintillator, Alpha interaction, gamma interaction.

Introduction

In the field of astrophysics, two complementary methods are extensively employed as a means of studying neutron-induced reactions with charged particles in the exit channel (n,z) reaction, the time-of-flight (ToF), and the neutron activation technique. The ToF technique is characterized by low values of neutron flux at the sample position because of the relatively long distances, typically several meters, between the neutron production target and the sample position [1.]. On the contrary, in the neutron activation technique, the sample is very close to the neutron production target and is characterized by a high neutron flux [2]. Therefore, detectors used to measure charged particles in such experiments should meet specific requirements, including high detection limits for the charged particle radiations and low detection limits for background radiation such as γ -radiation, electrons, and neutrons.

In the last few decades, gas ionization chambers have widely been used for the cross-section measurement of neutron-induced charged particle reactions [3]. The merit of this choice is the low sensitivity of these chambers to neutron radiation, which makes the counting process possible in the presence of the neutron beam. In addition, ionization chambers have the advantage of high detection efficiency. However, such detectors are difficult to operate, and the gas must be recycled to maintain the purity of the detection medium. Silicon detectors have also been investigated for (n,z) measurements. Unlike the ionization chambers, silicon detectors are very sensitive to neutron radiation and must be operated outside the neutron beam [8].

The scope of this work is to computationally test the performance of a thin layer of plastic scintillator material as a charged particle detector

in an environment full of background radiation, including gamma, electrons, and neutrons. The goal is to understand its operational behavior and optimize the scintillator dimensions according to experimental conditions. In this regard, a computer simulation model based on the Geant4 simulation package (version 10.3.0) was developed and employed to investigate the energy deposition spectra for alpha particles, gamma radiation, electrons, and neutrons. This simulation was performed for different initial kinetic energies and different scintillator material thicknesses.

Geant4 Simulation Overview

Geant4 (GEometry AND Tracking) is a multi-purpose object-oriented simulation toolkit developed at CERN [9]. It is used to accurately simulate particle interactions with matter across a very wide energy range using Monte Carlo methods. Nowadays, it is widely used to study the response of detectors for ionizing radiation, efficiency calculations, and radiation damage. All aspects of the simulation process are included in the toolkit, including geometry of the system, materials involved, fundamental

particles of interest, generation of primary events, tracking of particles through materials and electromagnetic fields, physics processes governing particle interactions, response of sensitive detector components, generation of event data, storage of events and tracks, visualization of the detector and particle trajectories, and analysis of simulation data at different levels of detail and refinement [10].

Figure 1 shows the information flow of the simulation developed for this work. The simulation started by defining the geometry, which in this study was composed of a primary mother volume called “world” that included all the components that the simulation had to consider. The world’s shape was a cube with 20 m sides. To simulate realistic conditions, the “air” material, as recommended by the U.S. National Institute of Standards and Technologies (NIST) libraries, was assigned as the world material [11]. Inside the world volume, the detector volume was defined, which was a simple parallel rectangular plastic scintillator plate.

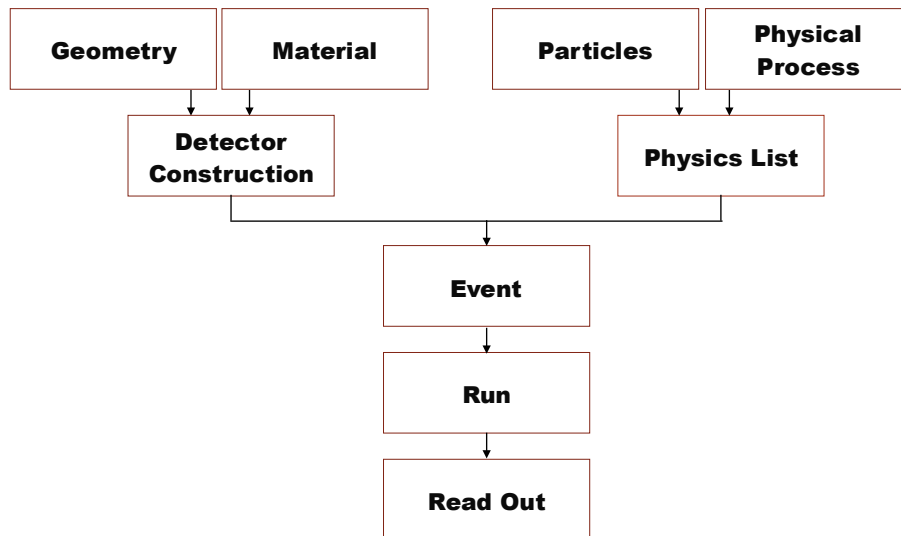


FIG. 1. Workflow diagram of the simulation program implemented in this work.

The plate had dimensions of $26 \times 7 \text{ cm}^2$ surface area in the YZ-plane. At this stage, for comparison, different scintillator thicknesses in the X-direction were defined. The plastic scintillator material composition was determined based on its atomic number and density values. The compositions of the different materials used are summarized in Table 1.

Implementation of the primary particle generator was achieved through the use of the

G4GeneralParticleSource (GPS) [12], which generates a particle beam by specifying its type, position, kinetic energy, and angular distribution. In this study, a point source with an isotropic distribution was created (see Table 1). The source was positioned at the center of the world volume, in direct contact with the scintillator volume (i.e., the distance between the point source and the scintillator plate surface was approximately 0 cm).

The physical processes considered in this simulation were the electromagnetic interactions governing energy loss for primary particles,

including photons, electrons, positrons, and other charged particles.

TABLE 1. Composition and densities of the different materials used in these simulations. All particle types, shapes, and angular distributions are also given.

Geometry	Volume	Material	Composition	Density [mg/cm ³]
	World	Air	N (79%) O (21%)	1.290
	Scintillator	Polyvinyltolunene	C (91.5%) H (8.5%)	1.032
Generalized Particle Source (GPS)	Particle	Type	Angular Distribution	
	Alpha	Point	Isotropic	
	Gamma	Point	Isotropic	
	Electrons	Point	Isotropic	

Geant4 provides many models for electromagnetic physical processes [13]. This simulation focused on the energy deposition of charged particles, gamma radiation, and neutrons, where a significant amount of low-energy secondary electrons are expected. The Low Energy EM package was used, as it is optimized for electrons with energies below 250 eV [14]. Once the geometry and the primary particle generator were created, the simulation was executed. In the Geant4 structure, each “run” contains a specific number of “events” that share the same geometry, physics list, and particle generator settings. Each event is composed of one or more primary particles. Once these primary particles enter the detector geometry, they undergo various interactions, generating secondary particles. All particles, both primary and secondary, were tracked within the detector volume until they either decayed, stopped, or exited the world volume. The energy deposition at each step was recorded, and only the total energy deposition in the detector volume at the end of each event was stored using the `GetTotalEnergyDeposit()` method.

It is worth pointing out that this simulation considered only total energy deposition without incorporating optical processes related to scintillation effects. As a result, in practical experiments, some discrepancies may arise between the experimentally measured detection efficiency and the absorption efficiency calculated in this study. These variations are primarily due to statistical fluctuations in light production and transmission, photo-multiplication, and electronic pulse processing.

Material Sensitivity to Alpha Particles

Using the described simulation model, the scintillator material’s response to a beam of alpha particles was explored. For this purpose, the alpha range in the scintillator material and its full peak absorption efficiency were calculated. A prior analysis of the energy deposition spectrum produced by a beam of alpha particles is crucial to verify the reliability and validity of the physical processes implemented in the simulation and to emphasize the understanding of the energy deposition mechanism in the scintillator material.

A beam of alpha particles was emitted isotropically toward the center of a bare scintillator foil. Each alpha particle entering the scintillator undergoes simultaneous interactions with numerous orbital electrons, leading to ionization or excitation. As a result of these interactions, the particle gradually slows down and eventually comes to a stop.

Depending on the initial energy of the alpha particle, a large number of secondary electrons are generated with relatively low energies (≈ 0.25 keV). These secondary electrons undergo multiple scatterings within the scintillator volume. If all secondary electrons deposit their energy within the scintillator, the full energy of the alpha particle is deposited. However, some electrons may escape the scintillator and deposit their energy in the surrounding air, resulting in an energy deposition lower than the initial incident energy. Conversely, alpha particles originating in the air also undergo multiple scatterings due to interactions with air

molecules. As a result, a significant fraction of secondary electrons successfully deposit energy within the scintillator body.

This behavior is illustrated in Fig. 2, which presents the energy deposition spectrum of a mono-energetic beam consisting of 10^9 alpha particles. The initial energy was set to 1000 keV, and the scintillator thickness was 1 mm.

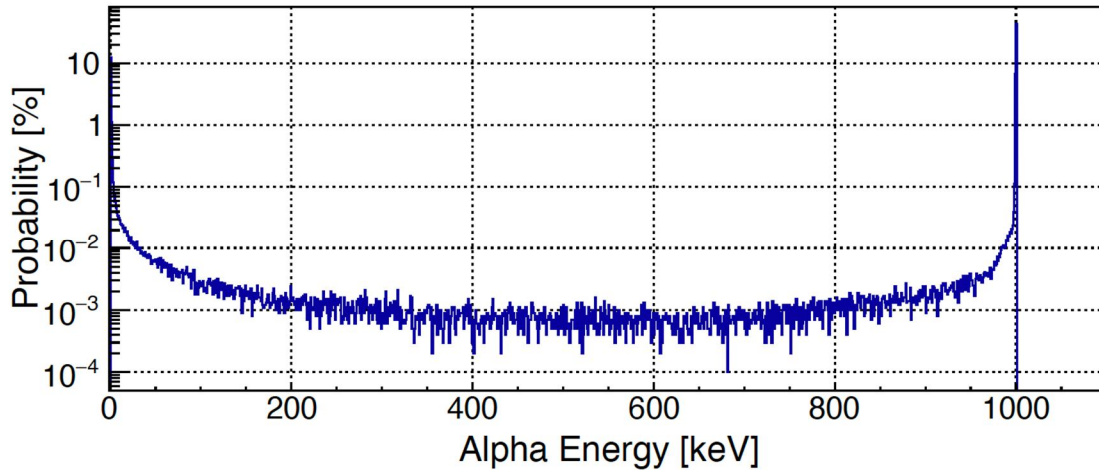


FIG. 2. Geant4-simulation of the energy deposition spectrum for a beam of 1 MeV α -particles in a 1 mm thick plastic scintillator.

Next, the proper scintillator thickness that optimizes full peak absorption efficiency was investigated. The full peak absorption efficiency is defined as the probability that an alpha particle deposits all of its initial energy in the scintillator body. For instance, an alpha particle with an initial energy of ≈ 5.5 MeV (Amaracium-241 and Polonium-210) was measured. Therefore, the alpha energy of the isotropic point source defined earlier was set to 5500 keV. This step was repeated for different scintillator thicknesses.

The full peak absorption efficiency (ϵ_α) was calculated as the ratio of the number of alpha events recorded under the full energy peak to the total number of alpha events originally emitted

from the isotropic source, as expressed by the equation:

$$\epsilon_\alpha = \frac{\text{Number of events under the full energy peak}}{\text{Total Number of events emitted from the source}} \quad (1)$$

Figure 3 shows the full peak absorption efficiency as a function of scintillator thickness. As the material thickness increases, the probability of complete energy deposition also rises, leading to higher efficiency. However, this increasing trend ceases when the scintillator thickness reaches the range of alpha particles (in this example = 40 μm). At this thickness, a maximum efficiency of 50% is achieved for an isotropic source. Any further increase in scintillator thickness does not improve efficiency.

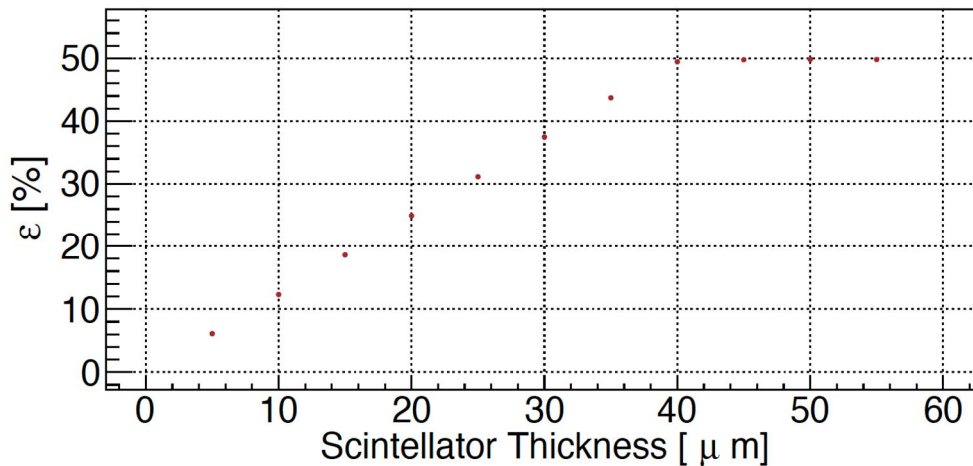


FIG. 3. Full peak absorption efficiency for a 5.5 MeV alpha particle in a scintillator material for different material thicknesses.

To determine the alpha particle's range in the scintillator material, the isotropic point source was replaced with a point source that emitted alpha particles in the scintillator direction. This was achieved using the G4GeneralParticleSource by setting the beam direction of the point source as *gps/direction 1 0 0*. This means that all the emitted particles are focused on the X-axis. Each alpha particle was tracked within the scintillator volume with a step-size of 200 nm.

During the tracking process, a production cut of 0.5 μm was implemented, meaning that once an alpha particle energy reached a value where the produced secondary particles had ranges shorter than 0.5 μm , the tracking process was terminated, and the remaining kinetic energy was deposited locally. For each event, the final stopping position (X, Y, Z) within the scintillator volume was recorded. The range value was

determined as the distance between its starting and stopping points along the shooting direction (X-direction).

In low-energy nuclear physics, alpha particle energies typically fall within the multi-MeV range. Therefore, the range calculation was performed for initial alpha energies from 1 to 7 MeV in steps of 0.5 MeV.

Table 2 presents the calculated range values for different initial alpha particle energies, comparing them with values obtained from SRIM [15]. A typical relative error of $\sim 10\%$ was observed, attributed to the different computational approaches used in SRIM and Geant4. While SRIM employs a semi-empirical model based on interaction probabilities, Geant4 utilizes interaction cross-sections derived from direct measurements or extrapolations [9, 15].

TABLE 2. The range of an alpha particle values in the scintillator material as measured using Geant4. Values obtained from SRIM are also listed.

Alpha Energy [keV]	Range [μm]	
	Geant4	SRIM
1000	4.52	4.91
1500	6.78	7.28
2000	9.46	10.02
2500	12.56	13.15
3000	16.08	16.67
3500	20.01	20.58
4000	24.35	24.87
4500	29.10	29.54
5000	34.23	34.59
5500	39.77	40.02
6000	45.70	45.83
6500	52.00	52.01
7000	58.68	58.55

Material Sensitivity to Gamma Radiation

Due to the low effective atomic number and density of plastic scintillator material, the photoelectric effect mechanism for thin layers is not probable. Here, Compton scattering is the dominant interaction mechanism. Additionally, for layers thinner than 1 mm, the multiple scattering process is negligible, and energy deposition is due to single Compton scattering.

In Compton scattering, the produced electrons have relative energies higher than those produced by alpha particles. For instance, a 1 MeV photon produces a single electron with a

maximum energy of ≈ 0.79 MeV (scattering angle = π). The range of such a high secondary electron is several orders of magnitude greater than the thickness of a thin scintillator material, making the full energy deposition improbable.

To study the effect of the material thickness on the energy deposition spectrum, an isotropic beam of monoenergetic gamma radiation of 1 MeV was directed toward the center of the scintillator. Figure 4 illustrates the energy deposition spectra for three different scintillator thicknesses: 0.04, 0.1, and 1 mm. The optimal thickness for measuring alpha particles of ≈ 5.5 MeV was determined to be 0.04 mm.

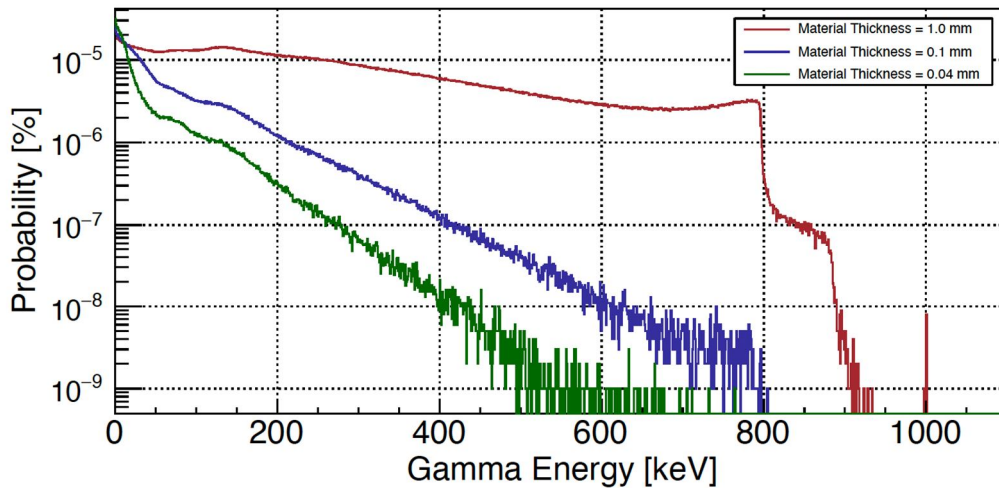


FIG. 4. Geant4 simulation of the energy deposition spectrum from a gamma radiation beam in a scintillator material with thicknesses of 1, 0.1, and 0.04 mm.

The photo-peak was observed only with a 1 mm scintillator thickness, with a very low probability (0.001 %). For thinner materials, the continuous Compton spectrum is the only distinguishing feature. The total energy deposition by secondary electrons depends on the material thickness. If the scintillator's dimensions exceed the range of the secondary electrons, these electrons will deposit their full energy within the scintillator. Otherwise, only partial energy deposition will occur.

The probability of a gamma event resulting in full or partial energy deposition within the scintillator was also examined. The simulation was conducted over an energy range of 100-2000 keV, with a step of 100 keV, for three different material thicknesses: 1, 0.1, and 0.04 mm. The total absorption efficiency for a given energy (ϵ_γ) was calculated as the ratio of the total number of gamma events under the full spectrum

to the total number of gamma events initially emitted from the isotropic source:

$$\epsilon_\gamma = \frac{\text{Total of events under the full spectrum}}{\text{Total Number of events emitted from the isotropic source}} \quad (2)$$

Based on this calculation, the total absorption efficiency of the gamma radiation beam is shown in Fig. 5. The first notable observation is that the total absorption efficiency is relatively low, remaining below 5%. For instance, a scintillator with a 1 mm thickness achieves an efficiency of approximately 3% for low-energy gamma rays ($E = 100$ keV), which sharply decreases at higher gamma energies. For a given gamma energy, total absorption efficiency strongly depends on the material thickness, with thinner materials exhibiting significantly lower absorption efficiency. For example, the total absorption efficiency for 1 MeV gamma rays was calculated to be 1.7%, 0.26%, and 0.12% for material thicknesses of 1, 0.1, and 0.04 mm, respectively.

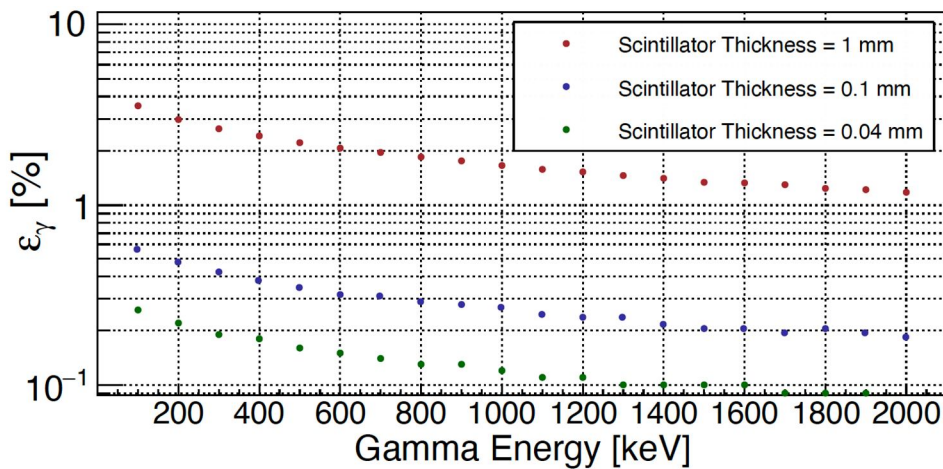


FIG. 5. Total absorption efficiency of a gamma radiation beam.

Material Sensitivity to Electrons

When electrons enter the scintillator body, they undergo elastic and inelastic scatterings with orbital electrons. As a result of these interactions, electrons lose energy and change direction. The probability of either partial or full energy deposition in the scintillator body is a function of both the electron energy and the scintillator dimensions.

To verify the effect of material thickness on total energy deposition, an isotropic beam of monoenergetic electrons was used. In this example, the initial energy was set to 389 keV (the most probable energy in the ^{210}Bi beta spectrum). The simulation was performed for

three different scintillator thicknesses: 1, 0.1, and 0.04 mm.

Figure 6 presents the energy deposition spectrum. Due to multiple scattering processes within the scintillator (including surface interactions), the probability of electrons depositing their full energy is low. In this example, for a 1 mm thick scintillator, the probability of full energy deposition is approximately 30%. However, as the material thickness decreases, the deposited energy significantly decreases: for 0.1 mm thickness, the probability drops to 0.78%, and for 0.04 mm thickness, it further reduces to 0.07%. In thinner materials, electrons are more likely to undergo partial energy deposition before escaping the scintillator.

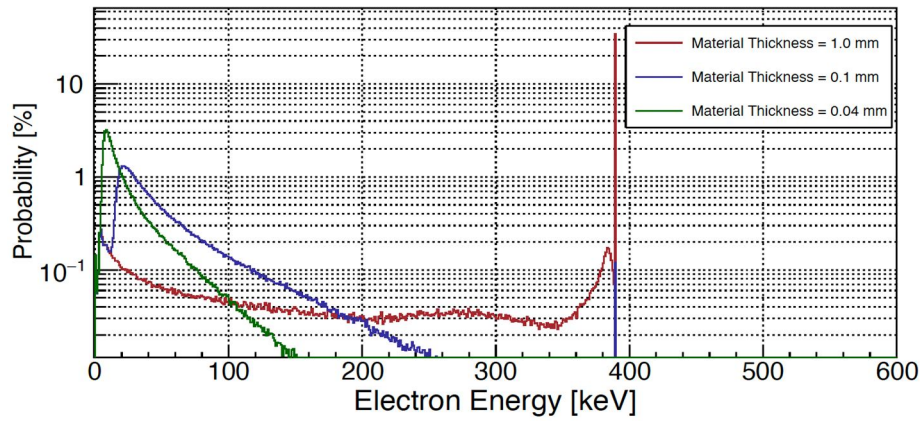


FIG. 6. Geant4 simulation of the energy deposition spectrum for a 389 keV electron beam in scintillator material with different thicknesses.

For thin scintillators, the peak observed at low energies represents the most probable energy loss, known as the Landau peak [16]. Unlike gamma radiation, decreasing the material thickness does not reduce the total absorption efficiency but rather lowers the average energy deposition by electrons. This reduction can, to some extent, decrease the light output and thus

the experimental detection efficiency. However, since optical processes are not included in this study, this behavior cannot be illustrated. However, the full peak absorption efficiency for different initial electron energies, ranging from 100 to 2000 keV, was estimated and is presented in Fig. 7.

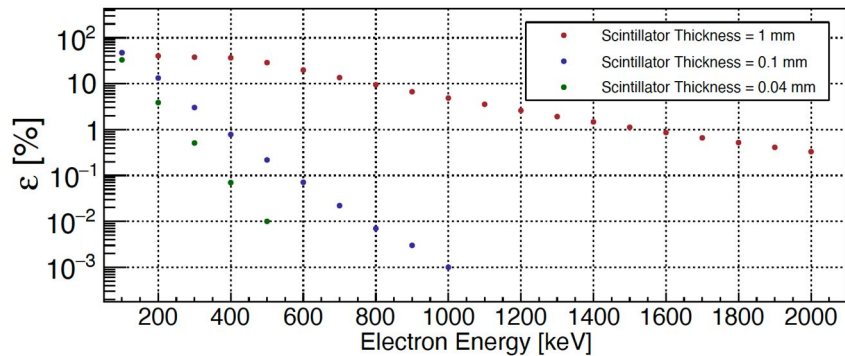


FIG. 7. Full peak absorption efficiency for electrons in a scintillator material at different electron energies and material thicknesses.

In the low-energy range, each electron that reaches the scintillator volume undergoes full energy deposition, but the energy deposited decreases for more energetic electrons because the probability of escaping is higher.

Material Sensitivity to Neutrons

Plastic scintillator materials have very low relative densities, making interactions with scattered neutrons improbable. In order to verify this, the QGSP BERT HP physics list was introduced. This physics list includes high-precision neutron tracking models and provides information about various interaction models for low-energy neutrons (≤ 20 MeV), such as elastic, inelastic, capture, and fission processes [17].

The probability of interaction with scattered neutrons was assessed using a neutron beam with energies ranging from 0.025 keV to 100 keV. The results confirmed that, given the scintillator thicknesses used in this study, neutron interactions are highly improbable.

Discussion and Conclusions

The main goal of this study is to investigate the scintillator material's response to different ionizing radiation. These materials can be used for charged particle measurement in neutron-induced reactions with charged particles in the exit channel (n, z). Based on the above simulation results, a scintillator thickness of 40 μm is sufficient for measuring alpha particles with 5 MeV, obtaining an alpha detection efficiency of 50% while maintaining a very low detection efficiency for background radiation. For instance, electrons with an energy of 389 keV exhibit a detection efficiency of just 0.07%, and gamma radiation of various energies has a detection efficiency below 10%. This work can be further improved by implementing optical processes in the plastic scintillator, allowing for a more accurate estimation of experimental detection efficiency.

Acknowledgment

Authors gratefully acknowledge the financial support by the DFG-project NICE (RE 3461/3-1).

References

- [1] Reifarh, R., Lederer, C., and Käppeler, F., J. Phys. G Nucl. Part. Phys., 41 (2014) 053101.
- [2] Reifarh, R., Erbacher, P., Fiebiger, S., Göbel, K., Heftrich, T., Heil, M., Käppeler, F., Klapper, N., Kurtulgil, D., Langer, C., Lederer-Woods, C., Mengoni, A., Thomas, B., Schmidt, S., Weigand, M., and Wiescher, M., Eur. Phys. J. Plus, 133 (2018) 424.
- [3] Schatz, H., Jaag, S., Linker, G., Steininger, R., and Käppeler, F., Phys. Rev. C, 51 (1995) 379.
- [4] Popov, Yu.P., Przytula, M., Rumi, R.F., Stempinski, M., and Frontasyeva, M., Nucl. Phys. A, 188 (1972) 212.
- [5] Wilkinson, D.H., "Ionization Chambers and Counters" (Cambridge University Press, New York, 1950).
- [6] Koehler, P.E., Harvey, J.A., and Hill, N.W., Nucl. Instrum. Methods Phys. Res. A, 361 (1995) 270.
- [7] Goeminne, G., Wagemans, C., Wagemans, J., Serot, O., Loiselet, M., and Gaelens, M., Nucl. Phys. A, 678 (2000) 11.
- [8] Woods, P.J. et al. (n_TOF Collaboration), Phys. Rev. C, 104 (2021) L032803.
- [9] Geant4 Simulation Toolkit, URL: <http://geant4.web.cern.ch/geant4/>.
- [10] Agostinelli, S., Allison, J., and Amako, K., Nucl. Instrum. Methods Phys. Res. A, 506 (2003) 250.
- [11] National Institute of Standards and Technology, URL: <http://www.nist.gov>.
- [12] Geant4 User's Guide for Application Developers, Version: Geant4 10.3.9, Geant4 Collaboration (2016).
- [13] Allison, J. et al., IEEE Trans. Nucl. Sci., 53 (2006) 270.
- [14] Golovko, V.V., Iacob, V.E., and Hardy, J.C., Nucl. Instrum. Methods Phys. Res. A, 594 (2) (2008) 266.
- [15] Ziegler, J.F., Ziegler, M.D., and Biersak, J.P., Nucl. Instrum. Methods Phys. Res. B, 268 (2010) 1818.
- [16] Aderholz, M., Lehraus, I., and Matthewson, R., Nucl. Instrum. Methods, 193 (1975) 45.
- [17] Geng, C., Tang, X., Guan, F., Johns, J., Vasudevan, L., Gong, C., Shu, D., and Chen, D., Radiat. Prot. Dosim., 168 (4) (2016) 433.

Dust Ion Acoustic Solitary Waves in A Relativistic Ion Plasma with Kappa Described Electrons and Positrons

Jeslin Sara Jose^a, P.S. Abishek^b, Anjumol Babu^a, S. Shilpa^{c,d},
Sijo Sebastian^{e,f}, Lini Devassy^b and Manesh Michael^b

^a Department of Physics, Morning Star Home Science College, Angamaly, Kerala, 683573, India.

^b Department of Physics, Bharata Mata College, Kochi, Kerala, 682021, India.

^c International School of Photonics, Cochin University of Science and Technology, Kochi, 682022, Kerala, India.

^d Present affiliation: Department of Physics, Cochin University of Science and Technology, Kochi, 682022, Kerala, India.

^e Department of Physics, St. Aloysius College, Edathua, Alappuzha – 689 573, Kerala, India.

^f Present affiliation: Department of Physics, S.B. College, Changanassery, Kerala, 686 101, India.

Doi: <https://doi.org/10.47011/18.1.10>

Received on: 29/03/2024;

Accepted on: 04/08/2024

Abstract: The propagation features of ion-acoustic solitary waves in a dusty plasma containing relativistic ions, as well as kappa-distributed electrons and positrons, are studied. The negative dust is defined by q-nonextensive distribution. The Korteweg-de Vries (KdV) equation is formulated using the reductive perturbation technique to study the evolution of dust-ion-acoustic solitary waves (DIASW). The variations in amplitude, width, and phase velocity of solitary waves along with spectral index κ , non-extensive parameter q , and relativistic factors are studied. We observed that the persistence of dust particles enhances the strength of solitary structures formed in relativistic plasma. The relativistic factors and the spectral indices of electrons and positrons enhance the amplitude of solitary structures. Our results may be useful for studying the dynamics of solitary structures existing in any astrophysical dusty plasma composed of relativistic streaming ions, such as those found in interplanetary space and the relativistic winds of pulsars.

Keywords: Dust-ion-acoustic solitary waves, Kappa distribution, q-nonextensive distribution, Korteweg-de Vries (KdV) equation.

1. Introduction

Over the past few decades, the studies regarding the nonlinear wave propagation in various kinds of multicomponent astrophysical and space plasma systems have steadily grown, which is also the case for relativistic dusty plasmas. Nonlinear waves such as solitons, shocks, super solitons, and double layers have

been investigated in these plasma environments. A soliton is characterized by the balance between nonlinearity and dispersion, which counteract each other equally, allowing the wave to maintain a constant speed and amplitude. In contrast, shocks possess an additional dissipative property.

The perusal of multicomponent plasmas, such as electron-ion (e-i), electron-positron (e-p), electron-positron-ion (e-p-i), and electron-positron-ion-dust (e-p-i-d) plasmas, is helpful in the understanding of early universe, atmospheres of various stages of stars, interstellar medium, and galactic environments in which they are found [1, 2]. These plasmas can also be generated and analyzed in laboratory settings using high-intensity lasers. Under intense laser-plasma interactions, ions and electrons can be accelerated to relativistic speeds, enabling the study of relativistic astrophysical plasmas [3].

Relativistic magnetized e-p-i plasma is observed in pulsar wind nebulae and black hole magnetospheres [4]. Here, the non-thermal electrons and positrons are highly energetic, occupying the tail region of the Maxwellian velocity distribution. As a result, they are described using the nonthermal kappa distribution function. Shah *et al.* derived the Korteweg-de Vries (KdV) equation for solitons in a non-thermal e-p-i plasma composed of kappa-distributed electrons and positrons, along with weakly relativistic ions. They found that soliton amplitude increases with the cold ion streaming factor and kappa parameters but decreases with positron concentration [5].

By deriving the modified Korteweg-de Vries (mKdV) equation, Das *et al.* studied higher-order DIASWs in weakly relativistic dusty plasma. According to their research, an increase in dust charge causes a corresponding increase in the amplitude of DIASWs [6].

In a recent research, Das and Das studied the impact of various parameters on relativistic DIASWs using the relativistic factor within the framework of the Kaniadakis distribution (KD). Their findings indicate that DIASWs are observed only within a specific range of dust concentrations [7].

The reductive perturbation method has been employed to establish the coexistence of both compressive and rarefactive solitons in electron-positron-ion (e-p-i) plasma consisting of thermal positrons, nonthermal electrons, and highly relativistic thermal ions [8]. It has been observed that variations in ion species temperature significantly influence the fundamental characteristics of solitary wave amplitude and width.

Madhukalya *et al.* investigated ion-acoustic solitary disturbances in a magnetized plasma composed of relativistic electrons and nonthermal ions [9]. By deriving the Sagdeev potential equation, they demonstrated that in a magnetized relativistic plasma, only rarefactive solitons exist under both subsonic and supersonic conditions.

Another significant study on e-p-i plasma, which includes highly relativistic thermal ions, nonthermal electrons, and thermal positrons, also confirmed the existence of only rarefactive solitons, particularly in the fast ion-acoustic mode [10].

Plasma environments that contain dust grains enable electrons or ions to collide with them, causing the dust to acquire either a negative or a positive charge. Charged dust and dusty plasmas are ubiquitous in the cosmos. Dusty plasmas occur in planetary rings, Earth's mesosphere, comet tails, the interstellar medium, zodiacal dust clouds, and solar nebulae [11-13]. Dust plays a significant role in astrophysics as it is responsible for the formation of stars and planets.

The existence of electrostatic dust-acoustic (DA) solitons and periodic waves in Saturn's magnetosphere has been analyzed using data acquired from the Voyager space mission and the Freja satellite [14]. The Korteweg-de Vries-Burgers (KdVB) equation, which governs small-amplitude nonlinear DA waves in a collisionless, unmagnetized, dissipative dusty plasma with superthermal electrons, has been derived and examined by Hanbaly *et al.* Additionally, the Sagdeev potential method has been used to investigate large-amplitude DA waves in the system [15].

Dust is also observed in relativistic astrophysical environments such as accretion disks around rotating black holes and neutron stars, active galactic nuclei, stellar winds, supernova explosions, and pulsar magnetospheres [16-18]. The Zakharov-Kuznetsov (ZK) equation has recently been analyzed for a relativistic magnetized four-component plasma consisting of thermal ions, nonthermal electrons and positrons, and negatively charged dust. It was found that the Mach number of dust-ion acoustic (DIA) solitons lies within the supersonic range and is influenced by the nonthermal properties of both electrons and positrons, positron density, dust

density, and relativistic effects associated with ions [19].

The characteristics of compressive and rarefactive DIA solitons have been examined in a plasma model containing weakly relativistic ions, negative dust, and electrons [20]. Furthermore, Banerjee and Maitra employed Sagdeev's pseudo-potential approach to establish the concurrence of negative and positive potential double layers and solitary waves in a nonthermal, unmagnetized dusty plasma [21]. Their study revealed that this phenomenon occurs within a specific range of the nonthermal parameter at very low positron densities.

DIASWs have been examined using the kappa distribution of electrons and positrons in weakly relativistic complex plasma. The effects of the relativistic factor and superthermal parameters on higher-order phase shifts of the wave have been studied in the context of pulsars [22]. Ion-acoustic solitons in an electron-positron-ion (e-p-i) plasma with weakly relativistic cold ions have been investigated using the Korteweg-de Vries (KdV) equation, revealing that the nonextensive parameter of q-distributed electrons causes the existence of only compressive solitons [23]. By deriving the Burgers equation, the DIA multi-shock waves have been explored in relativistic dusty plasmas containing positrons, q-nonextensive electrons, and stationary dust [24]. Some of the recent investigations by Khater have provided in-depth analyses of solitary waves in various plasma contexts using advanced mathematical methods. His work offers analytical solutions to equations describing solitary waves, which may accurately explain the stability and properties of nonlinear waves in quantum and magnetized multicomponent plasmas, as well as in multi-dimensional settings [25–31].

In this study, we discuss the propagation characteristics of small-amplitude solitary waves in a dusty plasma composed of relativistic ions, kappa-distributed electrons, and positrons by deriving the KdV equation. Our results may contribute to ongoing research on relativistic plasmas in interstellar and space environments.

2. Theoretical Model and Governing Equations

Our investigation involves the mathematical modelling of unmagnetized, collisionless, tetra-

component e-p-i-d plasma consisting of superthermal electrons and positrons, weakly relativistic cold ions, and dust grains which are negatively charged. The highly energetic electrons are kappa-distributed, while the dust particles are q-nonextensively distributed.

The quasineutrality condition is written as:

$$n_{i0} + n_{p0} - z_d n_{d0} - n_{e0} = 0 \quad (1)$$

where n_{i0} , n_{p0} , n_{d0} , and n_{e0} are equilibrium densities of ions, positrons, dust, and electrons, respectively. All normalizations are done using the electron. Normalizing the densities of the plasma species using n_{e0} , we obtain:

$$\frac{n_{i0}}{n_{e0}} = 1 - p + d \quad (2)$$

where $p = \frac{n_{p0}}{n_{e0}}$ is the normalized positron density and $d = \frac{z_d n_{d0}}{n_{e0}}$ is the normalized dust density.

The normalised fluid equations governing mass and momentum conservations for relativistic ions are given by:

$$\frac{\partial n_i}{\partial t} + \frac{\partial(n_i u_i)}{\partial x} = 0 \quad (3)$$

$$\frac{\partial(\gamma u_i)}{\partial t} + u_i \frac{\partial(\gamma u_i)}{\partial x} + \frac{\partial \Phi}{\partial x} = 0 \quad (4)$$

The normalized Poisson's equation is:

$$\frac{\partial^2 \Phi}{\partial x^2} = n_e - p n_p - (1 - p + d) n_i + d n_d \quad (5)$$

In Eqs. (3)–(5), we normalize the electrostatic potential using the quantity T_e/e , where e is the charge of electron. The spatial variable x is normalized using the electron Debye length $\lambda_{De} = \sqrt{\frac{T_e}{4\pi n_{e0} e^2}}$, the ion velocity u_i is normalized using

the acoustic speed $c_s = \sqrt{\frac{T_e}{m_e}}$, and the time variable is normalized using the inverse of the

electron plasma frequency $\omega_{pe}^{-1} = \sqrt{\frac{m_e}{4\pi n_{e0} e^2}}$. In

Eq. (4), the relativistic streaming factor is given by: $\gamma = \left(1 - \frac{u_i^2}{c^2}\right)^{-1/2}$, with c being the speed of light. It is approximated to $\left(1 + \frac{u_i^2}{2c^2}\right)$ for weakly relativistic ions [5].

The normalized kappa distributions for electrons and positrons are given by:

$$n_e = \left[1 - \frac{\Phi}{(\kappa_e - \frac{3}{2})}\right]^{-\kappa_e + \frac{1}{2}} \quad (6)$$

$$n_p = \left[1 + \frac{\delta\Phi}{(\kappa_p - \frac{3}{2})} \right]^{-\kappa_p + \frac{1}{2}} \quad (7)$$

and the q-nonextensive distribution for dust is:

$$n_d = [1 + \sigma(q-1)\Phi]^{\frac{3q-1}{2(q-1)}} \quad (8)$$

Here, $\delta = T_e/T_p$ and $\sigma = T_e/T_d$, where T_e , T_p , and T_d denote the temperatures of electrons, positrons, and dust, respectively. The q-nonextensive distribution approaches the Maxwellian distribution in the limit $q \rightarrow 1$ [32]. Also, within the limit of $\kappa_e = \kappa_p \rightarrow \infty$, the kappa distribution reduces to the Maxwellian velocity distribution [33].

3. Derivation of the KdV Equation

Here, we formulate the KdV equation for small-amplitude solitary waves travelling in one dimension using the reductive perturbation method. This involves transforming the space and time coordinates and expanding various parameters [5]. They are given as:

$$\xi = \varepsilon^{\frac{1}{2}}(x - \lambda_0 t), \tau = \varepsilon^{\frac{3}{2}}t \quad (9)$$

and

$$n_i = 1 + \varepsilon n_i^{(1)} + \varepsilon^2 n_i^{(2)} + \varepsilon^3 n_i^{(3)} + \dots \quad (10)$$

$$u_i = u_0 + \varepsilon u^{(1)} + \varepsilon^2 u^{(2)} + \varepsilon^3 u^{(3)} + \dots \quad (11)$$

$$\Phi = \varepsilon \Phi^{(1)} + \varepsilon^2 \Phi^{(2)} + \varepsilon^3 \Phi^{(3)} + \dots \quad (12)$$

Here, λ_0 denotes the Mach number or phase velocity of the soliton, and ε is a small parameter representing the perturbation magnitude in the system. By substituting Eqs. (6)–(12) into Eqs. (3)–(5) and equating the lowest-order terms of ε , we obtain the following relations:

$$u^{(1)} = \frac{\Phi^{(1)}}{\gamma_1(\lambda_0 - u_0)}; n_i^{(1)} = \frac{\Phi^{(1)}}{\gamma_1(\lambda_0 - u_0)^2} \quad (13)$$

The phase velocity of the soliton is given by

$$\lambda_0 = u_0 + \frac{2(2\kappa_e - 3)(2\kappa_p - 3)(1 - p + d)}{\gamma_1(2(2\kappa_e - 1)(2\kappa_p - 3) + 2p\delta(2\kappa_p - 1)(2\kappa_e - 3) + d\sigma(3q - 1)(2\kappa_e - 3)(2\kappa_p - 3))} \quad (14)$$

By equating the next highest order of ε , we derive the following set of equations:

$$\frac{\partial n_i^{(1)}}{\partial \tau} - (\lambda_0 - u_0) \frac{\partial n_i^{(2)}}{\partial \xi} + \frac{\partial u^{(2)}}{\partial \xi} + \frac{\partial}{\partial \xi} (n_i^{(1)} u^{(1)}) = 0 \quad (15)$$

$$\gamma_1 \frac{\partial u^{(1)}}{\partial \tau} - (\lambda_0 - u_0) \gamma_1 \frac{\partial u^{(2)}}{\partial \xi} + \left(\gamma_1 - 2\gamma_2 \frac{\lambda_0 - u_0}{u_0} \right) u^{(1)} \frac{\partial u^{(1)}}{\partial \xi} + \frac{\partial \Phi^{(2)}}{\partial \xi} = 0 \quad (16)$$

$$\frac{\partial^2 \Phi^{(1)}}{\partial \xi^2} - \left\{ \frac{2\kappa_e - 1}{2\kappa_e - 3} + \frac{2\kappa_p - 1}{2\kappa_p - 3} p\delta + \frac{3q - 1}{2} d\sigma \right\} \Phi^{(2)} + \left\{ \frac{4\kappa_e^2 - 1}{(2\kappa_e - 3)^2} - \frac{4\kappa_p^2 - 1}{(2\kappa_p - 3)^2} p\delta^2 + \frac{(3q - 1)(q + 1)}{4} \sigma^2 d \right\} \frac{[\Phi^{(1)}]^2}{2} + (1 - p + d) n_i^{(2)} = 0 \quad (17)$$

where $\gamma_1 = 1 + \gamma_2$, $\gamma_2 = 1.5\beta^2$, and $\beta = u_0/c$, which is the relativistic cold-ion streaming factor.

By substituting Eq. (13) into Eqs. (15)–(17) and simplifying by removing second-order terms we get the KdV equation for DIASW in our e-p-i-d plasma model::

$$\frac{\partial \Phi^{(1)}}{\partial \tau} + A \Phi^{(1)} \frac{\partial \Phi^{(1)}}{\partial \xi} + B \frac{\partial^3 \Phi^{(1)}}{\partial \xi^3} = 0 \quad (18)$$

where

$$A = \frac{1}{\gamma_1(\lambda_0 - u_0)} - \frac{\gamma_1(\lambda_0 - u_0)^3}{2(1 - p + d)} \left\{ \frac{4\kappa_e^2 - 1}{(2\kappa_e - 3)^2} - \frac{4\kappa_p^2 - 1}{(2\kappa_p - 3)^2} p\delta^2 + \frac{(3q - 1)(q + 1)}{4} \sigma^2 d \right\} + \frac{1}{2\gamma_1^2(\lambda_0 - u_0)} \left(\gamma_1 - 2\gamma_2 \frac{\lambda_0 - u_0}{u_0} \right) \quad (19)$$

and

$$B = \gamma_1 \frac{(\lambda_0 - u_0)^3}{2(1 - p + d)} \quad (20)$$

Here, A is the coefficient of nonlinearity, and B is the coefficient of dispersion.

4. Solution of the KdV Equation

The standard solution of the KdV Eq. (20) is given in [5, 34] as:

$$\Phi^{(1)}(\zeta) = \Phi_0 \operatorname{sech}^2 \left(\frac{\zeta - v\tau}{\Delta} \right) \quad (21)$$

where the new stretched variable is $\zeta = \xi - v\tau$, and $\Phi^0 = \frac{3v}{A}$ is the amplitude of soliton, while $\Delta = \sqrt{\frac{4B}{v}}$ represents the soliton width. Here, v is the constant speed of the soliton.

The amplitude of the soliton is inversely proportional to the nonlinearity coefficient A, and its width has a direct relationship with the dispersive effects.

5. Results and Discussions

We thoroughly execute the numerical analysis of the DIASW solution [Eq. (21)] in our e-p-i-d plasma model.

Figure 1 represents the variation of the solitary profile as a function of the relativistic streaming factor (β) of ions. The parameters used for this analysis are $\delta = 1$, $p = 0.2$, $\kappa_e = \kappa_p = 3$, $d = 0.2$, $\sigma = 0.3$, and $q = 0.2$. It can be seen that as the relativistic streaming factor of ions increases, the solitary wave becomes more pronounced. This behavior can be attributed to a decrease in the nonlinearity coefficient A due to the rise in the relativistic streaming factor. Our findings are consistent with the results reported by Saed *et al.* and El-Wakil *et al.* [35, 36].

In Fig. 2, the influence of spectral index κ_e of electron on the solitary profile is studied. Here, we fix $\kappa_p = 3$ and $\beta = 0.1$. All other parameters are the same as in Fig.1. The results clearly show that an increase in κ_e enhances both the amplitude and width of the solitary wave. This occurs because a higher κ_e value leads to an

increase in electron pressure, which provides the necessary restoring force for the solitary wave. The stronger restoring force, in turn, contributes to the growth of the soliton amplitude.

Similarly, an increase in the positron kappa index (κ_p) also strengthens the soliton, as depicted in Figure 3. Notably, smaller values of the kappa indices indicate a higher presence of suprathermal particles in the plasma. Consequently, suprathermal electrons and positrons significantly influence the solitary wave profile. The solitary waves reach their maximum strength when the plasma approaches a Maxwellian distribution ($\kappa_e = \kappa_p \rightarrow \infty$).

Figure 4 depicts the variation in the solitary wave profile with respect to the normalized positron density (p). It is evident that an increase in positron concentration weakens the solitary wave structures. A higher positron concentration reduces the positive ion density in the plasma, thereby diminishing the driving force of the ion acoustic solitary wave. This reduction in driving force ultimately leads to a decrease in the strength of the solitary wave profile [5].

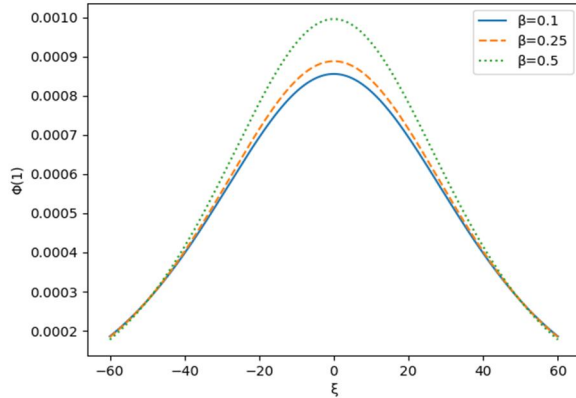


FIG. 1. Change in the soliton profile as a function of the relativistic streaming factor of ions (β).

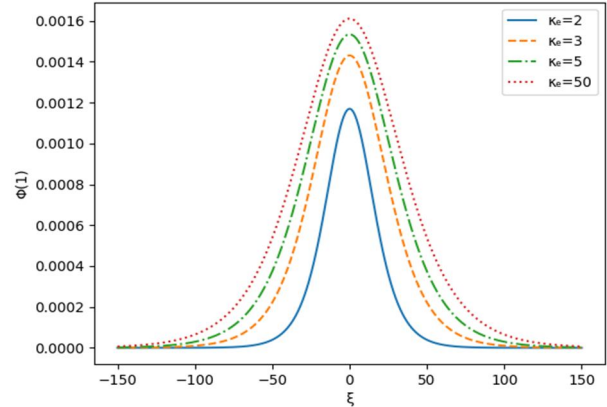


FIG. 2. Change in the soliton profile as a function of spectral indices of electron (κ_e).

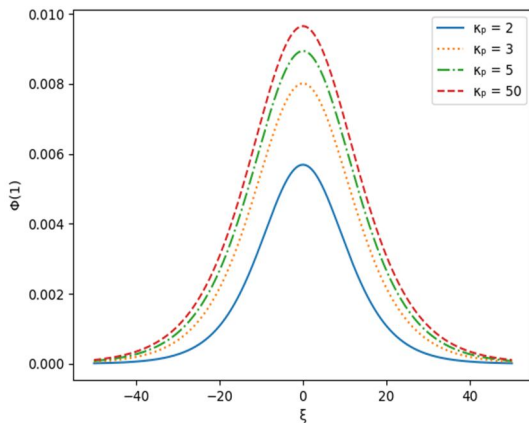


FIG. 3. Change in the soliton profile as a function of spectral indices of positron (κ_p).

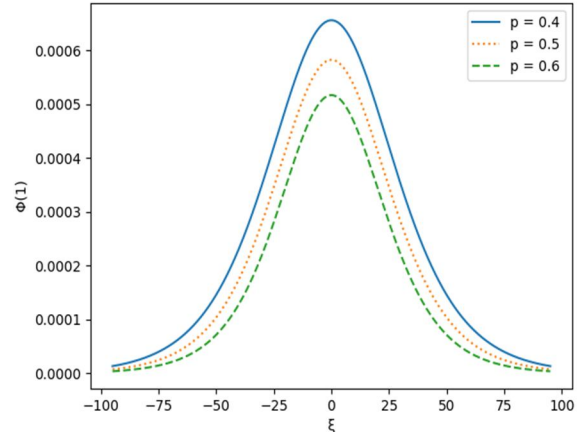


FIG. 4. Change in the soliton profile as a function of normalized positron density p .

Figure 5 shows variations in the solitary profile with respect to the electron-to-positron temperature ratio ($\delta = T_e / T_p$) for a relativistic parameter $\gamma_1 = 0.2$. We observed that the strength of the solitary profile decreases along with increasing electron-to-positron temperature ratios. The solitary structure exhibits its maximum amplitude at lower electron temperatures. This behavior can be explained by the fact that a decrease in electron temperature reduces the system's nonlinearity, as the solitary wave amplitude is inversely related to the nonlinearity coefficient A . This variation is similar to the results obtained by Saed *et al.* and El-Wakil *et al.* [35, 36].

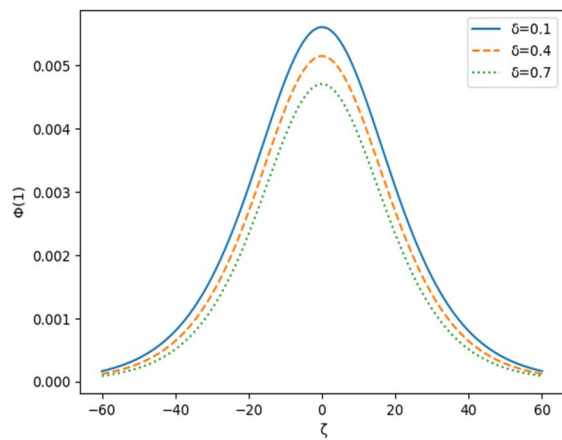


FIG. 5. Change in the solitary profile as a function of electron to positron temperature ratio δ .

Figure 6 illustrates the change in the nonlinearity coefficient A with the relativistic parameter γ_1 as a function of the q -nonextensive parameter of dust particles. We found that the nonlinearity coefficient A increases along with

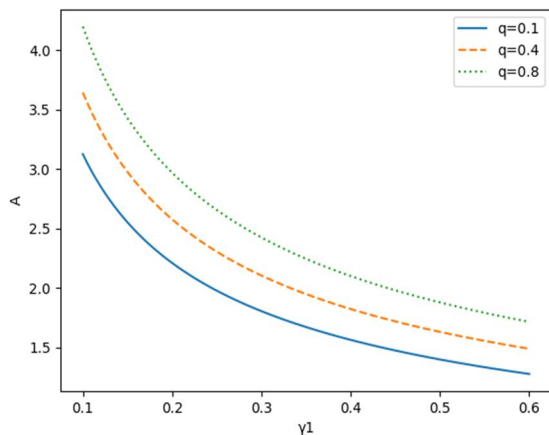


FIG. 6. Variation of the nonlinearity coefficient A with the relativistic parameter γ_1 as a function of q -nonextensive parameter.

an increase in q and decreases with the relativistic parameter γ_1 . This implies that higher relativistic velocities of ions reduce the nonlinearity coefficient A , thereby enhancing the amplitude of solitary waves at higher relativistic limits, as the amplitude is inversely proportional to A .

At larger values of the q -nonextensive parameter ($q \rightarrow 1$), the nonthermal distribution approaches the Maxwellian distribution. This indicates that the presence of nonthermal dust particles significantly influences the amplitude of solitary structures. Conversely, the strength of solitary waves diminishes when the plasma approaches the Maxwellian limit ($q \rightarrow 1$).

Figure 7 further illustrates the variation of A with the normalized dust particle density (d) as a function of the q -nonextensive parameter. An increase in dust concentration decreases the nonlinearity. As the density of dust grains increases in plasma, more charged electrons and ions accumulate on the dust surface, reducing their contribution to nonlinearity.

For zero dust concentration, the nonlinearity coefficient A exhibits a single maximum for different values of q . However, as dust concentration increases, A diverges. These findings clearly indicate that the presence of dust particles enhances the strength of solitary structures in relativistic plasma. These results are consistent with the observations reported by Dev *et al.* [19].

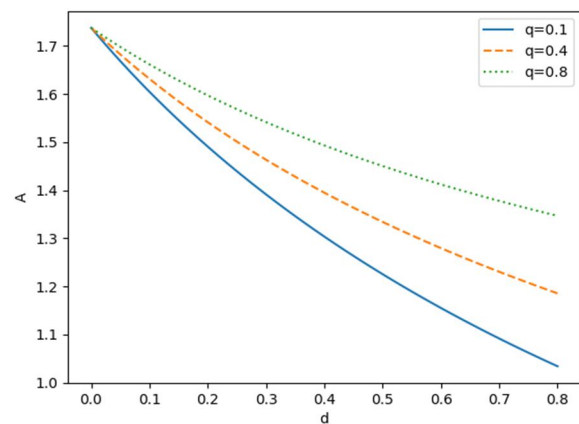


FIG. 7. Variation of the nonlinearity coefficient A with normalized densities of dust as a function of q -nonextensive parameter.

Figure 8 depicts the plot of phase velocity of solitons (λ_0) versus positron concentration (p) as a function of the nonextensive parameter (q). We observed that the Mach number (or phase velocity) of solitary waves decreases with an increase in both positron concentration and the q -nonextensive parameter of dust in the relativistic plasma. The presence of positrons reduces the restoring force of solitary waves. As the population of positrons in the plasma system

increases, the corresponding decrease in the restoring force leads to an increase in ion concentration. This, in turn, enhances ion interactions, ultimately reducing the phase velocity of the solitons.

Since q tends to 1 corresponds to the Maxwellian distribution, it can be concluded that the presence of nonthermal dust particles enhances the phase velocity of solitary waves.

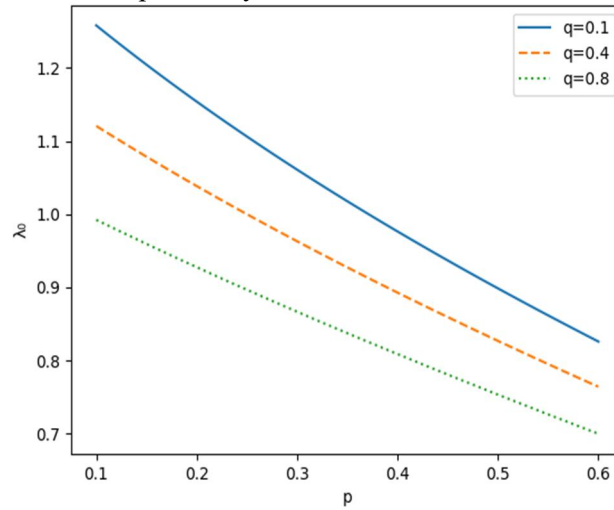


FIG. 8. Change in phase velocity (λ_0) of solitary wave with positron densities (p) as a function of q -nonextensive parameter.

6. Conclusions

Presence of dust is very relevant for laboratory, space and astrophysical plasmas. We have done mathematical modelling of an unmagnetized collisionless relativistic four component e-p-i-d plasma contains kappa distributed electrons and positrons. The dust particle is described by q -nonextensive distribution. By deriving KdV equation, nonlinear dynamics of the DIASW in relativistic astrophysical plasma environment are examined. From our investigation, we find that presence of dust particles enhances strength of solitary structures formed in relativistic plasma. The relativistic factors (β and γ_i), and the spectral indices of electrons and positrons have an enhancing impact on the amplitude of solitary structures; whereas amplitude decreases with an increase in positron concentration, q -nonextensive parameter of dusts and electron-to-positron temperature ratios. We also noticed that phase velocity of solitary waves decreases with

an increase in concentration of positron and q -nonextensive parameter of dust in the plasma.

Given the critical significance of e-p-i-d plasma applications, including interstellar medium studies and astrophysics, there exists an imperative to explore relativistic ion dynamics amidst the existence of superthermal/non-Maxwellian electrons and positrons. Consequently, our present investigation aims to explore the dynamics of solitary structures existing in any astrophysical dusty plasma with relativistic streaming ions like interplanetary space and relativistic wind of pulsars.

7. Acknowledgements

Financial assistance from Department of Biotechnology, Government of India under DBT STAR College Scheme (HRD-11011/22/2022-HRD-DBT dated 24/08/2022) to Bharata Mata College is gratefully acknowledged.

References

- [1] Gailis, R.M., Dettmann, C.P., Frankel, N.P., and Kowalenko, V., *Phys. Rev. D*, 50 (6) (1990) 3847.
- [2] Kaplan, A.S. and Tsytovich, V.N., *Phys. Rep.*, 7 (1) (1973) 1.
- [3] Umstadter, D., *J. Phys. D: Appl. Phys.*, 36 (8) (2003) R151.
- [4] Punsly, B. and Coroniti, F.V., *Astro. J.*, 350 (1990) 518.
- [5] Shah, A., Mahmood, S., and Haque, Q., *Phys. Plasm.*, 18 (2011) 114501.
- [6] Das, D.C. and Das, S., *J. Korean Phys. Soc.*, 84 (2024) 231.
- [7] Das, M. and Das, R., *Braz. J. Phys.*, 54 (2024) 161.
- [8] Kalita, J., Das, R., Hosseini, K., Baleanu, D., and Hincal, E., *Partial Differ. Equ. Appl. Math.*, 8 (2023) 100579.
- [9] Madhukalya, B., Das, R., Hosseini, K., Baleanu, D., and Salahshour, S., *Int. J. Appl. Comput. Math.*, 9 (5) (2023) 102.
- [10] Kalita, J., Madhukalya, B., and Das, R., *J. Korean Phys. Soc.*, 84 (24) (2024) 120.
- [11] Merlino, R., *Adv. Phys.*, X 6 (1) (2021) 1873859.
- [12] Shukla, P.K., *Phys. Plasm.*, 8 (5) (2001) 1791.
- [13] Mandal, G., Roy, K., and Chatterjee, P., *Indi. J. Phys.*, 83 (2009) 365.
- [14] Shohaib, M., Masood, W., Siddiq, M., Alyousef, H.A., and El-Tantawy, S.A., *J. Low Freq. Noise Vib. Act. Control*, 41 (3) (2022) 896.
- [15] Hanbaly, A.M.E., Shewy, E.K.E., Sallah, M., and Darweesh, H.F., *Comm. T. Phys.*, 65 (5) (2016) 606.
- [16] Schroyen, K., Hackmann, E., and Lämmerzahl, C., *Phys. Rev. D*, 96 (6) (2017) 063015.
- [17] Czerny, B., Zajacek, M., Naddaf, M.-H., Sniegowska, M., Panda, S., R'ozanska, A., Adhikari, T.P., Pandey, A., Jaiswal, V.K., Karas, V., Borkar, A., Mart'inez-Aldama, M.L., and Prince, R., *Eur. Phys. J. D*, 77 (2023) 56.
- [18] Banerjee, G. and Maitra, S., *Ameri. J. Appl. Mathe. Comp.*, 1 (1) (2020) 27.
- [19] Dev, A.N., Deka, M.K., Kalita, R.K., and Sarma, J., *Euro. Phys. J. Plu.*, 135 (2020) 843.
- [20] Kalita, B.C. and Das, S., *Astro. Spa. Sci.*, 352 (2014) 585.
- [21] Banerjee, G. and Maitra, S., *Phys. Plasm.*, 23 (2016) 123701.
- [22] El-Shamy, E.F., El-Shewy, E.K., Abdo, N.F., Abdellahi, M.O., and Al-Hagan, O., *Contr. Plasma Phys.*, 59 (3) (2019) 304.
- [23] Pakzad, H.R., *Astro. Spac. Sci.*, 334 (2) (2011) 337.
- [24] Hafez, M.G., Singh, S., Sakthivel, R., and Ahmed, S.F., *AIP Adv.*, 10 (6) (2020) 065234.
- [25] Khater, M.M.A., *Results Phys.*, 44 (2023) 106193.
- [26] Khater, M.M.A. and Salama, S.A., *J. Ocean Eng. Sci.*, 7 (3) (2022) 237.
- [27] Khater, M.M.A. and Salama, S.A., *J. Ocean Eng. Sci.*, 7 (3) (2022) 264.
- [28] Khater, M.M.A., *Phys. Lett. A.*, 480 (2023) 128945.
- [29] Khater, M.M.A., *Eur. Phys. J. Plus.*, 138 (2023) 715.
- [30] Khater, M.M.A., *Int. J. Thor. Phys.*, 62 (2023) 152.
- [31] Khater, M.M.A., *Int. J. Thor. Phys.*, 62 (2023) 151.
- [32] Manesh, M., Anu, V., Neethu, T.W., Sijo, S., Sreekala, G., and Venugopal, C., *Plasm. Phys. Rep.*, 46 (5) (2019) 541.
- [33] Pierrard, V. and Lazar, M., *Sol. Phys.*, 267 (2010) 153.
- [34] Khater, M.M.A., *Opt. Quant. Electr.*, 56 (2024) 6.
- [35] Saeed, R., Shah, A., and Noaman-ul-Haq, M., *Phys. Plasm.*, 17 (2010) 102301.
- [36] El-Wakil, A.S., Abulwafa, E.M., and El-Shewy, E.K., *Adv. Spac. Res.*, 49 (2012) 1721.

Identifying Leachate Plume Accumulation Zones at Lapite Dumpsite in Nigeria Employing Very Low Frequency Electromagnetic (VLF-EM) Method

Saheed A. Ganiyu

Department of Physics, Federal University of Agriculture Abeokuta, Ogun State, Nigeria.

Doi: <https://doi.org/10.47011/18.1.11>

Received on: 12/05/2023;

Accepted on: 10/12/2023

Abstract: A geophysical investigation involving the use of the very low frequency-electromagnetic (VLF-EM) method was carried out at the Lapite dumpsite, which has been operational since 1998. The aim was to map conductive lineament features and the extent of contaminant plume in the subsurface for potential groundwater pollution. The VLF-EM survey was deployed at 10 m intervals with the aid of ABEM WADI VLF-EM meter. Nine VLF-EM profiles with lengths stretching between 120 and 250 m were arranged inside the dumpsite. A control profile of VLF-EM data was placed approximately 500 m from the dumpsite. The VLF-EM measurements were construed using Fraser and Karous-Hjelt filtering processes. Fraser graphs and current density pseudo-sections show the existence of west-orientated conductive structures/leachate accumulation zones at various depths, cutting across the dumpsite. The 2D current density sections indicate that leachate accretion/fluid-filled structures have high conductivity values (low resistivity), aligning with the outcomes acquired from the preceding electrical resistivity survey. The contaminant leachate may infiltrate the shallow groundwater system situated on the west side of the dumpsite.

Keywords: Leachate plume, VLF-EM, Current density pseudo-section, Dumpsite, Shallow groundwater.

1. Introduction

Wastes generated from daily anthropogenic activities are of different forms and sizes. Households, organizations, and factories generate solid wastes that must be disposed of properly in an approved landfill or open dumpsite [1]. In many African countries, limited land availability for waste disposal has led to unrestrained dumping of wastes on the outskirts of the cities and main road channels, posing serious environmental and public health hazards [2-3]. There has been a significant rise in the generation of municipal solid wastes in Nigeria over the past decades [3-4]. Among the explanations for the increase in municipal solid waste generation are population growth, rural-urban migration, and inadequate provision of

suitable disposal systems by relevant environmental agencies [5-6]. Indiscriminate disposal of solid waste affects air quality, soil, and nearby shallow aquifer units [1, 5, 7]. The composition of municipal solid waste (MSW) deposited in a particular landfill/dumpsite depends on social status, consumption pattern, urban setting, and nearness to industries [8-10]. MSW consists of unused plastics, animal remains, household materials, factory solid wastes, papers, fertilizers, toxic materials, and many biodegradable materials. Besides polluting dumpsite soil, MSW causes different appealing and public health problems [11-13]. The solid waste deposited in open dumpsite experiences gentle, anaerobic disintegration over the years

and produces considerable expanse of leachate plumes in addition to other disintegrating formations like dumpsite gas, metalloids, and perilous contaminants that may trickle out of the dumpsite into nearby shallow groundwater units, consequently contaminating greatly required groundwater bodies [13-14]. Leachate, a liquid formed from putrefied waste, has been reported to have a higher conductivity (lower electrical resistivity) value [13, 15]. Therefore, the existence of leachate in lithologies and the soil matrix can enhance their electrical conductivity from weak/modest to exceptionally high [16-17]. Pollutants such as leachate plumes hardly ever remain at the point of release but are rather distributed via the soil matrix by four principal transport methods: advection, diffusion, dispersion, and sorption [4, 18-19]. Besides, leachate settles near the surface or beneath the dumpsite, with the resultant piezometric head stimulating both the downward and outward movement of the leachate plume out of the dumpsite to the nearby shallow aquifer units [13, 15]. Pollution of shallow groundwater sources by leachate plumes from nearby dumpsites occurs typically as a result of the percolation of contaminants through the permeable soil/ parent materials into shallow groundwater [20-21].

Many authors have investigated the geophysical and geochemical impacts of leachate on soil and nearby groundwater resources [15, 22-25]. Researchers have also assessed the environmental impacts of contaminant leachate from the Lapite dumpsite on air quality [5] as well as soil and groundwater [1, 5]. Specifically, Popoola and Fakunle [1] used the geophysical method to depict leachate plume regions and the extent of leachate migration, respectively.

The VLF-EM is an electromagnetic technique that utilizes radio waves from global network transmitter stations in the frequency range of 15 - 30 KHz [26]. This method relies on transmitted currents prompting secondary responses in conductive subsurface structures [17, 27]. The VLF-EM survey is particularly used to locate subsurface conductors that may act favorably as conduits for the leachate movement [28-30]. Oladejo *et al.* [31] investigated the groundwater potential of a granitic area using VLF-EM, while Monteiro Santos *et al.* [29], Moradzadeh *et al.* [32], and Abdullahi *et al.* [30] applied this

method to detect leachate accumulation zones and extent of their migration.

In this present study, the VLF-EM technique was utilized to examine the accumulation and spreading of leachate plumes within the dumpsite. The core aims of this study were: (a) delineation of conductive features within the dumpsite, which is underlain by basement complex formation, and (b) delimitation of the extent and depth of the contaminant leachate plume.

2. Depiction of the Survey Area

Lapite dumpsite (Fig. 1) is situated in Ibadan city and delimited by longitudes 3.91160°E and 3.91464°E and latitudes 7.5825°N and 7.57032°N [4]. The inspected dumpsite was opened in 1998 and is still in use to this day. It spans approximately 20 ha along Old Oyo Road [1, 15]. According to records from the Oyo State Waste Management Authority (OSWMA, 2016), the Lapite dumpsite receives approximately 31% of the generated solid wastes [5]. The site experiences a humid climate typical of southwestern Nigeria, with an average annual rainfall of about 1270 mm, an average annual potential evapotranspiration of 1467 mm, and a mean annual maximum temperature of 33°C [33].

A detailed description of the geological setting and other physical features of the study area has been previously reported [4].

3. Methodology

The very low frequency electromagnetic (VLF-EM) survey was carried out on the dumpsite to detect potential linear conductive features such as faults, fracture zones, and leachate plumes. A previous study by Ganiyu *et al.* [4] investigated part of the study area using the electrical resistivity imaging method.

The present study offers several advantages, as the survey profiles were oriented approximately in a north-south direction with uniform inter-profile spacing. This acquisition methodology is expected to enhance the accuracy of delineating and mapping contaminant leachate pathways.

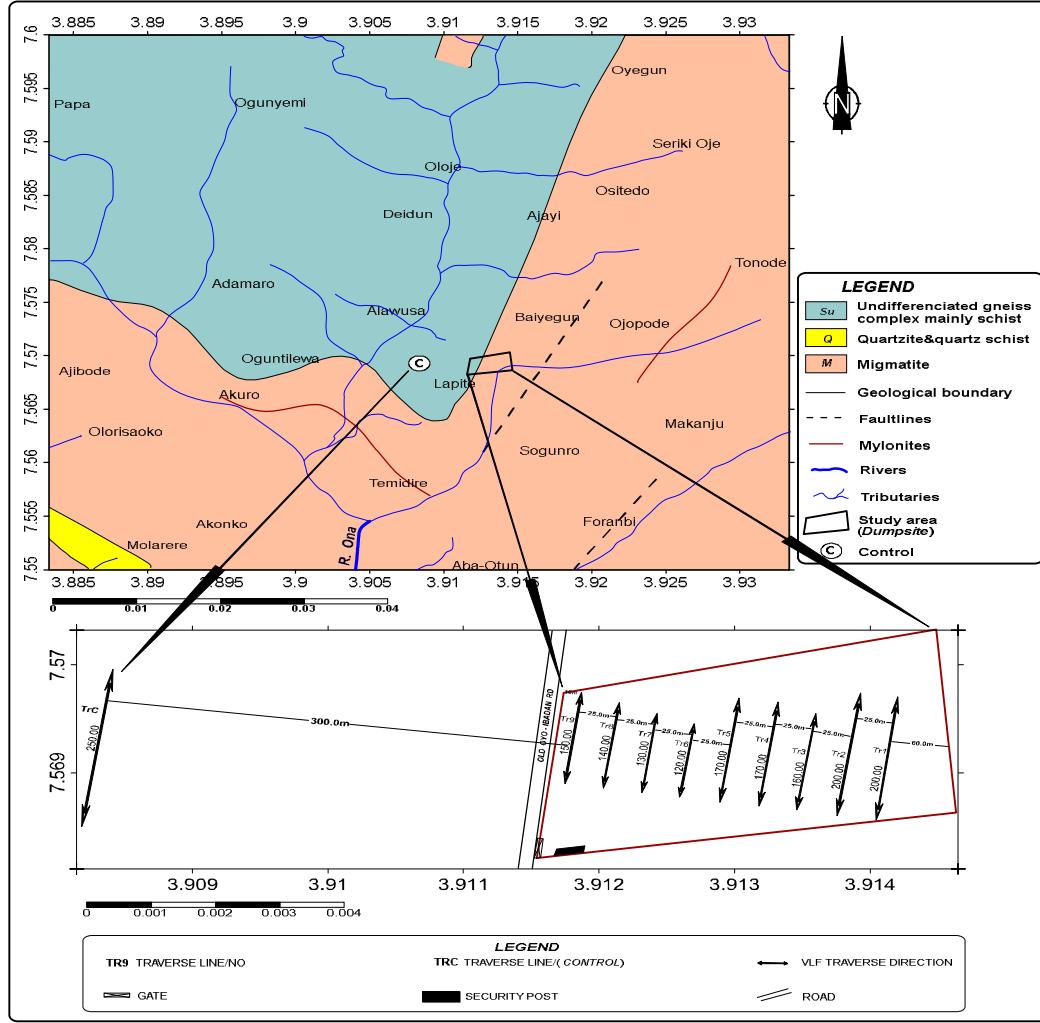


FIG. 1. Geological map of the study area showing the field layout for the VLF-EM survey.

Nine (9) parallel VLF-EM traverses with inter traverse separation of 25 m and length varying between 120 and 250 m were planned inside the dumpsite. Additionally, a control profile was laid along the road, approximately 500 m away from the dumpsite. VLF-EM data were acquired along each profile utilizing the ABEM WADI VLF meter at a measurement interval of 10 m. A frequency of 18.2 KHz was used for the measurements. All VLF-EM profiles were oriented in a north-south direction across the dumpsite. The data acquisition layout for the VLF-EM survey is depicted in Fig. 1.

The WADI VLF meter recorded both the perpendicular (H_z) and parallel (H_x) components of the secondary electromagnetic field along the laid profiles at 10 m intervals. The ratio H_z/H_x gives a scalar B, tipper that has real and imaginary parts [17, 29, 34]. The real constituent of B is utilized in this study. The acquired real VLF-EM data were processed

using Fraser and Karous-Hjelt filtering methods [35-36] to generate response graphs against station positions. Fraser filtering transforms every genuine crossover or inflection point in the real anomaly into a positive peak, whereas reverse crossovers become negative peaks. The Fraser filter Q [35] was computed using a filter operator given by:

$$Q = f_{2,3} = (M_4 + M_3) - (M_2 + M_1) \quad (1)$$

where $Q = f_{2,3}$ refers to the EM data, and the subscripts are station positions (i.e., M_1 , M_2 , M_3 , and M_4 are the readings of the measured real at stations 1, 2, 3, and 4, respectively). The values are plotted between M_2 and M_3 points. The resulting plots of both raw and filtered real values against station positions for each profile are presented as Fraser plots.

The KHFILT inversion software was used to obtain relative current density pseudosections based on the real component [37].

4. Results and Discussions

4.1. Interpretation of VLF-EM Profiles

The VLF-EM profiles were interpreted using the response signal of the Fraser graph for the identification of conductive features and/or leachate accumulation zones, while Karous-Hjelt current density pseudosections were employed to detect leachate plumes and map their spatial distribution. These are shown in Figs. 2 to 6.

Profile 1 shows diagnostic points indicative of conductive features and/or leachate accumulation zones between horizontal distances

of 52–80 m on the Fraser graph. Correspondingly, the Karous-Hjelt pseudosection shows high positive current density values at 48 m (near the base) and 75 m (toward the top) of the profile, suggesting the presence of a conductive structure that may facilitate the migration of leachate plumes, as seen in Fig. 2(a).

Profile 2, depicted in Fig. 2(b), reveals multiple locations with relatively high current density values, signifying significant occurrences of conductive materials and leachate plume accumulation zones with varying depth extensions.

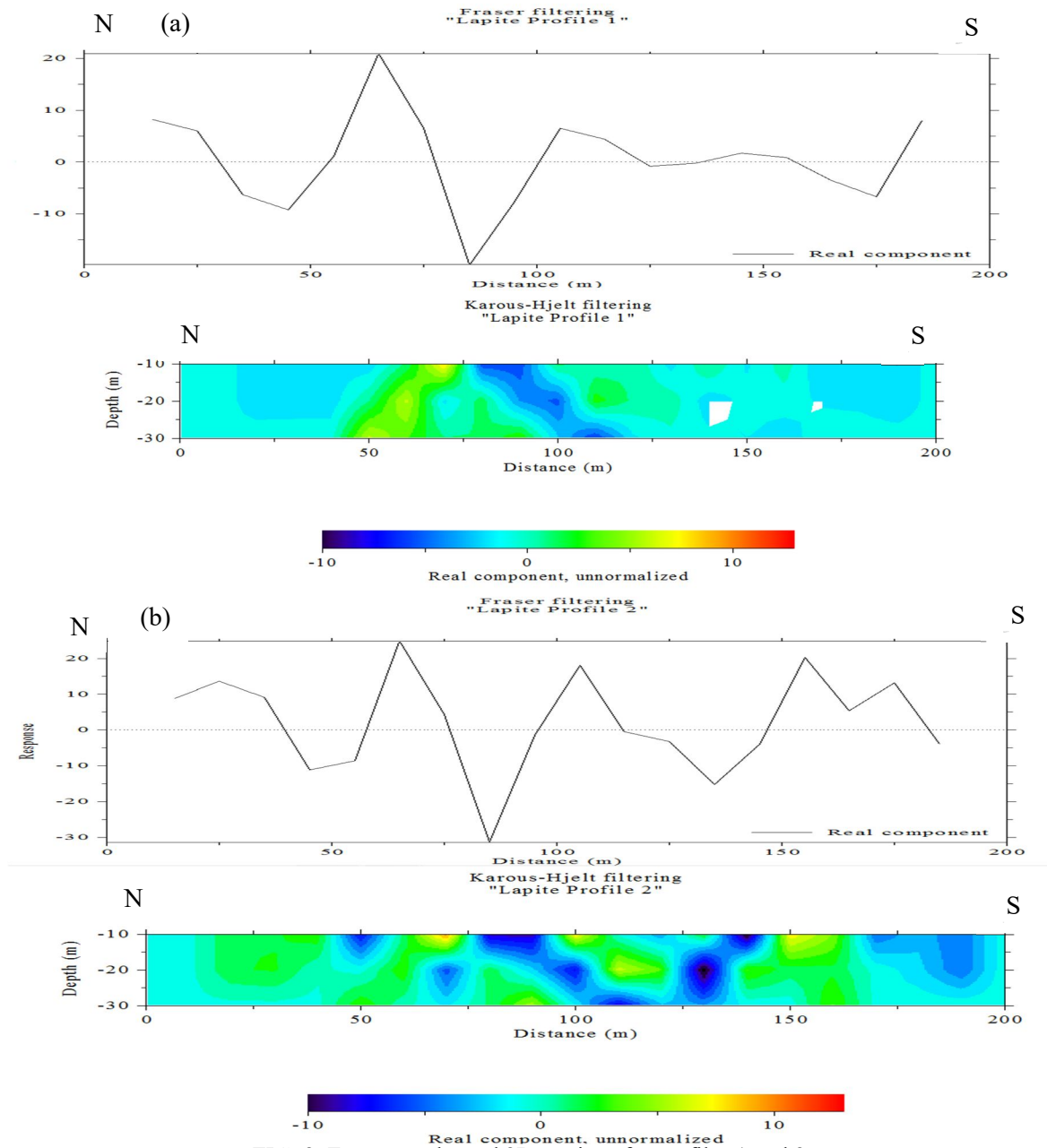
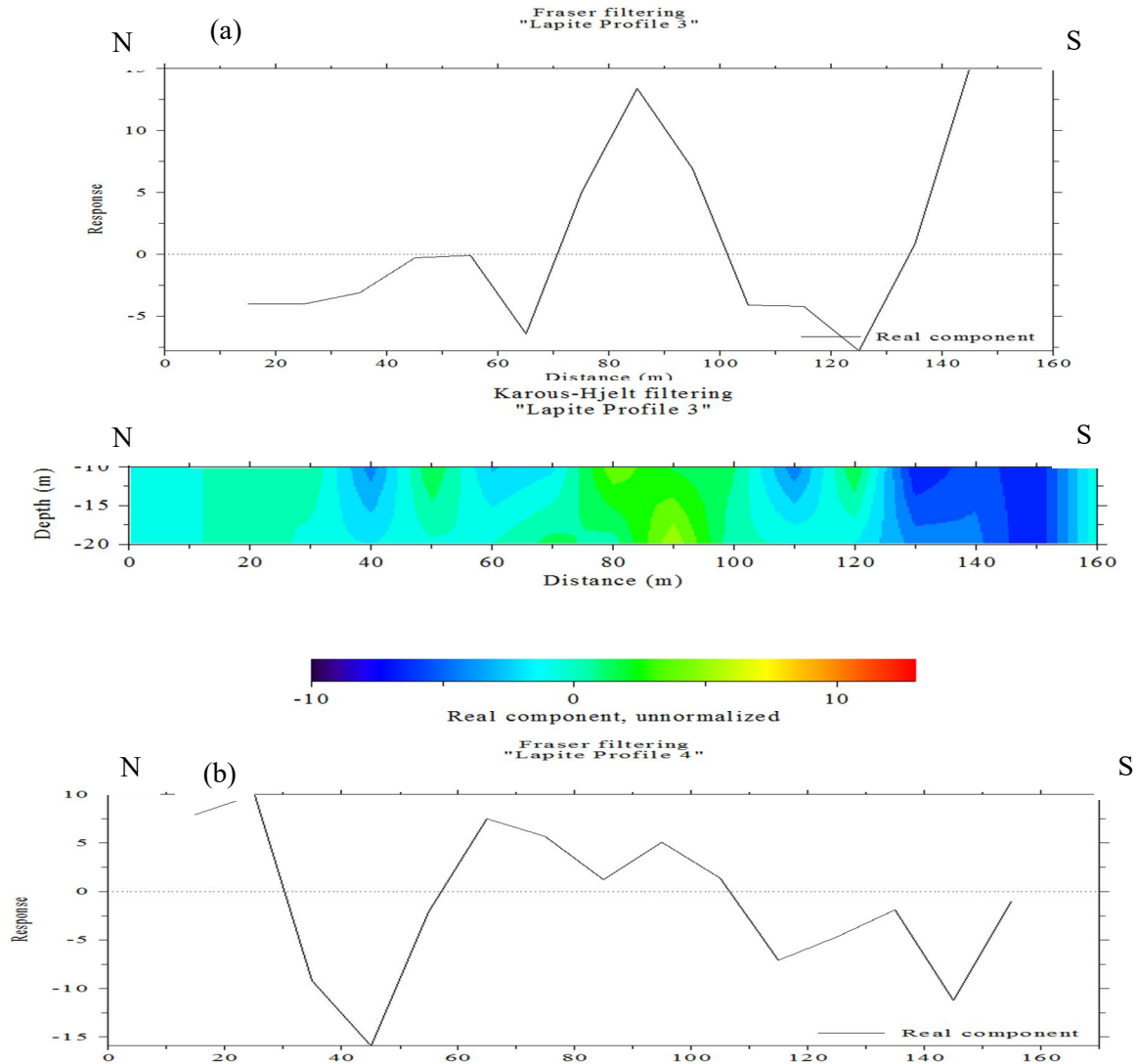


FIG. 2. Fraser graphs and 2D sections for profiles 1 and 2.

The Fraser filtering graph of the VLF-EM profile 3, located on the southern side of the landfill, reveals points diagnostic of a conductive zone, suggesting the presence of a contaminant plume at horizontal distances of 70–105 m and 135–145 m along the traverse, as illustrated in Fig. 3(a). The Karous-Hjelt pseudosection for profile 3 exhibits a slightly elevated positive conductivity anomaly, indicating leachate accumulation or a conductive structure. This centrally located conductive region extends from 78 m at the top to 98 m at the bottom of the profile, as depicted in Fig. 3(a).

A slightly high conductivity response, likely corresponding to a leachate plume or conductive lineament features, was observed at horizontal distances of 18–25 m and 55–105 m along profile 4, as seen in Fig. 3(b). The Karous-Hjelt pseudo-section for profile 4 reveals weakly conductive zones at a horizontal distance of 18–30 m and an approximate depth of 25 m. Additionally, another linear conductive body was detected at 65 m at the top, extending to 88 m at the base of the profile, as illustrated in Fig. 3(b).



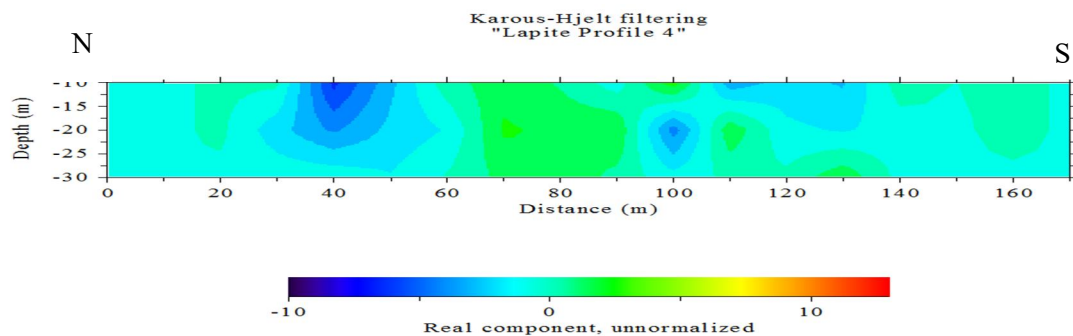
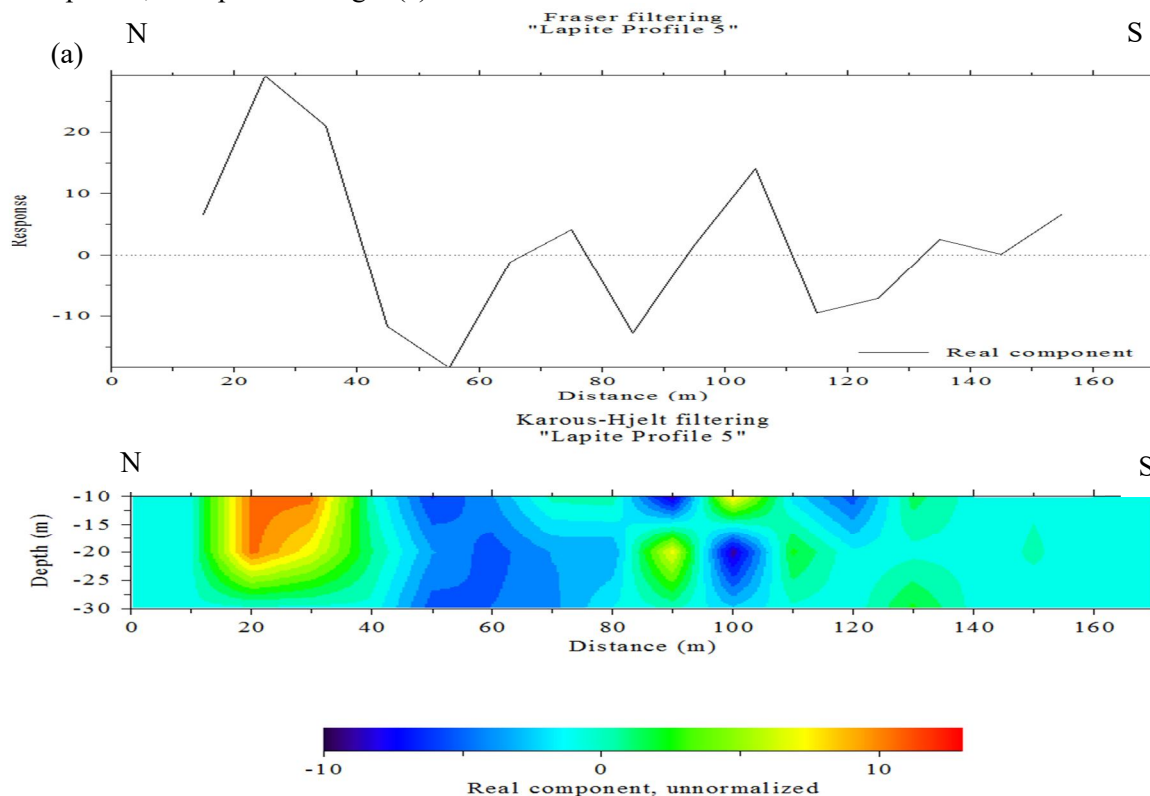


FIG. 3. Frazer graphs and 2D sections for profiles 3 and 4.

The Fraser graph of profile 5 indicates a high conductivity response at a horizontal distance of 12–42 m. The Karous-Hjelt filtering section further reveals a contaminant leachate plume or conductive subsurface structure, characterized by a higher positive current density at a horizontal distance of 12–38 m, at an approximate depth of 27 m below the surface, as shown in Fig. 4(a). Additionally, a narrow conductive region extends between station points 98–104 m, along with several other closures of conductive bodies on the profile, as depicted in Fig. 4(a).

The Fraser filtering graph of profile 6 indicates that the presence of conductive material extends from a horizontal distance of 88 m to 105 m along the profile, as seen in Fig. 4(b). The Karous-Hjelt pseudo-section of profile 6 further reveals a conductive subsurface structure or leachate accumulation, which is visible between coordinates 89 and 115 m towards the end of the profile, as shown in Fig. 4(b).



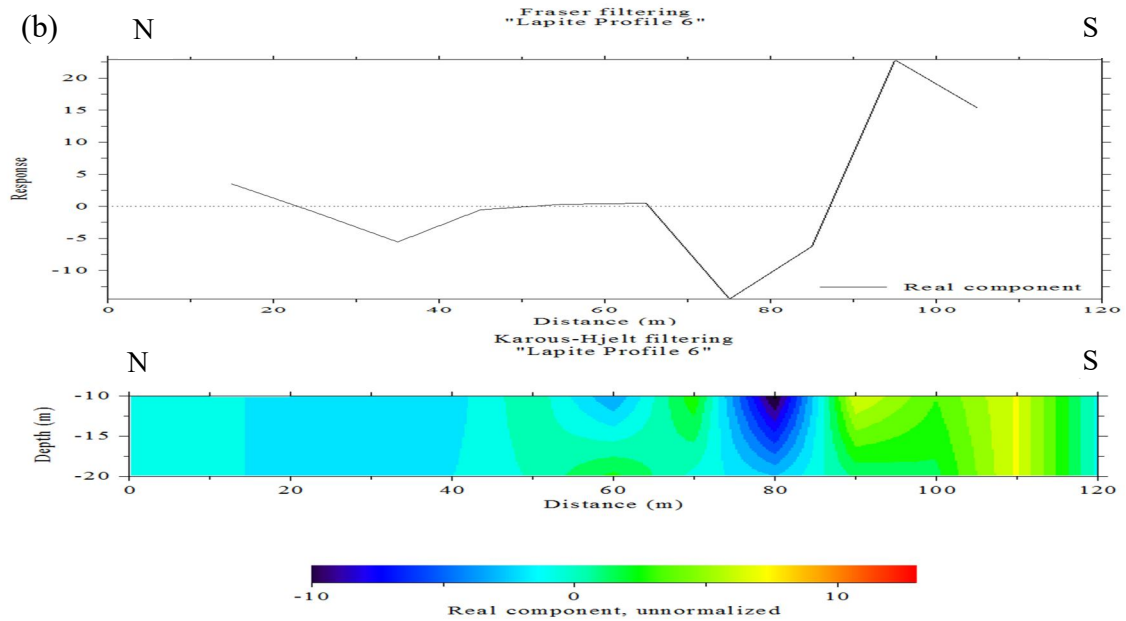
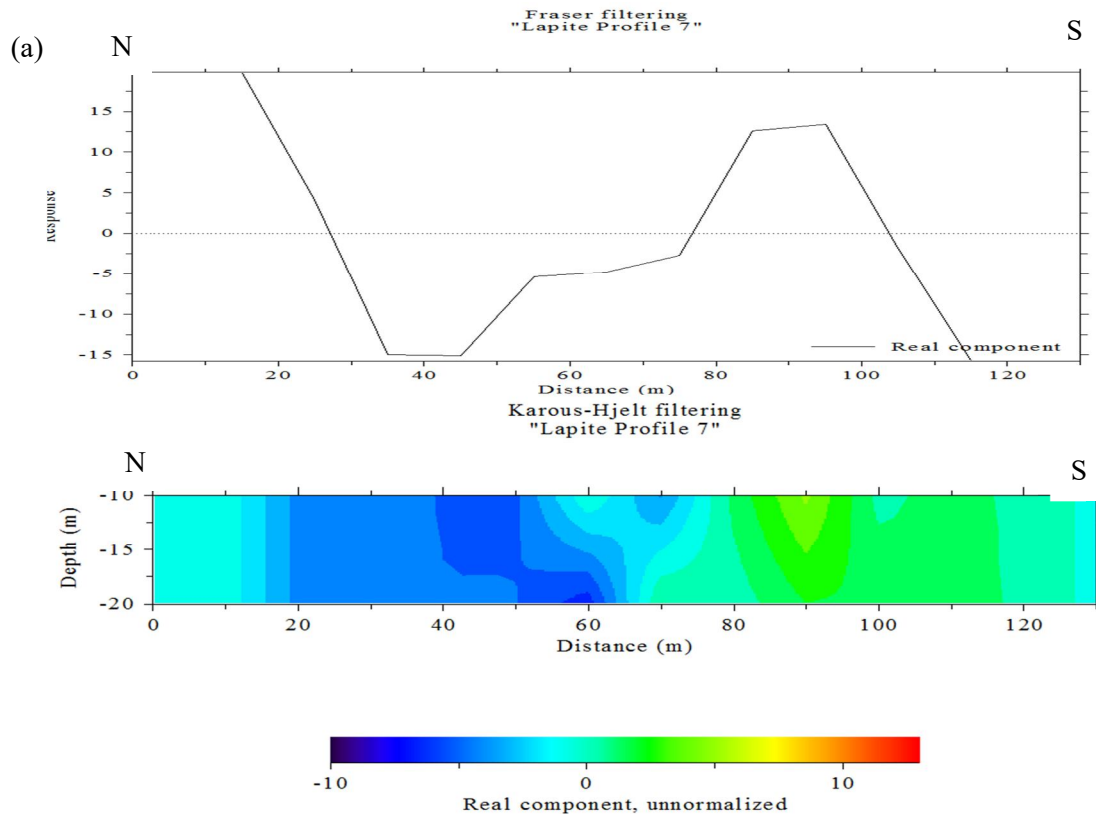


FIG. 4. Fraser graphs and 2D sections for profiles 5 and 6.

The Fraser filtering graph of profile 7, depicted in Fig. 5(a), shows the response of a slightly conductive body with a wide base at a horizontal distance of 78-105 m along the profile. The current density anomaly value on the Karous-Hjelt section of profile 7 is relatively high positive at a horizontal distance of 82-96 m, at a depth of 20 m below the surface, revealing the presence of leachate accumulation or a conductive structure.

The Fraser graph of profile 8 shows diagnostic points of a conductive zone at horizontal distances of 30-48 m and 70-92 m along the profile, as seen in Fig. 5(b). The Karous-Hjelt pseudosection of profile 8 further reveals thinly conductive bodies extending to varying depths between station distances of 38-42 m and 70-82 m across the profile.



(b)

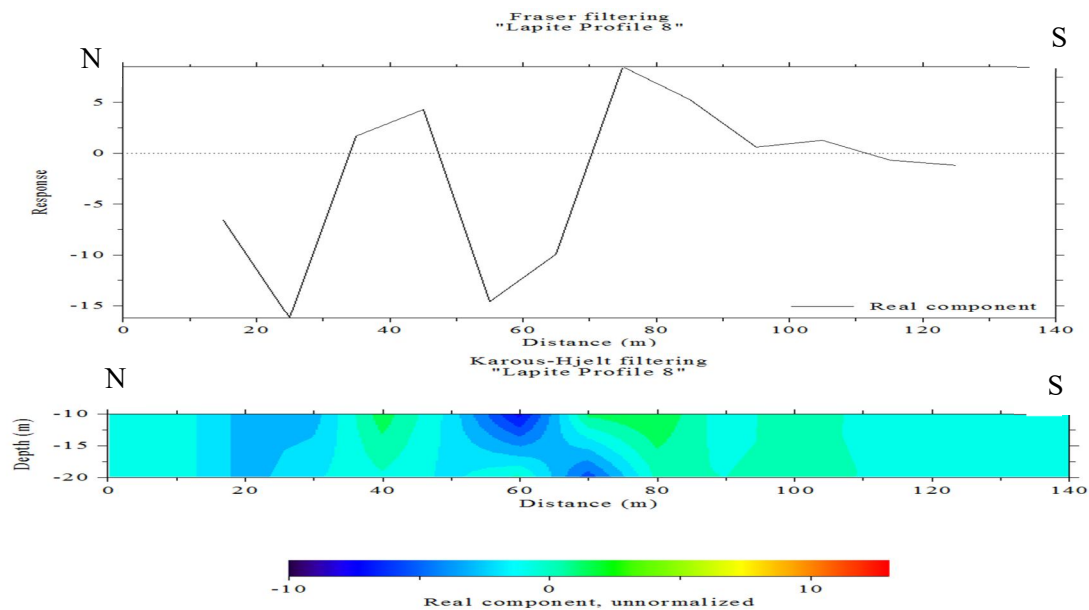
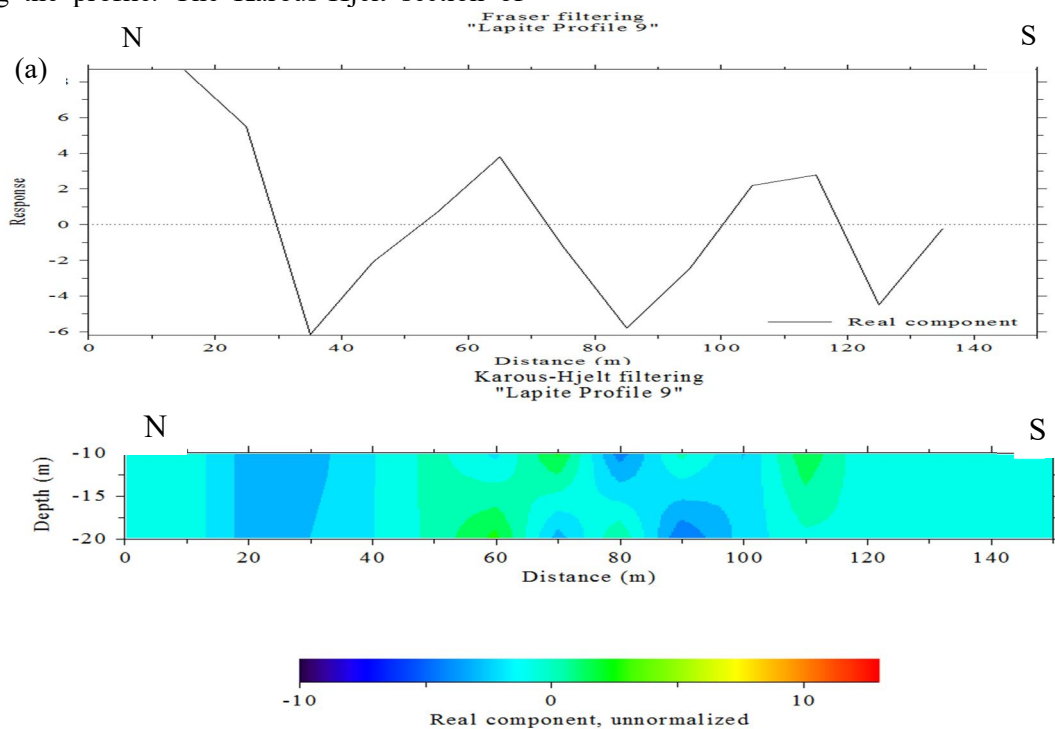


FIG. 5. Fraser graphs, VLF-EM plots of real parts, and 2D sections for profiles 7 and 8.

A low positive conductivity response on the Fraser graph of traverse 9 occurs at horizontal distances of 50–72 m and 100–120 m along the profile, as depicted in Fig. 6(a). The Karous-Hjelt pseudosection of profile 9 indicates weakly conductive bodies at 48–72 m and 106–117 m along the profile.

The Fraser graph of the control traverse, depicted in Fig. 6(b), located 300 m away from the dumpsite, exhibits a high conductivity response at a horizontal distance of 80–105 m along the profile. The Karous-Hjelt section of

the control traverse reveals a high conductivity value in the apparent current density section at a profile distance of 97–103 m. This could be attributed to clay formation beneath the ground surface rather than the presence of a leachate plume. Conductivity anomalies diminish to natural values at a horizontal distance of 152 m along the profile, indicating the absence of leachate on the control profile. However, a lower current density (highly resistive thick overburden) is observed at station positions 120–150 m along the profile.



(b)

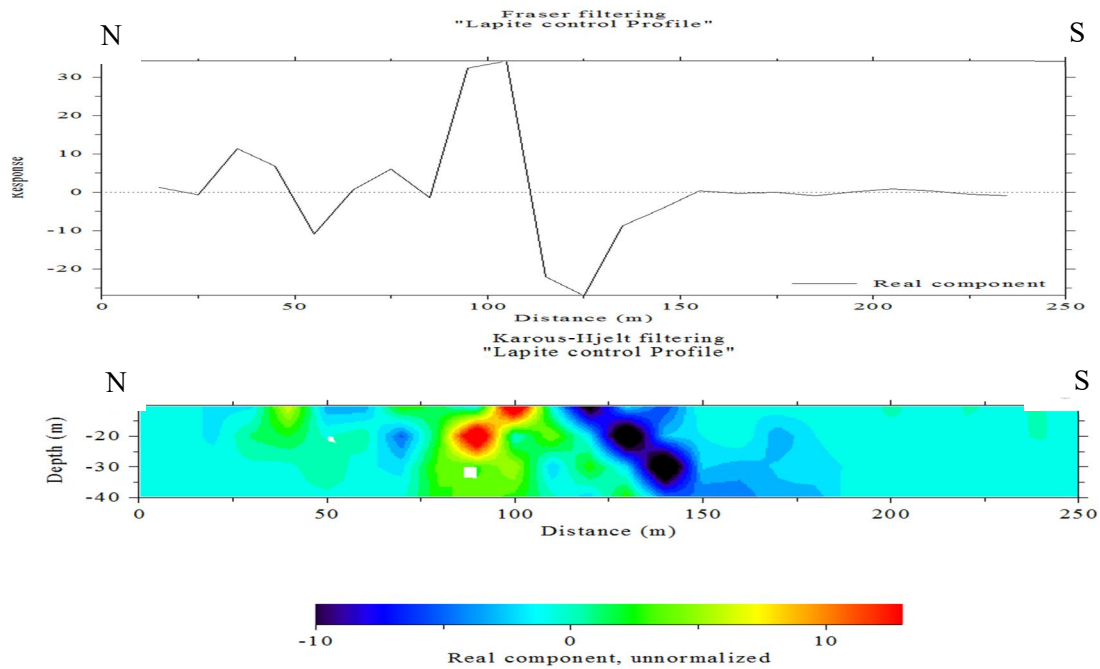


FIG. 6. Fraser graphs, VLF-EM responses, and 2D sections for profiles 9 and the control.

The VLF-EM data models depict the contaminant leachate plumes as high-conductivity values in the apparent current density pseudosections. Generally, the results from the Karous-Hjelt sections for the surveyed profiles reveal a strong presence of subsurface conductive structures and/or leachate accumulation in the western part of the dumpsite. A similar observation was reported in the interpretations of the 2D ERT inverted sections from a previous study [4].

Furthermore, Popoola and Fakunle [1] reported that the lowest resistivity value (an indication of dumpsite leachate) and the maximum horizontal distance (X_{MHD}) traveled by the leachate were observed on the western side of the dumpsite. The westward flow of the leachate plume is further supported by findings from [38], which indicate that the northwest part of the site has a relatively lower elevation compared to other areas of the dumpsite.

Conclusions

The study shows the practicability of investigating solid waste dumpsites with the VLF-EM technique. The VLF-EM method serves as a suitable technique for the detection of conductive subsurface structures/leachate accumulation zones with low resistivity values and high conductivity responses. The current density pseudo-sections indicate conductive features/ leachate plumes at different depths. A close agreement exists between the Fraser-filtered responses of the VLF-EM data and 2D current density pseudo-sections. The interpretation of the 2D current density sections suggests that the leachate plume extends deepest towards the western end of the dumpsite. Consequently, the contaminant leachate may infiltrate the shallow groundwater system located on the west side of the dumpsite.

References

- [1] Popoola, O.I. and Fakunle, M.A., An. Univ. Vest Timiş., 56 (2016) 8.
- [2] Bello, I.A., Ismail, M.N., and Kabbashi, N., Int. J. Waste Resour., 6 (2) (2016) 216.
- [3] Orhorhoro, E.K. and Oghoghorie, O.J., Appl. Sci. Environ. Manage., 23 (9) (2019) 1729.
- [4] Ganiyu, S.A., Badmus, B.S., Oladunjoye, M.A., Aizebeokhai, A.P., and Olurin, O.T., Geosciences, 5 (2) (2015) 70.
- [5] Ipeaiyeda, A.R. and Falusi, B.A., S. Afr. J. Chem., 71 (1) (2018) 166.
- [6] Ugbor, C.C., Ikwaagwu, I.E., and Ogboke, O.J., Sci. Rep., 11 (2021) 1854.

- [7] Ganiyu, S.A., Mabunmi, A.A., Olurin, O.T., Adeyemi, A.A., Jegede, O.A., and Okeh, A., *Environ. Monit. Assess.*, 193 (2021) 126.
- [8] Oluranti, O.I. and Omosalewa, A.E., *Int. J. Econ. & Fin.*, 4 (4) (2012) 219.
- [9] Abdel-Shafy, H.I. and Mansour, M.S.M., *Egypt. J. Pet.*, 27 (2018) 1275.
- [10] Liu, J., Li, Q., Gu, W., and Wang, C., *Int. J. Environ. Res. Public Health*, 16 (2019) 1717.
- [11] Ojo, A.O., Olurin, O.T., Ganiyu, S.A., Badmus, B.S., and Idowu, O.A., *Arab J. Geosci.*, 13 (2020) 620.
- [12] Akintola, O.O., Adeyemi, G.O., Ariyo, S.O., and Bodede, A.I., *FULafia J. Sci. Technol.*, 5 (2) (2019) 88.
- [13] Badmus, G.O., Ogungbemi, O.S., Enuiyin, O.V., Adeyeye, J.A., and Ogunyemi, A.T., *Sci. Afr.*, 17 (2022) e01308.
- [14] MacDonald, A.M., Bonsor, H.C., Dochartaigh, B.E.O., and Taylor, R.G., *Environ. Res. Lett.*, 7 (2012) 024009.
- [15] Ganiyu, S.A., Badmus, B.S., Oladunjoye, M.A., Aizebeokhai, A.P., Ozebo, V.C., Idowu, O.A., and Olurin, O.T., *Environ. Earth Sci.*, 75 (2016) 64.
- [16] Karlik, G. and Kaya, A., *Environ. Geol.*, 40 (6) (2001) 34.
- [17] Raji, W.O. and Adeoye, T.O., *J. King Saud Univ. Sci.*, 29 (2016) 348.
- [18] Yates, M.V. and Yates, S.R., *ASM News*, 56 (6) (1990) 324.
- [19] Memarianfard, M. and Poshtegal, M.K., *Water Resour.*, 42 (2) (2015) 247.
- [20] Abdullahi, N.K., Osazuwa, I.B., and Sule, P.O., *Ozean J. Appl. Sci.*, 4 (1) (2011) 7.
- [21] Naveen, B.P., Sumalatha, J., and Malik, R.K., *Geo-Eng.*, 9 (2018) 27.
- [22] Morita, A.K.M., Pelinson, N.S., Elis, V.R., and Wendland, E., *J. Contam. Hydrol.*, 230 (2020) 103623.
- [23] Olurin, O.T., Ganiyu, S.A., Hamed, O.S., Ogunsanwo, F.O., Akangbe, D.S., and Bolaji, A.J., *J. Solid Waste Manag.*, 47 (4) (2021) 682.
- [24] Adenuga, O.A., Popoola, O.I., Bayewu, O.O., Balogun, A., Adekoya, S.A., Oladunjoye, H.T., and Ariyo, S.O., *FUW Trends Sci. Technol. J.*, 6 (3) (2021) 945.
- [25] Ojo, A.O., Olurin, O.T., Ganiyu, S.A., Badmus, B.S., and Idowu, O.A., *Sci. Afr.*, 17 (2022) e01330.
- [26] Shendi, E., Aziz, A., Mamoun, K., and Gamal, M., *Environ. Earth Sci.*, 76 (2018) 783.
- [27] Alabi, A.A., Ganiyu, S.A., Idowu, O.A., Ogabi, A.F., and Popoola, O.I., *Appl. Water Sci.*, 11 (2021) 70.
- [28] Benson, A.K., Payne, K.L., and Stubben, M.A., *Geophysics*, 62 (1997) 80.
- [29] Monterio Santos, F.A., Mateus, A., Figueiras, J., and Goncalves, M.A., *J. Appl. Geophys.*, 60 (2006) 115.
- [30] Abdullahi, N.K., Jegede, S.I., and Ango, A., *Am. J. Eng. Res.*, 5 (10) (2016) 37.
- [31] Oladejo, O.P., Sunmonu, L.A., Ojoawo, A., Adagunodo, T.A., and Olafisoye, E.R., *Res. J. Appl. Sci. Eng. Technol.*, 5 (5) (2013) 1811.
- [32] Moradzadeh, A., Amirkhani, F., Ardejani, F.D., and Arab-Amiri, A.R., "Investigation of Contaminated Plumes Caused by Pyrite Oxidation from a Coal Refuse Pile at the Alborz Sharghi Coal Washing Plant Using VLF Geophysical Method" (Aachen, Germany, IMWA, 417, 2011).
- [33] Akintola, J.O., "Rainfall Distribution in Nigeria, 1892-1983" (Impact Publishers, Ibadan, 1986), pp. 380.
- [34] McNeill, J.D. and Labson, V., "Geological Mapping Using VLF Radio Fields, in *Electromagnetic Methods*" Ed. M.N. Nabighian (SEG, Tulsa, OK, 1991) 521.
- [35] Fraser, D.C., *Geophysics*, 34 (1969) 958.
- [36] Karous, M. and Hjelt, S.E., *Geophys. Prospect.*, 31 (1983) 782.
- [37] Pirttijarvi, M., "Karous-Hjelt and Fraser Filtering of VLF Measurements", (Manual of the KHFFILT program, 2004).
- [38] Akintola, O.O., Adeyemi, G.O., and Bodede, A.I., *J. Bioresour. Manag.*, 8 (2) (2021) 98.

Exploring the Relationship Linking the Radius and Potential Difference in Hemispherical Analyzer Energy

Ataullah. A. Alsheikh Essa^a, Khalid. Q. Kheder^b and
Abdullah I. M. Alabdullah^a

^a Department of Physics, College of Science, Mosul University, Mosul, Nineveh 00964, Iraq.

^b Department of Medical Physics, College of Science, Mosul University, Mosul, Nineveh 00964, Iraq.

Doi: <https://doi.org/10.47011/18.1.12>

Received on: 11/07/2023;

Accepted on: 10/12/2023

Abstract: The development of a hemispherical energy analyzer was a part of this research and study. The instrument was specifically designed to measure the kinetic energy of electrons inside the analyzer at various energies, while the electrons' initial kinetic energy was set to remain constant before they entered the analyzer. Different mean radius values were selected for the energy analyzer to explore their influence on its performance. The relationship between the mean radius and the potential difference within the analyzer was examined, revealing an inverse correlation. As the mean radius increased, the potential difference decreased. The performance of the analyzer was assessed based on the energy resolution achieved for each radius of the hemispherical energy analyzer. The potential difference within the analyzer decreased as the mean radius increased. In addition, in the comparison of the axial electric field values along the x-axis for different values of the mean radius, it was observed that the design with the lowest value of the central radius had the highest value of the electric field. This suggests an inverse relationship between the central radius and the electric field strength along the x-axis. Furthermore, a comparison was conducted on the axial electric potential profile values along the x-axis for different mean radius values, revealing that the design with the smallest central radius exhibited the highest electric potential.

Keywords: Hemispherical energy analyzer, Radius, Potential difference.

1. Introduction

The study of electron behavior and energy distribution is crucial for understanding various phenomena in fields such as materials science, surface physics, and nanotechnology. To obtain comprehensive insights into the energy states and trajectories of electrons, researchers have developed numerous sophisticated instruments. Among these, the hemispherical electron energy analyzer has emerged as a powerful tool for characterizing electron energies and angular distributions with exceptional precision. The hemispherical energy analyzer (HEA) is

extensively employed as an electrostatic energy selector in the realm of low-energy atomic collision physics and serves as a secondary stage following electrostatic lenses and electron gun systems [1, 2]. It pertains to an energy analyzer commonly utilized in surface science and condensed matter physics. Its primary purpose is to assess the kinetic energy and angular distribution of electrons released from a sample surface through diverse interactions like photoemission or electron scattering. The HEA disperses electrons based on their kinetic energy,

akin to how a prism disperses light according to its wavelength [3].

In 1929, it was known that electrons enter the analyzer at small angles and in a cylindrical shape within a circle of radius that depends on the speed of the electrons [4]. In 1967, Kuyatt and Simpson developed a monochromatic design in which they carefully examined the slit width and electron energy [5]. Imhof (1976) measured the transit time of electrons inside the analyzer [6]. In 1979, Jost performed a simulated spherical electron spectrometer with spherical equipotential lines in the region of the beam trajectories [7]. Benis and Zouros (2008) studied the focusing and dispersive properties of an ideal $1/r$ [8]. Dogan *et al.* (2013) established a relationship between the radius of the hemispherical electron analyzer and the entry potential [3]. The effects of fringing fields on the performance of the HEA have been studied by Sise and Zouros (2015) [10]. Tusche *et al.* (2019) published a research work concerning the imaging properties of hemispherical electrostatic energy analyzers for high-resolution momentum microscopy [1].

The hemispherical analyzer energy accelerates and concentrates electrons onto a position-sensitive detector using a combination of electrostatic or magnetic fields. The photoelectrons are concentrated in the analyzer and they are dispersed inside the analyzer depending on their kinetic energy and the electron beam that enters the analyzer with different energies. Particles with kinetic energies below the pass energy are deflected and do not reach the exit aperture. On the other hand, particles with kinetic energies equal to or greater than the pass energy overcome the electric field and continue along the hemispherical path, exiting through the exit aperture [3]. Each electron travels around a fixed-radius circle. The transit power voltage of the analyzer, which is the internal potential difference between the analyzer and the external voltage applied to it, is calculated.

Due to their high degree of spherical symmetry, hemispherical aberration analyzers are the energy filters with the most usage in the most recent electronic spectroscopic methods.

Indeed, careful consideration of the design aspects related to analyzer efficiency is crucial for the development of accurate and reliable spherical analyzers. By paying attention to

factors such as energy resolution, transmission efficiency, energy range, electric field uniformity, signal-to-noise ratio, detector sensitivity, stability, and calibration, researchers and engineers can optimize the performance of the analyzer.

In this research, the SIMION 8.0 simulation program was used. SIMION 8.0 is a widely utilized software package for calculating electric fields given an applied potential and for simulating the trajectories of charged particles within these fields. This program is particularly effective for studying electrostatic systems, such as hemispherical electron analyzers and electron sources. [2, 10].

The analyzer consists of two concentric hemispheres with radii R_1 and R_2 , which have potentials V_{in} and V_{out} , respectively, as shown in Fig. 1. The terms R_1 and R_2 refer to the inner and outer radii. R_o is the mean radius of the analyzer and denotes the path of the transit energy of the electron beam [3].

In this study, the performance of the electron energy analyzer was examined with different radii values which are obtained using the following relationship [3]:

$$R_o = \frac{R_1 + R_2}{2} \quad (1)$$

The operating characteristics including the electric field distribution (E) along the x-axis, as well as the electric potential, are calculated for each value.

If E_p , denoting pass energy, represents the kinetic energy of an electron moving within an orbit of radius R_o , the voltages applied to the inner and outer hemispheres, V_{in} and V_{out} , can be expressed as [11]:

$$V_{in,out} = V_o \left(\frac{2R_o}{R_{in,out}} - 1 \right) \quad (2)$$

The two spherical electrodes that make up the hemispherical analyzer are concentrically connected to form a hemisphere respectively as shown in Fig. 1. This figure shows that electrons at the pass energy follow a path of constant radius through the analyzer, while those with lower energy approach the inner shell and those with higher energy approach the outer shell. In this way, different energies are converted into different real space positions on the microchannel plate (MCP) detector [12].

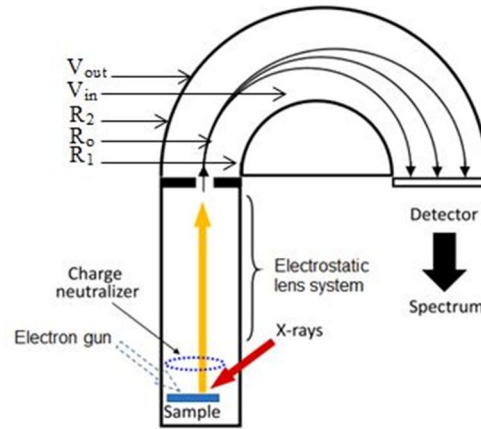


FIG. 1. Operating principle of a hemispherical electron analyzer [13].

The present research work aims to investigate the relationship between the mean radius and potential difference within the analyzer.

2. Design Considerations

When designing a hemispherical energy analyzer, numerous factors must be carefully considered to ensure optimal efficiency, accuracy, and overall performance. Among these considerations, the accuracy of energy measurement stands out as a crucial aspect. This accuracy enables the distinction between energy levels of particles, whether they are electrons or ions, within the analyzer, thereby influencing its sensitivity.

Transmission efficiency also holds significant importance in the design process. The analyzer's geometry, constituent materials, and electrical components must be meticulously selected to minimize energy loss during the transportation of particles. By addressing these factors, designers can enhance the overall performance of the analyzer.

Additionally, the energy range plays a vital role in reducing noise in the input signal. This aspect involves mitigating the effects of fringing fields, which occur when the electric field gradually diminishes away from the central region. These marginal fields can affect the behavior of particles inside the analyzer and introduce undesirable noise. By carefully managing the energy range and addressing the associated fringing fields, designers can

minimize noise and optimize the performance of the hemispherical energy analyzer [14].

In this study, the design of the hemispherical energy analyzer required a careful selection of values for the inner radius (R_1) and outer radius (R_2). The mid-gap radius between these radii, denoted as R_o and illustrated in Fig. 2, was also chosen as a fixed value. This gap served as the entry point for the electron beam, which possessed a constant kinetic energy, through the analyzer's entry aperture. The electron beams then passed through the analyzer, undergoing energy analysis and exiting through the analyzer's exit aperture with modified kinetic energy.

The values of R_1 were selected as 30, 40, 50, 60, 70, 80, 90, and 100 mm. Considering that the air gap between the two hemispheres was kept constant at 18 mm, the corresponding values of R_2 were 48, 58, 68, 78, 88, 98, 108, and 118 mm. Consequently, the values of R_o were 39, 49, 59, 69, 79, 89, 99, and 109 mm. These values were chosen to align with practical design constraints and to avoid fractional numbers, facilitating numerical calculations for the simulation.

The electron beam path and behavior can be controlled within the analyzer through applied voltages on the hemispherical energy analyzer electrodes. This setup allowed for precise measurements and enabled a detailed investigation of the behavior of particles with different kinetic energies.

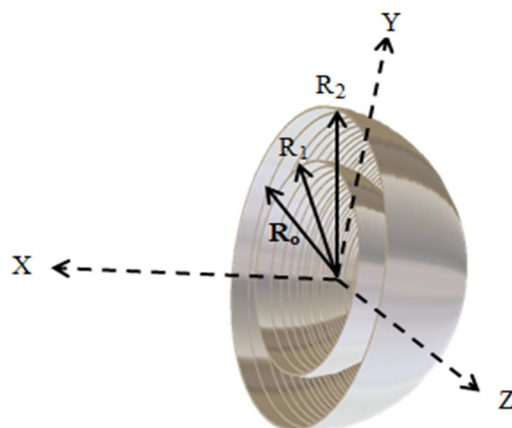


FIG. 2. Schematic representation of the HEA design showing inner, outer, and central radii (R_1 , R_2 , & R_0), respectively.

3. Results and Discussions

Based on electrostatic theory and the geometry of the analyzer, it is possible to define the relationship between the various radii and the potential field in a hemispherical analyzer. By applying an electric potential difference between the inner and outer surfaces of the hemisphere, the potential field inside the hemispherical analyzer is established. The electric field

produced by this potential difference has an impact on the trajectory of charged particles inside the detector. The chosen values of the potential difference are based on the determination of the best value of the energy resolution that depends on the potential difference. Table 1 shows the resolution values for each potential difference.

TABLE 1. The values of the resolution values for each potential difference.

Hemispherical analyzer radius (mm)	Potential difference $\times 10^{-2}$ (Volts)	Energy resolution (mm)
39	5.25	5.91
49	4.05	7.62
59	3.35	9.05
69	2.82	10.74
79	2.45	12.29
89	2.18	13.77
99	1.97	15.34
109	1.78	17.03

It was discovered that the disparity in the net internal and external potential difference applied to the hemispherical energy analyzer exhibits an inverse relationship with the rise in the central radius of the electron path. Consequently, as the central radius of the analyzer increases, the gap between the applied potential differences decreases.

The mathematical relationship between the potential difference and the radius of the hemispherical analyzer for energy can be expressed as follows:

$$\Delta V \propto 1/R_0$$

where ΔV represents the difference in electric potential and R_0 represents the mean radius of the hemispherical analyzer.

This relationship suggests that as the radius of the analyzer increases, the difference in potential difference decreases. Conversely, a smaller radius results in a greater potential difference. Understanding this relationship is important for analyzing and interpreting the data obtained from the hemispherical energy analyzer. It helps researchers adjust the applied potential difference to achieve precise energy measurements and optimize the analyzer's performance.

$$\Delta V = \frac{2}{R_0} \quad (3)$$

The axial potential distribution (V_x) was calculated for each mean radii ($R_0 = 39, 49, 59, 69, 79, 89, 99$, and 109 mm) while applying the corresponding potential differences to the inner

and outer electrodes, as shown in Fig. 3. These calculated values are represented in Fig. 4, which demonstrates that the potential initially increases

to a maximum before rapidly decreasing. Additionally, the peak potential values decrease as R_o increases.

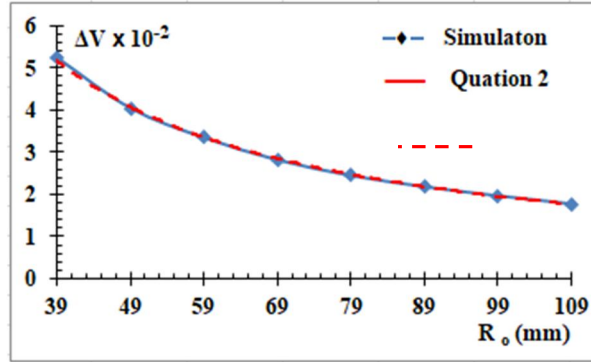


FIG. 3. Variation of the potential difference due to the changing of the mean radius of the hemispherical analyzer for the $R_o = 39, 49, 59, 69, 79, 89, 99$, and 109 mm.

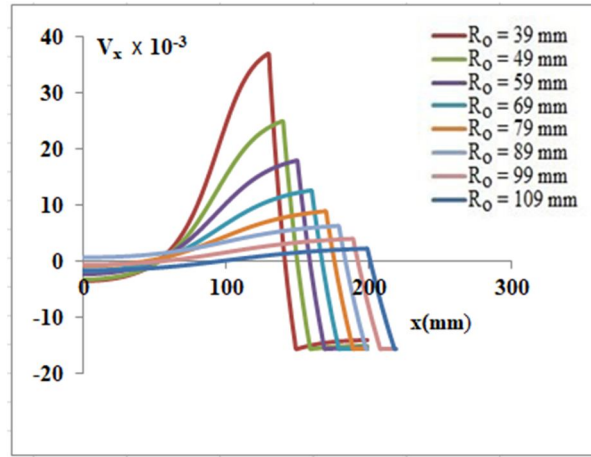


FIG. 4. Comparison of the axial electric potential (V_x) for mean radius values $R_o = 39, 49, 59, 69, 79, 89, 99$, and 109 mm calculated at $\Delta V = 5.25, 4.05, 3.35, 2.28, 2.45, 2.18, 1.97$, and 1.78 V, respectively.

The distribution of the axial field (E_x) was computed for various mean radii ($R_o = 39, 49, 59, 69, 79, 89, 99$, and 109 mm) of the HEA. During these calculations, the field differences on the outer and inner electrodes were applied based on the corresponding values shown in Fig. 3.

The results of these calculations are presented in Fig. 5. The figure illustrates that the axial field values initially increase to a maximum before rapidly declining. Furthermore, it is observed that the maximum axial field values decrease as the mean radius (R_o) increases.

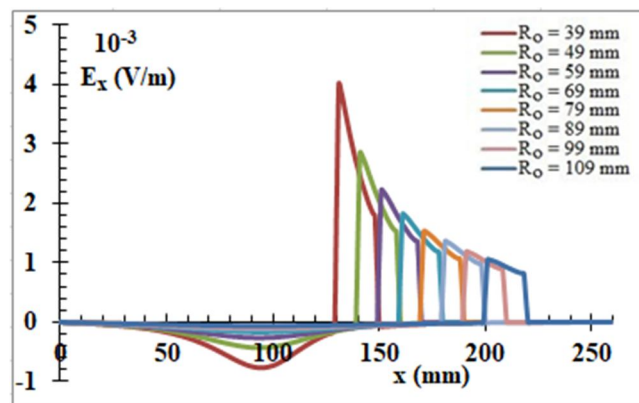


FIG. 5. Comparison of the axial field distribution (E_x) for $R_o = 39, 49, 59, 69, 79, 89, 99$, and 109 mm) calculated at $\Delta V = 5.25, 4.05, 3.35, 2.28, 2.45, 2.18, 1.97$, and 1.78 V, respectively.

4. Conclusion

This research focused on developing a hemispherical energy analyzer device and investigating the relationship between the mean radius and voltage difference. The study revealed an inverse correlation between the voltage difference and the mean radius. The design with the smallest central radius exhibited the highest electric field strength, indicating an inverse

relationship between the central radius and the electric field along the x-axis. A mathematical relationship ($\Delta V = 2/R_0$) was established to quantify the relationship between the mean radius and the applied voltage difference. These findings contribute to the optimization of hemispherical energy analyzers in scientific applications.

References

- [1] Tusche, C., Chen, Y.J., Schneider, C.M., and Kirschner, J., *Ultramicroscopy*, 206 (2019) 112815.
- [2] Alabdullah, A.I., *Optik*, 268 (2022) 16976.
- [3] Dogan, M., Ulu, M., Gennarakis, G.G., and Zouros, T.J.M., *Rev. Sci. Instrum.*, 84(4) (2013) 043105.
- [4] Hughes, A.L. and Rojansky, V., *Phys. Rev.*, 34(2) (1929) 284.
- [5] Kuyatt, C.E. and Simpson, J.A., *Rev. Sci. Instrum.*, 38(1) (1967) 103.
- [6] Imhof, R. and King, G.C., *J. Phys. E*, 9(2) (1976) 138.
- [7] Jost, K., *J. Phys. E*, 12(10) (1979) 1001.
- [8] Benis, E.P. and Zouros, T.J.M., *J. Electron Spectrosc. Relat. Phenom.*, 163(1-3) (2008) 28.
- [9] Sise, O. and Zouros, T.J., *J. Spectrosc.*, 2015 (2015) 1.
- [10] Dahl, D.A., *Int. J. Mass Spectrom.*, 200(1-3) (2000) 3.
- [11] Sise, O., Ulu, M., and Dogan, M., *Nucl. Instrum. Methods Phys. Res., Sect. A*, 554(1-3) (2005) 114.
- [12] Dogan, M., Sise, O., and Ulu, M., *Radiat. Phys. Chem.*, 76(3) (2007) 445.
- [13] Greczynski, G. and Hultman, L., *Prog. Mater. Sci.*, 107 (2020) 100591.
- [14] Sise, O., *UPB Sci. Bull., Ser. A*, 77 (2015) 213.

الجدول: تعطى الجداول أرقاماً متسلسلة يشار إليها في النص. ويجب طباعة كل جدول على صفحة منفصلة مع عنوان فوق الجدول. أما الحواشي التفسيرية، التي يشار إليها بحرف فوقي، فتكتب أسفل الجدول.

الرسوم التوضيحية: يتم ترقيم الأشكال والرسومات والرسومات البيانية (المخططات) والصور، بصورة متسلسلة كما وردت في النص.

تقبل الرسوم التوضيحية المستخرجة من الحاسوب والصور الرقمية ذات النوعية الجيدة بالأبيض والأسود، على أن تكون أصيلة وليست نسخة عنها، وكل منها على ورقة منفصلة ومعرفة برقمها بالمقابل. ويجب تزويد المجلة بالرسومات بحجمها الأصلي بحيث لا تحتاج إلى معالجة لاحقة، وألا تقل الحروف عن الحجم 8 من نوع Times New Roman، وألا تقل سماكة الخطوط عن 0.5 وبكثافة متجانسة. ويجب إزالة جميع الألوان من الرسومات ما عدا تلك التي ستنشر ملونة. وفي حالة إرسال الرسومات بصورة رقمية، يجب أن تتوافق مع متطلبات الحد الأدنى من التمايز (1200 dpi Resolution) لرسومات الأبيض والأسود الخطية، و 600 dpi للرسومات باللون الرمادي، و 300 dpi للرسومات الملونة. ويجب تخزين جميع ملفات الرسومات على شكل (jpg)، وأن ترسل الرسوم التوضيحية بالحجم الفعلي الذي سيظهر في المجلة. وسواء أرسل المخطوط بالبريد أو عن طريق الشبكة (Online)، يجب إرسال نسخة ورقية أصلية ذات نوعية جيدة للرسومات التوضيحية.

مواد إضافية: تشجع المجلة الباحثين على إرفاق جميع المواد الإضافية التي يمكن أن تسهل عملية التحكيم. وتشمل المواد الإضافية أي اشتقاق رياضية مفصلة لا تظهر في المخطوط.

المخطوط المنقح (المعدل) والأقراص المدمجة: بعد قبول البحث للنشر وإجراء جميع التعديلات المطلوبة، فعلى الباحثين تقديم نسخة أصلية ونسخة أخرى مطابقة للأصلية مطبوعة بأسطر مزدوجة، وكذلك تقديم نسخة إلكترونية تحتوي على المخطوط كاملاً مكتوباً على Microsoft Word for Windows 2000 أو ما هو استجد منه. ويجب إرفاق الأشكال الأصلية مع المخطوط النهائي المعدل حتى لو تم تقديم الأشكال إلكترونياً. وتخزن جميع ملفات الرسومات على شكل (jpg)، وتقدم جميع الرسومات التوضيحية بالحجم الحقيقي الذي ستظهر به في المجلة. ويجب إرفاق قائمة ببرامج الحاسوب التي استعملت في كتابة النص، وأسماء الملفات على قرص مدمج، حيث يعلم القرص بالاسم الأخير للباحث، وبالرقم المرجعي للمخطوط للمراسلة، وعنوان المقالة، والتاريخ. ويحفظ في مغلف واقٍ.

حقوق الطبع

يُشكّل تقديم مخطوط البحث للمجلة اعترافاً صريحاً من الباحثين بأن مخطوط البحث لم يُنشر ولم يُقدّم للنشر لدى أي جهة أخرى كانت وبأي صيغة ورقية أو إلكترونية أو غيرها. ويشتترط على الباحثين ملء أنموذج ينصّ على نقل حقوق الطبع لتصبح ملكاً لجامعة اليرموك قبل الموافقة على نشر المخطوط. ويقوم رئيس التحرير بتزويد الباحثين بأنموذج نقل حقوق الطبع مع النسخة المُرسلة للتنقيح. كما ويُمنع إعادة إنتاج أي جزء من الأعمال المنشورة في المجلة من دون إذن خطي مُسبق من رئيس التحرير.

إخلاء المسؤولية

إن ما ورد في هذه المجلة يعبر عن آراء المؤلفين، ولا يعكس بالضرورة آراء هيئة التحرير أو الجامعة أو سياسة اللجنة العليا للبحث العلمي أو وزارة التعليم العالي والبحث العلمي. ولا يتحمل ناشر المجلة أي تبعات مادية أو معنوية أو مسؤوليات عن استعمال المعلومات المنشورة في المجلة أو سوء استعمالها.

الفهرسة: المجلة مفهرسة في:

	Emerging Sources Citation Index (ESCI) Journal Impact Factor 2022 0.7
 ULRICHSWEB™ GLOBAL SERIALS DIRECTORY	

معلومات عامة

المجلة الأردنية للفيزياء هي مجلة بحوث علمية عالمية متخصصة مُحكمة تصدر بدعم من صندوق دعم البحث العلمي والابتكار، وزارة التعليم العالي والبحث العلمي، عمان، الأردن. وتقوم بنشر المجلة عمادة البحث العلمي والدراسات العليا في جامعة اليرموك، إربد، الأردن. وتنشر البحوث العلمية الأصلية، إضافة إلى المراسلات القصيرة Short Communications، والملاحظات الفنية Technical Notes، والمقالات الخاصة Feature Articles، ومقالات المراجعة Review Articles، في مجالات الفيزياء النظرية والتجريبية، باللغتين العربية والإنجليزية.

تقديم مخطوط البحث

تقدم المخطوطات إلكترونياً عن طريق موقع المجلة: <https://jip.yu.edu.jo>

ويجري تحكيم البحوث الأصلية والمراسلات القصيرة والملاحظات الفنية من جانب مُحكمين اثنين في الأقل من ذوي الاختصاص والخبرة. وتشجّع المجلة الباحثين على اقتراح أسماء المحكمين. أما نشر المقالات الخاصة في المجالات الفيزيائية النشطة، فيتم بدعوة من هيئة التحرير، ويُشار إليها كذلك عند النشر. ويُطلب من كاتب المقال الخاص تقديم تقرير واضح يتسم بالدقة والإيجاز عن مجال البحث تمهيداً للمقال. وتنشر المجلة أيضاً مقالات المراجعة في الحقول الفيزيائية النشطة سريعة التغير، وتشجّع كاتبها مقالات المراجعة أو مُستكثبيها على إرسال مقترح من صفحتين إلى رئيس التحرير. ويُرفق مع البحث المكتوب باللغة العربية ملخص (Abstract) وكلمات دالة (Keywords) باللغة الإنجليزية.

ترتيب مخطوط البحث

يجب أن تتم طباعة مخطوط البحث ببنت 12 نوعه Times New Roman، وبسطر مزدوج، على وجه واحد من ورق A4 (21.6 × 27.9 سم) مع حواشي 3.71 سم، باستخدام معالج كلمات ميكروسوفت وورد 2000 أو ما استُجد منه. ويجري تنظيم أجزاء المخطوط وفق الترتيب التالي: صفحة العنوان، الملخص، رموز التصنيف (PACS)، المقدمة، طرق البحث، النتائج، المناقشة، الخلاصة، الشكر والعرفان، المراجع، الجداول، قائمة بدليل الأشكال والصور والإيضاحات، ثم الأشكال والصور والإيضاحات. وتكتب العناوين الرئيسة بخط غامق، بينما تكتب العناوين الفرعية بخط مائل.

صفحة العنوان: وتشمل عنوان المقالة، أسماء الباحثين الكاملة وعناوين العمل كاملة. ويكتب الباحث المسؤول عن المراسلات اسمه مشاراً إليه بنجمة، والبريد الإلكتروني الخاص به. ويجب أن يكون عنوان المقالة موجزاً وواضحاً ومعبراً عن فحوى (محتوى) المخطوط، وذلك لأهمية هذا العنوان لأغراض استرجاع المعلومات.

الملخص: المطلوب كتابة فقرة واحدة لا تزيد على مائتي كلمة، موضحة هدف البحث، والمنهج المتبع فيه والنتائج وأهم ما توصل إليه الباحثون.

الكلمات الدالة: يجب أن يلي الملخص قائمة من 4-6 كلمات دالة تعبر عن المحتوى الدقيق للمخطوط لأغراض الفهرسة.

PACS: يجب إرفاق الرموز التصنيفية، وهي متوافرة في الموقع <http://www.aip.org/pacs/pacs06/pacs06-toc.html>.

المقدمة: يجب أن توضح الهدف من الدراسة وعلاقتها بالأعمال السابقة في المجال، لا أن تكون مراجعة مكثفة لما نشر (لا تزيد المقدمة عن صفحة ونصف الصفحة مطبوعة).

طرائق البحث (التجريبية / النظرية): يجب أن تكون هذه الطرائق موضحة بتفصيل كاف لإتاحة إعادة إجرائها بكفاءة، ولكن باختصار مناسب، حتى لا تكون تكراراً للطرائق المنشورة سابقاً.

النتائج: يستحسن عرض النتائج على صورة جداول وأشكال حيثما أمكن، مع شرح قليل في النص ومن دون مناقشة تفصيلية.

المناقشة: يجب أن تكون موجزة وتركز على تفسير النتائج.

الاستنتاج: يجب أن يكون وصفاً موجزاً لأهم ما توصلت إليه الدراسة ولا يزيد عن صفحة مطبوعة واحدة.

الشكر والعرفان: الشكر والإشارة إلى مصدر المنح والدعم المالي يكتبان في فقرة واحدة تسبق المراجع مباشرة.

المراجع: يجب طباعة المراجع بأسطر مزدوجة ومرقمة حسب تسلسلها في النص. وتكتب المراجع في النص بين قوسين مربعين. ويتم اعتماد اختصارات الدوريات حسب نظام Wordlist of Scientific Reviewers.

Jordan Journal of

PHYSICSAn International Peer-Reviewed Research Journal issued by the
Support of the Scientific Research and Innovation Support Fund

Published by the Deanship of Research & Graduate Studies, Yarmouk University, Irbid, Jordan

Name: الأسم:
 Specialty:..... التخصص:
 Address: العنوان:
 P.O. Box:..... صندوق البريد:
 City & Postal Code: المدينة/الرمز البريدي:
 Country: الدولة:
 Phone: رقم الهاتف:
 Fax No:..... رقم الفاكس:
 E-mail:..... البريد الإلكتروني:
 No. of Subscription: عدد الاشتراكات:
 Method of Payment: طريقة الدفع:
 Amount Enclosed:..... المبلغ المرفق:
 Signature: التوقيع:

Cheques should be paid to Deanship of Research and Graduate Studies - Yarmouk University.

I would like to subscribe to the Journal
For

- ☐ One Year
☐ Two Years
☐ Three Years

One Year Subscription Rates

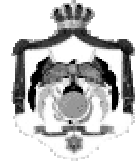
	Inside Jordan	Outside Jordan
Individuals	JD 8	€ 40
Students	JD 4	€ 20
Institutions	JD 12	€ 60

Correspondence**Subscriptions and Sales:**

Prof. Muhammad S. Bawa'aneh
 Deanship of Research and Graduate Studies
 Yarmouk University
 Irbid – Jordan
Telephone: 00 962 2 711111 Ext. 2074
Fax No.: 00 962 2 721121



جامعة اليرموك



المملكة الأردنية الهاشمية

المجلة الأردنية
للفيزياء

مجلة بحوث علمية عالمية متخصصة محكمة
تصدر بدعم من صندوق دعم البحث العلمي والابتكار

المجلة الأردنية
للفيزياء
مجلة بحوث علمية عالمية محكمة

المجلد (18)، العدد (1)، آذار 2025م / شوال 1446هـ

المجلة الأردنية للفيزياء: مجلة علمية عالمية متخصصة محكمة تصدر بدعم من صندوق دعم البحث العلمي والإبتكار، عمان، الأردن، وتصدر عن عمادة البحث العلمي والدراسات العليا، جامعة اليرموك، إربد، الأردن.

رئيس التحرير:

محمد سالم بواعنة

قسم الفيزياء، جامعة اليرموك، إربد، الأردن.
msbawaaneh@yu.edu.jo

هيئة التحرير:

محمد العمري

قسم الفيزياء، جامعة العلوم والتكنولوجيا، إربد، الأردن.
alakmoh@just.edu.jo

رياض مناصرة

قسم الفيزياء، الجامعة الأردنية، عمان، الأردن.
r.manasrah@ju.edu.jo

إبراهيم البصول

قسم الفيزياء، جامعة آل البيت، المفرق، الأردن.
Ibrahimbsoul@yahoo.com

أحمد الخطيب

قسم الفيزياء، جامعة اليرموك، إربد، الأردن.
a.alkhateeb67@gmail.com

خالد النوافلة

قسم الفيزياء، جامعة مؤتة، الكرك، الأردن.
knawafleh@yahoo.com

المدقق اللغوي: اولغا ياكوفلونا غولوبييفا غولوبييفا

سكرتير التحرير: مجدي الشناق

ترسل البحوث إلى العنوان التالي:

الأستاذ الدكتور محمد سالم بواعنة

رئيس تحرير المجلة الأردنية للفيزياء

عمادة البحث العلمي والدراسات العليا، جامعة اليرموك

إربد ، الأردن

هاتف 00 962 2 7211111 فرعي 2074

E-mail: jjp@yu.edu.jo Website: <http://jjp.yu.edu.jo>